ISAS - INTERNATIONAL SCHOOL FOR ADVANCED STUDIES

A High Resolution Hydrodynamical Code for the Study of Cosmological Structures

by

Claudio Gheller

Thesis submitted for the degree of
"Doctor Philosophiæ"

Astrophysics Sector

SUPERVISOR

Prof. John Miller

October 1997

SISSA - SCUOLA INTERNAZIONALE SUPERIORE DI STUDI AVANZATI
TRIESTE
Strada Costiera 11

TRIESTE

Table of Contents

Introduction

Most of the present cosmological models are based on the assumption that in the universe two different kinds of matter are present: the baryonic matter, which is directly observed and forms all of the bright objects, from stars to the hot gas present in X–ray clusters, and a dark, collisionless component which accounts for most of the gravitational mass in the Universe. A complete description of the behaviour of the two components can be obtained only by using numerical simulations. In particular N–body techniques have proved to be particularly effective in problems in which the dynamics is dominated by gravity, as happens for the collisionless matter or for cosmological structures on very large scales (more than $50h^{-1}$Mpc). On smaller scales different phenomena can play a significant role in the evolution of the structures. For example, pressure forces can become important on scale less that $10h^{-1}$Mpc. These phenomena can be included in numerical simulations only treating the baryonic component by a suitable hydrodynamic approach. This has the further advantage that thermodynamic variables are self–consistently calculated and quantities like the X–ray emission of the intracluster gas can be estimated and directly compared with observational data.

The development of cosmological codes which could treat both the dark and the baryonic matter has been delayed for years since they require a great computational effort, both in computer's memory and in computational time. In the last years adequate computational resources have became available and several cosmological codes have been developed. In this thesis we present a hydrodynamical code for cosmological simulations which uses

the Piecewise Parabolic Method to follow the dynamics of gas component and an N–body Particle–Mesh algorithm for the evolution of collisionless component. The gravitational interaction between the two components is regulated by the Poisson equation which is solved by a standard FFT procedure. In order to simulate cosmological flows we have introduced several modifications to the original PPM scheme which we describe in detail. Various tests of the code are presented, including adiabatic expansion, single and multiple pancake formation and three-dimensional cosmological simulations with initial conditions based on the cold dark matter scenario. The code has been used to simulate the evolution of the structures in various cosmological models both in one and in three dimensions. The one dimensional simulations allow to work with a dynamical range much larger than that achievable in three dimensional calculations. These are in fact limited by their high computational requirement. Then the one dimensional simulations can give useful information on how different scales influence the structure evolution and can be regarded as a guideline for any three dimensional application.

The three dimensional simulations are dedicated to the study of the properties of X-ray galaxy clusters in several cold dark matter models which differs for their content in baryonic matter. We have studied four models in which the baryonic density can range from 5 to 20 per cent of the total mean matter density of the universe. By comparing the predictions of the different models to a series of recent observational results, we have been able to conclude that only models with low baryonic content agree with the data, while models with larger baryon fraction are well outside the 1-σ error bar. Moreover we have found that, independently of the cosmological scenario, all the considered quantities, associated to galaxy clusters, present little redshift evolution.

The thesis is organized as follows. In chapter 1 we will give an overview of the cosmological framework, focusing on the theories of structures formation and on the the various analytical techniques developed to study this problem. Chapter 2 is dedicated to an introduction to the hydrodynamics involved here, focussing in particular on those aspects, like characteristic equations, particularly relevant for the present work. Furthermore, the equa-

tion that govern the behaviour of a fluid (both collisional and collisionless) are re–written in an expanding background using the cosmic scale factor. In chapter 3 we will describe in details the numerical method on which our code is based. We will first present the original one dimensional Piecewise Parabolic Method. Then we will show how this method must be modified in order to work in a cosmological framework and how it is extended to multi–dimensional problems. Finally we will describe the N–body Particle Mesh scheme and the modifications required in order to work together with the hydrodynamic code. In chapter 4 we will present the numerical tests by which we have verified the reliability and the accuracy of the code. Chapter 5 is dedicated to describe how the code has been paralelized, that is how it has been modified and structured in order to work on a multi–processors parallel computer. The performances of the parallel code are presented at the end of the chapter. In chapter 6 we will present a first application of our code studying the evolution of structures in the baryonic and in the dark matter in one dimensional models. Chapter 7 is dedicated to give a general introduction on the properties of clusters of galaxies, which will be the subject of the following chapter. In chapter 8 in fact, we will present a study of the properties of galaxy clusters in different cosmological models. The models are based on the standard Cold Dark Matter model, but the contribution of baryons to the total mean density of the universe is allowed to vary. Finally we will draw the conclusions and the possible future developments of this work.

1 Cosmological Overview

In this first chapter we want to give a brief description of the cosmological frame in which we have developed our work. In particular we will first analyze the Standard Model, focusing on the so–called Friedmann models. We will then talk about the theories of structure formation, both in the linear and in the non linear regime, and we will introduce the concept of power spectrum. This chapter is intended to be only an introduction to some aspects of cosmology. For a more detailed discussion we refer to Peebles (1993), Padmanabhan (1993) and Coles & Lucchin (1995).

1.1 The Standard Model

The cosmological Standard Model is based on the idea that the universe on large scales can be approximated as being homogeneous and isotropic. Under these assumptions the space–time metrics can be written in the Robertson–Walker form:

$$ds^2 = (cdt)^2 - a(t)^2 \left[\frac{dx^2}{1 - Kx^2} + x^2(d\theta^2 + \sin^2\theta d\phi^2) \right] , \qquad (1.1)$$

where x, θ and ϕ are the comoving spherical coordinates, t is the proper time, c is the speed of light, $a(t)$ is the cosmic scale factor, describing the expansion of the universe and K is the curvature parameter. The expansion factor is related to the proper distance r by the relation $r = a(t)x$. Depending on K the geometry of the universe can be positive curved ($K = 1$), flat ($K = 0$) or negatively curved ($K = -1$).

Solving the Einstein equations in absence of the cosmological constant in a Robertson–

Walker universe for a perfect fluid, we obtain the Friedmann cosmological equations:

$$\ddot{a} = -\frac{4\pi G}{3}\left(\varrho + 3\frac{p}{c^2}\right)a \tag{1.2}$$

$$\dot{a}^2 + Kc^2 = \frac{8\pi G}{3}\varrho a^2 , \tag{1.3}$$

where G is the gravitational constant and ϱ and p are the density and the pressure of the perfect fluid.

Equation (1.3) we can be written as:

$$\frac{K}{a^2} = \frac{H(t)^2}{c^2}\left(\frac{\varrho}{\varrho_c} - 1\right) , \tag{1.4}$$

where

$$\varrho_c = \frac{3}{8\pi G}\frac{\dot{a}^2}{a} , \tag{1.5}$$

is the critical density and

$$H(t) = \frac{\dot{a}(t)}{a(t)} \tag{1.6}$$

is the Hubble constant. Its present value is estimated observationally to be:

$$H_0 = 100 \times h \text{ Km s}^{-1}\text{Mpc}^{-1}, \quad 0.4 \leq h \leq 1 . \tag{1.7}$$

Since both $a(t)$ and $H(t)$ are positive quantities also $\dot{a}(t)$ is positive. This means that any pair of points in the universe move away from each other with a velocity that increases with their distance, i.e.

$$v_H(t) = \frac{dr}{dt} = \frac{d[a(t)x]}{dt} = \frac{\dot{a}(t)}{a(t)}a(t)x = H(t)r . \tag{1.8}$$

This relation is known as *Hubble law* and describes the expansion of the universe.

From equation (1.4) follows that the universe is closed, flat or open if the density parameter:

$$\Omega(t) = \frac{\varrho}{\varrho_c} \tag{1.9}$$

is greater, equal or less than one.

We define the *redshift* z of a luminous source moving with the expansion of the universe, the quantity

$$z = \frac{\lambda_0 - \lambda_e}{\lambda_e} , \tag{1.10}$$

where λ_0 is the wavelength of radiation observed at time t_0, emitted from the source with wavelength λ_e at some earlier time t_e. The redshift is related to the expansion parameter as

$$z = \frac{a(t_0)}{a(t_e)} - 1 , \tag{1.11}$$

The Friedmann equations can be solved assuming a specific equation of state. The resulting solution are known as *Friedmann models*. Particularly interesting for the following discussion are the the flat ($\Omega = 1$) models with the equation of state given by $p = w\varrho c^2$, c being the speed of light and w being defined in the range $0 \leq w \leq 1$. These are known as *Einstein–de Sitter* models. In particular, the case $w = 0$ corresponds to a collisionless fluid, while the case $w = 1/3$ corresponds to a relativistic fluid. Solving the Friedmann equations for the Einstein–de Sitter models we find that

$$a(t) = a(t_0)\left(\frac{t}{t_0}\right)^{2/3(1+w)} , \tag{1.12}$$

the mean density decreases as

$$\varrho = \varrho(t_0)\left(\frac{a(t)}{a(t_0)}\right)^{-3(1+w)} = \varrho(t_0)(1+z)^{3(1+w)} \tag{1.13}$$

and the time at which the Hubble constant has the value H_0 is

$$t_0 = \frac{2}{3H_0(1+w)} . \tag{1.14}$$

1.2 The Hot Big Bang Model

We indicate as Standard Hot Big Bang model the model of an homogeneous and isotropic universe that evolves according to the Friedmann equations whose main constituents are matter and radiation with the observed present time abundances and whose kinematic properties (i.e. Hubble expansion) match those observed in the real universe. This model

presents a singularity at the initial time $t = 0$ where the proper distance between any two points tends to zero and the energy density diverges. The singularity is known as *Big Bang.*

The present time total energy density of the universe can be expressed as

$$\varrho_0 = \varrho_{0,c}\Omega \sim 1.9 \times 10^{-29}\Omega h^2 \text{ g cm}^{-3} , \tag{1.15}$$

where $\varrho_{0,c}$ is the present value of the critical density. Observations and theoretical models set the value of Ω somewhere in the range $0.01 < \Omega < 2$. This value accounts for the contributions of radiation (r), baryons (BM), collisionless matter (DM) and possible relativistic particles (ν):

$$\Omega = \Omega_r + \Omega_{BM} + \Omega_{DM} + \Omega_\nu . \tag{1.16}$$

At present most of the radiation energy density is associated with the microwave background, which permeates all the universe at an average temperature $T_{r,0} = 2.73$ K. This corresponds to a density $\varrho_{0,r} \sim 4.8 \times 10^{-34}$g cm^{-3}. The resulting contribution to Ω is

$$\Omega_r \sim 2.6 \times 10^{-5} h^{-2} . \tag{1.17}$$

The standard model predicts the existence of a cosmological background of neutrinos. If these are massless their density is close to that of radiation, that is $\Omega_\nu \sim \Omega_r$. Furthermore, various arguments suggest that the energy density of any other possible relativistic particle must be at present much lower than that of matter.

In accordance with the *Big Bang nucleosinthesis model*, the amount of baryonic matter is constrained to be:

$$0.010 \leq \Omega_{BM} h^2 \leq 0.015 . \tag{1.18}$$

The contribution of the collisionless component depends on the particular model that one is dealing with. Also the nature of collisionless particles is model dependent. Elementary particle theory proposes several candidates for the collisionless matter. Any massive weakly interacting neutral fermion provides a possible candidate. In fact, any such particle would have existed in large number in the early universe. However, as the universe cools, the number density of these particles change depending on the details of their interactions.

Given a specific particle physics model the present time abundance of any such particle can be computed. Knowing the particle mass the contribution to Ω can be calculated. Only the particles which contribute significantly to the density parameter are of primary interest. The different properties of the various species of particles lead also to different cosmological structures formation scenarios, further discriminating between the different possibilities.

• **Equivalence epoch**

The previous discussion shows that at present the energy density of the universe is dominated by matter, while radiation gives a negligible contribution. Anyway, since in Friedmann models each component presents a different evolutive behaviour (see for example equation (1.13)) the relative "weight" of the different components changes with time. In the first phases of the evolution of the Hot Big Bang universe radiation gives a dominant contribution to the energy density of the universe. However, during the expansion of the universe the mean radiation density decreases faster than the matter density. In fact, for an Einstein–de Sitter model from equations (1.13) we obtain:

$$\varrho_r \propto a(t)^{-4} , \tag{1.19}$$

while

$$\varrho_M \propto a(t)^{-3} , \tag{1.20}$$

where with the subscript M we indicate a generic matter component. We define the *equivalence epoch* a_{eq} by the relation:

$$\varrho_r(a_{eq}) = \varrho_M(a_{eq}) . \tag{1.21}$$

From equations (1.13) and (1.21) we have

$$1 + z_{eq} = \frac{a(t_{eq})}{a(t_0)} = \frac{\Omega_M(t_0)}{\Omega_r(t_0)} . \tag{1.22}$$

In general, if there are several relativistic components, labelled i, each contributing a fraction $\Omega_{r,i}$ of the critical density, then the total relativistic contribution dominates for

$$1 + z \geq \frac{\Omega_M}{\sum_i \Omega_{r,i}} . \tag{1.23}$$

If in (1.23) we neglect all the contribution other than photons, we find $z_{eq} \sim 4.3 \times 10^4 \Omega h^2$.

• **Decoupling**

At present baryonic matter and radiation are practically completely decoupled from each other as the characteristic timescale for collisions between photons and neutral hydrogen atoms is much larger than the characteristic time for the expansion of the universe. In fact, if we assume that the collision cross–section between photons and atoms is constant, then the collision time τ_c simply scales as the inverse of the number density of atoms and therefore decreases with redshift much more rapidly than the characteristic time scale for the expansion τ_H. For example, in a flat universe,

$$\tau_c \propto \varrho_M^{-1} \propto (1+z)^{-3} , \tag{1.24}$$

$$\tau_H \propto \left(\frac{\dot{a}}{a}\right)^{-1} \propto (1+z)^{-3/2} . \tag{1.25}$$

In this last equation we have assumed matter domination, but analogous results hold for a radiation dominated universe. We define as *decoupling time* t_d the time at which

$$\tau_c = \tau_H . \tag{1.26}$$

After t_d, in absence of reheating processes, matter and radiation evolve separately. Assuming adiabatic expansion of the matter, standard thermodynamics gives

$$T_M = T_{M,0}(1+z)^2 . \tag{1.27}$$

Then the present mean value of the matter temperature would be $T_{M,0} = 0.0018$ K.

For the radiation using the relationship between the energy–density and the temperature of a black body, we find that

$$T_r = T_{r,0}(1+z) . \tag{1.28}$$

Before the decoupling matter and radiation are in equilibrium with each other at the same temperature, which presents a dependence from z intermediate between (1.27) and (1.28)

$$T \propto (1+z)^{1+\epsilon(z)} , \tag{1.29}$$

with $0 \leq \epsilon(z) \leq 1$.

• **Recombination**

At very high temperatures (high z), the matter is fully ionized. As T decreases, the fraction of ionized atoms falls. Therefore, there exist a time t_{rec} before which the matter is completely ionized and after which the ionization is very small. This transition is usually called *recombination*. The recombination is not instantaneous process and actually continues over a relatively large range of z. However a reliable choice of the redshift at which it takes place is $z_{rec} \sim 1500$.

• **The Standard Nucleosynthesis Model**

A major success of the Hot Big Bang scenario is the prediction of the cosmological origin of light elements (that is elements no more massive than ^{7}Li) with abundances which agree with observational data. The abundance of a given element is defined as the ratio between the mass of that element contained in a representative volume and the total mass in the same volume.

When the universe is at a temperature of about 10^9K light elements can be produced by the chain of reactions:

$$n + \nu_e \rightleftharpoons p + e^- \,, \quad n + e^+ \rightleftharpoons p + \bar{\nu}_e \tag{1.30}$$

$$n + p \rightarrow \mathrm{D} + \gamma \tag{1.31}$$

$$\mathrm{D} + \mathrm{D} \rightarrow {}^3\mathrm{He} + n \,, \quad {}^3\mathrm{He} + \mathrm{D} \rightarrow {}^4\mathrm{He} + p \tag{1.32}$$

$$\mathrm{D} + \mathrm{D} \rightarrow {}^3\mathrm{H} + p \,, \quad {}^3\mathrm{H} + \mathrm{D} \rightarrow {}^4\mathrm{He} + n \tag{1.33}$$

$$\mathrm{D} + \mathrm{D} \rightarrow {}^4\mathrm{He} + \gamma \tag{1.34}$$

where γ is the photon, n is the neutron, p is the proton, e^- and e^+ are the electron and the positron, ν_e and $\bar{\nu}_e$ are the neutrino and the antineutrino of the electron, γ is the photon and D indicates the deuterium. The production of heavier elements is suppressed by two factors. First direct reactions between two He nuclei or between He and H lead to nuclei with atomic masses 8 or 5. Since there are not tightly bound isotopes with such

masses , these reactions do not lead to any other synthesis. The three bodies interaction $^4\mathrm{He} + ^4\mathrm{He} + ^4\mathrm{He} \rightarrow ^{12}\mathrm{C}$ is suppressed because of the low number density of ^{4}He nuclei. This reaction helps further synthesis in stellar interiors, where much higher densities are reached. Second, the interacting nuclei must overcome their Coulomb repulsion. This become higher as the charge number increases, suppressing the reaction rate.

Small amounts of ^{7}Li are produced by the following reactions

$$^4\mathrm{He} + ^3\mathrm{H} \rightleftharpoons ^7\mathrm{Li} + n \tag{1.35}$$

$$^4\mathrm{He} + ^3\mathrm{He} \rightleftharpoons ^7\mathrm{Be} + \gamma\ , \quad ^7\mathrm{Be} \rightarrow ^7\mathrm{Li} + e^+ + \nu_e\ . \tag{1.36}$$

In this last reaction a small amount of ^{7}Be is left as a residue.

The observed cosmic abundance for H is $X \sim 0.76$ and that for ^{4}He is $Y \sim 0.24$. The average number density of ^{3}He+D, ^{7}Li and ^{7}Be are respectively less than 10^{-4}, 10^{-10} and 10^{-11} that of hydrogen. The Standard Nucleosynthesis model gives results which agrees with observational estimates if

$$0.010 \leq \Omega_{BM} h^2 \leq 0.015\ . \tag{1.37}$$

1.3 Problems of the Hot Big Bang Model

• The Big Bang

Standard Big Bang cosmology presents several unsolved problems. The first is that of the existence of the Big Bang singularity. This is likely to be just a consequence of extending a model based on the General Relativity into a situation where this theory is no longer valid. New laws of physics are needed to describe the behaviour of matter close to the Big Bang, when density and temperature are much higher than those achieved in laboratory experiments and when quantum effects are important on cosmological scales.

• The Particle Horizon

Since the universe has a finite age and information travel at most at the speed of light, there can exist a maximum distance between particles which have been able to interact at

some time in the past. This distance is called *particle horizon* and is defined as

$$r_H(t) = a(t) \int_0^t \frac{c\, ds}{a(s)} . \tag{1.38}$$

The presence of the horizon is hard to reconcile with the assumed isotropy of the universe, as this requires that there is a correlation between regions outside the respective horizons which have never got in touch with each other. This is for example what happens for the cosmic microwave radiation. The observed high isotropy of the microwave radiation implies a high degree of homogeneity and isotropy of the radiation at the time of recombination. But if we calculate the horizon of two regions which are in opposite direction, we find out that they never had the possibility of causal contact until t_{rec}.

• **The Flatness Problem**

The present value of the density parameter is of the order of the unity. It can be shown that the quantity $|\Omega - 1|$ tends to increase with time (unless $\Omega = 1$, in which case it remains always constant). In order to recover the estimated present value of this parameter we must have that at very early time (close to the planck time, $t_P = 10^{-43}$s after the Big Bang) the density were extremely close to one

$$\Omega(t_P) = 1 + (\Omega_0 - 1) \times 10^{-60} . \tag{1.39}$$

This create the so–called flatness problem, which consists in explaining why the density is so close to the critical value.

• **The Cosmological Constant Problem**

All known symmetries of nature and principles of general relativity allow for the presence of a term Λ in the Einstein equations which acts like matter with energy density $\varrho_\Lambda \propto \Lambda$ and pressure $p_\Lambda \propto -\Lambda$. The quantity Λ is called *cosmological constant.*

Observational data suggest that at present time the cosmological constant should be very small:

$$|\Lambda| \leq 10^{-55}\text{cm}^{-2} . \tag{1.40}$$

The cosmological constant problem lies in the fact that the values of Λ and of all the derived quantities are astonishingly and, apparently, "unnaturally" small. For example,

we can define a mass associated to Λ as $(|\varrho_\Lambda hc)^{1/4}$, where h is the Plank constant, which comes out to be less than 10^{-32}eV, much lower than the upper limit of the photon mass $m_\gamma < 3 \times 10^{27}$eV.

However, the possible consequences of having a non–null cosmological constant can be very interesting. In fact, although its present value should be too small to have relevant effects on the evolution of the universe, it could have been in the past the dominant energy density component. If we consider the Einstein equations with a cosmological constant we obtain the Friedmann equation in the form

$$\ddot{a} = -\frac{4\pi G}{3}\left(\varrho + 3\frac{p}{c^2} - 2\varrho_\Lambda\right) a \tag{1.41}$$

$$\dot{a}^2 + Kc^2 = \frac{8\pi G}{3}(\varrho + \varrho_\Lambda)a^2 \ . \tag{1.42}$$

Therefore if, before a certain time, ϱ_Λ is the dominant contribution to the energy density, it can happen that $\ddot{a} > 0$ and, therefore, the initial singularity can be avoided. In addition during this Λ dominated period the expansion of the universe is accelerated and the size of the horizon grows very rapidly. This event is called *inflation*. Solving the Friedmann equations assuming for example $w = -1$ gives the so called *standard inflationary* model for which

$$a(t) \propto \exp(t) \ . \tag{1.43}$$

The inflationary model solves the problems of the horizon and of the flatness. The former is solved observing that, due to their fast expansion, scales that previously were in causal contact, at some epoch exit the horizon, that is they become larger than the size of the horizon. As long as these scales are outside the horizon they do not evolve causally. At the end of inflation, they can enter again the horizon with the "memory" of the initial conditions. Therefore regions that are disconnected can have the same properties. The flatness problem is solved observing that during inflation, the curvature radius of the universe, measured on a fixed physical scale, increases exponentially. Thus, a piece of space looks essentially flat after inflation even if it had measurable curvature before.

The present day interpretation of the cosmological constant is as follows: ϱ_Λ and p_Λ represent the density and the pressure of the quantuum vacuum, which is the ground state of a quantum system, characterized by the equation of state $p_\Lambda = -\varrho_\Lambda c^2$. Inflation is a consequence of a phase transition in the early stages of the evolution of the universe. During this phase the density of the vacuum state of the scalar field which drives the transition became the dominant contribution to the energy density. Then the expansion factor grows accelerated and inflation can take place.

1.4 The Evolution of Cosmic Structures – Linear Phase

The hot Big Bang scenario is based on the hypothesis that the universe can be approximated as being homogeneous and isotropic. This must be actual regarded in a "statistical" sense, as it is clear that disomogeneities and anisotropies are present in the form of stars, galaxies, clusters of galaxies and any other object. Therefore homogeneity and isotropy must be sought in averaged properties of the universe where the average must be taken on volumes large enough to represent a fair sample of the underlying structure. For cosmological structures like galaxies and galaxy clusters this means samples of tens, if not hundreds, of megaparsecs. The birth and the evolution of these structures is described by models which are based on the assumption that the observable large scale structure of the universe has developed through gravitational instability of small fluctuations in a smooth primordial density field. In the following sections we will give an overview of the basic characteristics and properties of this process.

1.4.1 Jeans Theory

The gravitational instability theory, or Jeans theory, demonstrates that, starting from a static fluid which is, on average, homogeneous and isotropic, small fluctuations in the density and velocity fields, can evolve with time. In particular overdensities can grow due to attractive gravitational forces as long as pressure forces are negligible and finally can collapse to a gravitationally bound object. The simple criterion needed to decide whether a

fluctuation will grow with time is that the typical lengthscale of a fluctuation has to be greater than the *Jeans length*, λ_J, of the fluid. An approximate determination of λ_J can be obtained by the following simple considerations. At a given instant let us assume a spherical overdensity of radius λ in a medium of mean density ϱ_0. The fluctuation grows if the self–gravitational force per unit mass, F_g, overcomes the pressure force per unit mass, F_p:

$$F_g \sim \frac{G\varrho_0\lambda^3}{\lambda^2} > F_p \sim \frac{p\lambda^2}{\varrho_0\lambda^3} \sim \frac{c_s^2}{\lambda} , \tag{1.44}$$

where c_s is the sound speed. This relation implies that growth occurs for $\lambda > \lambda_J \sim c_s(G\varrho_0)^{-1/2}$. When this relations is not satisfied, pressure forces are greater than the self–gravity and the perturbation propagates like an acoustic wave with wavelength λ at velocity c_s. Associated to the λ_J we can define the *Jeans mass*

$$M_J = \frac{4}{3}\pi\varrho_0\lambda_J^3 . \tag{1.45}$$

A linear analysis of the evolution of the perturbations gives, for the fluctuations in the density field,

$$\delta = \frac{\delta\varrho}{\varrho_0} = \delta_0 \exp[i(\mathbf{k}\cdot\mathbf{r} \pm |\omega|t)] , \tag{1.46}$$

for $\lambda < \lambda_J$, and

$$\delta = \frac{\delta\varrho}{\varrho_0} = \delta_0 \exp[i(\mathbf{k}\cdot\mathbf{r})] \exp(\pm|\omega|t)] , \tag{1.47}$$

for $\lambda > \lambda_J$. In these equations δ is the density contrast, $\mathbf{k}$ is the wavevector and ω is the frequency. Equation (1.46) represents two sound waves that propagates in directions $\pm\mathbf{k}$, while equation (1.47) is a stationary wave of either increasing or decreasing amplitude.

Similar considerations holds also for a collisionless fluid, for which $p = 0$, provided the sound speed is replaced by a characteristic velocity v_* of order of the mean square velocity of the collisionless particles that compose the fluid. In this case if $\lambda < \lambda_J$ the velocity dispersion of the particles is too large for them to be held by self–gravity, and they undergo free streaming, a process which smears out and dissipates the fluctuations.

1.4.2 Jeans Theory in Friedmann Models

The original Jeans theory is formulated for a static universe; therefore it cannot be applied to an expanding cosmological model. The theory is further complicated by the presence of a multicomponent medium (radiation, collisionless and baryonic matter) and also general relativistic correction should be taken into account.

In an expanding model the density diminishes with time due to the increasing size of the universe. The linear analysis shows that we can still calculate a Jeans length λ_J of the same form of of that defined in the static case. Fluctuation on scale less that λ_J oscillate like acoustic waves. Fluctuations with wavelength greater than λ_J are unstable but grow at a reduced rate compared to the exponential form obtained in the previous section. In fact the fluctuations must attract material which is moving away according to the general expansion of the universe. The specific rate of expansion depends on which component dominates the energy density. For example, for a flat matter dominated universe we have:

$$\delta_+ \propto t^{2/3}, \qquad \delta_- \propto t^{-1}\,, \tag{1.48}$$

where δ_+ and δ_- are the growing and decaying modes respectively. For a flat universe dominated by radiation, instead, we have:

$$\delta_+ \propto t, \qquad \delta_- \propto t^{-1}\,, \tag{1.49}$$

1.4.3 Evolution of the Perturbations

The evolution of the cosmological perturbations depends on the properties of the medium in which they develop. In a universe composed by radiation, baryonic and collisionless matter we can distinguish between curvature and isocurvature perturbation modes. In the first mode all the three components are perturbed ($\delta_r \sim \delta_{BM} \sim \delta_{DM}$), while for the second mode only a non dominating component is perturbed. A further distinction can be made according to the characteristics of the dominating component of the universe. Several important effects, strictly related to these properties, can influence the basic picture of structure formations given by the gravitational instability model.

• **Evolution of the Jeans Length.**

The Jeans length depends both on the sound speed and on the density of the medium. Therefore it evolves with time. In general for baryonic matter, λ_J grows until the recombination and then it abruptly drops below scales of cosmological interest. Also for dark matter it grows until the equivalence time and then drops. We indicate with $\lambda_{J,M}$ the maximum value of the Jeans length in its evolution. A perturbation in the baryonic matter on a scale $\lambda \leq \lambda_{J,M}$ grows until $\lambda < \lambda_J$, then spends a certain time oscillating like an acoustic wave and at last start growing again. A perturbation with $\lambda > \lambda_{J,M}$, instead, never becomes an acoustic wave.

• **Dissipation of Acoustic Waves.**

Before recombination ionized baryonic matter and radiation are tightly coupled. The interaction of the two components leads to the phenomenon of diffusion, which scatters particles toward regions outside the perturbation. This cause the decrease of the amplitude of a perturbation until it is completely erased. The characteristic scale below which perturbations are erased is the dissipation scale λ_D. Also λ_D grows with time until recombination, reaching a maximum value $\lambda_{D,M}$. Then it drops below scales of interest. It turns out that, at any time, $\lambda_D < \lambda_J$: all the acoustic waves below $\lambda_{D,M}$ are dissipated. Therefore, after recombination, the only perturbation that have survived and that can still evolve according to the gravitational instability scenario are those on scales above $\lambda_{D,M}$.

• **Free Streaming.**

Collisionless particle cannot evolve as coherent acoustic waves. Below the Jeans scale, gravity is not sufficient to control their behaviour and they move freely and randomly erasing any fluctuation on scale $\lambda < \lambda_J$.

• **The Mezaros effect.**

A generic feature of models dominated by a relativistic component is the "stagnation" or *Mezaros* effect. This effect influence the evolution of the perturbation in the matter until the universe is radiation dominated, that is until the equivalence epoch. As long as the universe is radiation dominated the growing mode perturbations remain "frozen" as the

expansion of the universe is so fast that it prevents the gravitational collapse.

• **Radiation Drag.**

This effect is present only in models in which the baryonic component is perturbed while the radiation is smoothly distributed. Perturbations on scales larger than the Jeans length do not grow due to a kind of viscous friction force acting on particles which move through the radiation background. This phenomenon is present until matter and radiation decouple.

1.5 The Spectrum of the Fluctuations

A generic perturbation in the density field can be represented as a superposition of plane waves of the form

$$\delta(\mathbf{r}) = \int_{\mathbf{k}} \delta_{\mathbf{k}} \exp(i\mathbf{k}\cdot\mathbf{r}) d\mathbf{k} , \tag{1.50}$$

where $\mathbf{k}$ is the wave vector and $\delta_{\mathbf{k}}$ is the $\mathbf{k}$ (complex) Fourier coefficient. An estimate of the dispersion of the fluctuations field is given by the variance σ defined as

$$\sigma^2 = \frac{1}{2\pi^2}\int_0^\infty P(k)k^2 dk , \tag{1.51}$$

where $P(k)$ is the power spectrum that, due to the homogeneity and isotropy of the universe, depends only from the norm of the wave vector k. The power spectrum is defined as

$$P(k) = \langle|\delta_{\mathbf{k}}|^2\rangle , \tag{1.52}$$

where $\langle|\delta_{\mathbf{k}}|^2\rangle$, is the average of the square norm of the $\mathbf{k}$ Fourier coefficient calculated over an ensemble of realizations of the same models. For each k, the quantity $P(k)$ indicates the "weight" of the k–th wave mode of the fluctuations field.

The variance σ^2 contains no information about the relative contribution to the fluctuations from the different modes. Furthermore it may also be formally infinite, if integral (1.51) does not converge. Therefore it is convenient to define a statistical description of the fluctuation field as a function of some resolution scale R. Let $\langle M\rangle$ be the average mass in a spherical volume V of radius R

$$\langle M\rangle = \frac{4}{3}\pi\langle\varrho\rangle R^3 . \tag{1.53}$$

We can define the *mass variance* inside the volume V to be the quantity $\sigma^2(M)$ given by:

$$\sigma^2(M) = \frac{\langle (M - \langle M \rangle)^2 \rangle}{\langle M \rangle^2} , \tag{1.54}$$

where the average is calculated over all spatial volumes V. In terms of the spectrum of the fluctuations the mass variance is calculated as

$$\sigma^2(M) = \frac{1}{2\pi} \int_0^\infty P(k) W^2(kR) k^2 dk , \tag{1.55}$$

where $W(kR)$ is the *window function* which determines the weights of the various wavelengths λ to the variance such that the dominant contribution is given by the components with $\lambda \geq R$.

The initial spectrum of fluctuations is indicated as the *primordial* power spectrum. It is usual to assume that $P(k)$ is given, at least for a certain range of k, by the power–law

$$P(k) = Ak^n , \tag{1.56}$$

where the exponent n is the *spectral index* while A is the normalization. The particular case in which $n = 1$ is known as *Harrison–Zel'dovich* spectrum. It was first proposed in the 70's and taken to be the most natural form, according to various physical arguments. Further motivations for this models arrived in 1982 with the inflationary models which predicts a spectrum in scale–invariant form.

As far as the evolution of the perturbation spectrum is concerned, the theory depends on the nature of the particles that dominate the universe at various epochs (radiation, baryonic or dark matter) and on the nature of the fluctuations themselves (adiabatic or isothermal, curvature or isocurvature). The combined effect of the various processes involved in the evolution of the primordial spectrum can be summarized in a single quantity, the *transfer function* $T(k)$ which relates the evolved power spectrum to its original form via the transformation:

$$P(k, t_f) = \left[\frac{b(t_f)}{b(t_p)}\right] T^2(k, t_f) P(k, t_p) , \tag{1.57}$$

where t_p is the time at which the primordial spectrum $P(k, t_p)$ formed and t_f is the time at which the considered modulating processes have stopped; since most of these processes

stop at the recombination it is appropriate to take $t_f \geq t_{rec}$. Finally, $b(t)$ is the liner growth factor for perturbations above the Jeans length (e.g. $b(t) \propto t^{2/3}$ for an Einstein de Sitter matter dominated universe).

1.5.1 The Origin of the Fluctuations

Theories which explain the origin of the primordial fluctuations have still a speculative character. The most popular rely on a phase transition in the early universe which leads to inflationary expansion of the universe or to the formation of topological defects. In an inflationary scenario the density perturbations originate in quantum fluctuations and they get blown up to the size of cosmological structures during the inflationary phase. The produced spectrum is found to be nearly perfectly scale free in most of the inflationary scenarios. In fact, the spectrum of quantum fluctuations is constant during the inflationary stage and produces equal power on every scale. The perturbations in the density field can be produced also by topological defects like cosmic strings. Very roughly cosmic strings can be imagined as one–dimensional very massive, fast moving structures. Strings through their motion produce fluctuations in the density field. Strings of different size perturb different scales. The resulting spectrum of fluctuations does not have to be scale–free but it *can be.*

1.6 Some Models

The first cosmological models incorporating structure formation described in terms of gravitational instability theory were proposed in the 1970s. These were two–components models containing baryons and radiation. The perturbations could involve both matter and radiation which were coupled together so that $\delta_{BM} \sim \delta_r$, where δ_r indicates the fluctuation in the radiation field. In this case we talk about *adiabatic perturbations* (corresponding to the curvature modes). Alternatively we can have that only the baryonic component presents fluctuation, the radiation field being unperturbed. This is the case of the *isothermal perturbations* (corresponding to isocurvature modes). Soon it was realized that both of these models when compared to observations presented substantial incompatibility. At the same

time the discovery of the existence in the universe of the dark matter led to three components cosmological models. In the 80s, the most fashionable models become the Hot Dark Matter (HDM) and Cold Dark Matter Models (CDM). The first are characterized by the assumption that the universe is dominated by collisionless particles with a very large velocity dispersion. In the second the universe is again dominated by collisionless particles but with a small velocity dispersion. Due to the differences in the typical velocity of the particles the two models give rise to completely different scenario of structure evolution. HDM particles have a very high Jeans length (this quantity being proportional to the typical velocity of the particles) with a $\lambda_{J,M}$ that corresponds to masses of about $10^{14} - 10^{15} M_{\odot}$, masses typical of the largest clusters of galaxies. Then, since free streaming dissipates all the perturbation below $\lambda_{J,M}$, the first structures to form are those on the scale of clusters. Structures on smaller scales form by a successive process of fragmentation. These are known as *top–down* scenarios. A typical form of the HDM transfer function (Bond & Szalay 1983)

$$T(k) = \exp[-4.61(k/k_{\nu})^{3/2}] , \tag{1.58}$$

where $k_{\nu} = 0.16\ \mathrm{Mpc}^{-1}(m_{\nu}/30\mathrm{eV})$ and m_{ν} is the mass of the HDM particle.

CDM particles present a much lower Jeans length, corresponding to $M_J \sim 10^5 - 10^6 M_{\odot}$, which is the typical size of globular clusters. Therefore in these models the first objects to form are those on small scales (galaxies). Larger structures form by a process of *hierarchical*, or *bottom–up*, clustering which follows from the gravitational collapse of larger and larger scales. For CDM models the transfer function can be defined as (Bardeen *et al.* 1986):

$$T(q) = \frac{\ln(1+3.34q)}{2.34q} \times [1 + 3.89q + (16.1q)^2 + (5.46q)^3 + (6.71q)^4]^{-1/4} , \tag{1.59}$$

where $q = k/h\Gamma$. The shape parameter Γ takes into account the dependence on the Hubble parameter h, on the total density Ω_0 and on the baryon density Ω_{BM} (Sugiyama 1995):

$$\Gamma = \Omega_0 h \exp(-\Omega_{BM} - (h/0.5) * *0.5\Omega_{BM}/\Omega_0) . \tag{1.60}$$

Assuming a scale invariant primordial spectrum, the transfer function goes approximatively as k^{-3} for big k and as k^{-1} for small k. The bending of the function is at a scale of about $12\ (\Omega h^2)^{-1}\mathrm{Mpc}$.

The HDM models were the first to show serious problems. These are related with the epoch of galaxy formation. In order to have sufficient time to collapse, the first large structures that form in HDM model appear at about $z \sim 1$. Since smaller structures form by the fragmentation process, their birth should be at $z < 1$. On the other hand observations find galaxies and quasars at $z \sim 3 - 4$. CDM scenarios do not suffer this problem, since smaller fluctuations collapse much sooner. However also the CDM model is unable to fit the observational data. This is largely because, when normalized to reproduce the microwave anisotropies detected by the Cosmic Background Explorer (COBE) satellite (Bennet *et al.* 1996), the resulting power spectrum has too much short–scale power.

A number of alternative models have been proposed to solve the problems connected with the standard CDM (hereafter SCDM) scenario.

The great initial success of the CDM theory, its simplicity and its predictive power, have led to study in great detail models which are variants of the SCDM. The most promising of these variants, in the sense that their predictions are in good (although not complete) agreement with observations, are the ΛCDM and the HCDM models (see Primack 1997 and references therein).

If we assume that the present value of the Hubble constant is $h = 0.7$, then only low–Ω_0 models can be consistent with general relativity. If we want to retain a flat universe hypothesis, a cosmological constant Λ must be introduced such that $\Omega_0 + \Omega_\Lambda = 1$. Assuming a Zel'dovich primordial spectrum, also this ΛCDM model, when normalized to COBE, can fail in reproducing the observed clusters abundance. In particular if $\Omega_0 > 0.3$ the model predicts more rich clusters than those observed. In this case, it is necessary to add some "tilt", i.e. to assume that primordial spectral index n is less than unity. The ΛCDM model is in agreement with the galaxy correlation data on large scales. In order to see if this model predicts the correct galaxy distribution on smaller scales ($\leq 10h^{-1}$ Mpc), on which the structure evolution is non linear, it is necessary to use numerical simulations. However, at present these are not entirely reliable on these scales and the results cannot be considered definitive.

If $h \sim 0.5$–0.6, the models with $\Omega_0 = 1$ are allowed. In order to decrease the fluctuation power on cluster scales (too high for COBE normalized SCDM models) it is necessary to tilt the spectrum or to change the assumed dark matter composition. The first possibility has the problem that if one tilts the spectrum sufficiently to remove the unwanted power, then the resulting spectrum of the microwave background anisotropies is not consistent with observations (White *et al.* 1995b, White 1996).

The dark matter composition can be changed including a fraction of hot dark matter (HCDM models). This component in fact, cannot preserve fluctuations on small scales. Then its effect is to decrease the amount of cluster scale power. A possible problem is that both tilting and adding hot dark matter also decreases the amount of power on smaller scales, which means that protogalaxies form at lower redshift. Therefore these models must be checked against data indicating the amount of small–scale structure at $z \geq 3$. Acceptable models must also fit the data on large and small scale galaxy distribution. HCDM models can do this if the hot fraction is $\Omega_\nu \sim 0.2$

Leaving the assumption of a flat universe, we can consider $\Omega_0 < 1$ open models, (see, for example, Liddle *et al.* 1996a), with a COBE normalized primordial spectrum with $n = 1$. Allowing arbitrary values of the Hubble parameter a good fit to observational data is available for any $\Omega_0 > 0.35$, although for Ω_0 close to the unity the required h is lower than commonly accepted. Models with $\Omega_0 < 0.35$ seem unable to fit observations while keeping the universe old enough (more than 10^{10} years). If one assume $h > 0.6$, as suggested by recent observations, concordance with data is possible only in the narrow range $0.35 < \Omega_0 < 0.55$.

1.7 The Evolution of Cosmic Structures – Non Linear Phase

After recombination the density fluctuations δ evolve according to the theory presented in the previous sections as long as $|\delta| \ll 1$. Thus such theory is suitable for describing the first phases of structures evolution, but it can not be used to follow this process into the strongly non–linear regime where overdensities can exist with $\delta \gg 1$. This is a much harder problem

than the linear case and exact solution are difficult to achieve. Numerical simulations provide a powerful tool to follow the evolution of cosmological structures and chapter 3 is dedicated to an introduction to these methods. Here, instead, we want to describe some analytical approximated solutions which, even in their more restricted applicability, give useful physical information which permit a deeper comprehension of the mechanisms which control the formation of cosmological structures.

It is useful at this point to introduce the comoving form of Euler equation, which determines the peculiar velocity $\mathbf{v}$ of a particle that moves in an expanding background, subjected to the peculiar gravitational potential ϕ. For the definitions of the comoving coordinates and of the peculiar velocity we refer to section 2.4.1, while for the definition of the peculiar gravitational potential we refer to section 2.4.3.

$$\frac{d\mathbf{v}}{dt} + \frac{\dot{a}}{a}\mathbf{v} = -\frac{\nabla\phi}{a} . \tag{1.61}$$

It is also convenient to re–write equation (1.61) in terms of the variable

$$\mathbf{u} = \frac{d\mathbf{x}}{da} = \frac{\mathbf{v}}{\dot{a}} . \tag{1.62}$$

Assuming a flat, matter dominated universe, from (1.61) and (1.62) we obtain

$$\frac{d\mathbf{u}}{da} + \frac{3}{2a}\mathbf{u} = -\frac{3\nabla\varphi}{2a} . \tag{1.63}$$

where $\varphi = (3/2)a\phi$.

1.7.1 Spherical Collapse

The simplest model to describe the growth of non–linear structures by gravitational instability is the homogeneous spherical collapse model. Let us consider a spherical perturbation with constant density which, at the initial time t_i, has amplitude $\delta_i > 0$ and $|\delta_i| \ll 1$. This perturbation expand with the background universe such that its initial peculiar velocity at its edge v_i is zero. Due to the symmetry of this problem we can treat the perturbation just like a separate sub–universe. Assuming that pressure gradients are negligible, the spherical

perturbation evolves as a Friedmann model with an initial density parameter given by

$$\Omega_p(t_i) = \frac{\varrho(t_i)(1+\delta_i)}{\varrho_c(t_i)} = \Omega(t_i)(1+\delta_i) , \tag{1.64}$$

where the suffix p denotes the quantity relevant for the perturbation, while $\varrho(t)$ and $\Omega(t)$ refer to the unperturbed background universe. The spherical perturbation collapses if $\Omega_p(t_i) > 1$. It can be shown that this condition is true for any initial overdensity if $\Omega(t_i) \geq 1$ while the fluctuation must exceed the critical value $(1-\Omega)/\Omega(1+z_i)$ in a open universe, where Ω is the value of the density parameter at present time.

In a flat background universe the time evolution of such perturbation is well known. At early times the density is very close to that of the background universe and the density contrast evolves as $\delta \propto a(t)$. As δ approaches unity the growth rate increase. When the universe has expanded by a factor $1.06/\delta_i$ the inhomogeneity reaches the maximum expansion radius and starts to collapse. At this time the overdensity is 5.5 times the mean background density. Ideally, the pressureless sphere collapses to a singularity with infinite density when the universe has expanded by a factor $1.86/\delta_i$. For a realistic collapse with any appreciable degree of inhomogeneity, the collapsing perturbation violently relaxes and forms a virialized sphere with a virial radius equal to one half the radius at maximum expansion. The density of the perturbation in this stable configuration is about 170 times that of the background universe and about eight times the overdensity at the time of the maximum expansion.

This result can be generalized to an open universe. In the limit $\Omega \to 0$, the perturbation virialize at a density of about 80 times the average background value. In presence of baryonic matter the effect of pressure can be no more negligible. When the gas is compressed, shocks appear and move outward. The stable virialized configuration is then reached after shocks have heated the gas converting some of the kinetic energy of the collapse into thermal energy.

1.7.2 Zel'dovich Approximation

The model discussed in the previous section suffers from some fundamental defects. First of all, reasonable models of structure formation do not contain primordial fluctuation which are organized into homogeneous spherical regions with zero peculiar velocity at their edge. Furthermore even if the initial conditions have these properties, such configuration is strongly unstable with respect to the growth of non radial motions and the collapse tend to occur not to a point, but to a flattened structure usually called *pancake*. Finally, when baryonic matter is considered, pressure forces must be included and the dissipation can became significant during the collapse.

Zel'dovich (1970a,b) has proposed an analytical approximation which describe the growth of the perturbations in terms of the motion of a set of collisionless particles. The particles are initially uniformly distributed in space and their comoving coordinates at the initial time t_0 are indicated with $\mathbf{q}$. The comoving position of a particle at time t is calculated as

$$\mathbf{x}(t,\mathbf{q}) = \mathbf{q} - b(t)\nabla_{\mathbf{q}}\Phi_0(\mathbf{q}) , \tag{1.65}$$

where $b(t)$ describes the linear evolution of a perturbation and the quantity $\Phi_0(\mathbf{q})$ is the peculiar velocity potential. In fact, Φ_0 is related to the peculiar velocity as:

$$\mathbf{v} = -a\dot{b}\nabla_{\mathbf{q}}\Phi_0(\mathbf{q}) . \tag{1.66}$$

This means that the velocity field is irrotational. In the linear phase, The potential is related to the density perturbation δ by the relation

$$\delta = b\nabla^2_{\mathbf{q}}\Phi_0(\mathbf{q}) . \tag{1.67}$$

In practice, the Zel'dovich approximation is a linear approximation with respect to the linear displacement rather than the density, as is the linear solution. Obviously, for small displacement one recovers the usual linear regime. Equation (1.65) defines a unique mapping between the coordinates $\mathbf{q}$ and $\mathbf{r}$ as long as trajectories do not cross. The epoch of the *shell crossing* represents the limit of applicability of the Zel'dovich approximation. Before the

shell crossing $\varrho(\mathbf{r},t)d\mathbf{r} = \langle\varrho(t_i)\rangle d\mathbf{q}$ or

$$\varrho(\mathbf{r},t) = \frac{\langle\varrho(t)\rangle}{|\partial\mathbf{q}/\partial\mathbf{r}|}, \tag{1.68}$$

where $|\partial\mathbf{q}/\partial\mathbf{r}|$ is the determinant of the Jacobian of the mapping between $\mathbf{q}$ e $\mathbf{r}$. Since the flow is irrotational the Jacobian is symmetric and can therefore be locally diagonalized. Thus

$$\varrho(\mathbf{r},t) = \frac{\langle\varrho(t)\rangle}{\prod_{i=1}^{3}(1+b(t)\lambda_i(\mathbf{q}))}, \tag{1.69}$$

where $1 + b(t)\lambda_i$, $i = 1,2,3$ are the eigenvalues of the Jacobian.

Equation (1.68) shows that at some time t_{sc}, when $b(t_{sc}) = -1/\lambda_i$, a singularity appears and the density diverges. This condition corresponds to the shell crossing and the region in which this phenomenon occurs is called caustic. For a fluid element to be collapsing at least one of the λ_i must be negative. If more than one is negative, then collapse occurs first along the axis corresponding to the axis corresponding to the most negative eigenvalue. If there is no special symmetry , one therefore expects collapse to be generically one dimensional, i.e. to a sheet or pancake. Only if two or three negative eigenvalues are equal in magnitude the collapse can occur to a filament or a point.

The Zel'dovich approximation matches very well the evolution of density perturbation in N–body simulations until the first shell crossing. After this event, the approximation breaks down completely. The particles continue to move according to equation (1.65) through the caustic in the same direction as they did before and pass out to the other side. Therefore the pancake appears instantaneously and is rapidly smeared out. Actually, the matter in the caustic would be decelerated by the strong gravitational forces present there and in general could not escape from the potential well. Since the Zel'dovich approximation is only kinematic it does not account for the close–range forces and the behaviour in the strongly non linear regime is very poorly described.

1.7.3 Other Approximations

- **The Adhesion Model**

The *adhesion* model avoids the difficulties that arise from the phenomenon of the shell crossing, introducing a term of artificial viscosity in the equation of motion of the particles. Using the quantity $\mathbf{u}$ defined by equation (1.62) and in the hypothesis of irrotational motion, we have

$$\frac{d\mathbf{u}}{da} = \nu\nabla^2\mathbf{u} , \tag{1.70}$$

where ν is the viscosity coefficient (Burgers equation; Burgers, 1974). The artificial viscosity mimic the action of short range gravitational interactions with the consequent formation of stable structures, avoiding the singularity (Gurbatov, Saichev & Shandarin, 1985; Kofman & Shandarin, 1988; Shandarin & Zel'dovich, 1989).

Defining the gravitational potential Φ such that $\mathbf{v} = \nabla\Phi$ and choosing, in particular, the Hopf–Cole approximation:

$$\Phi = -2\nu \ln W , \tag{1.71}$$

W being a proper scalar field, equation (1.70) becomes

$$\frac{\partial W}{\partial a} = \nu\nabla^2 W . \tag{1.72}$$

Equation (1.72) can be solved exactly giving

$$\mathbf{u}(\mathbf{x},\tau) = \frac{\int d\mathbf{q}\,[(\mathbf{x}-\mathbf{q})/\tau]\exp|-S(\mathbf{x},\mathbf{q},\tau)/2\nu|}{\int d\mathbf{q}\exp|-S(\mathbf{x},\mathbf{q},\tau)/2\nu|} , \tag{1.73}$$

where $\tau = (a(t) - a(t_0))$ and

$$S(\mathbf{x},\mathbf{q},\tau) = \Phi_0(\mathbf{q}) + \frac{|\mathbf{x}-\mathbf{q}|^2}{2\tau} . \tag{1.74}$$

The particles comoving position is calculated solving the integral equation

$$\mathbf{x}(\mathbf{q},\tau) = \mathbf{q} + \int_0^\tau dt\ \mathbf{u}(\mathbf{x},t) , \tag{1.75}$$

while density is calculated using equation (1.68).

This model gives results comparable to those obtained with the Zel'dovich approximation until the shell crossing. Then the viscosity prevents the density from diverging reaching more advanced evolutionary phases. The adhesion technique describes efficiently the process of

merging of structures while it is limited the possibility of treating phenomenon like the fragmentation of pancake and filaments.

• **The Frozen Flow and LEP Models**

The *frozen flow* model (Matarrese *et al.* 1992) can be defined as a non–linear extension of the solution of the linearized Euler equation in the hypothesis of irrotational motion $\mathbf{u}(\mathbf{r},t) = \mathbf{u}_0(\mathbf{r}) = -\nabla\varphi_0(\mathbf{q})$. In this way equation (1.63) become

$$\frac{\partial \mathbf{u}}{\partial \tau} = 0 , \tag{1.76}$$

which describes a stationary flux of matter.

The comoving position of the particles is calculated as

$$\mathbf{x}(\mathbf{q},\tau) = \mathbf{q} - \int_0^\tau dt\ \nabla_{\mathbf{r}}\varphi_0(\mathbf{r}(\mathbf{q},t)) . \tag{1.77}$$

Finally, the density can be computed using the mass conservation.

With this approximation the stream lines are "frozen" to their initial configuration. Then shell crossing events cannot develop, unless they are already present in the initial conditions. This model is particularly suitable in describing the process of accretion of matter in cosmological structures. In fact, the particle velocity is null at the extrema of the potential, where structures form. When a particle moves toward the extremum it progressively slows down such that it can reach the extremum only asymptotically. The result is the formation of objects which continuously accretes matter. On the other hand this model cannot describe phenomena like merging and fragmentation of the structures.

Similar to the frozen flow model is the *Linear Evolved Potential* (LEP) approximation (Brainerd, Scherrer & Villumsen 1992). The potential is again frozen to its initial value but the velocity is calculated by the Euler equation assuming $\varphi = \varphi_0$. In this way the velocity present a intrinsic time evolution end does not depend only on value of the gravitational potential of the particle position. This method gives better results than the frozen flow approximation but loses the extreme simplicity of the second.

• **The Viscid Flow Model**

The *viscid flow* model (Matarrese et al. 1992) is based on the frozen flow approximation,

introducing an artificial viscosity term, such that of the adhesion model. Therefore equation (1.76) is written as

$$\frac{\partial \mathbf{u}}{\partial \tau} = \nu \nabla^2 \mathbf{u} \, . \tag{1.78}$$

In the same way the velocity potential is

$$\frac{\partial \Phi}{\partial \tau} = \nu \nabla^2 \Phi \, . \tag{1.79}$$

The velocity field is calculated as

$$\mathbf{u}(\mathbf{r}, \tau) = \left(\frac{1}{4\pi\nu\tau}\right)^{3/2} \int d^3q \frac{\mathbf{x} - \mathbf{q}}{\tau} \Phi_0(\mathbf{q}) \exp\left[-\frac{|\mathbf{x} - \mathbf{q}|^2}{4\nu\tau}\right] \, . \tag{1.80}$$

The comoving particle position is calculated integrating equation (1.80) while the density is computed using the mass conservation.

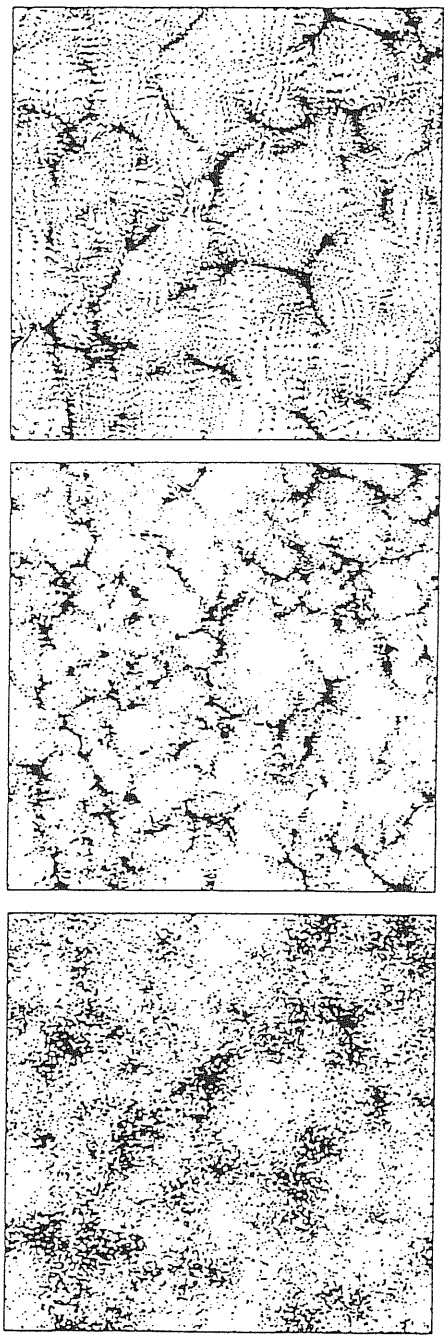

Figure 1.1: Slices with thickness 1000 km/s, at the same epoch, from simulations evolved from the same initial conditions. The particle distributions are taken form a N–body (PM) simulation (top panel), frozen flow approximation (central panel) and Zel'dovich approximation (botton panel). The figure is taken from Matarrese *et al.*(1992)

2 Hydrodynamics

In this chapter we will give a brief introduction to fluid dynamics. We define the basic hydrodynamical quantities and presenting the dynamical equations which describe the behaviour of a fluid. We then consider the characteristic form of the equations and introduce the Riemann problem. The hydrodynamical equations are then written in a form specific to the cosmological framework.

2.1 Notions of Fluid Dynamics

Fluid dynamics concerns the study of the behaviour of fluids (liquids and gases). Since the phenomena considered in fluid dynamics are macroscopic, a fluid is regarded as a continuous medium. The description of the state of a moving fluid is completely determined calculating the three components of its velocity, $\mathbf{v}$, and any two thermodynamic quantities, like the matter density, ϱ, and the pressure, p. These variables are calculated as functions of time t and position $\mathbf{r}$ solving a set of hydrodynamical conservation equations.

In order to obtain the hydrodynamical conservation equations we start from a microscopical description of the fluid representing it as a set of N particles (its molecules). Since we are not interested in following the behaviour of each particle, but we want to determine the global properties of the ensemble, we calculate the distribution function $f(t, \mathbf{r}, \mathbf{v}_p)$, so defined that:

$$f(t, \mathbf{r}, \mathbf{v}_p) d\mathbf{r} d\mathbf{v}_p \qquad (2.1)$$

is the number of particles which, at time t, have positions lying in a volume element $d\mathbf{r}$

around $\mathbf{r}$ and velocities lying within a velocity–space element $d\mathbf{v}_p$ around $\mathbf{v}_p$. The distribution function is normalized such that:

$$\int f(t,\mathbf{r},\mathbf{v}_p)d\mathbf{r}d\mathbf{v}_p = N \,. \tag{2.2}$$

The volume elements $d\mathbf{r}$ are not to be taken literally as mathematically infinitesimal quantities. They are finite volumes which are large enough to contain a very large number of particles and yet small enough so that compared to macroscopic dimensions they are essentially points. Then $f(t,\mathbf{r},\mathbf{v}_p)$ can be regarded as a continuous function of its arguments and the elementary volumes can be seen as fluid elements, recovering the continuous description of the fluid.

The evolution of the distribution function is described (see, for example, Landau & Lifshits, 1959 and Huang, 1987, for more details) by the Boltzmann equation

$$\frac{\partial f(t,\mathbf{r},\mathbf{v}_p)}{\partial t} + \mathbf{v}_p \cdot \frac{\partial f(t,\mathbf{r},\mathbf{v}_p)}{\partial \mathbf{r}} + \mathbf{F} \cdot \frac{\partial f(t,\mathbf{r},\mathbf{v}_p)}{\partial \mathbf{v}_p} = \left(\frac{\partial f}{\partial t}\right)_{coll} , \tag{2.3}$$

where $\mathbf{F}$ is the external force per unit mass and $(\partial f/\partial t)_{coll}$ is the interaction between particles.

Starting from the Boltzmann equation we can obtain the equation of conservation of the mass density, the momentum, and the energy density of the fluid. Multiplying by $d\mathbf{v}_p$ and integrating we obtain

$$\int \frac{\partial f}{\partial t} d\mathbf{v}_p + \int \frac{\partial f}{\partial \mathbf{r}} \mathbf{v}_p \cdot d\mathbf{v}_p + \int \frac{\partial f}{\partial \mathbf{v}_p} \cdot \mathbf{F} d\mathbf{v}_p = \int \left(\frac{\partial f}{\partial t}\right)_{coll} d\mathbf{v}_p \tag{2.4}$$

but

$$\int \frac{\partial f}{\partial t} d\mathbf{v}_p = \frac{\partial n(t,\mathbf{r})}{\partial t} , \tag{2.5}$$

the quantity $n(t,\mathbf{r}) = \int f d\mathbf{v}_p$ being the particle number density. Furthermore

$$\int \frac{\partial f}{\partial \mathbf{r}} \mathbf{v}_p \cdot d\mathbf{v}_p = \frac{\partial}{\partial \mathbf{r}} \int f \mathbf{v}_p \cdot d\mathbf{v}_p = \frac{\partial [n\mathbf{v}]}{\partial \mathbf{r}} , \tag{2.6}$$

where $\mathbf{v}$ is the average velocity of the particles in the elementary volume (hence the velocity of the fluid element) defined as:

$$\mathbf{v} = \frac{\int f \mathbf{v}_p \cdot d\mathbf{v}_p}{\int f d\mathbf{v}_p} . \tag{2.7}$$

Assuming that the external force depends only on the position, we have:

$$\int \frac{\partial f}{\partial \mathbf{v}_p} \cdot \mathbf{F} d\mathbf{v}_p = \mathbf{F} \cdot \int \frac{\partial f}{\partial \mathbf{v}_p} d\mathbf{v}_p = 0 , \tag{2.8}$$

as f is zero at the boundaries of the integration volume. Finally, if we assume that the particle number is conserved, the right–hand side of equation (2.4) is zero. Now multiplying all the terms by the particle mass (assumed to be the same for all the particles), we obtain the mass density conservation equation

$$\frac{\partial \varrho}{\partial t} + \frac{\partial}{\partial r_j}(\varrho v_j) = 0 , \tag{2.9}$$

where r_j and v_j are the j–th component of $\mathbf{r}$ and $\mathbf{v}$ and we implicitly sum (in (2.9) and in the following two equations) over the index j, for $j = 1, 2, 3$. Repeating the previous procedure multiplying the Boltzmann equation by $\mathbf{v}_p d\mathbf{v}_p$ and using the matter density conservation equation, we obtain the momentum conservation equation:

$$\frac{\partial \varrho v_i}{\partial t} + \frac{\partial}{\partial r_j}(\varrho v_i v_j + p\delta_{i,j}) + \varrho F_i = 0 . \tag{2.10}$$

Finally, multiplying the Boltzmann equation by $\mathbf{v}_p^2 d\mathbf{v}_p$, $\mathbf{v}_p^2$ being the square norm of the velocity and making use also of equations (2.9) and (2.10), we obtain the energy conservation equation:

$$\frac{\partial E}{\partial t} + \frac{\partial}{\partial r_j}[(E + p)v_j] + \varrho v_j F_j = 0 , \tag{2.11}$$

where F_j is the j–th component of the force and E is the total energy density defined as:

$$E = e + \frac{1}{2}\varrho \mathbf{v}^2 ; \tag{2.12}$$

in this equation e is the internal energy, related to the other hydrodynamical variables by a suitable equation of state:

$$e = e(\varrho, p) . \tag{2.13}$$

Related to the hydrodynamical variables, we can define the temperature and the sound speed. The temperature T is:

$$T = \frac{\mu m_p}{K_B}\frac{p}{\varrho} , \tag{2.14}$$

where μ is the mean molecular weight of the fluid particles, K_B is Boltzmann's constant and m_p is the proton mass. The velocity of an acoustic wave propagating in the fluid is given by:

$$c_s = \left(\frac{\partial p}{\partial \varrho}\right)^{1/2}_{s=const}, \tag{2.15}$$

where s is the specific entropy.

2.2 Characteristic Equations

When we deal with a hyperbolic system of equations, like the system of hydrodynamical conservation equations (2.9)-(2.11), it is often convenient to rewrite them in a *characteristic form* (Courant & Friedrichs, 1948).

Considering for simplicity the one dimensional case, we can write the system of hydrodynamical conservation equations in the general form:

$$\frac{\partial \mathbf{W}}{\partial t} + \frac{\partial \mathbf{F}}{\partial r} + \mathbf{G} = 0, \tag{2.16}$$

where $\mathbf{W}$ is the n–components vector of the conserved variables, $\mathbf{F}$ is the flux vector and the vector G accounts for inhomogeneous contributions associated, for example, to external forces, like gravity. It can be proved that this (and more generally, its three dimensional extension) is an hyperbolic system of equations. This means that the associated Jacobian matrix $\mathbf{J}$ of elements $J_{i,j} = (\partial F_i/\partial W_j)$ has n real eigenvalues and a corresponding complete set of eigenvectors. Related to each of the eigenvalues we can define a set *characteristic lines*, that characterize the paths along which a small disturbance in the fluid propagates. Along this paths hydrodynamical conservation equations assume the form of ordinary differential equations in the fluid variables which describe the evolution of the disturbance. In this form the equations are called *characteristic equations.*

In order to obtain the characteristic equations with respect to a set of dependent variables $\mathbf{U}$, convenient for the physical problem treated, we can rewrite the system of equations (2.16) in the form

$$\frac{\partial \mathbf{U}}{\partial t} + \mathbf{A}\frac{\partial \mathbf{U}}{\partial r} + \mathbf{C} = 0, \tag{2.17}$$

where $\mathbf{A}$ is a proper $n \times n$ operator. The variables $\mathbf{U}$ can be different from the vector of the conserved quantities $\mathbf{W}$. The two system of variables are related by:

$$\frac{\partial \mathbf{W}}{\partial t} = \mathbf{P}\frac{\partial \mathbf{U}}{\partial t} \tag{2.18}$$

$$\frac{\partial \mathbf{F}}{\partial r} = \mathbf{Q}\frac{\partial \mathbf{U}}{\partial r}, \tag{2.19}$$

with

$$P_{i,j} = \frac{\partial W_i}{\partial U_j} \tag{2.20}$$

$$Q_{i,j} = \frac{\partial F_i}{\partial U_j}, \tag{2.21}$$

where $P_{i,j}$ and $Q_{i,j}$ are the (i,j) components of the $n \times n$ operators $\mathbf{P}$ and $\mathbf{Q}$, respectively, and

$$\mathbf{A} = \mathbf{P}^{-1}\mathbf{Q} \tag{2.22}$$

$$\mathbf{C} = \mathbf{P}^{-1}\mathbf{G}\,. \tag{2.23}$$

Notice that the choice of $\mathbf{U}$ is not unique while the choice of the conserved variables is.

Now we indicate by $\mathbf{l}_i$ and $\mathbf{r}_i$ the sets of left (row) and right (columns) eigenvectors of $\mathbf{A}$. They are defined as

$$\mathbf{l}_i\mathbf{A} = \lambda_i\mathbf{l}_i \tag{2.24}$$

$$\mathbf{A}\mathbf{r}_i = \lambda_i\mathbf{r}_i\,, \tag{2.25}$$

where λ_i are the n real eigenvalues of $\mathbf{A}$, We define the diagonal matrix $\mathbf{\Lambda}$ by the transformation:

$$\mathbf{S}\mathbf{A}\mathbf{S}^{-1} = \Lambda\,, \tag{2.26}$$

where $\mathbf{S}$ is a matrix whose rows are the left eigenvectors and $\mathbf{S}^{-1}$ is a matrix whose columns are the right eigenvectors. The matrix $\mathbf{\Lambda}$ is diagonal with $\Lambda_{jj} = \lambda_j$.

Multiplying equation (2.17) by $\mathbf{S}$ we obtain:

$$\mathbf{S}\frac{\partial \mathbf{U}}{\partial t} + \mathbf{\Lambda}\mathbf{S}\frac{\partial \mathbf{U}}{\partial r} + \mathbf{S}\mathbf{C} = 0 \tag{2.27}$$

or

$$\mathbf{l}_i \frac{\partial \mathbf{U}}{\partial t} + \lambda_i \mathbf{l}_i \frac{\partial \mathbf{U}}{\partial r} + \mathbf{l}_i \mathbf{C} = 0 , \tag{2.28}$$

in component form. Equations (2.28) are the characteristic equations corresponding to the original form of hydrodynamical equations. The curves defined by

$$\frac{dr}{dt} = \lambda_i \tag{2.29}$$

are the characteristic curves. Along these paths the characteristic equations (2.28) become:

$$dV_i = \mathbf{l}_i d\mathbf{U} + \mathbf{l}_i \mathbf{C} dt = 0 . \tag{2.30}$$

Equations (2.29) integrated from a certain point of coordinate r and from a certain initial time, over a given time interval Δt define the *domain of dependence* for that point. This is the region of space that can influence the status of the fluid at r position in the time interval Δt. In other words the fluid or a perturbation propagating in the fluid can influence the point r in Δt only if it comes from a region of space inside that defined by the domain of influence.

The solution of hydrodynamical equations in characteristic form and the calculation of the domain of influence are basic ingredient of the PPM method. The explicit calculation of the characteristic form of the hydrodynamical conservation equations in a cosmological framework and their introduction in the numerical algorithm are presented in detail in section 3.2.1

2.3 The Riemann Problem

The Riemann problem plays a fundamental role in the development of high–resolution, shock capturing hydrodynamical codes. It was introduced in computational fluid dynamics by Godunov (1959) and then improved by many authors, like Sod (1977), Roe (1981), Colella (1982), Colella and Woodward (1984)

The Riemann problem consists in calculating the gas flow resulting from the decay of a discontinuity that separates two constant initial states L (left) and R (right). In general,

the initial discontinuity is not stable and decays giving rise to several elementary nonlinear waves. These can be shocks, rarefaction waves or contact discontinuities that move away from the position of the initial discontinuity. The time evolution of a general Riemann problem can be represented as:

$$L\ W_{-}\ L_{*}\ C\ R_{*}\ W_{-}\ R\ , \tag{2.31}$$

where W denote a shock or a rarefaction wave that propagates toward left ($_{-}$) or right ($_{-}$) with respect to the initial discontinuity, C is the contact discontinuity and L_{*} and R_{*} are the hydrodynamic states that appear behind the waves and that are separated by C. The new states L_{*} and R_{*} are characterized by the same pressure and velocity but have different density.

The nature of the different waves can be determined just looking at the values of the pressure. In fact for a shock we have that:

$$p_b > p_a\ , \tag{2.32}$$

where the subscripts a and b denote quantities ahead and behind the wave, while for a rarefaction wave:

$$p_b < p_a\ . \tag{2.33}$$

Finally for a contact discontinuity we have:

$$p_b = p_a\ ; \tag{2.34}$$

note that the fluid on the two sides of the contact discontinuity do not mix, as there is no motion of fluid through a tangential discontinuity.

There are five possible kind of break–up of the initial discontinuity. Following the previous representation and referring also to figure (2.1):

$$L\ S_{-}\ L_{*}\ C\ R_{*}\ S_{-}\ R\ , \tag{2.35}$$

$$L\ R_{w,-}\ L_{*}\ C\ R_{*}\ S_{-}\ R\ , \tag{2.36}$$

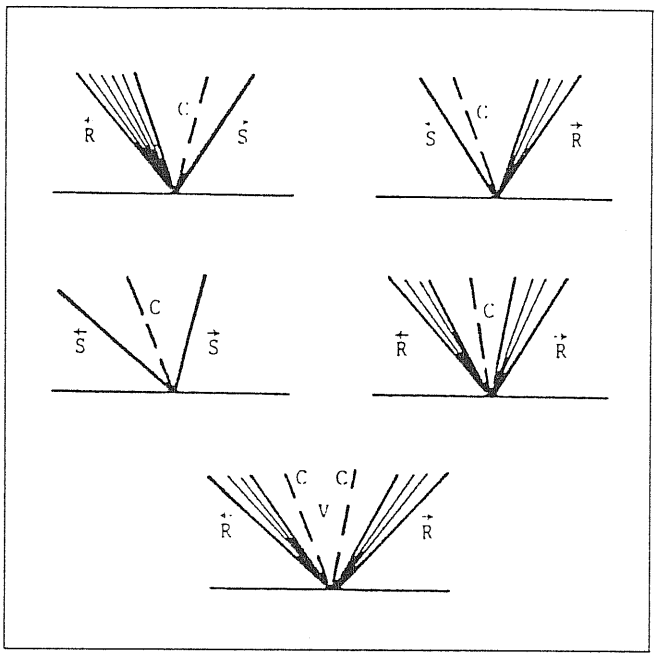

Figure 2.1: The five possible wave patterns in the solution of the Riemann problem, showing shocks (S) and rarefaction waves (R), separated by a contact surface (C). The last one has a vacuum (V) in the pattern center

$$L\ S_{-}\ L_{*}\ C\ R_{*}\ R_{w,-}\ R\ , \tag{2.37}$$

$$L\ R_{w,-}\ L_{*}\ C\ R_{*}\ R_{w,-}\ R\ , \tag{2.38}$$

$$L\ R_{w,-}\ V\ R_{w,-}\ R\ , \tag{2.39}$$

where S represents a shock, R_w a rarefaction wave and V a vacuum region. The two solutions (2.36) and (2.37) differs only in the sign of the difference $p_L - p_R$ (positive in the first case, negative in the second).

The solution of the Riemann problem consists essentially in computing pressure, density and velocity in L_*, R_*, W_-, W_- and the velocity at which the different waves propagate. In all of the five cases the solution is completely determined on the base of the initial left and right states (initial parameters).

The conditions which determine the way the initial discontinuity breaks up can be determined analytically as a function of the initial parameters. Following Landau and Lifshits (1959) for a politropic gas we have that solution (2.35) is obtained for:

$$v_L - v_R > (p_2 - p_1)[2/(\varrho_1((\gamma-1)p_1 + (\gamma+1)p_2)]^{1/2} , \tag{2.40}$$

where with the subscript 1 we indicate the side of minimal initial pressure and with the subscript 2 the side of maximal initial pressure; γ is the adiabatic index of the fluid.

The solutions (2.36) and (2.37) are obtained for:

$$-\frac{2c_2}{\gamma-1}[1-(p_1/p_2)]^{(\gamma-1)/2\gamma} < v_L - v_R < (p_2-p_1)[2/(\varrho_1((\gamma-1)p_1+(\gamma+1)p_2)]^{1/2} , \tag{2.41}$$

We have the case (2.38) for:

$$-\frac{2(c_1+c_2)}{(\gamma-1)} < v_L - v_R < -\frac{2c_2}{\gamma-1}[1-(p_1/p_2)]^{(\gamma-1)/2\gamma} . \tag{2.42}$$

Finally for:

$$v_L - v_R < -\frac{2(c_1+c_2)}{(\gamma-1)} , \tag{2.43}$$

we have the case (2.39). In these equations c_1 and c_2 are the sound speed associated to the two initial states of the fluid. Note that these limits depend only on the velocity difference $v_L - v_R$: therefore they do not depend on the particular frame chosen.

Once we have determined which of the previous cases we have to deal with, we can solve the corresponding Riemann problem. We start from the determination of the value of the fluid variables on the two sides of the contact discontinuity. We indicate this values as p_L^*, ϱ_L^*, v_L^* and p_R^*, ϱ_R^*, v_R^*. These unknowns can be obtained using the conservation of mass, momentum and energy and the equation of state. These laws reduce to the well–known Rankine–Hugoniot relations across shocks and to the isentropic characteristic equations across rarefaction waves. These equations can be used to jump across the moving wave from the known unperturbed state (p_S, ϱ_S, v_S) to the unknown state (p_S^*, ϱ_S^*, v_S^*) (here the subscript S represent either Left or Right). The conditions $p^* = p_L^* = p_R^*$ and $v^* = v_L^* = v_R^*$

across the contact surface reduce the problem to the solution of a single nonlinear algebraic equation in one unknown for any of the previous patterns. In the case of two rarefaction waves separated by the contact discontinuity the solution is:

$$p^* = p_L \left[\frac{\gamma - 1}{2} \frac{\tilde{v}_L - \tilde{v}_R}{c_L(1+z)} \right]^{2\gamma/(\gamma-1)} \tag{2.44}$$

$$v^* = \frac{\tilde{v}_L z + \tilde{v}_R}{1+z} , \tag{2.45}$$

where

$$\tilde{v}_L = v_L + \frac{2}{\gamma - 1} c_L, \qquad \tilde{v}_R = v_R - \frac{2}{\gamma - 1} c_R \tag{2.46}$$

and

$$z = \frac{c_R}{c_L} \left(\frac{p_L}{p_R} \right)^{\gamma - 1/2\gamma} . \tag{2.47}$$

In all the other cases the resulting equation is implicit and must be solved using an iterative scheme like that proposed by Van Leer (1979) and presented in appendix A.

The values of the density ϱ_L^* and ϱ_R^* depend on the particular pattern. Behind a wave the density ϱ_b is computed using proper relations once p_a, ϱ_a and p_b $(= p^*)$ are given. For a shock we use the so-called shock adiabatic relation that, for a polytropic gas, is:

$$\frac{\varrho_b}{\varrho_a} = \frac{(\gamma+1)p_b + (\gamma-1)p_a}{(\gamma-1)p_b + (\gamma+1)p_a} . \tag{2.48}$$

Behind a rarefaction wave, instead, the polytropic equation of state can be used (as rarefaction is an adiabatic process):

$$\varrho_b = \varrho_a (p_b/p_a)^\gamma . \tag{2.49}$$

Inside a rarefaction wave pressure and density can be determined as a function of the velocity:

$$p = p_a [1 - (\gamma - 1)|\bar{v}|c_a/2]^{2\gamma/(\gamma-1)} \tag{2.50}$$

and

$$\varrho = \varrho_a [1 - (\gamma - 1)|\bar{v}|c_a/2]^{2/(\gamma-1)} , \tag{2.51}$$

where $\bar{v} = v - v_a$ is determined as the similarity solution:

$$|\bar{v}| = \frac{2}{\gamma - 1}\left(c_a - \frac{r}{t}\right) , \tag{2.52}$$

where t is the time and $r = |r_a - r_r|$, with r_a position of the head of the wave, and r_r position of the point examined. Note that the velocity must satisfy the inequality:

$$|\bar{v}| \leq \frac{2c_a}{\gamma - 1} . \tag{2.53}$$

When the velocity reaches this limiting value the density and the pressure become zero and a vacuum state is formed.

Finally we have to determine the velocity of the waves. For the shock, using the jump conditions through the discontinuity, we obtain:

$$v_{sh} = \frac{\varrho^* v^* - \varrho_a v_a}{\varrho^* - \varrho_a} . \tag{2.54}$$

For the rarefaction wave we have:

$$v_t = v^* - c^* \quad v_h = v_L - c_L , \tag{2.55}$$

if the wave moves toward the left, and

$$v_t = v^* + c^* \quad v_h = v_R + c_R , \tag{2.56}$$

if the wave moves toward the right. In the previous equations $c^* = (\gamma p^*/\varrho^*)$ while v_t and v_h represent respectively the tail and the head of the wave, defined as the point of minimum and maximum pressure of the wave front respectively. The contact discontinuity moves with the fluid with velocity $v_c = v^*$. At this point the Riemann problem is solved.

2.4 Cosmological Equations

When we consider the cosmological framework we have to deal with two different species of matter, the baryonic and the collisionless matter. These two components have different properties, hence they have to be treated in different ways.

Baryons are interacting particles which have a short mean free path. This means that the mean collisional time between two molecules is much less than the dynamical time of the system, which is the typical timescale on which macroscopic changes occur when the system deviates seriously from mechanical equilibrium. Therefore baryons can be described as a *collisional fluid.* Dark matter particles instead interact only via gravitational forces on a time scale comparable to the dynamical time of the system. Then they can be represented as a pressureless fluid and each fluid element can be treated as an individual entity subjected only to gravitational forces. The dynamic of each element is calculated solving the corresponding equations of motion.

2.4.1 Baryonic Matter

Since the baryonic component is described as a fluid, its behaviour is determined solving equations (2.9)-(2.11). It is convenient to re–write hydrodynamical equations taking into account the expansion of the universe. This is done introducing cartesian comoving spatial coordinates, defined as $\mathbf{x} = \mathbf{r}/a(t)$, where $a(t)$ is cosmic the expansion factor. Then, we define the peculiar velocity $\mathbf{v}$ as the difference between the total velocity ($\mathbf{v}_T$) and its component due to the Hubble flow ($\mathbf{v}_H$):

$$\mathbf{v}_T = \frac{d\mathbf{r}}{dt} = \frac{d[a(t)\mathbf{x}]}{dt} = a(t)\frac{d\mathbf{x}}{dt} + a(t)H(t)\mathbf{x} = \mathbf{v} + \mathbf{v}_H \ . \tag{2.57}$$

In this way we separate the component of the motion due to a peculiar behaviour from that related to the global expansion of the universe. With this choice of coordinates and velocities, the mass conservation equation become:

$$\frac{\partial \varrho}{\partial t} + \frac{\partial}{\partial x_j}(\varrho v_j) + 3\frac{\dot{a}(t)}{a(t)}\varrho = 0 \ , \tag{2.58}$$

In order to recover a form of the equation of conservation of mass close to the initial one, it is convenient to introduce the comoving mass density

$$\tilde{\varrho} = a(t)^3 \varrho \ . \tag{2.59}$$

Then equation (2.58) assume the form:

$$\frac{\partial \tilde{\varrho}}{\partial t} + \frac{\partial}{\partial x_j}(\tilde{\varrho} v_j) = 0 \ . \tag{2.60}$$

Repeating the same procedure for the three components of the momentum and for the total energy density and including the gravitational forces we obtain:

$$\frac{\partial \tilde{\varrho} v_i}{\partial t} + \frac{1}{a}\frac{\partial}{\partial x_j}(\tilde{\varrho} v_i v_j + \tilde{p}\delta_{i,j}) = -\frac{\dot{a}}{a}\tilde{\varrho} v_i - \frac{1}{a}\varrho\frac{\partial \phi}{\partial x_i} \ , \tag{2.61}$$

$$\frac{\partial \tilde{E}}{\partial t} + \frac{1}{a}\frac{\partial}{\partial x_j}[(\tilde{E} + \tilde{p})v_j] = -2\frac{\dot{a}}{a}\tilde{E} - \frac{1}{a}\varrho v_j\frac{\partial \phi}{\partial x_j} \ , \tag{2.62}$$

where v_j is the j–th component of the peculiar velocity, $\tilde{E}$ is the total energy per unit comoving volume, $\tilde{p}$ is the comoving pressure. These two quantities are defined as the product of the proper total energy density and the pressure with a^3. The quantity ϕ is the peculiar gravitational potential (defined in section 2.4.3). The closure of this set of equations is obtained by assuming an equation of state for the fluid and calculating the gravitational potential as described in section 2.4.3.

Since baryons, in the standard hot big bang cosmological scenario, evolves from conditions close to those idealized by a smooth, low–density gaseous flow, they can be described as an ideal gas with adiabatic index $\gamma = 5/3$ for which:

$$\tilde{p} = (\gamma - 1)\left(\tilde{E} - \frac{1}{2}\tilde{\varrho}\mathbf{v}^2\right) \ . \tag{2.63}$$

In the rest of the work, unless explicitly stated, we will always use comoving quantities. Therefore, for simplicity, we will suppress the tilde that distinguish between comoving and proper quantities.

2.4.2 Dark Matter

The dark matter is collisionless. The behaviour of each particle is described solving the corresponding equation of motion. Using comoving coordinates and peculiar velocities the dynamics of a pointlike element of the collisionless component is governed by the following equations:

$$\frac{d\mathbf{x}}{dt} = \frac{1}{a}\mathbf{v} \ . \tag{2.64}$$

$$\frac{d\mathbf{v}}{dt} + \frac{\dot{a}}{a}\mathbf{v} = -\frac{1}{a}\nabla\phi \ . \tag{2.65}$$

2.4.3 Gravitational Potential

The gravitational potential Φ associated with a distribution of matter of density ϱ is calculated solving the Poisson equation:

$$\nabla_{\mathbf{r}}^2\Phi = 4\pi G\varrho_{tot} \ , \tag{2.66}$$

In a cosmological framework it is convenient to define the peculiar gravitational potential. This is calculated starting from the Lagrangian of a particle of mass m that moves in a gravitational field Φ:

$$L \ = \ \frac{1}{2}m\mathbf{r}^2 - m\Phi(\mathbf{r},t) \ . \tag{2.67}$$

Using comoving coordinates we obtain

$$L \ = \ \frac{1}{2}m(a\dot{\mathbf{x}} + \dot{a}\mathbf{x}) - m\Phi(\mathbf{r},t) \ . \tag{2.68}$$

The canonical transformation

$$L \ \rightarrow \ L - d\psi/dt, \qquad \psi = \frac{1}{2}ma\dot{a}\mathbf{x}^2 \ , \tag{2.69}$$

reduces the lagrangian to

$$L \ = \ \frac{1}{2}ma^2\dot{\mathbf{x}}^2 - m\phi \ , \tag{2.70}$$

with

$$\phi \ = \ \Phi + \frac{1}{2}a\ddot{a}\dot{\mathbf{x}}^2 \ , \tag{2.71}$$

Using equation (2.71), equation (2.66) becomes:

$$\nabla_{\mathbf{x}}^2\phi = \frac{4\pi G}{a}(\varrho_{tot} - \varrho_0) \ , \tag{2.72}$$

where ϱ_{tot} is the total comoving density (baryonic plus dark matter) and ϱ_0 is the total comoving mean density.

3 The PPM+PM Code

In chapter 1 we have shown that the evolution of the cosmological structures depends on the nature and the properties of the constituents of the universe. In particular, after recombination, this process is driven by the collisionless and the baryonic matter, which dominate the energy density of the universe. The behaviour of this system can only be described by following simultaneously the evolution of both components, looking at all of their internal processes and considering their mutual interaction. This can only be achieved by using numerical simulations which allow a general description of the non–linear evolution of the structures. In particular N–body techniques (Hockney & Eastwood 1981) have proved to be particularly effective for cosmological problems in which the dynamics is controlled by gravitational forces as in the case of the dark matter and also for baryonic structures on very large scales (more than $50h^{-1}$ Mpc). With these methods matter is described as a set of collisionless particles whose dynamics is governed by the equations (2.64) and (2.65). An introduction to N–body methods will be given in section (3.3).

The N–body approach, however, is not in general suitable for describing the behaviour of the baryonic component which is also influenced by pressure forces, heating and cooling processes. The inclusion of all these phenomena requires an enormous amount of computational resources as they act on a very wide range of scales. The lack of adequate computational resources has delayed the development of hydrodynamic cosmological codes and only in recent years a number of numerical algorithms have been proposed for following the evolution of baryonic matter.

A first family of these techniques derives directly from the N–body methods. It is called "Smoothed Particle Hydrodynamics" (SPH) and has been introduced independently by Lucy (1977) and Gingold & Monaghan (1977) to study problems of stellar astrophysics. The SPH methods represent fundamental fluid elements in terms of particles. This method is intrinsically Lagrangian and, since it follows the fluid elements in their motion, it has high spatial resolution and give an accurate description of high–density regions, where particles tend to concentrate. On the other hand, with this approach, it is difficult to treat properly low–density regions where few particles are present and mass resolution is poor. Several cosmological codes have been developed using the SPH technique like those of Evrard (1988), Hernquist & Katz (1989) and Steinmetz & Muller (1993). Due to the importance of the method and its wide application in cosmology we will describe it briefly later in this section. For a detailed introduction to SPH we refer to the works of Evrard and Hernquist & Katz.

Alternative Lagrangian methods which solve hydrodynamical equations on an adaptive grid which "follows" the fluid in its motion can are hard to use in cosmological simulations in which high supersonic flows produce strong distortion of the computational mesh.

Multi–dimensional hydrodynamic codes not based on SPH, usually adopt an Eulerian approach and dynamical equations are solved on a fixed (or adaptive) grid. Mean values of the fluid quantities are computed in each grid cell by solving the equations of conservation of matter, momentum and energy density once the equation of state for the matter is given. Eulerian methods have good mass resolution, and can describe low–density regions better than SPH but they are spatially limited by the cell size. However, the Eulerian approach seems to be preferable in the case of complicated three–dimensional structures (Woodward & Colella 1984). An Eulerian approach has been adopted in several hydrodynamical codes developed for studying large scale structures (Chiang, Ryu & Vishniac 1989; Cen 1992; Ryu *et al.* 1993; Bryan *et al.*; Anninos, Norman & Clarke 1994; 1995; Gnedin 1995; Quilis, Ibánez & Saez 1996; Sornborger *et al.* 1996). At the end of this section we present a brief review of the various works that uses mesh based techniques.

In our work we have chosen an Eulerian approach to describe the evolution of the

cosmological structures. The hydrodynamical problem has been solved using the Piecewise Parabolic Method (PPM) introduced by Colella & Woodward (1984). This is a higher order extension of Godunov's shock capturing method (Godunov 1959; 1961). It is at least second–order accurate in space (up to the fourth–order, in the case of smooth flows and small time steps) and second–order accurate in time. The high accuracy of this method allows minimization of errors due to the finite size of the cells of the grid and leads to a spatial resolution close to the nominal one. In a cosmological framework, the basic PPM technique has been modified to include the gravitational interaction and the expansion of the universe. The PPM algorithm has already been used for building a cosmological code by Bryan *et al.* (1995), however our approach differs in several respects from theirs. In the Bryan *et al.* work, the one–dimensional time integration is done by first performing a Lagrangian step and then remapping the results onto an Eulerian grid expressed in the usual coordinates comoving with the mean Hubble flow. We instead adopt a single–step Eulerian scheme. The construction of the effective left and right states for the Riemann problem is then more complicated than in the Lagrangian case, since the number of characteristics reaching the edge of a zone is not constant. On the other hand, this choice allows us to include in the characteristic equations both the gravitational interaction and the expansion of the universe and then the effect of all source terms is accounted for to second–order.

The hydrodynamical part has been coupled to a Particle Mesh (PM) N–body code that describes the evolution of the dark component. The standard PM code has been modified to work with a non–constant time step equal to that used in the hydrodynamical integration. The coupling is obtained by calculating the gravitational field due to both the components with an FFT procedure.

- **Smoothed Particle Hydrodynamics**

The Smoothed Particle Hydrodynamics method describes a fluid as a set of particles, which represent the elementary fluid elements. These particles experience local forces exerted by pressure gradients and by viscosity in the shocks and long range forces like the gravitational one. In cosmological applications the behaviour of the gas particles is con-

trolled, in comoving coordinates, by the dynamical equations

$$\frac{d\mathbf{x}}{dt} = \mathbf{v} \tag{3.1}$$

$$\frac{d\mathbf{v}}{dt} = -2H\mathbf{v} - \frac{1}{a^2}\frac{\nabla p}{\varrho} - \frac{1}{a^3}\nabla\phi \tag{3.2}$$

$$\frac{d\epsilon}{dt} = \frac{p}{\varrho^2}\frac{d\varrho}{dt} - \frac{\varrho\Lambda(\epsilon)}{(\mu m_p)^2} , \tag{3.3}$$

where m_p is the mass of a particle and Λ is a proper function which accounts for cooling and heating processes.

The main problem of the SPH is how to define, starting from a discrete distribution of particles, the continuous fluid quantities, like the matter density and the pressure gradients. The technique adopted in SPH is known as *kernel* estimation. The process is equivalent to convolving a field $f(\mathbf{x})$ with a smoothing, or filter, function $W(\mathbf{r}-\mathbf{x}, h)$ to produce a smoothed estimate of the field $f_s(\mathbf{r})$

$$f_s(\mathbf{r}) = \int d\mathbf{x}\ f(\mathbf{x})W(\mathbf{r}-\mathbf{x}, h) , \tag{3.4}$$

where both $\mathbf{x}$ and $\mathbf{r}$ represent comoving coordinates. A possible choice for the kernel W is a Gaussian function

$$W(u, h) = \frac{1}{\pi^{3/2}h^3}\exp(-u^2/h^2) . \tag{3.5}$$

The quantity h is called smoothing length and gives the actual spatial resolution of the method.

If we take $f(\mathbf{x})$ to be the density field due to a discrete distribution of particles

$$f(\mathbf{x}) \rightarrow \varrho(\mathbf{x}) = m_p \sum_j \delta(\mathbf{x}i - \mathbf{x}_j) , \tag{3.6}$$

where δ is the Kronecker function and x_j is the position of the j–th particle, the smoothed form of the density field is

$$\varrho_s(\mathbf{x}) = m_p \sum_j W(|\mathbf{x}-\mathbf{x}_j|, h) . \tag{3.7}$$

In these estimate we have assumed that the smoothing length is constant all over the space. This is not necessary and severely limits the ability to resolve the multiple levels

of substructure present in cosmological simulations. Furthermore a too small value of h can lead to problems in underdense regions, where very few particles are present, and then where the smoothed estimate of hydrodynamical quantities can be very inaccurate, if not actually wrong. It is much better to adapt the resolution to the local conditions. Then a specific smoothing length h_j is associated to each particle. The smoothing length can be dynamically adapted with time according to the relation

$$\frac{\delta h_j}{h_j} = -\frac{\delta \varrho_j}{3\varrho_j} , \tag{3.8}$$

where $\delta\varrho_j$ is the change in density in the position of the particle j over one time step. This ensures a roughly constant number of neighbours within a sphere of radius h_j around each particle at all times. The smoothing length may vary also in each coordinate direction, giving rise the a smoothing tensor $h_{i,j}$. However this extension is quite complicate and has been introduced only in very recent works.

The update of the hydrodynamical variables is obtained using a Leap–Frog scheme. This scheme consists in two steps. In the first step the velocity of the j–th particle is calculated at half time step as

$$\mathbf{v}_j^{n+1/2} = \mathbf{v}_j{}^{n-1/2} + (t^{n+1/2} - t^{n-1/2})\mathbf{a}_j{}^n , \tag{3.9}$$

where $\mathbf{a}_j{}^n$ is the acceleration felt by the particle (gravity plus pressure forces). The position of the particle is calculated at t^{n+1} using the time centered value of the velocity

$$\mathbf{x}_j^{n+1} = \mathbf{x}_j^n + (t^{n+1} - t^n)\mathbf{v}_j^{n+1/2} . \tag{3.10}$$

The internal energy equation (3.3) is advanced along together with the positions.

- **Grid–based Codes**

The first Eulerian three dimensional cosmological codes have been those proposed by Chiang, Ryu & Vishniac (1989) and Cen (1992). The former solved the dynamical equations employing a combination of first–order finite difference equations and a beam scheme method (Sanders & Prendergast, 1974). The hydrodynamical part of the Cen's code is based on the first–order modified Lax method (Roache 1982). The dark matter is instead

treated by a particle mesh N–body code. These methods are based on rather simple numerical algorithms in which it is relatively easy to introduce any kind of source term (like the cooling and heating functions of Chiang, Ryu & Vishniac) or account for the specific expressions that describe the evolution of the various chemical species and the possible non–equilibrium processes which contribute to cooling, heating and diffusion in the gas (like for Cen). On the other hand the spatial resolution of the method is intrinsically of several cells of the computational mesh and it is further degraded by the action of numerical diffusion, which must be artificially introduced in order to handle shock waves and other possible physical discontinuities in the flow. These phenomena in fact, developing below the size of a cell, cannot be described properly by these algorithm and lead to the rise of numerical ripples which make the results meaningless. This problem is overcame by the inclusion of a numerical viscosity that smears the discontinuity over a certain number of cells. For typical first order methods the actual spatial resolution is at last between five and eight cells. This is a severe limit in cosmological simulations for which the largest possible dynamical range is required. Moreover the numerical diffusion affects the dynamics of the system. Its effects can not be easily estimated and controlled and could strongly influence the results of the simulations.

This first generation of cosmological hydrodynamical codes has been followed by a new release of codes based on numerical techniques in which the previous problems are avoided. These codes are characterized by a spatial resolution close to the nominal one and no need of artificial diffusion. These are known as shock capturing methods and are usually based on the inclusion of a Riemann solver into the hydrodynamical equation integration procedure. Such methods are accurate both in describing smooth flows and in treating sharp gradients or even physical discontinuities in the fluid. An example is given by the "Total Variation Diminishing" scheme, originally developed by Harten (1983), and used for cosmological simulations by Ryu *et al.* (1993). Close to TVD is the technique used by Quilis, Ibanes & Saez (1994), also based on a characteristics approach. A different possibility is the PPM scheme, used also for our code, that has been implemented by Bryan *et al.*(1995) and

Sornborger *et al.*(1996), and that will be widely discussed in the following sections. The drawback of these techniques is their complexity that leads to a much higher computational resources requirement and the difficulty of introducing any external source term retaining at the same time the accuracy of the method.

A completely different approach is that followed by Kates *et al.*(1995) who used a Flux Corrected Transport (Boris & Book, 1973; Zalesak, 1979) method for their cosmological code. With this method the fluxes of the conserved quantities are computed using both a low–order and a high–order accurate difference scheme. A linear combination of these fluxes is calculated using weight factors which are nonlinear functions of the local conditions of the flow. This method gives good results for smooth flows and, due to the diffusive effect of the low–order scheme, it does not require the inclusion of an artificial viscosity. However the accuracy reached in describing sharp gradients is not comparable to that of shock capturing methods.

At present, the main effort is dedicated to improve the resolution of the codes in order to further extend the dynamical range of the simulations. Anninos, Norman & Clarke (1994) have proposed a two level Eulerian grid. On the coarser grid the gross properties of the system are calculated. The details are computed on a sub–box nested in the total mesh which has a resolution that is some fraction of the coarse cell size.

A more sophisticate approach is that of Gnedin (1995; see also Gnedin & Bertschinger 1996). Gnedin has presented a new approach to cosmological hydrodynamics called SLH (softened Lagrangian hydrodynamics) which uses a high–resolution Lagrangian code combined with a low–resolution Eulerian solver to deal with severe mesh distortion. Most of the computational volume is treated with the Lagrangian approach and only where this would fail, due to mesh distortions, the Eulerian part of the code steps in. The resolution of this method should be intermediate between that achievable by the Eulerian and the Lagrangian approaches.

3.1 The Basic PPM Scheme

The PPM algorithm, developed by Colella & Woodward (1984), is a higher order extension of Godunov's conservative shock capturing method. This method has two basic properties. First the solution is built up piecing together discontinuous solutions approximated by a parabolic interpolation function. These discontinuous solutions become smooth where this is appropriate, but they have the great advantage of approximating the true solution reasonably well even when the solution is not smooth. Second, the accuracy of the representation is improved by building into the numerical scheme the analytical solution of the Riemann problem, which describes the propagation and interaction of non–linear waves. In particular, such procedure leads to an accurate and well behaved treatment of shock discontinuities. The basic PPM scheme has been developed and will be illustrated in one dimension. Its extension to multi dimensional calculation in obtained by the direction splitting procedure described in section 3.2.4. We will also neglect any source term and the expansion of the universe as this will be introduced and discussed in detail in section 3.2.

The PPM method is implemented according to the following procedure. We start from the knowledge of a set of zone–averaged values of hydrodynamical quantities. To update these averages we solve hydrodynamical conservation equations: this requires the estimate of the fluxes of the conserved quantities at the zone interfaces. First, we construct a piecewise parabolic (third–order) one–dimensional interpolation function for each of the hydrodynamical variables. This leads to a more accurate representation of smooth spatial gradients as well as a sharper description of discontinuities. A detailed description of this reconstruction procedure is given in section 3.1.1. The interpolated distributions can then be used to estimate properly the averaged values of the variables to the left and right of each zone edge. This is performed in two further steps. In the first step, one determines the characteristic domain of dependence with respect to a zone edge, that is the regions of space to the left and to the right of the edge that contain all of the information that can reach the zone edge during the current time step. Then, using the interpolated distributions, the mean values of hydrodynamic variables are computed over the domains of dependence on each side of

the edge. In the second step, one solves the Riemann problem using as initial left and right states the mean values of hydrodynamical variables computed previously on each side of the zone edge. The solution of the Riemann problem gives the time averaged values of the variables at the zone edge which are used to compute inter–cell fluxes and then the fluid variables at the new time. These steps are described in detail in sections 3.1.2 and 3.1.3.

3.1.1 Piecewise Parabolic Interpolation

The basic limit of Eulerian methods is the discrete description of hydrodynamical quantities, which are estimated on the cells of a fixed mesh. The value over each cell is defined as a spatial average:

$$w_j^n = \frac{1}{\Delta x}\int_{x_{j-1/2}}^{x_{j+1/2}} w(\xi, t^n)d\xi \ , \tag{3.11}$$

where w_j is the mean value of the generic hydrodynamical variable $w(x,t)$ (density, pressure or velocity) over the j–th zone at the time t^n, $x_{j\pm1/2}$ are the positions of the zone interfaces and $\Delta x = x_{j+1/2} - x_{j-1/2}$. Due to the discrete representation any information about the behaviour of the quantities inside the cell got lost. The PPM method tries to approximate the correct behaviour inside the cell reconstructing the profiles of the hydrodynamical variables by a piecewise parabolic interpolation polynomial (see Figure 3.1).

The polynomial is built starting from the knowledge of the zone–averaged values of the hydrodynamical variables w_j^n according to some basic rules. The interpolation polynomial inside each zone is a parabola of the form:

$$w(\xi) = a\xi^2 + b\xi + c \ , \tag{3.12}$$

with

$$a = -w_{6,j}, \qquad w_{6,j} = 6\left[w_j^n - \frac{1}{2}(w_{L,j} + w_{R,j})\right] \tag{3.13}$$

$$b = \Delta w_j + w_{6,j}, \qquad \Delta w_j = w_{R,j} - w_{L,j} \ , \tag{3.14}$$

$$c = w_{L,j} \ , \tag{3.15}$$

and $\xi = (x - x_{j-1/2})/\Delta x$. The quantities $w_{L,j}$ and $w_{R,j}$ are the interpolation parameter of the parabola that can be read as the values of $w(\xi)$ respectively at the left and right edge

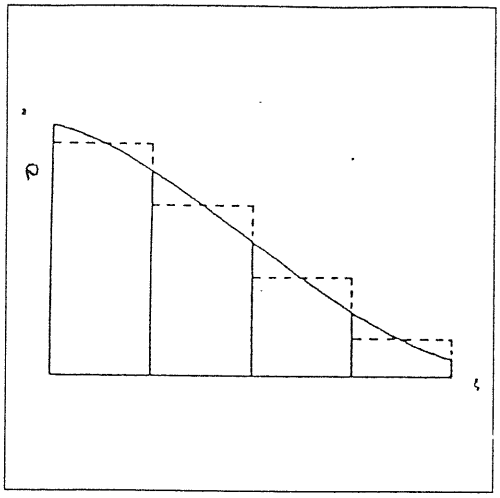

Figure 3.1: The profile of an hydrodynamical quantity at the beginning of the PPM integration procedure (dashed line), and after the piecewise parabolic interpolation (solid line)

of the j–th zone. They are defined such that the averaged value of the resulting polynomial over the cell is equal to the starting value of the hydrodynamical quantity w_j^n:

$$\frac{1}{\Delta x}\int_{x_{j-1/2}}^{x_{j+1/2}} w(\xi)d\xi \;=\; w_j^n \;. \tag{3.16}$$

The two parameters are calculated by estimating $w_{j+1/2}$, that is an approximation of the value of w at the zone edge $\xi_{j+1/2}$. The procedure adopted to calculate $w_{j+1/2}$ ensures that it does not fall out of the range of values given by w_j and w_{j+1} which are the averaged values of the hydrodynamical quantity in the j and $j+1$ cells, respectively. The quantity $w_{j+1/2}$ is calculated as:

$$w_{j+1/2} \;=\; w_j^n + \frac{1}{2}(w_{j+1}^n - w_j^n) - \frac{1}{6}(\delta_m w_j - \delta_m w_{j+1}) \;, \tag{3.17}$$

where:

$$\delta_m w_j \;=\; \min(|\delta w_{j+1}|, |w_j - w_{j-1}|, |w_{j+1} - w_j|,)\mathrm{sgn}(\delta w_{j+1}) \tag{3.18}$$

$$\text{if} \qquad (w_j - w_{j-1})(w_{j+1} - w_j) > 0 \tag{3.19}$$

$$\delta_m w_j \;=\; 0 \qquad \text{otherwise} \tag{3.20}$$

and

$$\delta w_j = \frac{1}{2}(w_{j+1} - w_{j-1}) . \tag{3.21}$$

The value $w_{j+1/2}$ is assigned to both $w_{L,j+1}$ and $w_{R,j}$ for most values of j. In these cases $w(\xi)$ is continuous even across the corresponding zone edges. There are some cases, however, where this would lead to an interpolation function which presents values not between $w_{L,j}$ and $w_{R,j}$, and this would introduce new unphysical extrema. Two cases are possible. First, if w_j^n is a local minimum or maximum; the second case is where w_j^n is between $w_{L,j+1}$ and $w_{R,j}$,

but sufficiently close to one of the values so that the interpolated parabola takes values outside this range. In these cases the expressions for the two parameters are given by:

$$w_{L,j} = w_j^n, \quad w_{R,j} = w_j^n \qquad \text{if} \quad (w_{R,j} - w_j^n)(w_{L,j} - w_j^n) \geq 0 \tag{3.22}$$

$$w_{L,j} = 3w_j^n - 2w_{R,j}, \text{if} \quad (w_{R,j} - w_{L,j})w_{6,j} > \frac{(w_{R,j} - w_{L,j})^2}{6} \tag{3.23}$$

$$w_{R,j} = 3w_j^n - 2w_{L,j}, \text{if} \quad (w_{R,j} - w_{L,j})w_{6,j} < -\frac{(w_{R,j} - w_{L,j})^2}{6} . \tag{3.24}$$

This complete the description of the calculation of the interpolation polynomial.

3.1.2 Zone–Edge Mean Values

The following step is that of determining the characteristic domain of dependence with respect to a zone edge, that is to identify the regions of space to the left and to the right of the edge that encompass all the information that can reach the zone edge during the current time step (see Figure 3.2) Then, using interpolated distributions, mean values of each hydrodynamic variable are computed over the left and right domains. This gives the initial states $w_{j+1/2,L}$ $w_{j+1/2,R}$ that will be used to solve the corresponding Riemann problem.

We define the averages of the interpolation functions as:

$$f^w_{j+1/2,L}(y) = \frac{1}{y}\int_{\xi_{j+1/2}-y}^{\xi_{j+1/2}} w(\xi)d\xi \tag{3.25}$$

$$f^w_{j+1/2,R}(y) = \frac{1}{y}\int_{\xi_{j+1/2}}^{\xi_{j+1/2}+y} w(\xi)d\xi \,, \tag{3.26}$$

where y is assumed to be positive. The correct averaged values are calculated constructing a first guess to the left and right states using the largest and smallest values of the characteristic speeds. These determine the maximum distances aside the zone edge from which an information propagating in the fluid can reach the edge during one time step Δt. The first guesses are calculated as:

$$\tilde{w}_{j+1/2,L} = f^w_{j-1/2,L}(x_{j+1/2} - x_{j+1/2,L}) \tag{3.27}$$

$$\tilde{w}_{j+1/2,R} = f^w_{j-1/2,R}(x_{j+1/2,R} - x_{j+1/2}) \,, \tag{3.28}$$

where

$$x_{j+1/2,L} = x_{j+1/2} - \max(0, \Delta t(v^n_j + c^n_j)) \tag{3.29}$$

$$x_{j+1/2,R} = x_{j+1/2} + \max(0, -\Delta t(v^n_{j+1} + c^n_{j+1})) \,. \tag{3.30}$$

In general, not all the information contained in this region can reach the edge of the zone in Δt and influence its status. Hence the first guess must be properly corrected. This is achieved using the linearized characteristic equations, which give:

$$w_{j+1/2,S} = w_{j+1/2,S} + F^w(\beta^+_{j+1/2,S}, \beta^0_{j+1/2,S}, \beta^-_{j+1/2,S}), \tag{3.31}$$

where $S = L, R$ and F^w is a proper linear combination of the quantities $\beta^+_{j+1/2,S}$, $\beta^0_{j+1/2,S}$ and $\beta^-_{j+1/2,S}$, functions of the hydrodynamical variables. For the detailed description of the calculation of these quantities and of the correction to the first guess we refer to section 3.2.1, where a general form of these quantities is derived including also the gravitational forces and the expansion of the universe.

3.1.3 The Riemann Problem and the Finite Differences Equations

The interaction between the left (L) and right (R) states is described by solving the corresponding Riemann problem, described in detail in section 2.3 (see Figure 3.2). The left and right estimates of the hydrodynamical quantities are first used to determine which of

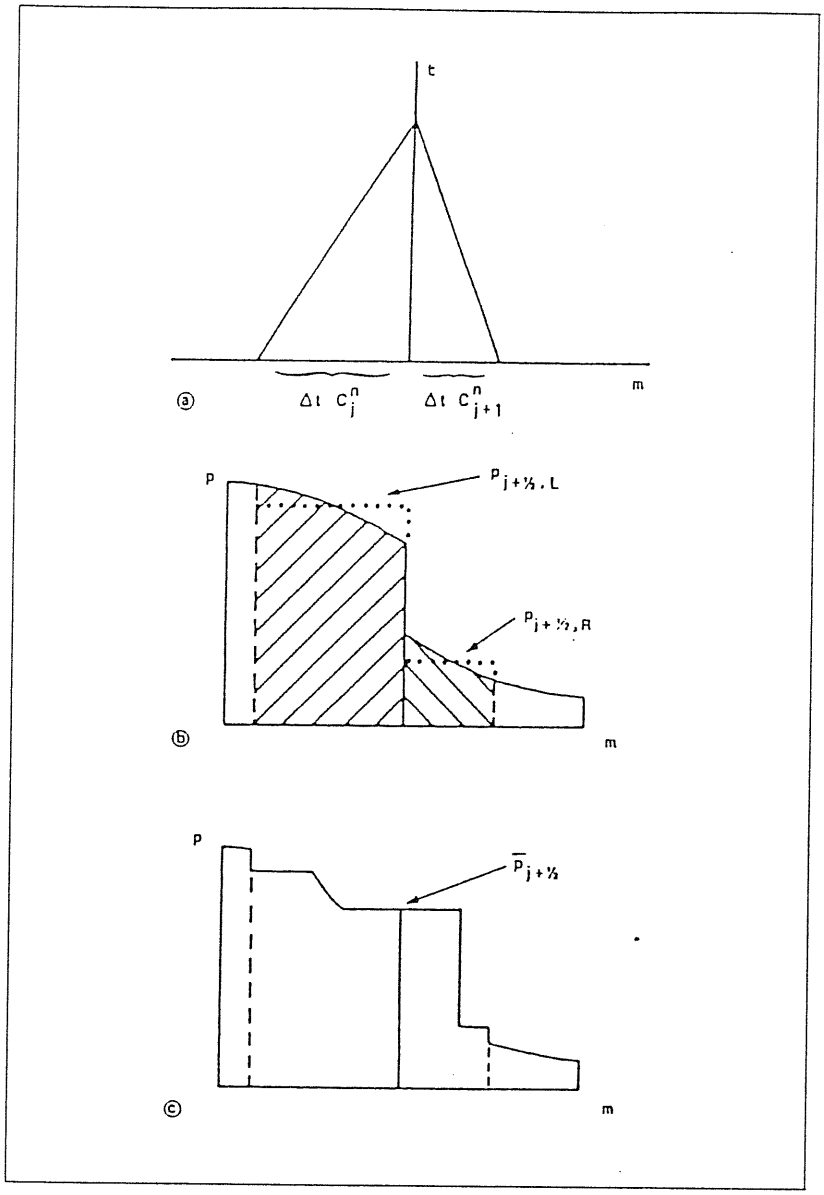

Figure 3.2: Computation of the fluxes with PPM in the case of null bulk velocity of the fluid ($v_j^n = v_{j+1}^n = 0$). (a) The left and right domains of dependence for a zone interface during the time step are determined. (b) The detailed interpolated distribution of each variable (in this case the pressure is shown) within each domain of dependence is replaced by its spatial average. This replacement facilitates the computation of the nonlinear interaction of the two domains. (c) The interaction of the two averaged states adjacent to the interface is described by the solution to the corresponding Riemann problem.

the five possible patterns (2.35)-(2.39) is the one in which our initial discontinuity breaks down. Then the corresponding Riemann problem can be solved. At this point, since we know the velocity at which the various waves moves with respect to initial discontinuity (the zone edge), we can determine which is the status of the fluid at the zone boundary at half time step. For example, a situation in which the bulk velocity of the fluid with respect to the zone edge is null and the pressure gradient is negative, corresponds to the case (2.36). Therefore the fluid at the zone edge is characterized by the post–shock values for pressure and velocity, while the density has the value behind the contact discontinuity. In the other extreme, we can have an initial situation with a "very" high bulk velocity toward right. In this case whatever is the resulting Riemann pattern, all the waves at half time step have been already convected away with the bulk flow, and the zone edge status is unperturbed R one.

The solutions of the Riemann problem are the time centered values of the variables at the zone edges $\bar{\varrho}_{j\pm1/2}$, $\bar{v}_{j\pm1/2}$ and $\bar{p}_{j\pm1/2}$, which are used to compute inter–cell fluxes and to solve the hydrodynamical equations by the conservative finite differences scheme:

$$\varrho_j^{n+1} = \varrho_j^n + \Delta t \left(\frac{\bar{\varrho}_{j-1/2}\bar{v}_{j-1/2} - \bar{\varrho}_{j+1/2}\bar{v}_{j+1/2}}{\Delta x} \right) \tag{3.32}$$

$$v_j^{n+1} = \frac{1}{\varrho_j^{n+1}} \left[\varrho_j^n v_j^n + \Delta t^{n+1/2} \left(\frac{\bar{\varrho}_{j-1/2}\bar{v}_{j-1/2}^2 + \bar{p}_{j-1/2} - \bar{\varrho}_{j+1/2}\bar{v}_{j+1/2}^2 - \bar{p}_{j+1/2}}{\Delta x} \right) \right] \tag{3.33}$$

$$E_j^{n+1} = E_j^n + \Delta t \left[\frac{\left(\frac{1}{2}\bar{\varrho}_{j-1/2}\bar{v}_{j-1/2}^2 + \frac{\gamma}{\gamma-1}\bar{p}_{j-1/2} \right) \bar{v}_{j-1/2} - \left(\frac{1}{2}\bar{\varrho}_{j+1/2}\bar{v}_{j+1/2}^2 + \frac{\gamma}{\gamma-1}\bar{p}_{j+1/2} \right) \bar{v}_{j+1/2}}{\Delta x} \right] . \tag{3.34}$$

3.2 The Cosmological PPM Scheme

For cosmological applications several important modifications must be introduced into the basic PPM scheme. The inclusion of gravitational forces and cosmic expansion changes the form of the usual hydrodynamical equations. The expansion of the universe enters the hydrodynamical equations in two different ways. First, all of the fluxes and the source

terms are multiplied by the factor $1/a(t)$. Second, two further terms, $(\dot{a}/a)\varrho v_j$ and $(\dot{a}/a)E$, appear in the equations for the conservation of momentum and energy, respectively (in the following we will refer to these terms as expansion terms). This leads to important changes both in the Riemann solver and in the final integration. Also gravitational forces are included in the Riemann solver and in the final integration step. In order to obtain a proper estimate of the force felt by a fluid element, its averaged value over the entire zone is calculated. For the detailed description of this procedure we refer to section 3.2.2

3.2.1 Characteristic Equations

The solution of the Riemann problem, which is the central feature of the Godunov approach, requires the knowledge of the characteristic form of hydrodynamic equations. Indicating by x the relevant space direction during the one–dimensional sweep, by v the velocity in the direction of the one–dimensional sweep and by u the velocity orthogonal to v, equations (2.9)–(2.11) can be rewritten in the form:

$$\frac{\partial \mathbf{U}}{\partial t} + \mathbf{A}\frac{\partial \mathbf{U}}{\partial x} + \mathbf{C} = 0 , \tag{3.35}$$

where

$$\mathbf{U} = \begin{pmatrix} \varrho \\ v \\ u \\ p \end{pmatrix} , \quad \mathbf{A} = \frac{1}{a}\begin{pmatrix} v & 0 & 0 & \varrho \\ 0 & v & 0 & 1/\varrho \\ 0 & 0 & v & 0 \\ 0 & \gamma p & 0 & v \end{pmatrix} , \quad \mathbf{C} = \begin{pmatrix} 0 \\ v\dot{a}/a - g \\ u\dot{a}/a \\ 2p\dot{a}/a \end{pmatrix} . \tag{3.36}$$

In order to find the characteristic form of this system, we first solve the corresponding eigenvalue equation:

$$\det(\mathbf{A} - \lambda \mathbf{I}) = 0 , \tag{3.37}$$

where $\mathbf{I}$ is the identity of elements $i_{i,j} = 1$ if $i = j$ and $i_{i,j} = 0$ otherwise. We obtain as eigenvalues:

$$\lambda_0 = \frac{v}{a} , \quad \lambda_- = \frac{v - c}{a} , \quad \lambda_+ = \frac{v + c}{a} , \tag{3.38}$$

where λ_0 is a double solution and c is the sound speed. The eigenvalues are used to compute the domain of dependence of a given fluid element. Notice that in expanding coordinates the domain must be rescaled by the factor $a(t)$ with respect to that in proper coordinates.

The corresponding left eigenvectors l_k are:

$$\mathrm{l}_{01} = (0,0,1,0) \tag{3.39}$$

$$\mathrm{l}_{02} = (1,0,0,-1/c^2) \tag{3.40}$$

$$\mathrm{l}_{-} = (0,-\frac{\varrho c}{2},0,\frac{1}{2}) \tag{3.41}$$

$$\mathrm{l}_{+} = (0,\frac{\varrho c}{2},0,\frac{1}{2})\,. \tag{3.42}$$

The characteristic form of hydrodynamical equations is (see section 2.2):

$$\mathrm{l}_k\frac{\partial \mathbf{U}}{\partial t} + \mathrm{l}_k\mathbf{A}\frac{\partial \mathbf{U}}{\partial x} + \mathrm{l}_k\mathbf{C}\;dt = 0\,, \tag{3.43}$$

$$\mathrm{l}_k\frac{\partial \mathbf{U}}{\partial t} + \lambda_k\mathrm{l}_k\frac{\partial \mathbf{U}}{\partial x} + \mathrm{l}_k\mathbf{C}\;dt = 0\,, \tag{3.44}$$

that is:

$$\mathrm{l}_k d\mathbf{U} + \mathrm{l}_k\mathbf{C}\;dt = 0, \qquad \text{along } \frac{dx}{dt} = \lambda_k\,. \tag{3.45}$$

Then, for our fluid, the characteristic equations are:

$$c^2 d\varrho - dp - 2\frac{\dot{a}}{a}p\;dt = 0 \tag{3.46}$$

$$du - \frac{\dot{a}}{a}u\;dt = 0 \tag{3.47}$$

along $dx/dt = v/a$, and

$$dp \pm \varrho c\;dv + \left[2\frac{\dot{a}}{a}p \pm \varrho c\left(\frac{\dot{a}}{a}v - g\right)\right]dt = 0 \tag{3.48}$$

along $dx/dt = (v \pm c)/a$.

Characteristic equations can now be used both for calculating the domain of dependence of a zone edge and for constructing the Riemann solver.

First of all the approximate guess to the initial states for the Riemann problem expressed by equation (3.27) and (3.28) are modified taking into account of the expansion of the universe

$$\tilde{w}_{j+1/2,L} = f^{w}_{j+1/2,L}(x_{j+1/2} - x_{j+1/2,L}) \tag{3.49}$$

$$\tilde{w}_{j+1/2,R} = f^{w}_{j+1/2,R}(x_{j+1/2,R} - x_{j+1/2}) \ , \tag{3.50}$$

where, in this case:

$$x_{j+1/2,L} = x_{j+1/2} - \max\left(0, \frac{\Delta t(v^n_j + c^n_j)}{a}\right) \tag{3.51}$$

$$x_{j+1/2,R} = x_{j+1/2} + \max\left(0, -\frac{\Delta t(v^n_{j+1} + c^n_{j+1})}{a}\right) \ . \tag{3.52}$$

Then we calculate the mean value of the hydrodynamic variables in the domains defined by each of the characteristic lines coming from the left and the right of the zone boundary $j + 1/2$:

$$w^k_{j+1/2,L} = f_{j+1/2,L}(x_{j+1/2} - x^k_{j+1/2,L}) \ , \tag{3.53}$$

$$w^k_{j+1/2,R} = f_{j+1/2,R}(-x_{j+1/2} + x^k_{j+1/2,R}) \ , \tag{3.54}$$

where $k = +, 0, -$ and

$$x^k_{j+1/2,L} = x_{j+1/2} - \Delta t\lambda_{j,k}, \qquad x^k_{j+1/2,R} = x_{j+1/2} + \Delta t\lambda_{j+1,k} \ . \tag{3.55}$$

Finally we correct the initial guess considering only those information which can reach the zone edge during the current time step. Using the characteristic equations we have:

$$p_{j+1/2,S} = \tilde{p}_{j+1/2,S} + \tilde{C}^2_{j+1/2,S}(\beta^+_{j+1/2,S} + \beta^-_{j+1/2,S}) \ , \tag{3.56}$$

$$v_{j+1/2,S} = \tilde{v}_{j+1/2,S} + \tilde{C}_{j+1/2,S}(\beta^+_{j+1/2,S} - \beta^-_{j+1/2,S}) \ , \tag{3.57}$$

$$\varrho_{j+1/2,S} = \left(\frac{1}{\tilde{\varrho}_{j+1/2,S}} - \sum_{k=+,0,-} \beta^k_{j+1/2,S}\right)^{-1} \ . \tag{3.58}$$

Here $\tilde{C}^2_{j+1/2,S} = (\gamma\tilde{p}_{j+1/2}\tilde{\varrho}_{j+1/2})$ and $S = L$ or R. Finally we have that

$$u_{j+1/2,L} = \tilde{u}_{j+1/2,L}, \qquad \beta^k_{j+1/2,L} = 0 \quad \text{if} \quad \lambda_{j,k} \leq 0 \ , \tag{3.59}$$

$$u_{j+1/2,R} = \tilde{u}_{j+1/2,R}, \qquad \beta^k_{j+1/2,R} = 0 \quad \text{if} \quad \lambda_{j+1,k} \leq 0 \,. \tag{3.60}$$

Otherwise

$$\beta^{\pm}_{j+1/2,S} = \mp \frac{1}{\tilde{C}_{j+1/2,S}} \left[(\tilde{v}_{j+1/2,S} - v^{\pm}_{j+1/2,S}) \pm \frac{\tilde{p}_{j+1/2,S} - p^{\pm}_{j+1/2,S}}{\tilde{C}_{j+1/2,S}} \right] \tag{3.61}$$

$$- \frac{\Delta t}{\tilde{C}_{j+1/2,S}} \left(2 \frac{\dot{a}}{a} \frac{p^{\pm}_{j+1/2,S}}{\tilde{C}_{j+1/2,S}} \pm \frac{\dot{a}}{a} v^{\pm}_{j+1/2,S} \mp g^{\pm}_{j+1/2,S} \right) \tag{3.62}$$

$$\beta^0_{j+1/2,S} = \left(\frac{\tilde{p}_{j+1/2,S} - p^0_{j+1/2,S}}{\tilde{C}^2_{j+1/2,S}} + \frac{1}{\tilde{\varrho}_{j+1/2,S}} - \frac{1}{\varrho^0_{j+1/2,S}} + 2 \frac{\dot{a}}{a} \frac{p^{\pm}_{j+1/2,S}}{\tilde{C}^2_{j+1/2,S}} \right) \tag{3.63}$$

$$u_{j+1/2,S} = u^0_{j+1/2,S} \,. \tag{3.64}$$

The time averaged estimates of the solution at $x_{j+1/2}$ are determined solving the Riemann problem with initial states determined by equations (3.56)-(3.58) following the procedure described in section 2.3.

3.2.2 Gravitational Step

The peculiar gravitational potential ϕ^n is computed at the full time step by the Poisson equation (2.72), which is solved using a standard FFT technique. We preferred to avoid computing directly the gravitational acceleration by the FFT's as this would require four Fourier transform instead of two and a higher requirement in computational time and memory.

At each time step we also need to compute the time-centered value of the potential $\phi^{n+1/2}$. This is done using a linear extrapolation from the previous two time steps:

$$\phi^{n+1/2} = \phi^n (1 + \frac{\Delta t^n}{2\Delta t^{n-1}}) - \phi^{n-1} \frac{\Delta t^n}{2\Delta t^{n-1}}. \tag{3.65}$$

As the gravitational potential varies little during a time step, the extrapolation (3.65) is sufficiently accurate during the whole evolution.

The value of the potential at the beginning of the step is used to compute the gravitational acceleration needed to solve properly the Riemann problem. Instead $\phi^{n+1/2}$ is used to calculate the time-centered value of the acceleration for the final integration step of the PPM scheme. In both the cases the acceleration required is the one felt by the whole zone

and not just from its center. We evaluate the mass weighted average acceleration over the zone following the same procedure used by Bryan *et al.*(1995); we expand the density and acceleration fields and retaining all terms up to second order in Δx:

$$g_j = \frac{1}{2a(t)\Delta x}\left[\phi_{j+1} - \phi_{j-1} + \frac{1}{12}(\phi_{j+1} - 2\phi_j + \phi_{j-1})\frac{\delta\varrho_j}{\varrho_j}\right]. \tag{3.66}$$

In order to avoid the introduction of new unphysical extrema we calculate the slope $\delta\varrho$ as:

$$\delta\varrho_j = \min(|\varrho_{j+1} - \varrho_{j-1}|, 2|\varrho_j - \varrho_{j-1}|, 2|\varrho_{j+1} - \varrho_j|)\mathrm{sgn}(\varrho_{j+1} - \varrho_{j-1}) \tag{3.67}$$

$$\mathrm{if}(\varrho_{j+1} - \varrho_j)(\varrho_j - \varrho_{j-1}) < 0 \tag{3.68}$$

$$\delta\varrho_j = 0 \text{ otherwise.} \tag{3.69}$$

Because of its smoothness, the gravitational potential does not require the same monotonicity constraint.

3.2.3 Correction to the Energy

In order for overall energy to be accurately conserved it is important to use the total energy density E directly as a dependent variable (equation (2.11)) rather than calculate it as the sum of the kinetic and internal energy densities ($\frac{1}{2}\varrho\mathbf{v}^2$ and e, respectively). The value of e is however required in order to calculate the thermodynamic quantities such as pressure and temperature and the original PPM code calculates e as the difference between E and $\frac{1}{2}\varrho\mathbf{v}^2$. However, this procedure is not always applicable in cosmological simulations where highly supersonic flows are often present. In these situations, the ratio between the kinetic and internal energies can reach values as high as 10^8 so that the errors in calculating e by the standard PPM procedure become much larger than the quantity itself.

In our code, we solved this problem by calculating both the total and internal energy per unit comoving volume. In comoving coordinates the equation for the internal energy density $e = p/(\gamma - 1)$ is the following:

$$\frac{\partial e}{\partial t} = -\frac{1}{a}\frac{\partial}{\partial x_j}(ev_j) - 2\frac{\dot{a}}{a}e - \frac{1}{a}p\frac{\partial v_j}{\partial x_j}, \tag{3.70}$$

where the sum over the index j is implied. Hence, at each time step, both the total and internal energy equations are solved and the results combined according to the local conditions in the fluid. The value obtained from equation (3.70) has to be only used when the internal energy cannot be calculated accurately as the difference between total and kinetic energy. This is usually the case in expanding or weakly compressing (comoving) regions, that is in regions in which one of the following conditions holds:

$$\nabla \cdot v \geq 0 , \qquad \frac{1}{p}|\nabla p| \leq \eta_1 . \tag{3.71}$$

If neither of these conditions is verified, the internal energy is computed according to the following criterion:

$$e = \begin{cases} E - \frac{1}{2}\varrho \mathbf{v}^2 & \text{if } E - \frac{1}{2}\varrho \mathbf{v}^2 / E \geq \eta_2 \\ e & \text{otherwise} , \end{cases} \tag{3.72}$$

where η_1 and η_2 are suitable parameters smaller than unity, fixed on the bases of numerical experimentation. Various tests have suggested the use of the following values: $\eta_1 = 0.3$ and $\eta_2 = 0.005$.

3.2.4 Extension to Three Dimensions

The PPM scheme described in the previous sections concern the integration in one dimension, even though the components of the velocity orthogonal to the integration direction are considered and properly treated. The extension to more dimensions is achieved using a direction splitting technique (Strang 1968). This family of methods is based on integrating the dynamical equations that govern the system in one direction at a time, using for each direction the data just updated in the previous direction. In other words, if we indicate with $L_k^{\Delta t}$ the PPM integration in the k–th direction for a time step Δt, the updated value for the generic hydrodynamical variable u is calculated as:

$$u^{new} = L_z^{\Delta t} L_y^{\Delta t} L_x^{\Delta t} u^{old} . \tag{3.73}$$

In order to preserve second–order accuracy in space and avoid the introduction of preferential directions, in successive time steps the order of directional integration is permuted as

follows:

$$L_z L_y L_x,\ L_x L_y L_z,\ L_x L_z L_y,\ L_y L_z L_x,\ L_y L_x L_z,\ L_z L_x L_y\ , \tag{3.74}$$

where for simplicity we have dropped the Δt superscript. Other directional splitting schemes are possible, however our tests have proved that the accuracy of their results is comparable with that obtained by the described method while, in general, they are more complicated and computationally more expensive.

3.2.5 Expansion Step

After the hydrodynamical quantities have been updated by the PPM step, they must be corrected for including the effect of the expansion terms. These terms in fact, being proportional to the integrated quantity itself, cannot be treated in the basic procedure and must be integrated in a separate step. If we indicate by $\varrho_{H,j}^{n+1}$, $\mathbf{v}_{H,j}^{n+1}$ and $p_{H,j}^{n+1}$ the hydrodynamical quantities obtained from the PPM integration part,we can use the following semi–implicit procedure:

$$\varrho_j^{n+1} = \varrho_{H,j}^{n+1} \tag{3.75}$$

$$v_j^{n+1} = \frac{2v_{H,j}^{n+1} - \Delta t^{n+1/2}(\dot{a}/a)^{n+1/2} v_j^n}{2 + \Delta t^{n+1/2}(\dot{a}/a)^{n+1/2}} \tag{3.76}$$

$$E_j^{n+1} = \frac{E_{H,j}^{n+1} - \Delta t^{n+1/2}(\dot{a}/a)^{n+1/2} E_j^n}{1 + \Delta t^{n+1/2}(\dot{a}/a)^{n+1/2}}\ . \tag{3.77}$$

The accuracy in the results tends to improve imposing slow variation of the expansion factor, which corresponds to introduce an appropriate time step constraint on the term $\Delta a/a$.

3.3 N–body Methods

The non–linear dynamics of the dark component is in general computed by N–body techniques (Hockney & Eastwood 1981). The basic idea is to follow the evolution of a set of N massive particles which interact only gravitationally. The position and the velocity of the particles are computed through equations (2.64) and (2.65), which define the position and the velocity of the particles at each time level. The fundamental step of this calculation

is the evaluation of gravitational forces. This problem has been solved in several different ways. The first N–body codes directly computed the force on each particle summing the contribution of all other particles:

$$\mathbf{F}_i = \sum_{j\neq i, j=1}^{N} \frac{G m_i m_j \mathbf{x}_{i,j}}{|\mathbf{x}_{i,j}|^3} , \tag{3.78}$$

where i and j indicates the i–th and j–th particle respectively, $\mathbf{x}_{i,j} = \mathbf{x}_i - \mathbf{x}_j$ and m_i and m_j are the particles' masses. This method, called Particle–Particle method (PP), is very accurate but the computational time required in the computation scales as $O(N^2)$ and for more than a few thousands particles it becomes prohibitively expensive. This limits strongly both the dynamical range and the resolution affortable with numerical simulation and therefore its possible applications to the cosmological context.

The limit on particle number of PP methods was later circumvented by approximating the gravitational potential by some different methods. A first possibility consists in calculating the gravitational field on a mesh of fixed resolution. Efficient solution methods for Poisson's equation on regular mesh, such as the FFT convolution, allows an algorithm with computational time which scales as $\sim O(N \log N)$, although the force resolution is limited to roughly two grid separations. These types of method are called Particle–Mesh (PM) algorithms. The PP and PM methods have been subsequently linked together in the P^3M methods. This method splits the gravitational force into two components, long and short–range. The PM algorithm is used to compute the long range component. On scales smaller than about two grid spacings the mesh force is corrected by a direct PP sum over near neighbours to include the short range component of the force. This technique produces a scheme with better resolution than the PM method and, in general, lower computational requirement than the PP method. The main difficulty occurs when the amount of clustering becomes high and the number of neighbours in the PP sum increases. Under these conditions the computational time tends to increase very rapidly, again as $O(N^2)$. More recently codes have been developed which represent the gravitational field via a multipole expansion. The two main variants of this approach are the various tree codes (Barnes & Hut 1986), and the true multipole expansion methods (Greengard & Rockhlin 1987). These

methods have the advantage over grid based codes that their resolution is not limited by the grid scale, while retaining a computational time that scales as $N \log N$. In addition, this kind of schemes, making no use of the grid, are more easily associated with particles based hydrodynamical codes, like SPH, rather than Eulerian codes.

Finally, we have to mention multigrid methods (Brandt 1982) that solve Poisson's equation using a multilevel grid together with some kind of relaxation procedure. The latter solve the equation minimizing the errors on the various grid scales. It is successively applied over grids of various coarseness reducing the error on the corresponding scales. Its computational time scales approximatively as a PM method, but it has the great advantage to allow the use of non–uniform grids and hence the introduction of local refinements where higher resolution is needed.

3.4 The PM Code

With the Particle Mesh method gravitational forces are calculated first smoothing the mass distribution on a uniform grid and then calculating the corresponding potential by solving the Poisson's equation with a Fast Fourier Transform (FFT) convolution method. The mass density is determined distributing the mass of each particle between the grid cells. In general:

$$\varrho(\mathbf{x}_{i,j,k}) = \frac{1}{\Delta x^3} \sum_{p=1}^{N} m_p W(\mathbf{x}_p - \mathbf{x}_{i,j,k}) , \tag{3.79}$$

where $\mathbf{x}_{i,j,k}$ is the position of the (i,j,k) cell, $\mathbf{x}_p$ and m_p are the position and the mass of the p-th particle respectively, Δx^3 is the cell volume and W is a suitable interpolation function. A common choice of the interpolation function is that given by the Cloud In Cell method (CIC):

$$w_i = 1 - \frac{|x_i - x_p|}{\Delta x}, \qquad \text{if } |x_i - x_p| \leq \Delta x , \tag{3.80}$$

$$w_i = 0, \qquad \text{otherwise} ; \tag{3.81}$$

where i indicates the i–th coordinate of the cell and x_p is the corresponding coordinate of the particle. Then:

$$W = w_i w_j w_k \ . \tag{3.82}$$

Another possibility is given by the more accurate but expensive Triangular Shaped Method:

$$w_i = 3/4 - \frac{|x_i - x_p|^2}{\Delta x}, \qquad \text{if } \frac{|x_i - x_p|}{\Delta x} \leq 1 \tag{3.83}$$

$$w_i = (1/2)\left[3/2 - \frac{|x_i - x_p|}{\Delta x}\right]^2, \qquad \text{if } 1/2 \leq \frac{|x_i - x_p|}{\Delta x} \leq 3/2 \tag{3.84}$$

$$w_i = 0, \qquad \text{otherwise ;} \tag{3.85}$$

also in this case:

$$W = w_i w_j w_k \ . \tag{3.86}$$

The CIC method has proved to be sufficiently accurate for our demands. Furthermore it requires a much lower computational effort than TSC thus it has been used for our code.

At this point we calculate the total density field as the sum of the collisionless and of the baryonic contributions and we transform the result to the Fourier space using a FFT method. In the Fourier space the Poisson equation is a simple algebraic equation of the form:

$$\phi_{\mathbf{k}} = G_{\mathbf{k}} \delta_{\mathbf{k}} \ , \tag{3.87}$$

where $\phi_{\mathbf{k}}$ and $\delta_{\mathbf{k}}$ are the Fourier transform of the gravitational potential and of the density contrast respectively, while $G(\mathbf{k})$ is the Green function of the Laplacian, commonly defined as:

$$G_{\mathbf{k}} \propto -\frac{1}{|\mathbf{k}|^2} \ . \tag{3.88}$$

Using an inverse FFT, $\phi_{\mathbf{k}}$ is calculated in the physical space. Differencing the potential by some finite differences method we obtain the forces at each grid point. For example the x component of the gravitational force on the cell i, j, k can be calculated as

$$F_{x;i,j,k} = -\frac{\phi_{i+1,j,k} - \phi_{i-1,j,k}}{2\Delta x} \ . \tag{3.89}$$

Alternatively, one can think of calculating the force directly in the Fourier space using the relation

$$F_s \propto ik_s \frac{1}{|\mathbf{k}|^2}\,, \tag{3.90}$$

where F_s and k_s are the Fourier transform of the force and the wave vector in the s direction. An inverse Fourier transform gives the s-component of the force in the physical space. This is an accurate method to calculate the force, however it has the drawback that it requires four Fourier transform to calculate all the components of the force, then more computational time, and higher memory requirement.

Finally, the force on each particle is calculated averaging forces on nearby grid points. To ensure the conservation of energy and momentum the average must be calculated using the same interpolation scheme adopted to compute the density.

In order to solve numerically equations (2.64) and (2.65), N–body techniques generally use the Leap-Frog method, which has second–order time accuracy and complete the integration in one step, minimizing computational time and memory requirement. However the Leap-Frog scheme requires constant time steps to work properly. The hydrodynamical part of the code imposes instead variable time intervals, determined by the Courant condition. In order to use these variable time intervals, the leapfrog integrator has been replaced by a second–order Lax–Wendroff scheme (Roache, 1982). This scheme works with non constant time steps and guarantees second order time accuracy. It is based on the following two steps procedure. In the first step the position and the velocity of the particles is updated to half the present time step by a first order one–side scheme:

$$\mathbf{v}_j^{n+1/2} = \mathbf{v}_j^n - \left(\dot{a}^n \mathbf{v}_j^n + \mathbf{g}_j^n\right) \frac{\Delta t^{n+1/2}}{2a^n} \tag{3.91}$$

$$\mathbf{x}_j^{n+1/2} = \mathbf{x}_j^n + \mathbf{v}_j^n \frac{\Delta t^{n+1/2}}{2a^n}\,, \tag{3.92}$$

where $\mathbf{x}_j$ and $\mathbf{v}_j$ are the position and the velocity of the j–th particle and $\mathbf{g}_j^n$ is the gravitational force on the j–th particle. In the second step the positions and the velocities are updated to the new time by a time centered scheme, making use of the results of the first

step:

$$\mathbf{v}_j^{n+1} = \mathbf{v}_j^n - \left(\dot{a}^{n+1/2}\mathbf{v}_j^{n+1/2} + \mathbf{g}_j^{n+1/2}\right)\frac{\Delta t^{n+1/2}}{a^{n+1/2}} \tag{3.93}$$

$$\mathbf{x}_j^{n+1} = \mathbf{x}_j^n + \mathbf{v}_j^{n+1/2}\frac{\Delta t^{n+1/2}}{a^{n+1/2}} \,. \tag{3.94}$$

The drawback of this method is the increase in computational time due to the two steps procedure. However this has proved to be a minor problem as most of the time is spent in the hydrodynamical part of the code and in the calculation of the gravitational forces.

3.5 Time Step

For determining the new time step at the end of the time step integration we impose several constraints. First of all, we require that the maximum variation of the expansion factor a during a time step is less than 2%. We impose also that dark matter particles move no more than half a cell in a single step and that the gas dynamics satisfies the Courant condition:

$$\Delta t \leq \min\left[\frac{C_c\, a(t)\Delta x}{[c + \max(|v_x|, |v_y|, |v_z|)]}\right] , \tag{3.95}$$

where C_c is the Courant number and the minimum is computed over all cells. We set $C_c = 0.5$. Finally, we require that in a single step the time step increases by no more than 20% from its previous value.

Our tests indicate that the expansion condition is important only in the first part of the simulation, when the amplitude of the fluctuations is still small. At later times the Courant condition becomes the dominant one.

3.6 Structure of the Code

In this section we make a summary of the main steps in the integration of the dynamical equations presented in the previous sections. The same grid of constant mesh size Δx is used for solving the hydrodynamical equations and for computing the total gravitational potential. We recall that the subscript j indicates zone centered values of grid quantities,

while subscript $(j+1/2)$ refers to values computed at the boundary between the j–th and $(j+1)$–th zones. Finally, in the dynamical equations for the dark matter the subscript j refers to the j–th particle. Superscripts indicate the time level at which variables are calculated. The same time interval $\Delta t^{n+1/2} = t^{n+1} - t^n$ is used for integrating the dynamical equations of both components.

The main steps in the integration of the dynamical equations are the following:

1 – At the time t^n we have $\varrho^n_{BM,j}$, $\mathbf{v}^n_{BM,j}$ and p^n_j for the baryonic matter. For the dark matter we have $\mathbf{x}^n_{DM,j}$ and $\mathbf{v}^n_{DM,j}$. First we calculate the dark matter density $\varrho^n_{DM,j}$ using a cloud–in–cell mass assignment scheme. Then we compute the total peculiar gravitational potential ϕ^n_j on the grid by solving the Poisson equation using a standard FFT technique. We also extrapolate the gravitational potential to $t^{n+1/2}$ using the values at t^n and t^{n-1}

$$\phi^{n+1/2} = \phi^n \left(1 + \frac{\Delta t^{n+1/2}}{2\Delta t^{n-1/2}}\right) - \phi^{n-1} \frac{\Delta t^{n+1/2}}{2\Delta t^{n-1}} \,. \tag{3.96}$$

2 – We start the hydrodynamical one–dimensional sweep. For a given direction we indicate by v the component of the velocity along the direction of integration and by u the component orthogonal to v. We then calculate the time averaged values of the hydrodynamical quantities at the zone interfaces $\bar{\varrho}_{j+1/2}$, $\bar{p}_{j+1/2}$, $\bar{v}_{j+1/2}$ and $\bar{u}_{j+1/2}$ using the PPM scheme, as described in Section 3.1, 3.2 and in Appendix A.

3 – We use the time averaged estimates calculated in point 2 to solve the one–dimensional hydrodynamical equations without the inclusion of the expansion terms (for simplicity in the following equations we have dropped the BM subscript):

$$\varrho^{n+1}_{H,j} = \varrho^n_j + \frac{\Delta t^{n+1/2}}{a^{n+1/2}} \left(\frac{\bar{\varrho}_{j-1/2}\bar{v}_{j-1/2} - \bar{\varrho}_{j+1/2}\bar{v}_{j+1/2}}{\Delta x} \right) \tag{3.97}$$

$$v^{n+1}_{H,j} = \frac{1}{\varrho^{n+1}_{H,j}} \left[\varrho^n_j v^n_j + \frac{\Delta t^{n+1/2}}{a^{n+1/2}} \left(\frac{\bar{\varrho}_{j-1/2}\bar{v}^2_{j-1/2} + \bar{p}_{j-1/2} - \bar{\varrho}_{j+1/2}\bar{v}^2_{j+1/2} - \bar{p}_{j+1/2}}{\Delta x} \right) \right] + \\ + \frac{\Delta t^{n+1/2}}{\varrho^{n+1}_{H,j}} \frac{\varrho^{n+1}_j + \varrho^n_j}{2} g_j \tag{3.98}$$

$$E^{n+1}_{H,j} = E^n_j + \frac{\Delta t^{n+1/2}}{a^{n+1/2}} \left[\frac{\left(\frac{1}{2}\bar{\varrho}_{j-1/2}\bar{v}^2_{j-1/2} + \frac{\gamma}{\gamma-1}\bar{p}_{j-1/2}\right)\bar{v}_{j-1/2} - \left(\frac{1}{2}\bar{\varrho}_{j+1/2}\bar{v}^2_{j+1/2} + \frac{\gamma}{\gamma-1}\bar{p}_{j+1/2}\right)\bar{v}_{j+1/2}}{\Delta x} \right] +$$

$$+ \Delta t^{n+1/2} \frac{\varrho_j^{n+1} v_j^{n+1} + \varrho_j^n v_j^n}{2} g_j \tag{3.99}$$

$$u_{H,j}^{n+1} = \frac{1}{\varrho_{H,j}^{n+1}} \left[\varrho_j^n u_j^n + \frac{\Delta t^{n+1/2}}{a^{n+1/2}} \left(\frac{\bar{\varrho}_{j-1/2} \bar{v}_{j-1/2} \bar{u}_{j-1/2} - \bar{\varrho}_{j+1/2} \bar{v}_{j+1/2} \bar{u}_{j+1/2}}{\Delta x} \right) \right] . \tag{3.100}$$

The quantity g_j is the time–centered value of the gravitational force averaged on the j–th cell calculated by equation (3.66). Points 2 and 3 are repeated for the other two orthogonal directions completing the three–dimensional hydrodynamical calculation.

4 – Energy is corrected to account for highly supersonic flows. The internal energy equation is solved first including the energy flux term by the standard PPM integration procedure:

$$\tilde{e}_{H,j}^{n+1} = e_j^n + \frac{\Delta t^{n+1/2}}{a(t^{n+1/2})} \left(\frac{\bar{p}_{j-1/2} \bar{v}_{j-1/2} - \bar{p}_{j+1/2} \bar{v}_{j+1/2}}{(\gamma - 1) \Delta x} \right) . \tag{3.101}$$

Then this value is corrected including the pressure forces as:

$$e_{H,j}^{n+1} = \tilde{e}_{H,j}^{n+1} + \frac{1}{a^{n+1/2}} \frac{\Delta t^{n+1/2}}{\Delta x} \frac{p_j^{n+1/2}}{\varrho_j^n} (\bar{v}_{j-1/2} - \bar{v}_{j+1/2}) , \tag{3.102}$$

where $p_j^{n+1/2} = (\bar{p}_{j-1/2} + \bar{p}_{j+1/2})/2$. Finally, we consider also the expansion term in the internal energy equation:

$$e_j^{n+1} = \frac{e_{H,j}^{n+1} - \Delta t^{n+1/2} (\dot{a}/a)^{n+1/2} e_j^n}{1 + \Delta t^{n+1/2} (\dot{a}/a)^{n+1/2}} . \tag{3.103}$$

This expression for internal energy is used if the following conditions hold:

$$\sum_{i=1,3} \frac{\partial v_j}{\partial x_j} \geq 0 ; \qquad \frac{1}{p_j} \left[\sum_{i=1,3} \left(\frac{\partial p_j}{\partial x_i} \right)^2 \right]^{1/2} \leq \eta_1 \qquad j = 1, 3 . \tag{3.104}$$

If neither of these conditions are verified, internal energy is computed as follows

$$e_j = \begin{cases} E_j - \frac{1}{2} \varrho_j \mathbf{v}^2 & \text{if } E_j - \frac{1}{2} \varrho_j \mathbf{v}^2 / \max(E_{j-1}, E_j, E_{j+1}) \geq \eta_2 \\ e_j & \text{otherwise .} \end{cases} \tag{3.105}$$

Notice that, as we are dealing with errors that can be advected with the total energy calculation, we have to consider not just the j–th cell but also its neighbourhood (in one dimension this means the two zones $j \pm 1$).

5 – The hydrodynamical quantities are corrected by considering the expansion terms:

$$\varrho_j^{n+1} = \varrho_{H,j}^{n+1} \tag{3.106}$$

$$\mathbf{v}_j^{n+1} = \frac{2\mathbf{v}_{H,j}^{n+1} - \Delta t^{n+1/2}(\dot{a}/a)^{n+1/2}\mathbf{v}_j^n}{2 + \Delta t^{n+1/2}(\dot{a}/a)^{n+1/2}} \tag{3.107}$$

$$E_j^{n+1} = \frac{E_{H,j}^{n+1} - \Delta t^{n+1/2}(\dot{a}/a)^{n+1/2}E_j^n}{1 + \Delta t^{n+1/2}(\dot{a}/a)^{n+1/2}} \,. \tag{3.108}$$

6 – Position and velocity of the N–body particles are updated by the two–step Lax–Wendroff scheme:

step 1

$$\mathbf{v}_{DM,j}^{n+1/2} = \mathbf{v}_{DM,j}^n - \left(\dot{a}^n\mathbf{v}_{DM,j}^n + \mathbf{g}_j^n\right)\frac{\Delta t^{n+1/2}}{2a^n} \tag{3.109}$$

$$\mathbf{x}_{DM,j}^{n+1/2} = \mathbf{x}_{DM,j}^n + \mathbf{v}_{DM,j}^n\frac{\Delta t^{n+1/2}}{2a^n} \,. \tag{3.110}$$

step 2

$$\mathbf{v}_{DM,j}^{n+1} = \mathbf{v}_{DM,j}^n - \left(\dot{a}^{n+1/2}\mathbf{v}_{DM,j}^{n+1/2} + \mathbf{g}_j^{n+1/2}\right)\frac{\Delta t^{n+1/2}}{a^{n+1/2}} \tag{3.111}$$

$$\mathbf{x}_{DM,j}^{n+1} = \mathbf{x}_{DM,j}^n + \mathbf{v}_{DM,j}^{n+1/2}\frac{\Delta t^{n+1/2}}{a^{n+1/2}} \,. \tag{3.112}$$

Here we indicate by $\mathbf{g}_j^n$ the gravitational force on the j–th particle, computed by interpolating the values of the corresponding components at the eight neighbouring cells using the cloud–in–cell scheme.

4 Tests of the Code

In order to determine the accuracy, the reliability and the performances of the PPM+PM code, it has been subjected to a series of numerical tests. In the first sections we will focus on the PPM based part of the code, presenting tests which range from the purely hydrodynamical to the cosmological ones, in one and more dimensions. Then we will concentrate on the results of the N–body code.

In all the tests the conservation of energy has been checked. For the cosmological tests this check has been performed by using the cosmic energy equation which for an ideal gas in an expanding frame is (Peebles 1980):

$$\frac{d}{dt}(E+W)+\frac{\dot{a}}{a}(2E+W) \;=\; 0\;, \tag{4.1}$$

where E is the total (internal plus kinetic) comoving energy and W is the gravitational energy of the gas.

Equation (4.1) can be rewritten as:

$$\frac{d}{dt}[a(E+W)]+\dot{a}E \;=\; 0 \tag{4.2}$$

and integrated with respect to the expansion factor giving:

$$a_2E(a_2)-a_1E(a_1)+\int_{a_1}^{a_2} E\;da \;=\; -[a_2W(a_2)-a_1W(a_1)]\;, \tag{4.3}$$

where a_1 and a_2 are the values of the expansion factor at two different times.

We checked energy conservation computing the quantity:

$$R \;=\; \frac{a_2E(a_2)-a_1E(a_1)+\int_{a_1}^{a_2} E\;da}{-[a_2W(a_2)-a_1W(a_1)]}\;. \tag{4.4}$$

For perfect energy conservation R should remain equal to unity.

We start testing the PPM part of the code by some pure hydrodynamical one dimensional simulation in which source terms and the expansion of the universe are neglected. The results are compared with the corresponding exact analytical solutions.

4.1 Convection Test

In this test we follow the evolution of a perturbation in the density of an incompressible and non diffusive fluid which moves with constant velocity v. In this case the fluid is said to be *convected* and the equations of hydrodynamics reduce to:

$$\frac{\partial \varrho}{\partial t} = -v\frac{\partial \varrho}{\partial x}. \tag{4.5}$$

For a more complete description of the convection problem we refer to Oran & Boris (1987).

The test problems are:

1) the square wave. Initially ϱ=2 over the first 20 cells and ϱ=0.5 on the rest of a grid composed by 250 cells. The perturbation is convected at a velocity which gives:

$$C_c = \frac{v\Delta t}{\Delta x} = 0.2\ . \tag{4.6}$$

In Figure 4.1 we show, compared to the exact solution, the calculated profile after 800 steps.

2) Gaussian profile. The profile is defined as:

$$\varrho(x) = 0.1 + 1.5\exp[-x^2/(2\sigma^2)] \tag{4.7}$$

where x is in units of Δx and the half width σ=2Δx. The maximum value of the density is 1.6 and the minimum is 0.1. The perturbation is convected at a Courant number C_c=0.1. In figure we show the solution after 600 steps.

3) The dome profile. The initial perturbation is defined over the first 31 cells as a parabolic profile

$$\varrho(x) = -0.0068x^2 + 0.21x + 0.1 \tag{4.8}$$

The density ranges from 0.1 to 1.6; the Courant number is C_c=0.1. The solution after 600 steps is presented in Figure 4.1

These tests are important for several reason: the first shows the effect of numerical diffusion on a discontinuity. The results show that for our code this effect is low and the discontinuity is spread over at most two cells. The second shows the effect of clipping, that is the numerical tendency of underestimating the density of narrow peaks. Also this effect has proved to be quite low. The third shows the effect of terracing, that is the flattening of the solution in the most curved parts of the density profile, as happens in two cases in the right part of the simulated profile.

4.2 One–Dimensional Shock Tube Test

The following test is the standard shock tube test (Oran & Boris 1987). Also in this case we solve the hydrodynamical equations (2.9)–(2.11) without the source terms and with $a = 1$. Initially the gas is at rest ($v = 0$) and density and pressure present a central jump from $\varrho_l = 1$, $p_l = 1$ to $\varrho_r = 0.1$, $p_r = 0.1$. The shock tube test is a typical Riemann problem and its exact solution can be calculated following the procedure described in section 2.3. The solution is of the kind (2.36), and consists in a rarefaction wave that propagates towards right and a contact discontinuity and a shock wave that move towards left. This test is particularly interesting as it verifies the accuracy of the code in simulating smooth flows, like the rarefaction wave, as well as discontinuities, like the shock or the contact discontinuity. The calculation is performed using a grid of 128 zones, the initial time is $t_i = 1$ and the final time, shown in the figure, is $t_0 = 20$. The numerical results (open circles) are presented in Figure 4.2: they are in very good agreement with the analytical solution (solid lines). In particular, shocks are typically resolved within one cell and contact discontinuities are represented in four or five zones. In order to reduce the diffusion of contacts we have used, for the density field, the discontinuity detection algorithm of Colella & Woodward (1984). We have not introduced artificial diffusion and/or numerical flattening since numerical ripples around steep gradients are either absent or very small and do not affect the solution during the whole evolution.

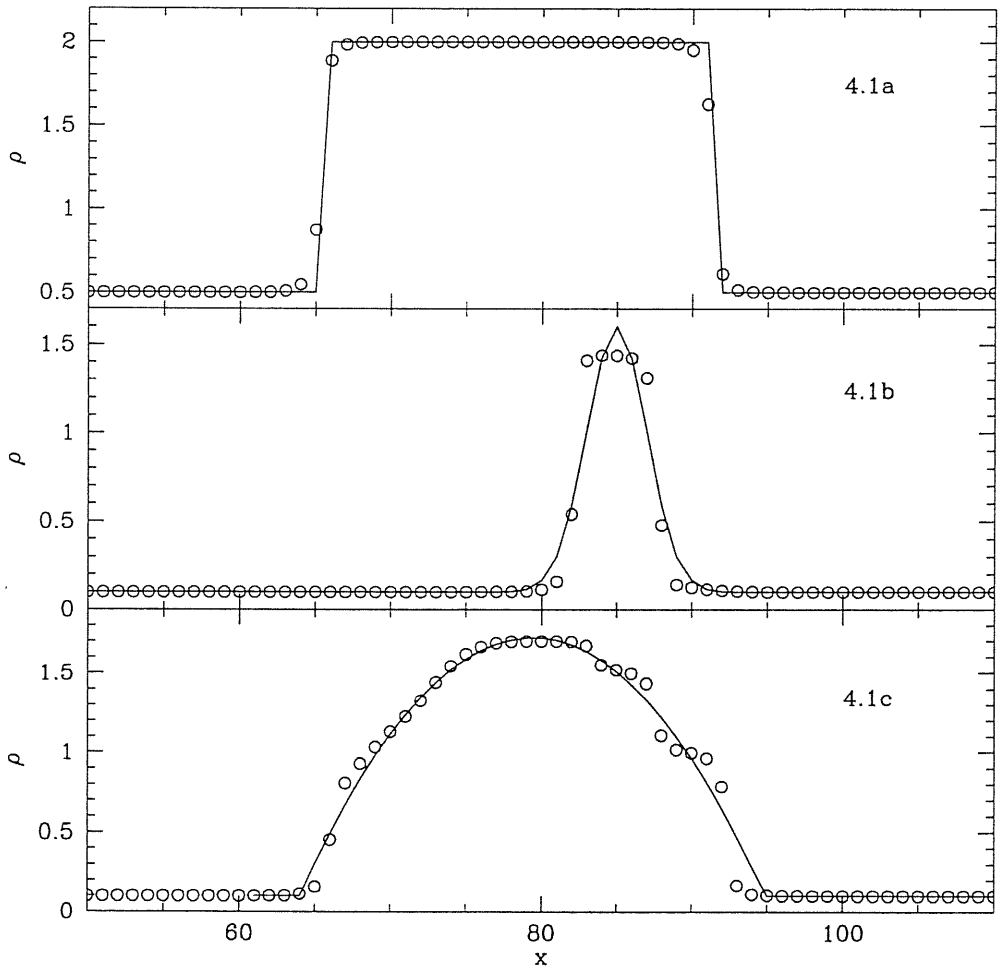

Figure 4.1: Convection test for a square wave (4.1a), a gaussian (4.1b) and a dome (4.1c). The solid line represent the exact solution while the circles are the corresponding numerical solution

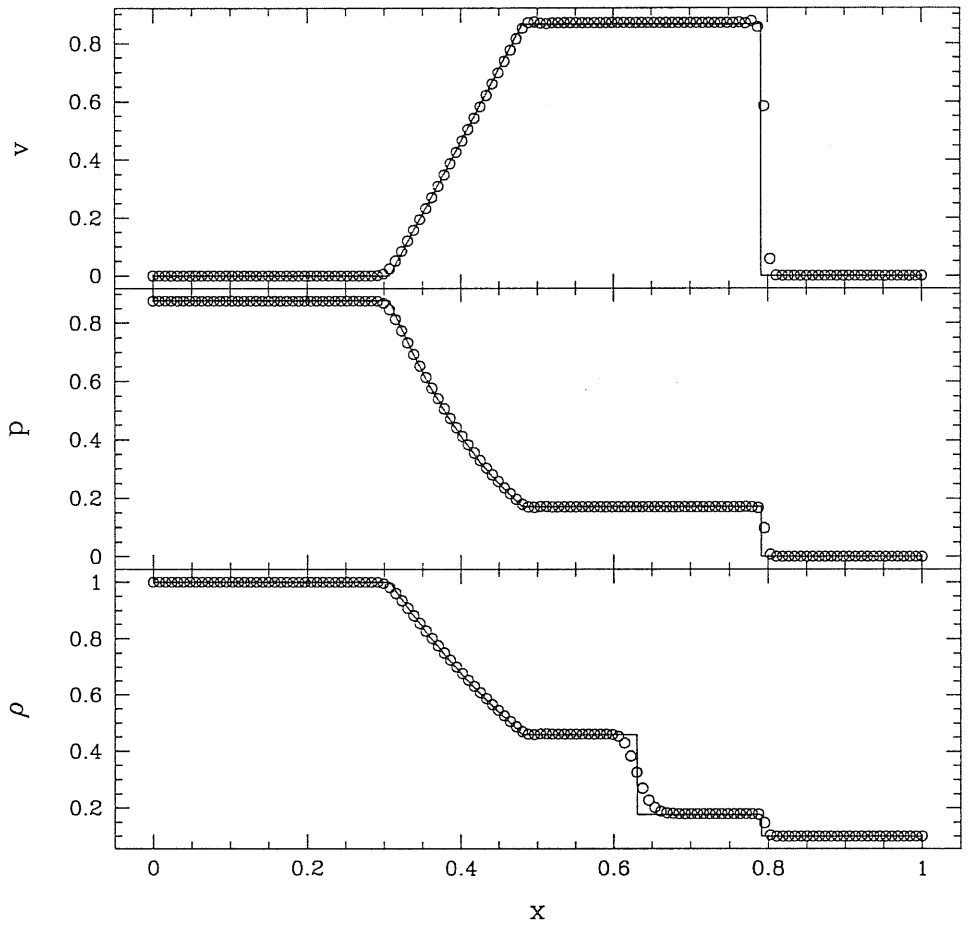

Figure 4.2: The velocity v, the pressure p and the density ϱ for the one–dimensional shock tube test at the final time $t_0 = 20$. The numerical result obtained with a grid of 128 zones (open circles) is compared to the analytical solution (solid line).

4.3 Adiabatic Expansion

The following tests describe physical situations that are expected in cosmological simulations. We have assumed an Einstein–de Sitter pure baryonic universe with vanishing cosmological constant and we have fixed the Hubble constant to $H_0 = 50$ km s^{-1}Mpc^{-1}. The comoving size of the computational box is $L = 64\ h^{-1}$Mpc. For this model our basic units of normalization are:

$$x_0 = L \qquad \varrho_0 = \frac{3H_0^2}{8\pi G} \qquad t_0 = \frac{1}{(6\pi G \varrho_0)^{1/2}} , \tag{4.9}$$

where G is the gravitational constant. The expansion factor depends on the cosmological time as

$$a(t) \propto t^{2/3} . \tag{4.10}$$

We have simulated the adiabatic expansion of an unperturbed universe, starting at time $t_i = 0.01$ from a homogenous distribution of matter with velocity $v_i = 100$ km s^{-1} and temperature $T_i = 4.6$ K. In this situation equations (2.10)–(2.11) are easily integrated giving:

$$v = v_i(a_i/a) , \qquad T = T_i(a_i/a)^2 , \tag{4.11}$$

where a, v and T are the expansion factor, the velocity and the temperature respectively, at time t. At the final time $t_0 = 1$ numerical and analytical solutions are compared and the errors calculated as:

$$\Delta T = \frac{|T_{num} - T_{an}|}{T_{an}} \qquad \Delta v = \frac{|v_{num} - v_{an}|}{v_{an}} , \tag{4.12}$$

where the subscripts *num* and *an* indicate, respectively, the numerical and analytical values of the variables. We have indicated with Δa the maximum fractional variation of the expansion factor in a timestep. Using $\Delta a = 0.1$ we have obtained $\Delta T = 6 \times 10^{-3}$ and $\Delta v = 3 \times 10^{-3}$. The errors decrease to $\Delta T = 8 \times 10^{-5}$ and $\Delta v = 4 \times 10^{-5}$ for $\Delta a = 0.01$. The value of the parameter Δa used in the simulations is fixed to 0.02 by the balance between accuracy and computational time requirements.

4.4 Zel'dovich Pancake

In this test we describe the formation of a one–dimensional pancake. The test is particularly important for cosmological studies as all of the related physics (hydrodynamics, expansion, gravity) is included. In addition, it represents the evolution of an initial sinusoidal wave and so can be seen as a single–mode analysis of the fully three–dimensional problem.

At the initial time, corresponding to $a_i = 0.01$, a sinusoidal velocity field has been imposed on the computational grid. The amplitude of the initial perturbation has been chosen such that the caustic forms at $a_c = 0.5$. At a_i the density and temperature fields are uniform. We set $\varrho = 1$ and $T = 100$ K. The final time corresponds to $a_0 = 1$. The same test has been repeated using eight different numbers of zones ranging from $N_c = 8$ to $N_c = 1024$.

During the first part of the evolution, we are in the linear phase and the numerical results can be directly compared with the analytical solution which holds for a non–collisional fluid since the effect of the pressure is negligible in this phase. This comparison gives a first estimate of the accuracy of the code. Moreover, using results obtained with different numbers of zones we can study the convergence of the numerical solution. The error is computed as:

$$\Delta\varrho = \frac{1}{N_g}\sum_{i=1}^{N_g}\frac{|\varrho(x_i) - \varrho_e(x_i)|}{\varrho_e(x_i)}\,, \tag{4.13}$$

where ϱ_e is the exact solution. We found that at $a \sim 0.1$, when shocks are not present, the error is below 1% already with only 16 zones.

The non–linear phase of the evolution is the most interesting. The strong shocks and large gradients that form are in fact a severe test for any Eulerian numerical code. The results at $a_0 = 1$ obtained using grids of 256 and 1024 zones are compared in Figure 4.3. The only important difference between the two solutions is the height of the central density peak, but this was expected as a consequence of the different resolutions in the two cases. All of the other features the solution are in very good agreement between the two simulations showing the convergence of the numerical solution. Shocks are resolved in one zone and there are no numerical postshock ripples.

In Figure 4.4 we present the results of the energy conservation test. We have calculated at the final time the conservation parameter R (defined in equation (4.4)) and the total gravitational (W), kinetic (E_{KIN}) and thermal (E_{TH}) energy of the fluid when a various number of cells N_c are adopted. The energy is plotted in the code units. The error in the energy conservation is of about 5% for $N_c = 32$ and decreases to 0.1% for $N_c = 1024$. The behaviour of the three energy terms shows that at least 32 zones are needed for starting to see the convergence of the solution. The poor resolution of the 8 and 16 zone cases, in fact, makes it impossible to describe correctly the narrow central peak, which remains too diffused. The shallower central potential wells induce a smaller acceleration in the infalling matter. The compression is low and the transformation from kinetic to internal energy is inefficient and so produces a pressure which is too low to support the infall of the matter. However the collapse of the peak is prevented by the artificial effect of the coarseness of the grid.

4.5 Multiple Pancake Formation.

The last one–dimensional test which we have performed consists of simulating the evolution of a random initial density field. In this test different wavelengths evolve together; hence we can verify the ability of the code for describing shock interactions and the merging of small structures.

The initial conditions are set by perturbing the density field according to a Gaussian random distribution characterized by a power–law spectrum of the general form

$$P(k) = P_0 k^n \exp(-k^2 R_f^2) \,, \tag{4.14}$$

where P_0 is the normalization constant and n is the spectral index. The short wavelength cut–off at the scale $R_f = 2$ grid–points ensures that the results are not affected by the sampling of modes whose size is close to that of the resolution of the simulation.

The normalization constant is fixed requiring that the one–dimensional variance σ^2 at the final time t_0 (corresponding to the expansion factor $a_0 = 1$) for linearly evolved

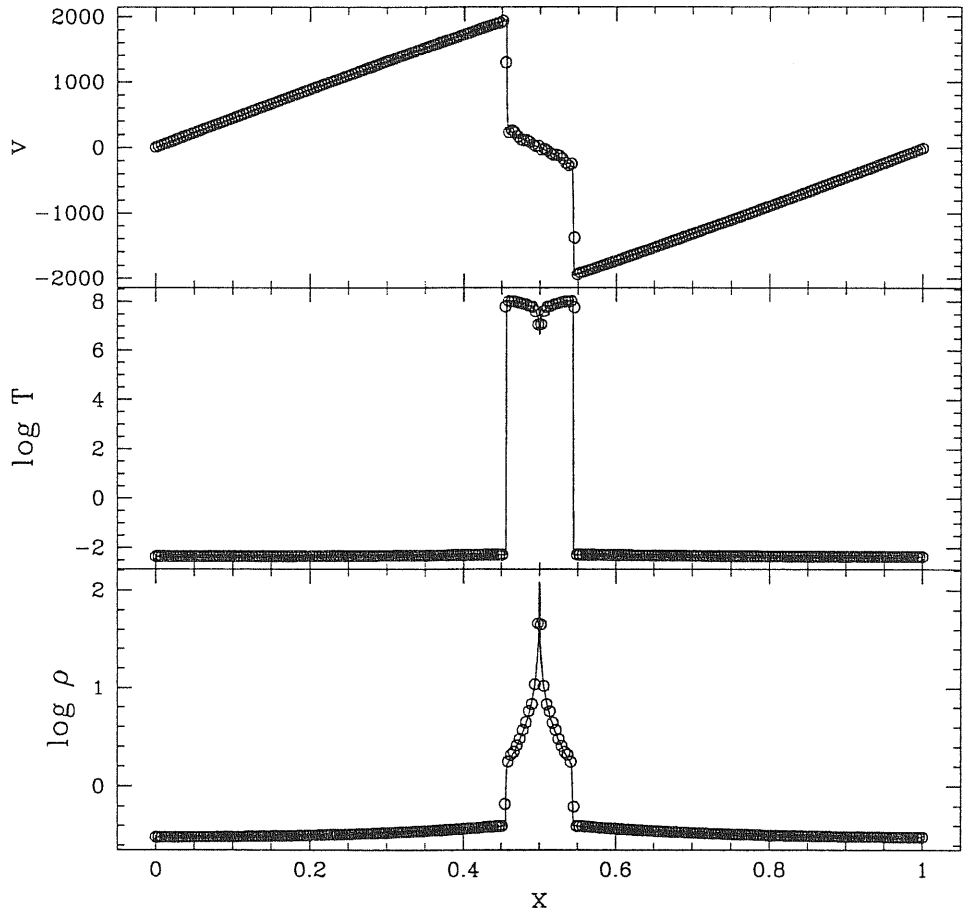

Figure 4.3: The velocity v, the temperature T and the density ϱ for the one–dimensional Zel'dovich pancake test at the final time $a_0 = 1$. The results obtained with grids of 256 (open circles) and 1024 zones (solid line) are compared.

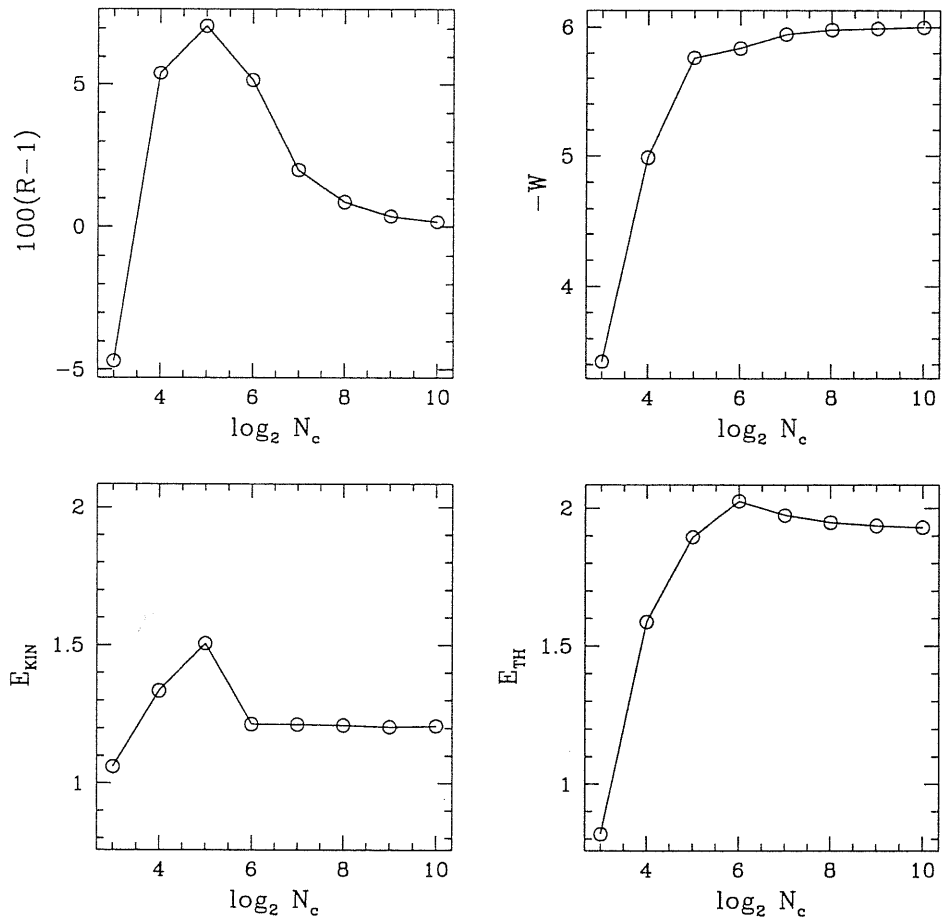

Figure 4.4: The energy conservation parameter R (top left), the gravitational energy W (top right), the kinetic energy E_{KIN} (down left) and the thermal energy E_{TH} (down right) for the one–dimensional Zel'dovich pancake test are plotted as function of the number of cells N_c.

perturbations is equal to unity on the scale $R_* = 10^{-1}L$ so that:

$$\sigma^2(R_*) = \frac{1}{\pi}\int_0^\infty P(k)W(kR_*)\,dk = 1\,, \tag{4.15}$$

where the function $W(kR_*)$ is a one–dimensional top–hat filter:

$$W(kR_*) = \frac{\sin(kR_*)}{kR_*}\,. \tag{4.16}$$

The initial time t_i is chosen by imposing that, at t_i, the largest density fluctuation is equal to 0.5.

As an example, we show in Figure 4.5 the results at the final time t_0 for a simulation with spectral index $n = 1$ when $N_c = 256$ is used, i.e. with the same number of cells used in the simulation of the single pancake. Shocked regions, characterized by the presence of typical double peaked maxima in the temperature field and by the smoothing of steep negative gradients in the velocity field, are at temperatures ranging from 10^4 to 10^6K. Underdense regions are instead at much lower temperature. Collapsing regions surrounding density peaks are, at the beginning, at low temperature, but heat up as soon as propagating shocks reach them. The errors in energy conservation are around 3%, slightly higher than the value obtained for the Zel'dovich pancake test.

4.6 Cold Dark Matter Test

As a final test we have simulated the evolution of a purely baryonic Einstein–de Sitter Universe with an initial cold dark matter (CDM) power spectrum. As in the previous tests, we fixed the Hubble constant to be $H_0 = 50$ km s^{-1} Mpc^{-1} and the comoving size of the computational box to be $L = 64\ h^{-1}$Mpc. In this way our numerical results can be compared with those obtained by Kang *et al.*(1994b), even if a different random realization of the initial conditions has been used. Perturbations are initially Gaussian distributed and the primordial density power spectrum can be written in the form:

$$P(k) = P_0 k^n T^2(k)\,, \tag{4.17}$$

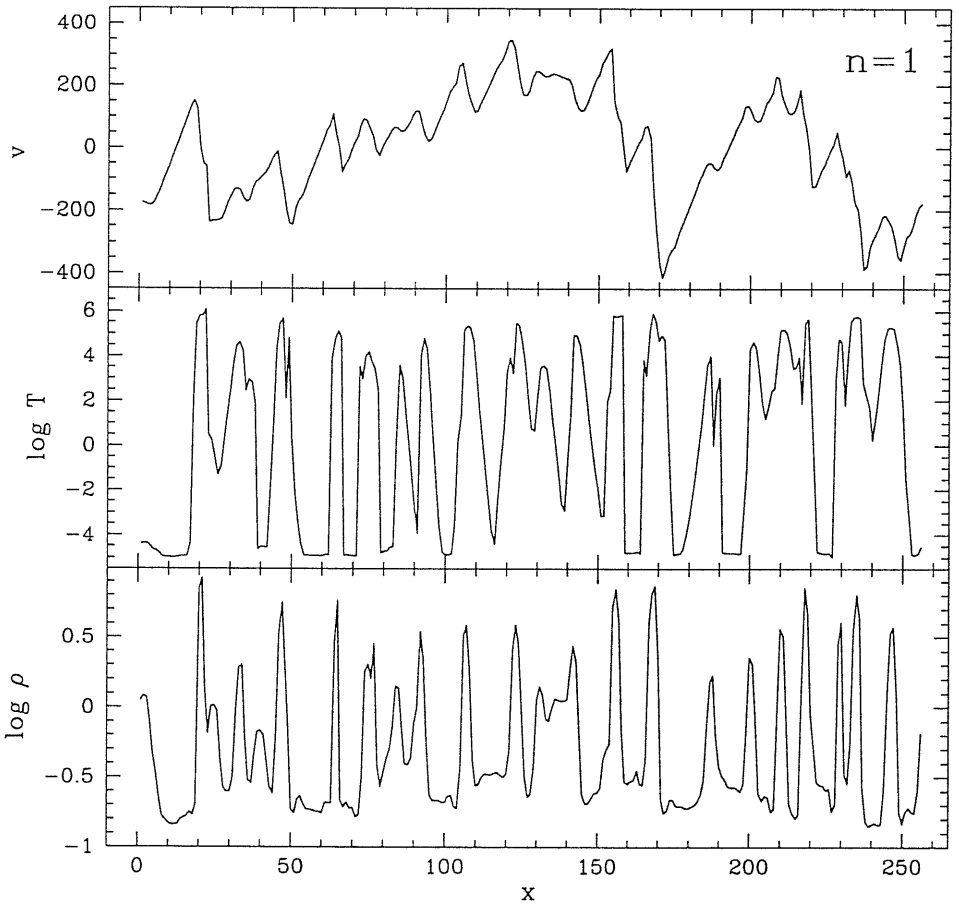

Figure 4.5: The velocity v, the temperature T and the density ϱ for the one–dimensional multiple pancake test at the final time $a_0 = 1$. A primordial power–law power spectrum with spectral index $n = 1$ is simulated using a grid of 256 zones.

where $T(k)$ is the CDM transfer function given by the Davis *et al.*(1985) fitting formula:

$$T(k) = (1 + 6.8k + 72.0k^{3/2} + 16.0k^2)^{-1} . \quad (4.18)$$

In the standard CDM model, the primordial spectral index has the Zel'dovich value $n = 1$.

The normalization constant P_0 is fixed such that the linear mass variance at the present time is unity in a sharp–edged sphere of radius $R_8 = 8h^{-1}$ Mpc:

$$\sigma^2(R_8) = \frac{P_0}{2\pi^2} \int_0^\infty k^{n+2} T^2(k) W_{TH}^2(kR_8)\, dk = 1 . \quad (4.19)$$

In the above equation, $W_{TH}(kR) = (3/kR) j_l(kR)$ is a top–hat window function and j_l denotes the lth–order spherical Bessel function. The velocity field at the initial time t_i has been calculated in the linear perturbation approximation (Peebles 1980) as:

$$\mathbf{v} = \frac{2\ \nabla\Phi}{3H(t_i)a(t_i)} . \quad (4.20)$$

We are interested in checking the convergence properties of our code, so we evolved the same initial conditions on three different grids with 32^3, 64^3 and 128^3 cells, respectively. The initial conditions are set up according to the previous prescriptions on the coarsest grid. The initial time, fixed by the condition that the maximum density fluctuation is unity, corresponds to a redshift $z \sim 20$.

We have first analyzed some integral properties of the results at the final time. We have calculated the mean temperature $\langle T \rangle$, the average mean temperature $\langle T \rangle_\varrho \equiv \langle T\varrho \rangle / \langle \varrho \rangle$, the average temperature weighted by the density squared $\langle T \rangle_{\varrho^2} \equiv \langle T\varrho^2 \rangle / \langle \varrho^2 \rangle$ and the variance of the density fluctuation field $\sigma^2 \equiv (\langle \varrho^2 \rangle / \langle \varrho \rangle^2 - 1)$. As in Kang *et al.*(1994b), the calculation has been performed for the data rebinned to a 16^3 grid. The results are presented in Table 4.1.

The average temperature for the rebinned data seems to have converged already in the 64^3 simulation. However, the behaviour of the rms density fluctuation suggests that a higher resolution is needed for the convergence of the density field. The variation of the density weighted temperatures between the 64^3 and 128^3 grids depends essentially on variations of

Table 4.1: The simulations. Column 1: the number of zones in each dimension N_c; Column 2: the mean temperature $\langle T \rangle$. Column 3: the average mean temperature $\langle T \rangle_\varrho$. Column 4: the average temperature weighted by the density squared $\langle T \rangle_{\varrho^2}$. Column 5: the r.m.s. of the density fluctuation field σ.

N_c	$\langle T \rangle$	$\langle T \rangle_\varrho$	$\langle T \rangle_{\varrho^2}$	σ
32	1.48	6.02	19.49	2.17
64	2.02	10.61	28.63	2.48
128	2.02	11.91	32.95	2.77

density distribution. As already noticed by Kang *et al.*(1994b) for all the Eulerian codes considered in that paper, the values of σ appear to converge from below.

In Figure 4.6 we show a cell–by–cell comparison of density and temperature for the rebinned data of the three simulations. We always observe a good correlation between the values of the densities obtained from simulations with different resolutions; the spread of the points is reduced as we compare simulations with the highest resolution. The same holds for the high temperature cells. The distribution at lower temperatures is due to the formation of substructures as we increase the grid resolution. The large number of points which accumulate in the lower part of the panel represents cells that in the lower resolution simulation are cooling according to the expansion of the Universe while in the higher resolution run are site of some structure. Also this effect decreases when the resolution is higher.

In the left and right columns of Figure 4.7 we show the volume and mass weighted density histograms, $f(N)$ and $f(M)$ respectively, for the 16^3 rebinned data. The tendency to form higher density peaks as we increase the resolution clearly appears in these histograms. As we go from 32^3 to 128^3 the amount of mass contained in the high density regions increases.

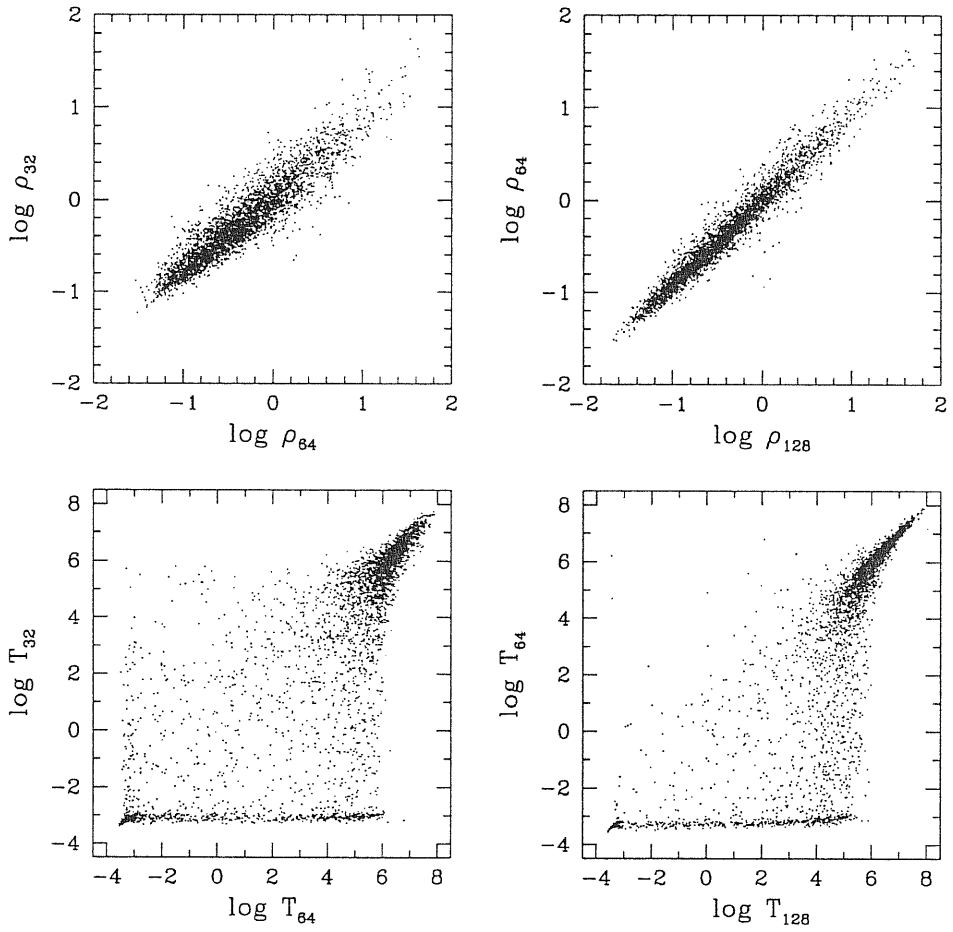

Figure 4.6: A cell–by–cell comparison of density ϱ (upper row) and temperature T (lower row) for the 16^3 rebinned data at $z = 0$ for three simulations with the same initial conditions but different numbers of zones, as indicated by the subscripts.

However, in relation to the convergence of the numerical results, it is encouraging to see that the density distribution both in volume and in mass is very similar for the 64^3 and 128^3 runs.

The corresponding histograms for the temperature are shown in Figure 4.8. Comparing the rebinned data from different runs we can observe higher gas temperatures when the resolution of the simulation is increased. We notice both an increase in volume fraction and in mass fraction of the gas at high temperature. The $f(N)$ peak at low temperature is almost absent in the 128^3 simulation, but this is only due to the averaging procedure in constructing the rebinned data. Small scale structures are present in the high resolution run which could not appear in the simulations with a smaller number of cells and they have the effect of raising the average temperature in the rebinned data.

The same effect is evident if we look at Figure 4.9 which presents the same histograms for the original data of the 128^3 simulation: a large fraction of the volume is still at low temperature. However, the mass fraction distribution confirms that about 70% of the mass is at temperatures higher than 10^6 K.

In Figure 4.10 we show two different slices of the simulation with 0.5 h^{-1} Mpc thickness (1 cell). For each slice contour plots are presented for the density contrast $\delta = \varrho/\langle\varrho\rangle - 1$ and the temperature. Structures appear well resolved and strong temperature gradients indicate shock positions. High density peaks are surrounded by high temperature regions which have been heated by the shock propagation.

Finally in Figure 4.11 the contour plots of the volume (left) and mass (right) fraction with given temperature and density are shown. We observe that most of gas is at high density and temperature. On the other hand most of the volume is at low density with either high or low temperatures depending on whether it has been crossed by shocks or not.

4.7 N–body Tests

The PM method is a well–known and highly tested N–body technique used in many applications. Our implementation differs from that presented in Moscardini (1990) only for

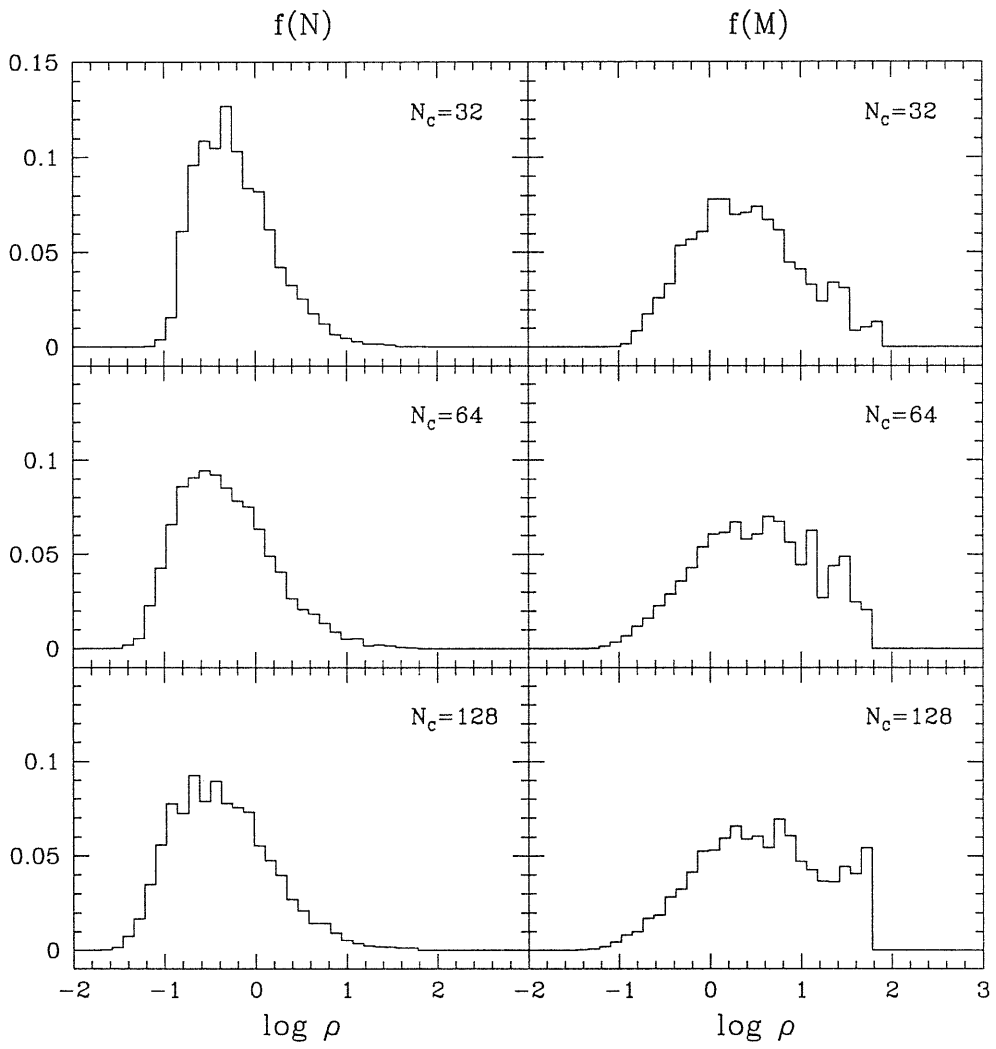

Figure 4.7: The six panels show the volume–weighted $f(N)$ (left column) and mass–weighted $f(M)$ (right column) histograms at $z = 0$ for the density ϱ at $z = 0$ for the 16^3 rebinned data. The results obtained with different numbers of cells are shown: $N_c = 32$ (upper row), $N_c = 64$ (central row) and $N_c = 128$ (lower row).

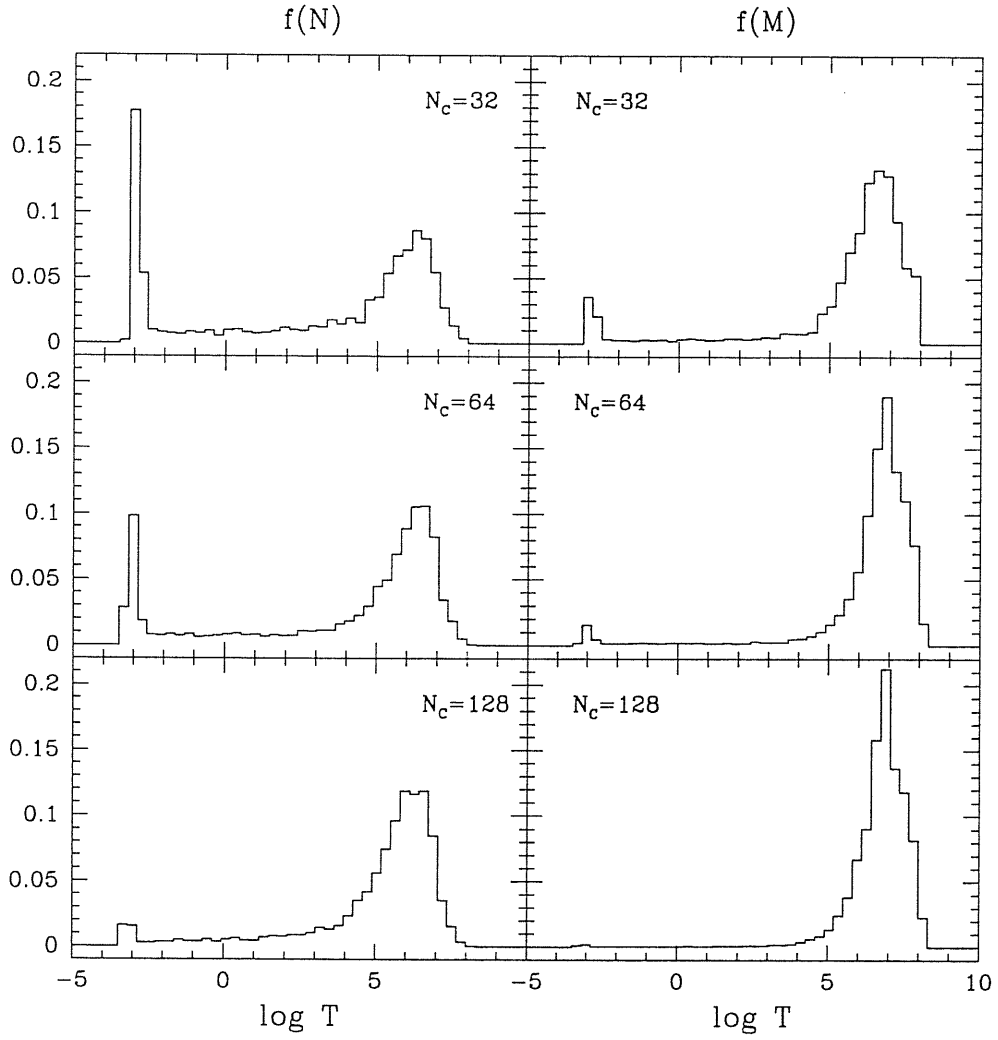

Figure 4.8: The six panels show the same quantities as Figure 4.7 but for the temperature T

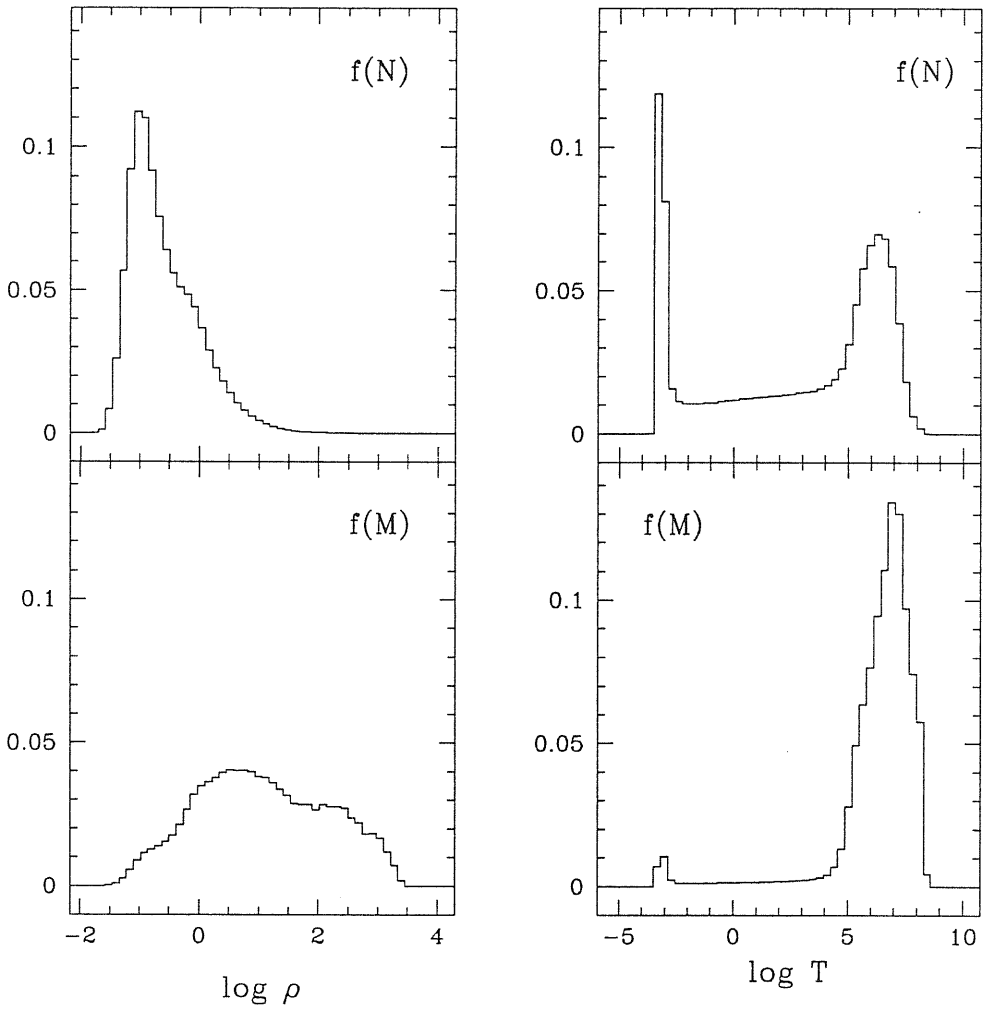

Figure 4.9: The volume–weighted $f(N)$ (upper panels) and mass–weighted $f(M)$ histograms (lower panels) for density ϱ (left column) and temperature T (right column) at $z = 0$ for the original unbinned data of the 128^3 simulation.

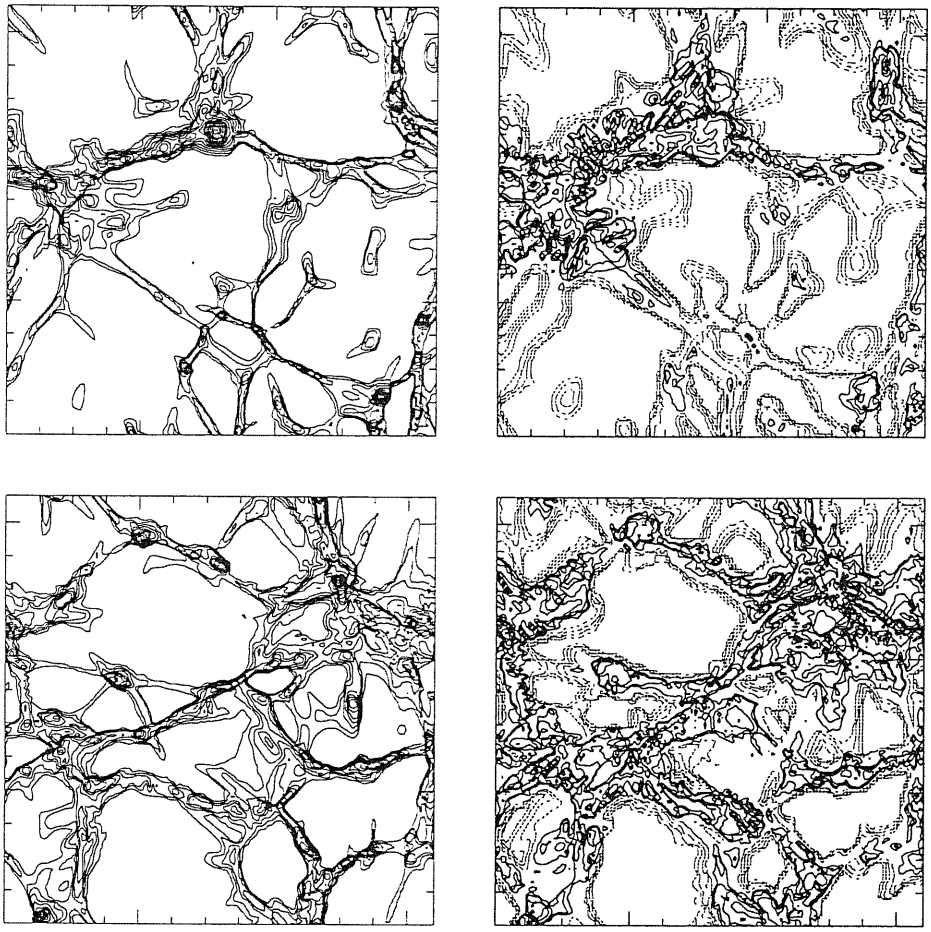

Figure 4.10: Density (left column) and temperature (right column) contour plots of two different slices of 0.5 h^{-1} Mpc thickness in the 128^3 run are shown. Density is normalized to the mean density while the temperature is in units of 10^6 K. The density contour levels correspond to $10^{(i-3)/4}$, while the temperature levels are $5^{i/2}$ (solid lines) and 5^{-2i} (dashed lines), where $i = 1, 2, ...$

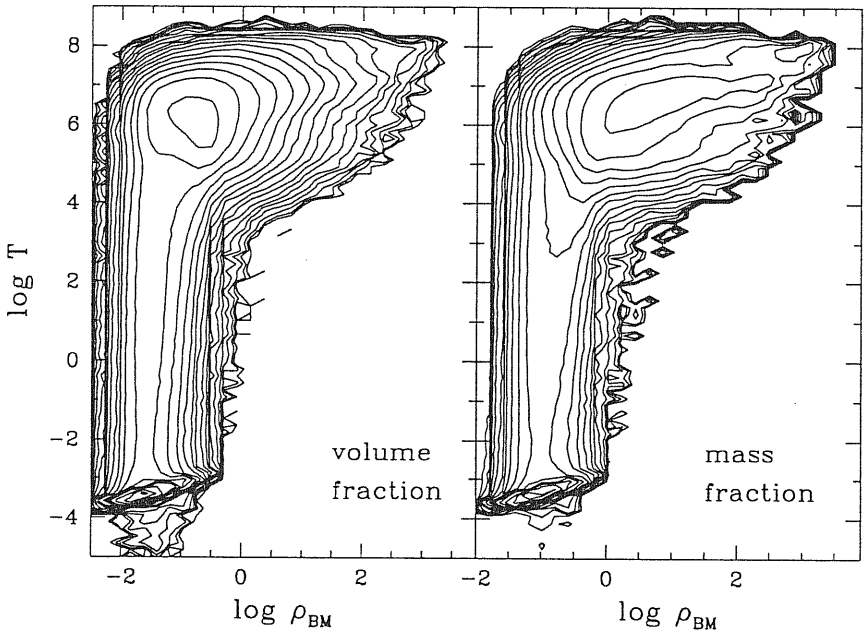

Figure 4.11: Contour plots of the volume fraction (left) and mass fraction (right) with given temperature and density. The results at $z = 0$ from the 128^3 simulation are shown. Contour levels correspond to $10^{i/4}$, where $i = 1, 2, ...$

the use of the Lax–Wendroff instead of the Leap–Frog scheme to integrate dynamical equations. Therefore we present only some tests which verify essentially the reliability and the accuracy of the Lax–Wendroff scheme. In these tests we compare the results obtained by our implementation of the PM method when used to solve several cosmological problems, with those obtained for the same problems by the PM code presented by Moscardini. In particular we have simulated the evolution of the cosmological structures in a Standard CDM model on a box of $64h^{-1}$Mpc using different versions of the PM N–body code. The starting redshift of the simulation is ~ 18 and the number of cells of the computational mesh is 32^3, equal to the number of particles.

We have run a first simulation using the original Leap–Frog PM code. The run is completed in 500 constant time steps. The same model has been simulated using our Lax–Wendroff PM code, first adopting the same constant time step used with the Leap–Frog and then allowing the time step to vary. In this case the time step is calculated requiring that the maximum variation of the expansion factor in a single step is less than 2% (the same condition imposed to the whole PPM plus N–body code). This simulation is completed in 150 steps. We indicate the three simulations as RUN1, RUN2 and RUN3 respectively.

In Figure 4.12 we show the redshift dependence of the variance and of the maximum mass density for the three simulations. For both the quantities the three curves are very close and the differences are at most of some percent. A more severe test is the direct comparison of the position and the velocity of the particles at different redshift for the three simulations. At $z = 0$ the position of the particles in RUN1 differs on average of the 0.4% from the particles position in RUN2. The similarity of the results is confirmed by Figure 4.13, which shows the distribution of the particles projected along the z and x axis. The comparison of the velocities gives a mean difference of the 3%. Actually we have found that some particles present differences either in position or in velocity of more than 10%. However their number is low and they never affect the results of the simulation.

The differences in the particles position and velocity tend to be smaller with increasing the redshift. For example, at $z = 1$, they reduce to 0.2% for the position and 2.5% for

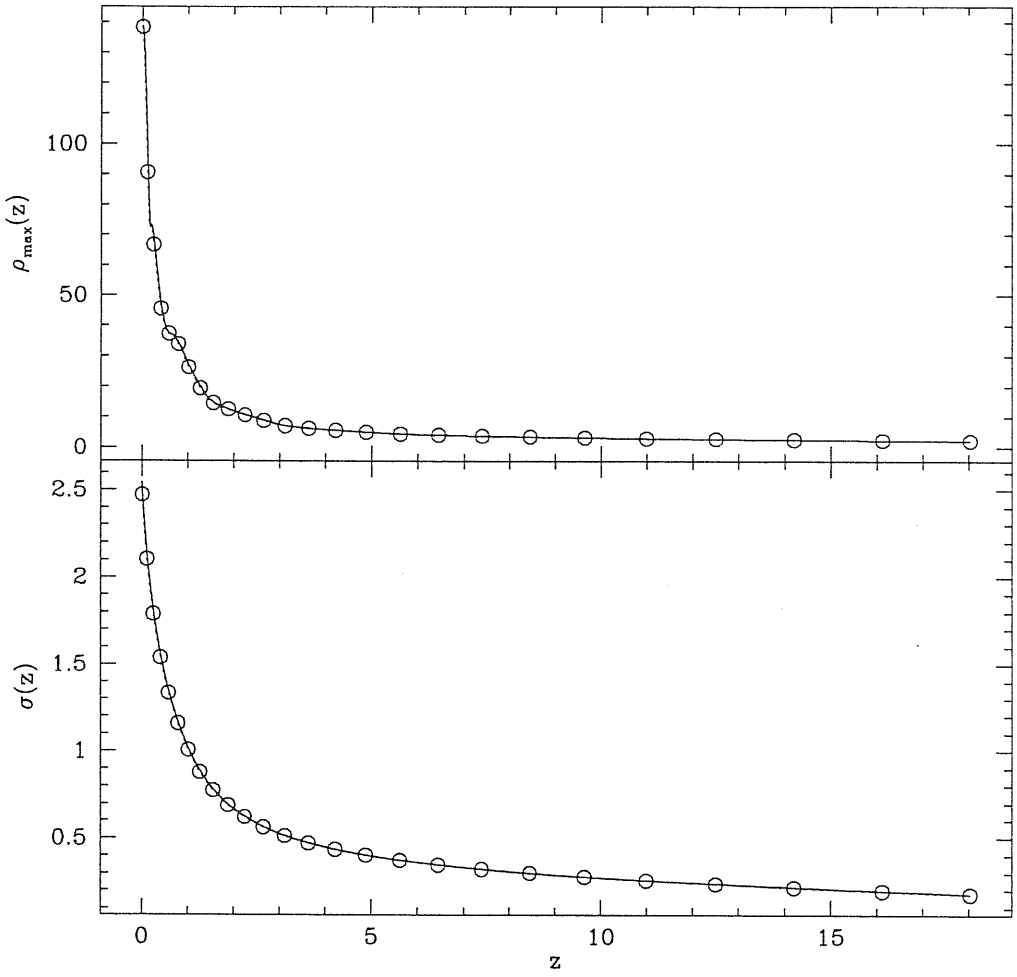

Figure 4.12: Redshift dependence of the variance and the maximum density of RUN1 (solid line), RUN2 (dotted line) and RUN3 (open circles)

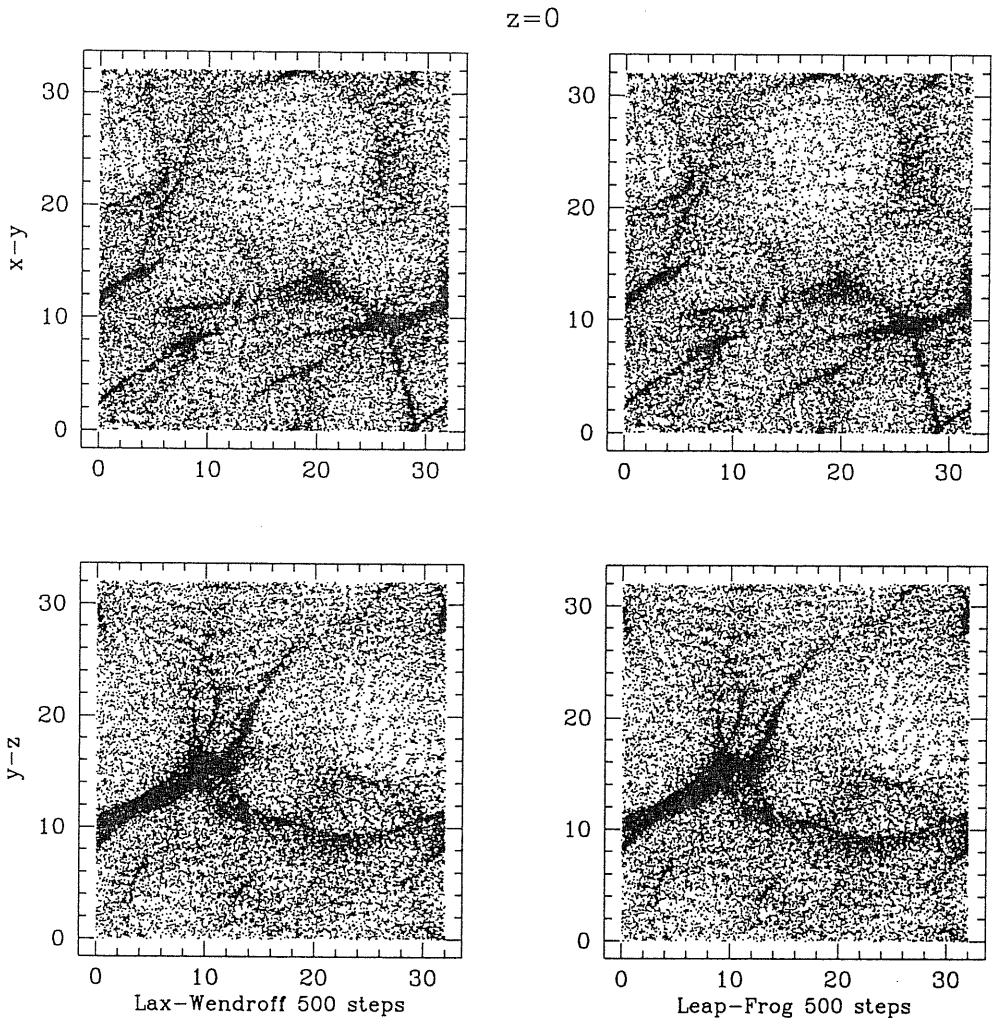

Figure 4.13: Particles distribution for RUN1 and RUN2 at $z = 0$x projected along the z direction (upper row) and x direction (lower row)

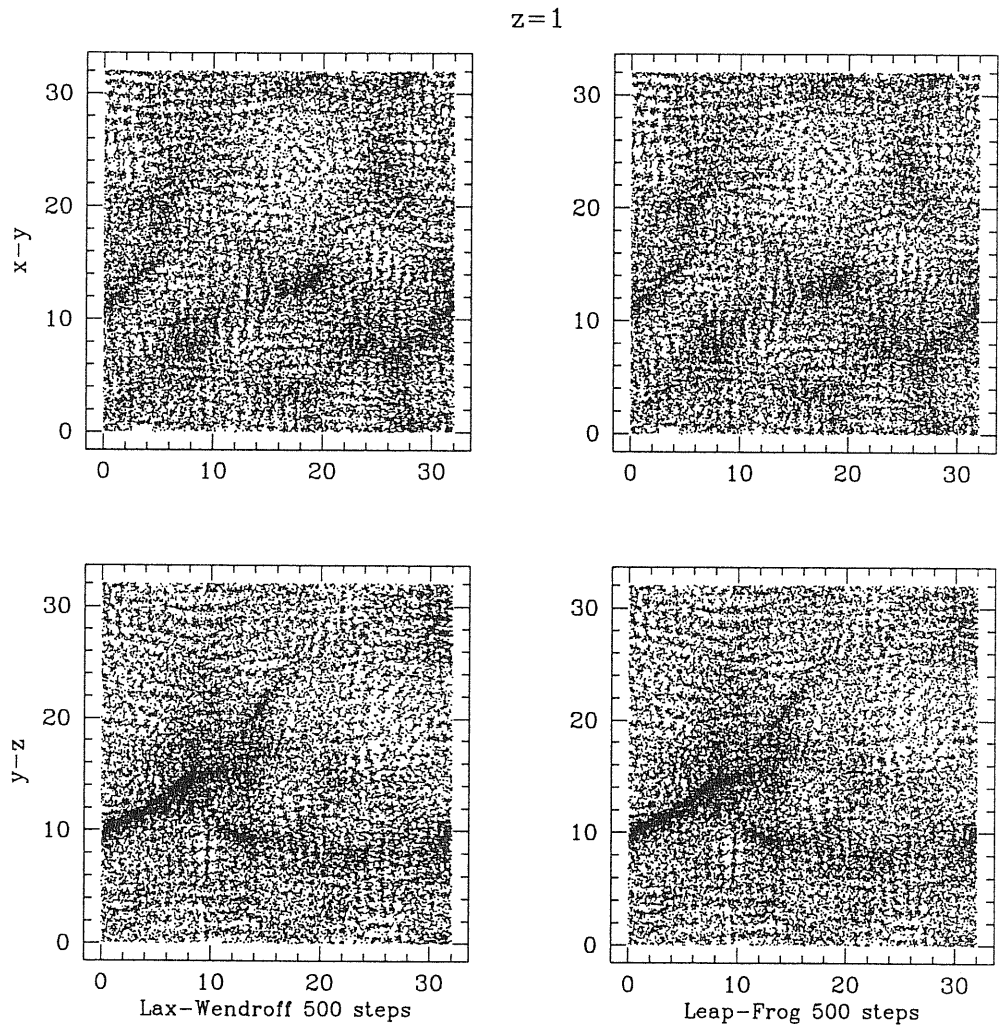

Figure 4.14: Particles distribution for RUN1 and RUN2 at $z = 1$ projected along the z direction (upper row) and x direction (lower row)

the velocity. The distribution of the particles at $z = 1$ is presented in Figure 4.14. The comparison between RUN1 and RUN3 leads to the same conclusions of that between RUN1 and RUN2. When we compare RUN2 and RUN3 we find average differences of 0.004% for the position and of 0.08% for the velocity. In Figure 4.15 we show the distribution of the particles for RUN3 compared to that of RUN1 at $z = 0$

Similar results are obtained repeating the test with different generations of initial data or different cosmological models. We can then conclude that the Lax–Wendroff scheme can be safely used for the integration of the N–body dynamical equations.

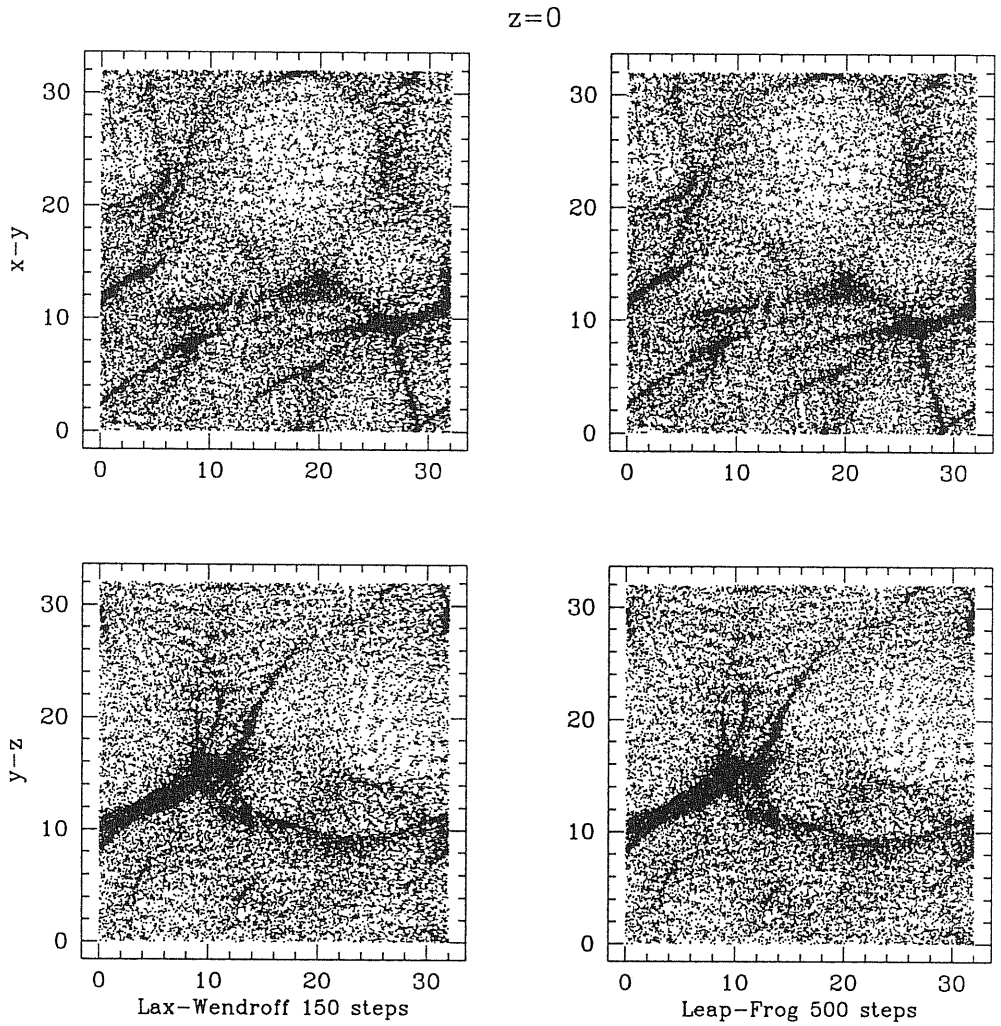

Figure 4.15: Particleis distribution for RUN1 and RUN3 at $z = 0$ projected along the z direction (upper row) and x direction (lower row)

5 The Parallel Code

A major difficulty of numerical simulations is represented by the extremely large dynamical range involved in cosmological structure formation process. One would ideally like to simulate volumes comparable to the size of the universe ($\sim 10^3$Mpc), but resolve star forming regions in galaxies ($\sim$ 1 pc). Therefore, the spatial dynamical range required per dimension is $\sim 10^9$, well beyond the $\sim 10^3$ that any kind of code can currently achieve. Even to reach this maximum dynamical range it is necessary to leave scalar computers and use parallel supercomputers, which can account for hundreds of processors that can work together on "common" sets of data. Besides having much larger memories, these machines can share work among the processors, strongly reducing the computational time. On the other hand, parallel supercomputers require programming languages and "strategies" different from those usual for scalar computers and so a redesigning of codes with respect to their scalar version. In the following sections we will present the parallel implementation of our PPM+PM code and the major algorithmic changes required to work on a parallel system. The parallel version of the code has run on the Cineca's Cray T3D (Cineca is the SuperComputing Center of Casalecchio di Reno - Italy), a 128 processor machine. Each node has a 150 MHz DEC Alpha EV4 and 64 MBytes memory. The processors are linked with a 3D toroidal network (see Figure 5.1). The memory is physically distributed, but logically shared by means of a global address space. The Cray proprietary software CRAFT allows to use this feature.

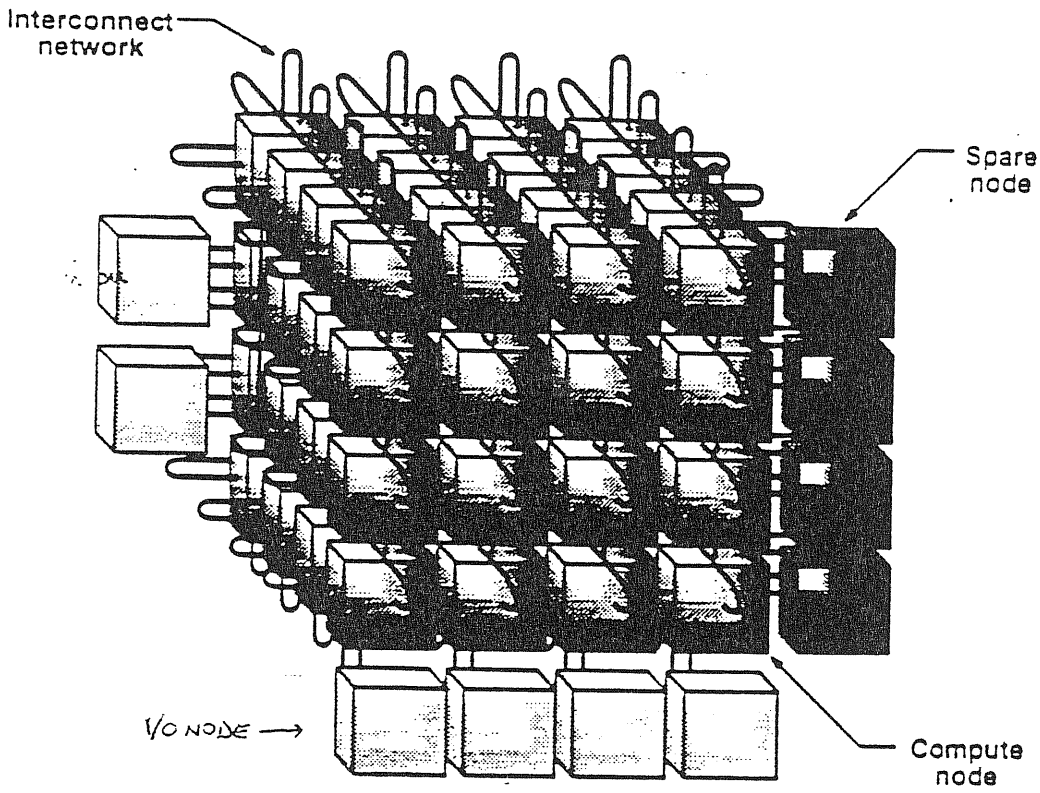

Figure 5.1: CRAY T3D configuration

5.1 Parallel Programming Models

Any kind of numerical computation uses two basic devices: the computer memory, in which the values of all the variables are stored, and the processor (from now on PE – Processor Element), which perform all the tasks requested for the computation. Traditional scalar computers have a single PE which operates on a single memory. Parallel super–computers are multi–processor systems; each PE can have its own associated memory, that anyway can be accessed by any other processor, or can operate on a single memory, common to all the PEs. In the first case we talk about *distributed memory* systems and in the second about *shared memory* systems. The CRAY T3D is a distributed system whose memory is *logically shared*. This means that some variables (the shared variables) have a unique memory address that can be accessed directly from any PE, independently from its "physical" position.

5.1.1 Parallel Programming Paradigms

For general distributed memory systems the most popular programming paradigm is the *message passing*. The messages (data) are sent by a PE specifying the task to which the message is to be sent, a message tag labeling the message and the data, and are received by a different PE which specifies the task from which the message is expected, the expected message tag and where to store the data. Therefore the communication is controlled explicitly by the programmer. The great advantage of this method is its portability as it can be used on any kind of parallel machine. Its limits are the time wasted in passing the information and the high risk of errors due to the explicit nature of the message exchange. The common standard for message passing is the Parallel Virtual Machine (PVM) language, which is a library of primitives that can be used indifferently by Fortran or C compilers on any network of heterogeneous systems.

On systems with physically distributed but logically shared memory the message passing paradigm is being substituted by the *data parallel* paradigm, in which there are some shared data that have a global address directly accessible from all the PEs without an explicit control by the programmer. We may say that the communication become "transparent" to the programmer. For example with message passing a two–dimensional array $A(N, M)$ can be distributed as:

$$A(i,j) \qquad i = 1, N \; ; \quad j = 1, M/N_{PE} \; , \tag{5.1}$$

where N_{PE} is the number of processors used for the computation. Each PE sees directly only its own $N \times M/N_{PE}$ part of the array, while it must ask the other PEs for all the other data contained in A. With data parallel instead all the array is directly accessible from any PE. Obviously a PE can access faster data defined in its own memory (local data) than to those defined on a remote memory, as this is done via the interconnection network that slows down the procedure. Data parallel methods have developed more slowly than message passing as they are much more linked to the features of the hardware, hence their portability can be very limited. For example CRAY has developed the Cray Research Adaptive ForTran programming model (CRAFT) which is an extension of Fortran 77 to

be used specifically on the T3D parallel system. At present there is an important effort to introduce a data parallel standard language with the High Performance Fortran (HPF) and its extension to CRAFT based commands, HPF/CRAFT. Both CRAFT and HPF/CRAFT have been developed to work with a Singol Program Multiple Data (SPMD) philosophy. With SPMD each PE owns and run the same copy of the program on a given fraction of the whole set of data. The amount of data assigned to a given PE depends on the total number of PEs used and on the way the programmer decides to distribute data between the processors.

5.1.2 Data Sharing

The CRAFT language (and the same holds for HPF/CRAFT) has all the statements of Fortran 77 (Fortran 90 for HPF/CRAFT). In addition there is a set of specific commands which permit to decide how to distribute data and work between the PEs. In other words it allows *data and work sharing*. Furthermore it allows to control the synchronization of the process.

The data sharing is to be done such that as many PEs as possible perform operations on their own local data rather than going off to another PE's memory to get the necessary information. Operation on local data are in fact faster than those on remote data. Therefore it is useful to have the possibility to decide how to distribute the data between the PEs in order to optimize the data sharing. Typical distributions of the array A are block, degenerate or cyclic. The block distribution method divides arrays into blocks of size equal to the array size divided by N_{PE} along each dimension; the degenerate distribution forces an entire dimension to be allocated on the same PE while the cyclic distribution allocates one element at a time on successive PEs. The CRAFT directive that set the distribution of data between the PEs is

$$CDIR\$\ SHARED\ A(geom); \tag{5.2}$$

The same directive in HPF is

$$!HPF\$\ DISTRIBUTE\ A(geom) \tag{5.3}$$

```
REAL A(8,4)
CDIR$ SHARED A(:BLOCK(2),:)
```

A:				PE Allocation:			
a_{11}	a_{12}	a_{13}	a_{14}	0	0	0	0
a_{21}	a_{22}	a_{23}	a_{24}	0	0	0	0
a_{31}	a_{32}	a_{33}	a_{34}	1	1	1	1
a_{41}	a_{42}	a_{43}	a_{44}	1	1	1	1
a_{51}	a_{52}	a_{53}	a_{54}	2	2	2	2
a_{61}	a_{62}	a_{63}	a_{64}	2	2	2	2
a_{71}	a_{72}	a_{73}	a_{74}	3	3	3	3
a_{81}	a_{82}	a_{83}	a_{84}	3	3	3	3

Figure 5.2: Block distribution of the two dimensional array A between four processors.

These directives are built such that they are interpreted as comments by a common Fortran compiler. In fact all the "parallel" commands are written starting from the first column and beginning with *C* for CRAFT and ! for HPF. These are the comments tag for standard Fortran 77 and Fortran 90 respectively. In this way the same code can be run (if properly written) both on a scalar and on a parallel machine. In (5.2) and (5.3) *geom* is the selected geometry by which the data are distributed between the PEs. For example (see also Figure 5.2) the directive:

$$CDIR\$\ SHARED\ A(:, BLOCK(2), :) \tag{5.4}$$

with $A(8,4)$ and $N_{PE} = 4$, gives a distribution in which the elements $A(1,1)$ to $A(2,4)$ are on the first PE (identified by the logical number 0), the elements $A(3,1)$ to $A(4,4)$ are on the second PE (logical number 1) and so on.

The data sharing directives and the geometry definitions must be written at the beginning of the code, just after the definition of the variables.

5.1.3 Work Sharing

The work sharing method distributes the statements of the program among the computer's PEs with the goal of executing them in parallel. In particular the iterations of a DO loop can be divided among the processors. In order to achieve the highest performances possible with the hardware used, each PE should have the same load of work (load balancing) and make its iteration only on local data. A shared loop is defined by the statement:

$$CDIR\$\ DO\ SHARED\ (i_1, ..., i_N)\ ON\ A(i_1, ..., i_N) \tag{5.5}$$

for CRAFT, and by:

$$!HPF\$\ INDEPENDENT\ (i_1, ..., i_N)\ ON\ A(i_1, ..., i_N) \tag{5.6}$$

for HPF. Here $(i_1, ..., i_N)$ indicates the indices of the shared loop and "$ON\ A(i_1, ..., i_N)$" indicates that the iteration defined by the indices $i_1, ..., i_N$ is performed by the PE for which the corresponding element of the array A is local.

In the following example we show how we have applied the work sharing procedure in a particular part of our code:

```
CDIR$   DO SHARED (k) on p3d(1,1,k)
 do k=1,ngrid
   do j=1,ngrid
     do i=1,ngrid
      pres(i)=p3d(i,j,k)
     enddo
   enddo
 enddo
```

Here the first statement indicates that the following do loop in the k index (and only that one, since the *DO SHARED* statement must be repeated for each loop) will be performed with work sharing. In particular the calculations which involve the index k will be made by the processor that in its own local memory has the component (i, j, k) of the vector $p3d$, for any value of i and j.

Finally, the process could need to be from time to time synchronized. In fact parallel procedures do not guarantee the order in which they proceed. At a certain moment some PEs could have finished a given procedure, while other are still working. If the following step requires that all the data have been updated, then we must stop the faster PEs and wait for all the processors to finish their work. This is obtained by the *BARRIER* statement both in CRAFT and in HPF. Obviously, excessive, not strictly necessary synchronization can cause poor performances.

5.2 Parallelization of the Code

The parallel version of our code has been originally implemented using the CRAFT model, as its original target was a CRAY T3D system. This version has been now updated using HPF/CRAFT in order to make it portable on a CRAY T3E machine.

5.2.1 Hydrodynamic Part

The parallelization of the hydrodynamic part of the code is extremely efficient. This is due to essentially two fundamental characteristics of the integration scheme. First, all the hydrodynamical quantities are calculated solving hydrodynamical equations on a fixed mesh. This allows to divide equally the work between processors, obtaining an optimal load balance. Second, the PPM integration is intrinsically one dimensional, the extension to more dimensions being obtained by a direction splitting procedure. This means that if we select a line along any coordinate direction this contains all the information required to complete the update of the hydrodynamical variables along that line. In the same way any plan orthogonal to a coordinate direction, say a $x - y$ plan, contains all the data required to perform the integration along the x and y directions for any fixed value of z. Therefore we can divide the computational box in slices of dimension $N_g \times N_g \times N_g/N_{PE}$ along the z–axis direction (see Figure 5.3) by a $CDIR\$\ SHARED(:,:,:BLOCK)$ directive.

Then all the shared hydrodynamical variables are divided with the same geometry. In this way each slice contains all the data needed by the L_x and L_y operators. The work is

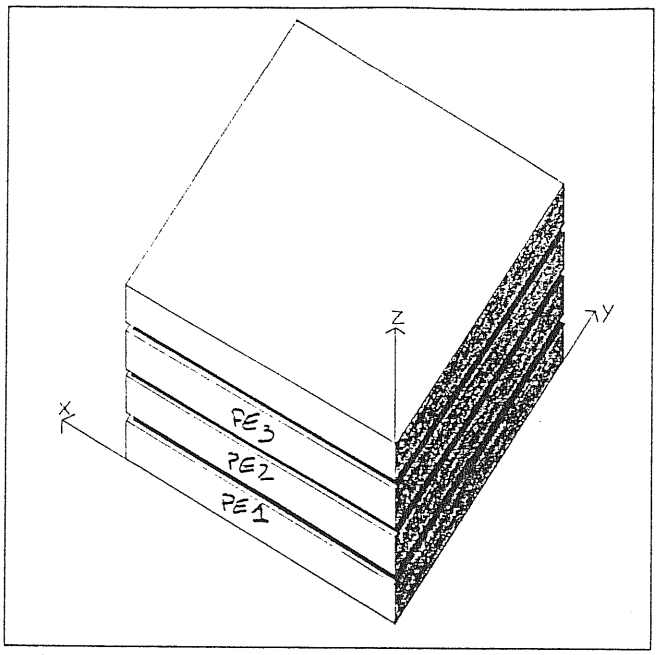

Figure 5.3: Distribution of the three dimensional computational mesh between processors

divided between the processors by a DO SHARED loop on the k index, representing the z direction, and is performed by the processor that owns the element (1,1,k) of any shared hydrodynamic variable (e.g. the pressure). The L_z operator instead has to collect data from all the other processors. Also in this case the work is distributed by a DO SHARED loop on k. However the processor cannot be identified by the element (1,1,k) otherwise only one processor, that which owns the first slice, would perform the whole work (see Figure 5.3). In this case the condition is that the processor owns the element (i,1,i), the index i representing the x direction. Also for the integration in the z direction the method has important advantages. First, each processor loads the necessary data only once in a step, at the beginning of the procedure, and writes the results again just once in a step, at the end of the PPM integration. Therefore, the subsequent calculation is completely local. Second, every processor does the same amount of work both in terms of computation and of communication. Finally, each processor update a different set of data (a "line" at a time in

the z direction), hence there is no possibility of using incorrect data (for example quantities already updated by another processor) and there is no need to stop any process waiting for other processors to finish their calculation. The only need for such a stop is at the end of each one dimensional calculation, hence just three times per time step.

5.2.2 N–body Part and Gravity

The parallel implementation for the steps of PM consists of the following steps (Carretti *et al.*, 1995a; Carretti *et al.*, 1995b).

Density assignment. To implement this part we have divided the cubic grid in the same way it has been done for the hydrodynamic part, hence in parallel slices of the same size which are assigned to the PEs with a one to one correspondence.

The particles are assigned to the PE to which their slice is assigned and each processor computes the density contributions of all its particles to its grid points. In this way the particles that contribute to the same grid point are treated by the same PE.

A problem is given by the particles that are near the slice bound. These particles contribute both to the grid points of their slice and to the grid points of the near slice.

To treat these contributions we use an auxiliary grid point plane. In this plane are stored the contributions of boundary particles to the near slice. At the end of density assignment the PE of the near slice gets the values of the auxiliary plane and adds them to the proper grid points. In this way no contribution is lost.

Potential and force computing. To compute the potential and force fields we use the real-to-complex and complex-to-real 3D Fast Fourier Transform (FFT) of the *scilib* library of Cray T3D.

Force interpolation. For the force interpolation we use the same implementation of density assignment because it is the inverse operation.

Particle Motion. We update the particle positions and velocities distributing the particles to the PEs such that each PE has the same number of particles.

The main advantages of this implementation are a total local computing and little remote

loading and storing. Furthermore the update of the position and the velocity of the particles is load balanced, as each processor perform exactly the same work. The main drawback is a possible load unbalancing in the calculation of the density, in correspondence to situation of strong clustering. In this case many particles are treated by the same processor. This leads to an overload of work of some PEs which slow down the speed of the whole process. Also the interpolation of the gravitational forces can slow down. In fact, particles that belongs to a PE, say PE1, can concentrate in a slice which is assigned to a different PE. Then PE1 must operate on many remote data. Furthermore, due to the high concentration of particles in the same slice, more processors need to access the same set of data. Since the data can only be accessed by one PE at a time, the procedure slows down.

As we will show in section 5.3, these are not major problems in the tests that we have performed, since in each considered case the time spent in calculating the density and the forces is much less than the time required from the PPM step. However, in situations where higher concentrations are present the slow down can become important (see Figures 5.5 and 5.6) and the algorithm must be better load balanced.

This can be obtained for the calculation of the density using a *dynamic* load balancing (at present in a preliminary test phase, Carretti & Messina, 1997). This method should guarantee a very good load balancing in all cosmological situations from the large scale structure study to the galaxy cluster formation.

As in the first implementation, the particle arrays are divided in N_{PE} subarrays and assigned to the N_{PE} processors. The grid arrays instead are divided with respect to the third dimension in N_{PE} sheets of $N_c \times N_c \times N_c/N_{PE}$ cells. Further the sheets are divided respect to the second dimension in N_{col} columns of $N_c \times N_c/N_{col} \times N_c/N_{PE}$ cells. Each particle is inside a column. To link the particles to their column we use a *linked–list* (Hockney & Eastwood, 1981). Since the particles move through the grid and can cross to another column, we perform the linked–list each time step. Moreover for the particle mobility the processor assigned to a particle and the processor assigned to its column can be different.

To have a good load balancing it is necessary that the processors perform their calcula-

tions on the same number of particles: N_p/N_{PE}. If the particle distribution were uniform, each column should be linked to $N_p/(N_{col} \times N_{PE})$ particles, and to have a good balancing, each processor should treat N_{col} columns. However the particle distribution can be clustered and a few columns can be linked to great number of particle. Hence it is necessary a dynamic load balancing.

This is performed as follows. We construct a column lock-array. As the density is computed, each processor scrolls it until finds an unlocked column, locks it and takes it. In this way no one else can take the same column. Then the processor distributes all particles linked to the column and stores their contributions in an auxiliary column. Since each particle assigns its mass to many grid points, the auxiliary array adds an edge to the column of density array. For example in the CIC scheme it need to add one element either to the second and third dimension.

After the density computation, the density array is updated with the values in the auxiliary column. However the edge belongs to another column. Therefore more processors can update the same column simultaneously. If this happens some cells could lose some contributions giving a wrong final result. To avoid this, we use the lock procedure. If a processor must update a column, it locks the column, updates it and finally unlocks it. If another processor must update the same column and find it locked, it must wait for it to be unlocked.

In the following step the processor scrolls again the column list and repeats the previous operations until all columns are treated. In this way we obtain a dynamic load balancing. If a processor takes a column with many linked particles, it spends a lot of time to treat it, and operates on few columns. Instead if a processor takes columns with few particles, it calculates many columns. If the number of columns per processor N_{col} is high, each processor treats a number of particles near to the mean (N_p/N_{PE}), obtaining a good load balancing.

5.3 Performances of the Code

Table 5.1: Time in seconds spent in the basic part of the codes for each timestep for different number of PEs Column 1: N_{PE}=8 Column 2: N_{PE}=16 Column 3: N_{PE}=32 Column 4: N_{PE}=64

	N_{PE}=8	N_{PE}=16	N_{PE}=32	N_{PE}=64
Total	67.23	33.82	17.80	9.55
Gravity	1.82	0.93	0.49	0.26
PPM	56.75	28.46	15.01	8.08
N–body	6.97	3.57	1.86	0.97

The memory requirement for a simulation of N_c cells and N_p particle is about:

$$M \sim 14 \times N_c + 6 \times N_p \text{ w} , \tag{5.7}$$

where w indicates the word unit: $1 \times \text{w} = 8$ bytes. In fact the hydrodynamical problem requires the storage of twelve three dimensional vectors, the calculation of the gravitational field needs two three dimensional vectors and, finally, the N-body code requires six three dimensional vectors. A simulation with $N_c = N_p = 128^3$ requires about 29 Mw (235 Mbytes) of memory. This is the largest run possible on our scalar machine, an ALPHA 2000 with two processors of 64 Mw of memory each, which work independently. On the CRAY T3D instead it is possible to perform simulations a factor two larger. The vectors are distributed such that each PE stores the same amount of variables and hence uses the same quantity of memory.

We have run a series of simulations of the same cosmological model, fixing $N_c = N_p = 64^3$, and varying the number N_{PE} of processors. The model used is that indicated in section 8.1 as BM15. We have analyzed at each number of PEs the total time required to complete a single step, the fractions of the total time spent to perform the basic calculations, the scalabilty and the load balancing.

• **Time estimates**

In Table 5.1 and 5.2 we present the time in seconds and in fractions of the total time

Table 5.2: As table t1 but in fractions of the total time

	N_{PE}=8	N_{PE}=16	N_{PE}=32	N_{PE}=64
Gravity	0.03	0.03	0.03	0.03
PPM	0.84	0.84	0.84	0.85
N–body	0.10	0.11	0.10	0.10

spent to complete the basic parts of a timestep. These estimates have been calculated as averaged values over 10 timesteps.

We indicate with Gravity the part of the code dedicated to the calculation of the density of the particles by the CIC scheme and of the gravitational field, using, essentially, two FFT. With PPM we indicate the procedure of integration of the hydrodynamical equations, while N–body consists in the interpolation of the gravitational force acting on each particle by the CIC scheme and in the update of its position and velocity. The PPM part is definitely the most expensive, accounting for about the 84% of the total time, while the time spent for the calculation of the gravitational forces is practically negligible. Table 5.2 shows that the different weight of the various parts of the code is independent from the number of PEs, even though these result could change depending on the degree of clustering of the simulation (see the part on the load balancing).

Since our simulation requires about 200 timesteps to be completed we have that the scalar code needs about 8900 seconds to complete a run, while the 64 PEs simulation finishes in about 2000 seconds.

• **Scalabilty**

Ideally, the speed of the code should scale linearly with the number of PEs. However, due to the increasing communication overhead, the speed degrades with the number of processors. Table 5.3 presents the speed–up of the code when doubling the number of PEs (for linear scaling this should be equal to two).

Table 5.3: Speed–up of the code with increasing the number of PEs

	8/16	16/32	32/64
Total	1.99	1.90	1.88
Gravity	1.96	1.90	1.88
PPM	1.99	1.90	1.86
N–body	1.95	1.92	1.92

Figure 5.4 shows the comparison of the real speed–up of the code and the ideal linear speed–up with increasing the number of PEs. The figure shows that the code is highly scalable in all of its parts. Notice that, as expected, the scalabilty improves as the number of PEs decreases (as the communication is less important). In any case the loss of speed is at most of the 6% for the whole code, of the 7% for the PPM step, of the 4% for the N–body part and finally of the 6% for the Gravity step. All the maximum slow down correspond to the step from 32 to 64 PEs. In the case of 64 PEs there in fact, is the maximum distribution of data, one plane at a processor. Therefore also the communication is maximum and the speed–up is less than in the other cases.

• **Load Balancing**

In Figure 5.5 we show the time required to complete the various steps of the code as a function of the redshift, and so of the degree of clustering, of a simulation of a BM15 models with $N_c = N_p = 256^3$ on 128 PEs. In Figure 5.6 we have plotted the fractional variation of this time, defined as

$$\Delta t_l = \frac{t(z) - t_i}{t_i} , \tag{5.8}$$

where $t(z)$ is the time required to complete a certain procedure at redshift z (averaged over the three timesteps around z) and t_i is the same quantity at the beginning of the simulation.

Due to the optimal load balancing between the processors the computational time for the PPM part depends little from the degree of clustering. The maximum Δt_l is, in fact,

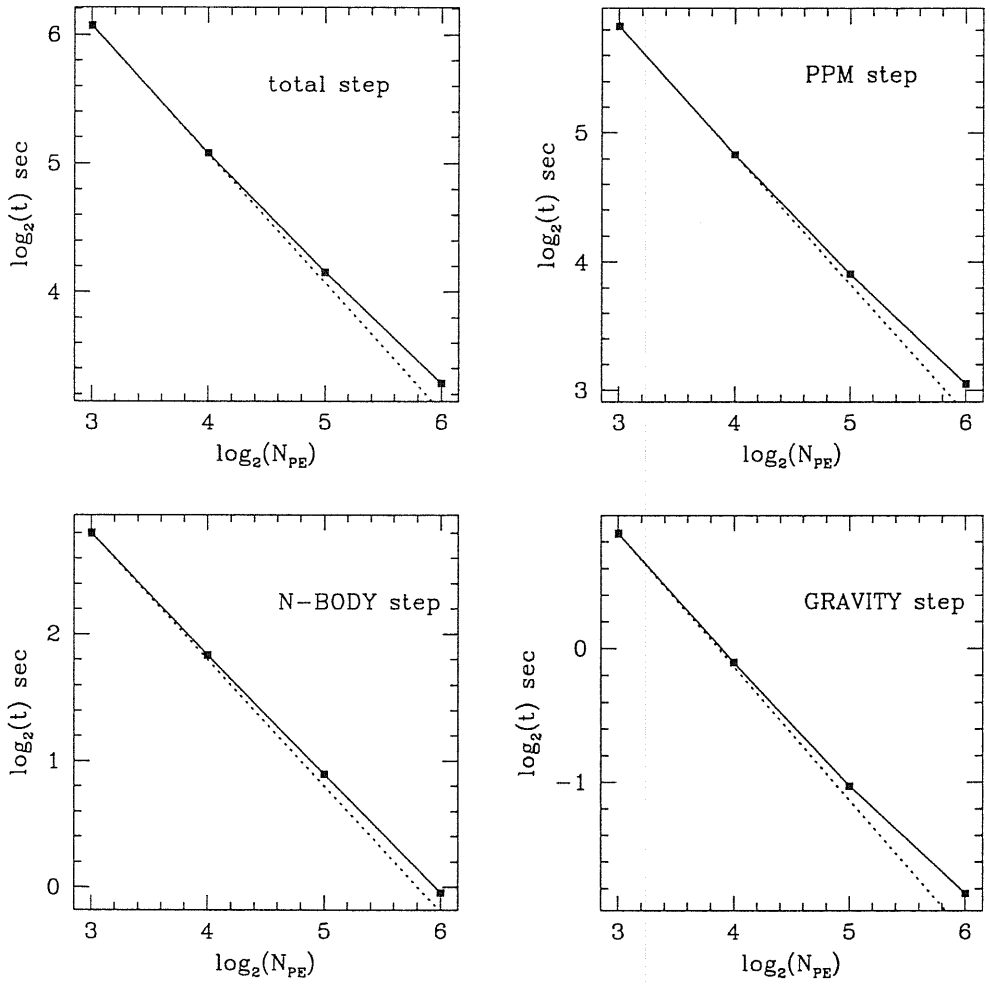

Figure 5.4: Scalability of the code. The time required to complete a total step (upper-left panel), a PPM step (upper-right), a N–body step (lower-left) and a Gravity step (lower-right), as a function of the number of PEs. The results (solid lines) are compared to the ideal linear speed–up (dotted line).

of about the 5%. The load balancing instead is not so good for the Gravity and for the N–body parts. The calculation of the density on the computational mesh depend on the degree of clustering. In Figure 5.6 we see that the time spent to calculate the density at the end of the simulation becomes more than two times that at the beginning. This is due to the fact that in overdense regions more and more particles contribute to the density of the same cells. Therefore the PE which has to calculate the density of the cells in overdense regions has to work more than on average and much more than a PE which operates in an underdense zone.

Also the N–body calculation tend to slow down with the degree of clustering. This trend is less strong than for the Gravity part and is due to the forces interpolation step.

In any case, in our tests the N–body and the Gravity computational times are always much less than the PPM time and so also much less than the total time required to complete a single step, as shown in the first panel of Figure 5.5. For this reason at the moment we have not included further optimization to the parallel implementation of this parts, leaving this task to a further version of the code.

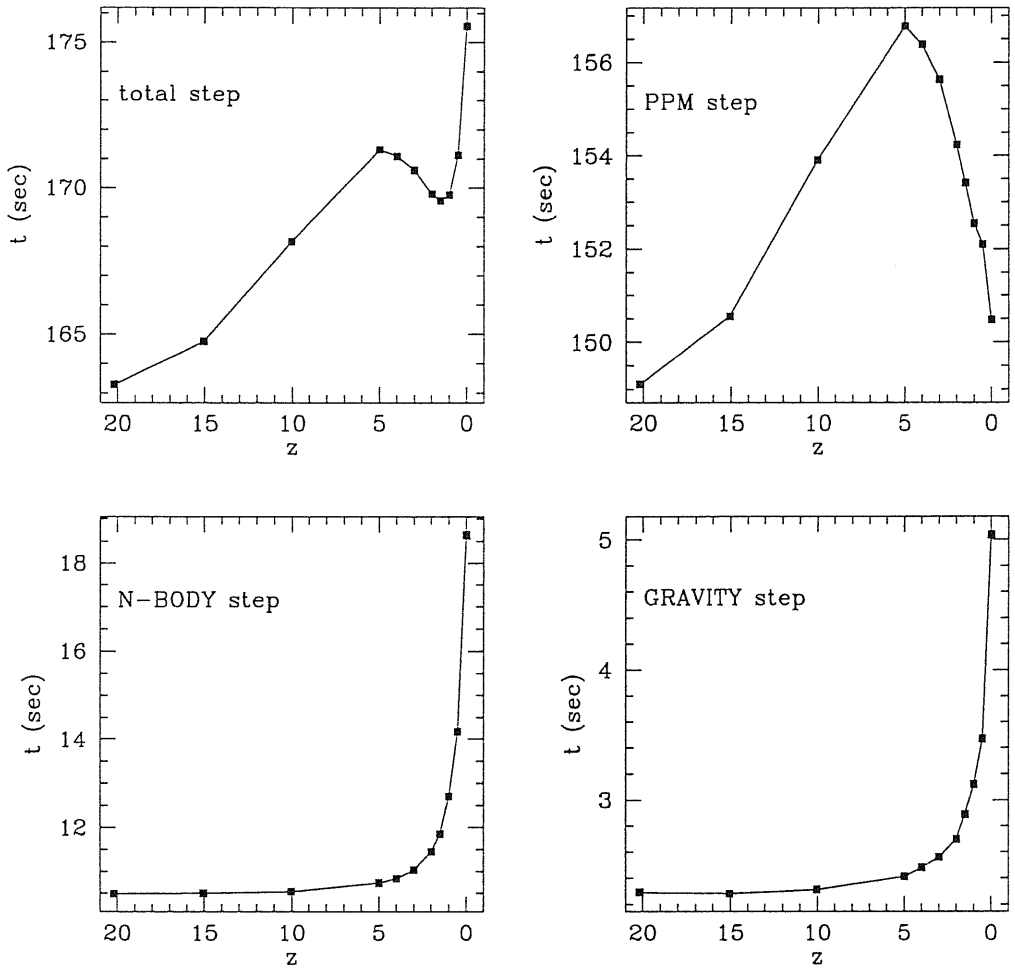

Figure 5.5: Dependence of the computational time from the redshift z.

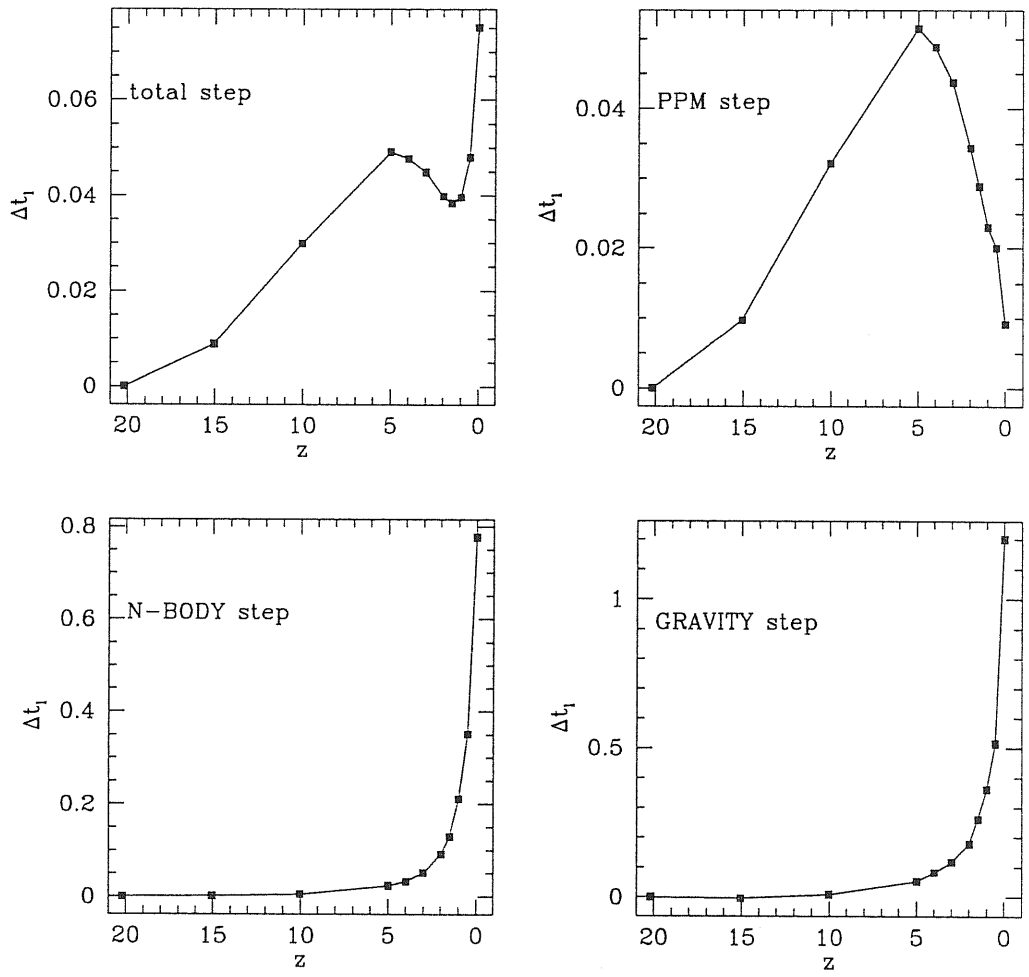

Figure 5.6: Dependence of the fractional variation of the computational time from the redshift z.

6 One Dimensional Scale Free Models

As a first application of our cosmological code we have chosen to perform some high–resolution one dimensional simulations. A one dimensional analysis, in fact, is the only possibility of strongly increasing (a factor of ten or more) the resolution of numerical simulations. As we have already observed, the limited resolution reachable in three–dimensional codes is a major problem of cosmological simulations. In fact, if one wants to consider all the phenomena that can influence the structures evolution, it would be necessary to have the capability of spanning an enormous dynamical range. This would require at least 10^9 computational cells per dimension, while present day codes can work at most with 10^3 cells. Therefore part of the physical processes that could affect the evolution of the cosmological structures cannot be accurately treated or even included in the simulations. With the following series of one–dimensional simulations we want to explore the differences in the statistical properties of the one–dimensional clustering of baryonic and dark matter components in an expanding background when a large dynamical range is achievable. We analyze, in particular, the effect of pressure forces and adiabatic heating in the dynamics of the gas. This can be used as guideline for any following three dimensional lower–resolution development.

Since the simulations are one–dimensional it is meaningless to directly relate their scales with cosmological physical scales associated with some particular cosmological model. Therefore the only possible choice is that of scale–free models. This means that the back-

ground cosmology should have no characteristic length or time scales. Therefore we consider a flat universe, with zero cosmological constant. Furthermore, in order to avoid the introduction of some characteristic length scales, the initial spectrum of perturbation must have a power law form:

$$P(k) = Ak^n . \tag{6.1}$$

In these models the evolution of the collisionless component is expected to be self–similar. It is clear that the requirements for self–similar gravitational clustering are idealizations which cannot apply rigorously to the real universe. All the cosmological models present fluctuation spectra with some specific scales. For example the evolved power spectrum for a CDM model changes slope at a scale $\sim 12(\Omega h)^{-2}$Mpc. Nevertheless a power law approximation to the local slope of the spectrum is a reasonable approximation for many cosmological models. In addition scale free models allows to understand how the formation of cosmological structures depends on the basic physical processes considered and on the initial spectral index.

6.1 Numerical Simulations

We consider a grid of comoving length L, whose physical size grows according to the expansion parameter a. We divide our grid into 2^{13} nodes and adopt periodic boundary conditions. The number of particles used in the N–body part of the code is 2^{14}. We assume a flat universe ($\Omega = 1$) in which the BM component accounts for 10% of the total mass ($\Omega_{BM} = 0.1$) and the rest is in the form of DM ($\Omega_{DM} = 0.9$). The evolution of the system is simulated using a one–dimensional version of our PPM+PM code. The initial conditions are generated following the same procedure described in section 4.5

In the first stages of the evolution we assume that both the DM and the BM can be treated as collisionless particles. Then we use only the N–body code for following the behaviour of both components. When $a = 10^{-3}$, i.e. just after the recombination epoch, we start to evolve separately the two components. At this time the gas quantities are fixed according the following prescriptions. The temperature of the BM is simply computed by

using the polytropic equation of state under the assumption of an adiabatic evolution up to this time. This is a reasonable assumption since the amplitude of fluctuations in the first part of the simulation is too small to produce shocks and we neglect other possible heating and cooling processes. The gas velocity is computed from the gravitational potential by using linear theory.

As already pointed out, our simulations are completely scale–free: the final amplitude of the fluctuations depends only on the scale $R_\star$ relative to which the initial normalization is fixed. In order to make more clear the implications of these results at the cosmological scales, we have fixed the present time value of $R_\star$ equal to 8 h^{-1} Mpc, corresponding to the scale where observationally the variance is found to be unity. The length of the whole box has been chosen such that $R_\star$ is $L/50$. Consequently $L = 400\ h^{-1}$ Mpc.

6.2 Results

We consider three different models with primordial spectral index $n = -1,\ 1,\ 3$: in three dimensions, these would correspond to $n = -3,\ -1,\ 1$ (the so–called Harrison–Zel'dovich spectrum) respectively, covering in this way the range of values usually adopted for cosmological models. For each model we run three simulations with different realizations of the initial conditions in order to obtain more accurate estimates of the relevant quantities. Here we consider various statistical tests, such as the distribution of density perturbations, the number of peaks and the evolution of the density power–spectrum. We also discuss thermodynamical quantities and their correlations.

6.3 Distribution of Density Perturbations

In Figures 6.1, 6.2 and 6.3 we show the behaviour of δ_{BM} and δ_{DM} at final time $a = 1$ in a realization for each model $n = -1, 1, 3$, respectively. The results refer to a quarter of the whole grid. Different runs of the same model show a very similar qualitative behaviour. The density fluctuations are computed with respect to the mean value of the corresponding

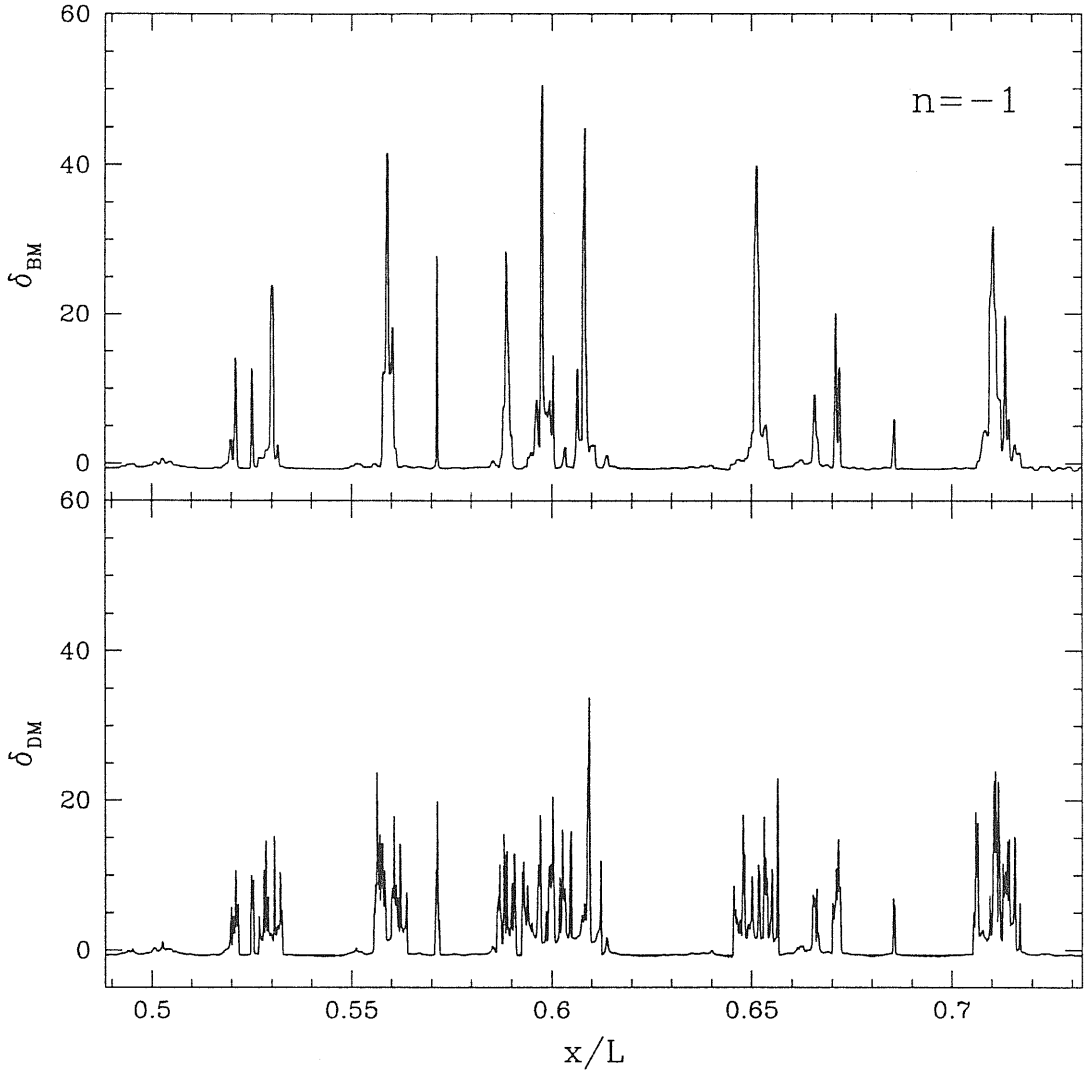

Figure 6.1: The density fluctuation distribution at the final time $a = 1$ for the model $n = -1$. The upper and lower panels refer to the baryonic and dark matter components, respectively. Only about a quarter of the whole grid is displayed.

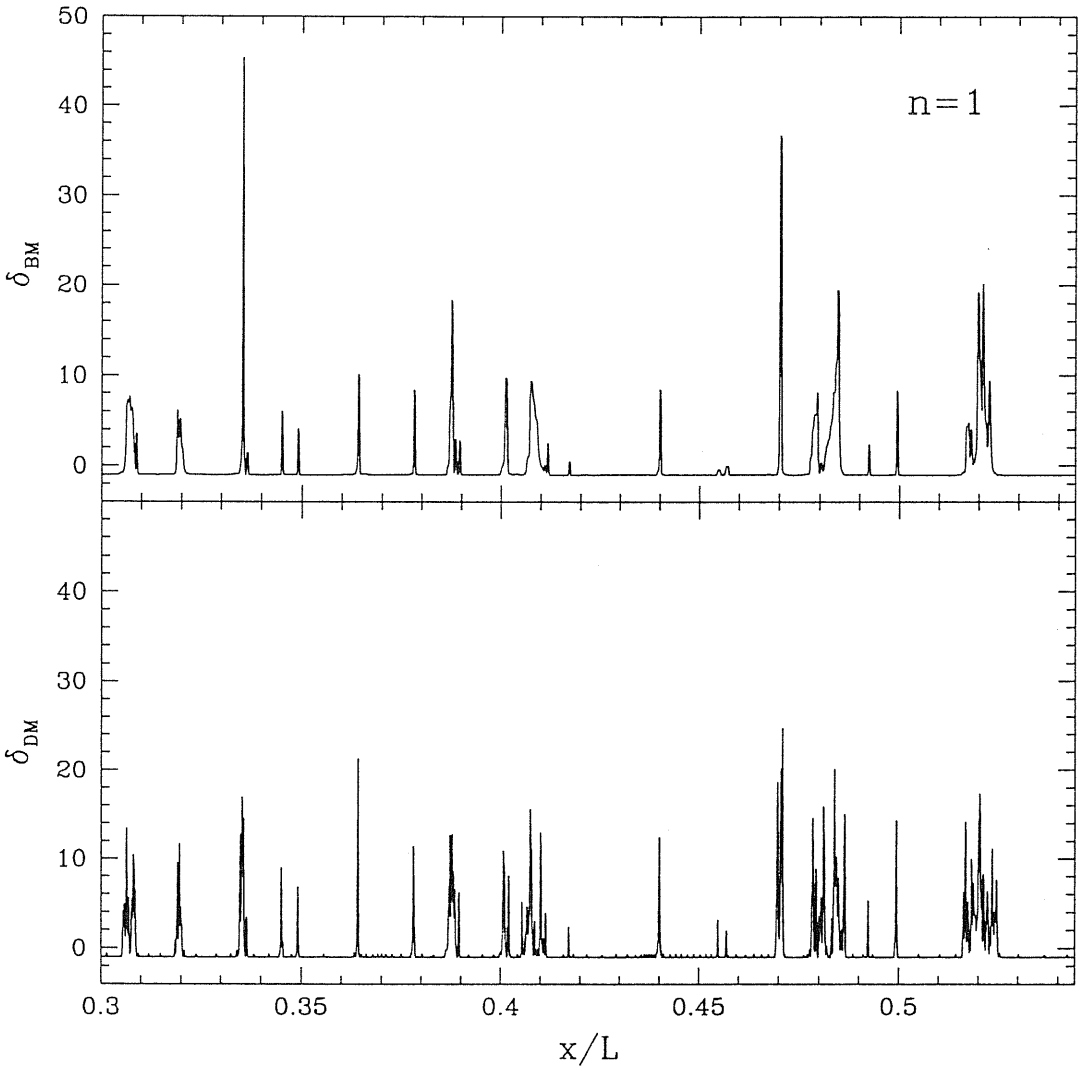

Figure 6.2: As Figure 6.1, but for the model $n = 1$

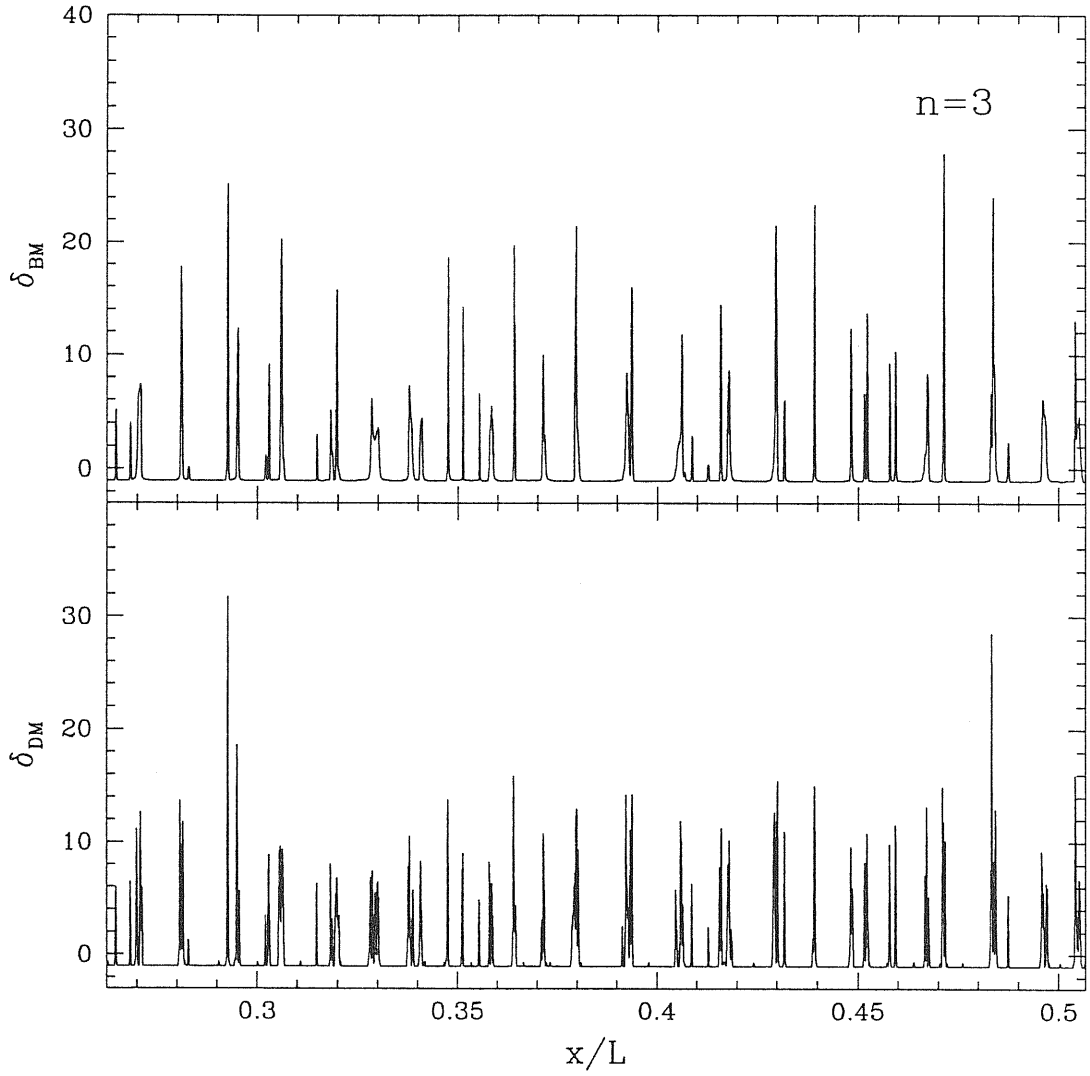

Figure 6.3: As Figure 6.1, but for the model $n = 3$.

component. As expected, increasing the spectral index n, we have less power on large scales and, consequently, density peaks are more frequent, but they have a smaller density contrast, while underdense regions are less extended.

In all cases there is a correspondence between the distribution of DM and BM. However, the baryonic component appears in general more clumped than the dark counterpart which stays more spread with small substructures. This behaviour is enhanced as we decrease the spectral index. In particular, in the model with $n = -1$, the collisionless matter is distributed over a region which can be several times larger than that corresponding to the BM peak. In these regions, the baryonic contribution to the local gravitational field starts to be comparable to that of the dark component.

The analysis of results at different epochs (not shown) points out the tendency to a continuous merging of substructures which produces higher peaks and larger voids. This behaviour is more evident in simulations with more power on large scales. The phenomenon is less pronounced for DM: this is due to the absence of dissipation for the collisionless component. On the contrary the conversion of kinetic into thermal energy for the baryonic counterpart leads to the production of more concentrated structures, even if cooling processes are not included.

A quantitative estimate of the spatial correspondence between the BM and DM density distributions can be obtained studying the cross–correlation coefficient (see e.g. Coles, Melott & Shandarin 1993)

$$S(R) = \frac{\langle \delta_{BM}(R)\, \delta_{DM}(R) \rangle}{\sigma_{BM}(R)\, \sigma_{DM}(R)} \,, \tag{6.2}$$

where $\delta_{BM}(R)$ and $\delta_{DM}(R)$ are respectively the density contrasts in the BM and DM components, smoothed with a Gaussian window of radius R and $\sigma_i = \langle \delta_i^2 \rangle^{1/2}$ are the corresponding r.m.s.. The mean is computed over all grid–points. Definition (6.2) implies $\mid S \mid \leq 1$. The limit $S = +1$ corresponds to $\delta_{BM} = C\delta_{DM}$, where C is a constant: in this case there is a perfect agreement in the positions of the structures in the two components. In Figure 6.4, the cross–correlation coefficient S is plotted as a function of the Gaussian filtering radius R for the three models when $a = 0.5$ (dotted lines) and $a = 1$ (solid lines). The error

bars, shown for clarity only at the final time, represent the scatter r.m.s. between the three different realizations of each model. At earlier times these errors are found to be always smaller. As expected, decreasing the filtering radius and/or allowing for a longer evolution, the differences between the two components increase and, consequently, the coefficient S decreases. This is particularly true for the model with $n = -1$, where, for $R \leq 10^{-3}L$, the cross–correlation is even less than 0.5. On the contrary, a value of S close to unity is obtained in the simulations with $n = 3$, even when a small filtering radius is adopted.

The study of high–density regions in BM is particularly interesting because they are expected to be related to the positions where galaxy formation occurs. We define as peaks all the grid–points having $\delta \geq 0$ which are local maxima of the density fluctuation field. In Figure 6.5 we show, at two different times, the number of peaks N_{pk} having a height greater than a given threshold δ, both for BM (dotted lines) and DM (solid lines) components. The comparison between the models with different spectral indices shows a similar behaviour. The number of high peaks in BM is always larger than that of DM at both considered times. The time evolution produces a slight flattening of all the curves denoting the tendency to merge of the smaller peaks into larger structures. Note that the height of the largest baryonic peaks at the final time is slightly smaller than at $a = 0.5$: the formation of shocks can change in fact the direction of the velocity leading to a matter outflow from the peak.

6.4 Thermodynamical Quantities

In Figures 6.6 and 6.7 we show the behaviour of the baryonic quantities v, T and ϱ_{BM} for the intermediate case $n = 1$ at $a = 0.5$ and $a = 1$, respectively. The results refer to the same realization shown in Figures 6.1–6.3. In absence of heating from external sources and cooling processes, we notice the presence of regions where the temperature is as high as 10^7 K already at $a = 0.5$: they are in proximity of the highest baryonic peaks. In the figure it is easy to pick out the positions of the shocks produced during the collapse and characterized by very steep gradients in the velocity and the temperature. Comparing the results at the two different times, it is possible to notice the enlargement of high temperature regions, due

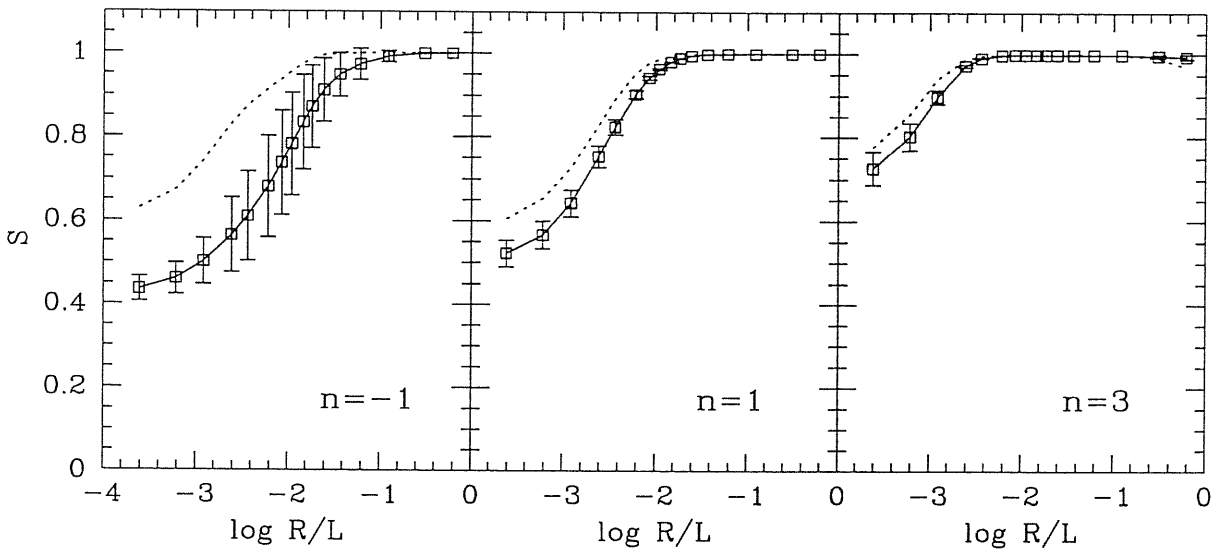

Figure 6.4: The cross–correlation coefficient S as a function of the Gaussian filtering radius R (in units of the whole grid L) at the time $a = 0.5$ (dotted line) and $a = 1$ (solid line) for the different models: $n = -1$ (left), $n = 1$ (centre) and $n = 3$ (right). Error bars (displayed for clarity only at $a = 1$) represent the r.m.s. scatter between the different simulations.

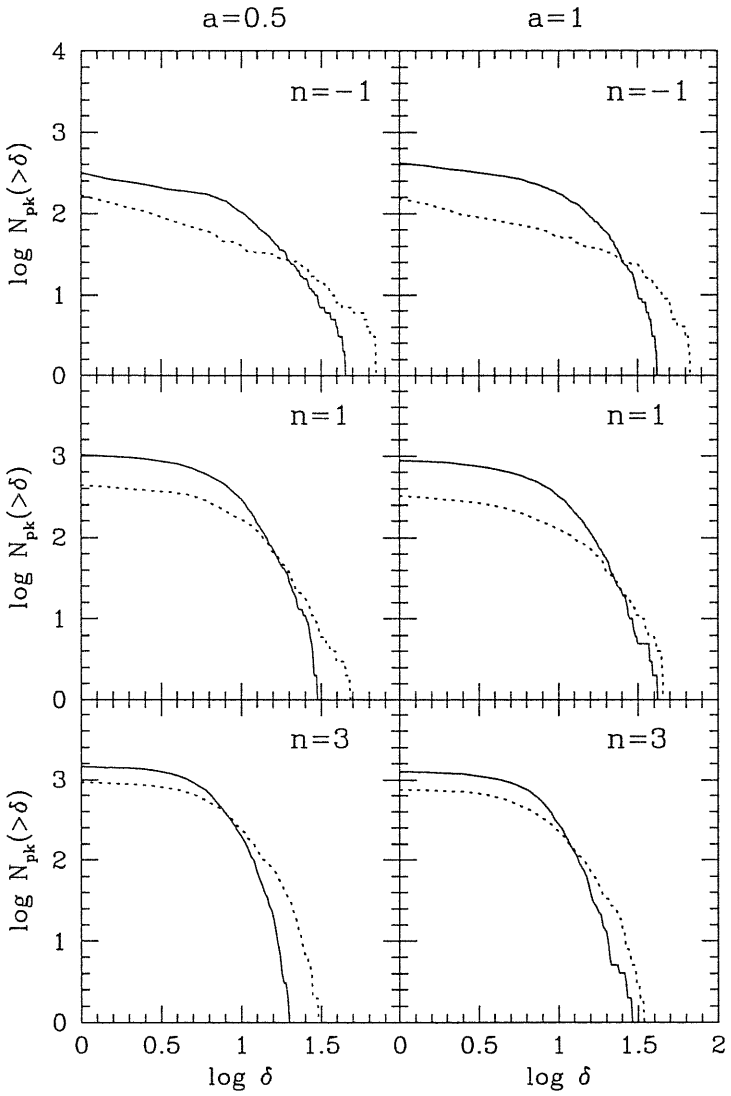

Figure 6.5: The number of peaks N_{pk} in dark (solid line) and baryonic (dotted line) components as a function of their height δ when $a = 0.5$ (left column) and $a = 1$ (right column) for the different models: $n = -1$ (top), $n = 1$ (centre) and $n = 3$ (bottom).

to the propagation of the shock from high density peaks.

The behaviour of the baryonic quantities for the model $n = -1$ is shown in Figure 6.8 only for $a = 1$. Due to the presence of more power on large scales, the structures are surrounded by large underdense cold regions. The highest temperatures in the plotted region are of the same order as in the case $n = 1$ but values as high as 10^9 K can be reached. In the lower panel it is possible to notice some overdensities at very low temperatures: they correspond to regions which are still adiabatically collapsing.

Figure 6.9 shows the corresponding results for the model with $n = 3$, again at the final time $a = 1$. The highest temperatures obtained in this case are at least one order smaller than in the previous cases. This is an effect of the initial large power at small scales. The structures are in fact produced earlier than in the other two models and, due to the shallower potential wells, shocks are weaker and the final temperatures are lower.

The temperature distribution in the different models is better illustrated by the cumulative volume filling factor and mass fraction F as a function of the temperature T. Figure 6.10 shows the behaviour of these quantities at $a = 1$ as obtained by summing over the contribution of all three realizations for each model. We notice that the fraction of matter at high temperature (e.g. $T \geq 10^6$ K) increases as we decrease the spectral index: it is approximately 56% and 47% for $n = -1$ and $n = 1$, respectively, while less than 1% of grid–points has such a high temperature in the $n = 3$ model. The comparison of the cumulative volume filling factor (solid lines) with the mass fraction (dotted lines) strengthens our previous comments. In particular, in the case $n = -1$, due to the dominance of empty regions, more than 90% of the volume has $T \leq 10^{-2}$ K. On the contrary, the two cumulative functions are more similar in the model with $n = 3$, where structures are smaller and more uniformly distributed. These results confirm that, even in absence of other dissipative or heating effects (viscosity, thermal conduction, starbursts, etc.), it is possible to obtain in one–dimensional cosmological simulations temperatures as high as those seen in X–ray observations.

Figure 6.11 shows contour plots for the number of cells characterized by a given tempe-

rature and baryonic density. In the case $n = 1$ and $n = 3$ we can recognize three distinct regimes: high temperature overdense regions, shocked regions with lower density and cold underdense regions. The result for $n = -1$ shows that at $a = 1$ there is a large amount of matter which is still in the adiabatic collapse phase and consequently has a large overdensity but low temperature. Note also that, due to the small number of shocks and their late formation, low density shocked matter is almost absent in this model.

6.5 Power–spectrum and Bias

In order to study the time evolution of clustering at different scales, we have computed the power–spectrum $P(k)$. If the density fluctuations remain linear, $P(k)$ is expected to grow as a^2. In Figure 6.12 we show the behaviour of the power–spectrum both for BM and DM for the three models at different times. The units of the wavenumbers k are such that $k = 1$ corresponds to the fundamental wavelength of the computational grid. We notice that the time evolution for the power–spectra of both DM and BM components is similar. We see that at small wavenumbers (i.e. at large scales) the growth of the perturbations is in good agreement with linear theory. At larger wavenumbers deviations from linear theory are found, as expected. In particular for the baryonic component we can notice that at the final time the small–scale power decreases with respect to the previous times. Moreover the amplitude of $P(k)$ for the BM is slightly smaller than that for the DM. Once more this is due to the shock action which reduces the height of peaks (as seen in Figure 6.5) and smooths out the smallest overdensities. This effect is in fact not present in the DM component where shocks do not form.

In addition, we notice that there is a faster evolution for the models with $n = -1$: the non–linear growth produces the coupling of high– and low–k modes. In the model with $n = 3$, where initially the large–scale power is small, this effect does not appear. The case $n = 1$ is intermediate. Then, our simulations, even if starting with a power–law spectrum, seem to exclude the possibility of having self–similar evolution when large scale power is present. Only the model with $n = 3$ presents a self–similar evolution in the DM at least for

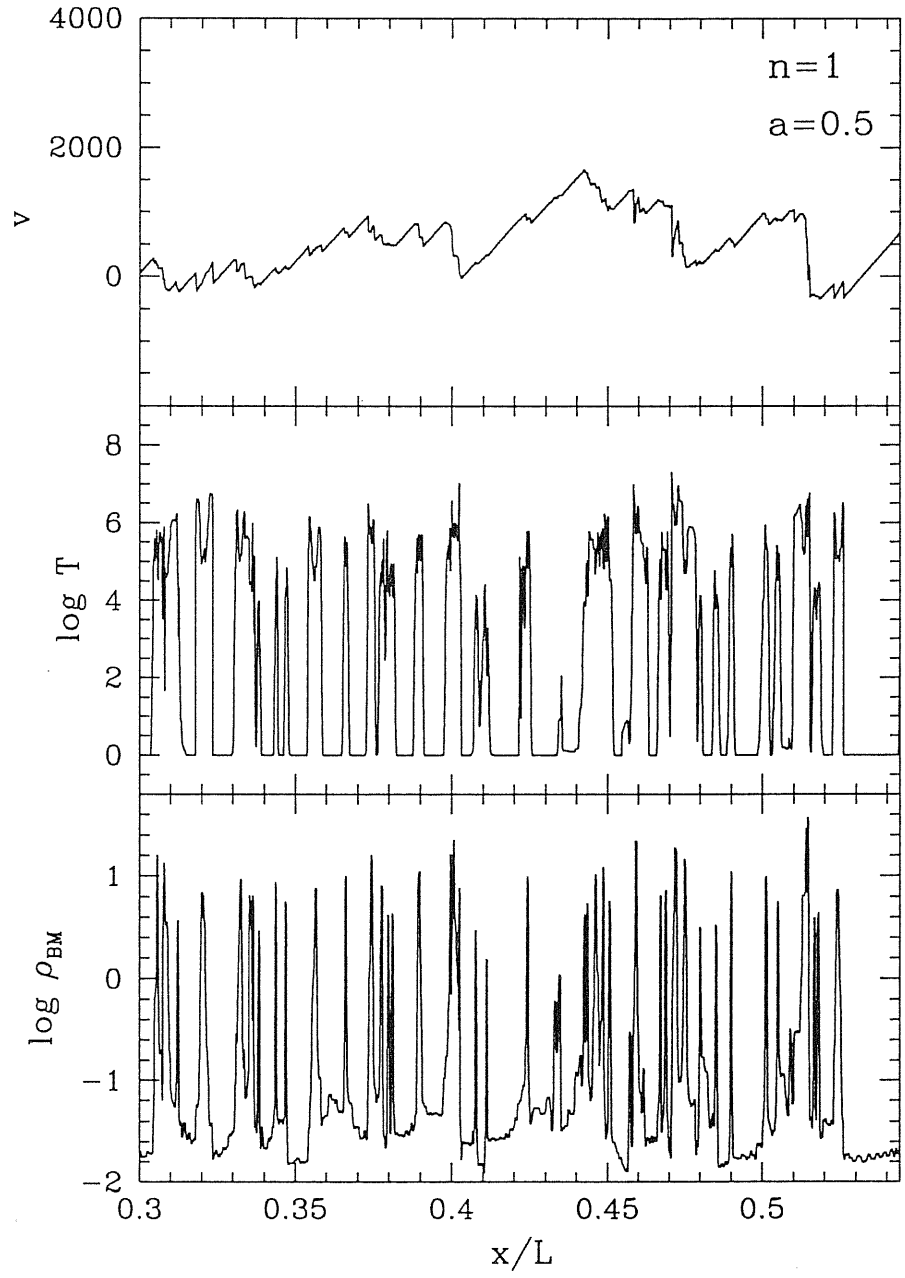

Figure 6.6: The distribution of velocity v (in km s^{-1}), temperature T (in Kelvin degrees) and baryonic density ϱ_{BM} (in units of its average density) for the case $n = 1$ at $a = 0.5$. Only one quarter of the whole grid is displayed. Temperature lower than 1 K are artificially raised to this value for clarity.

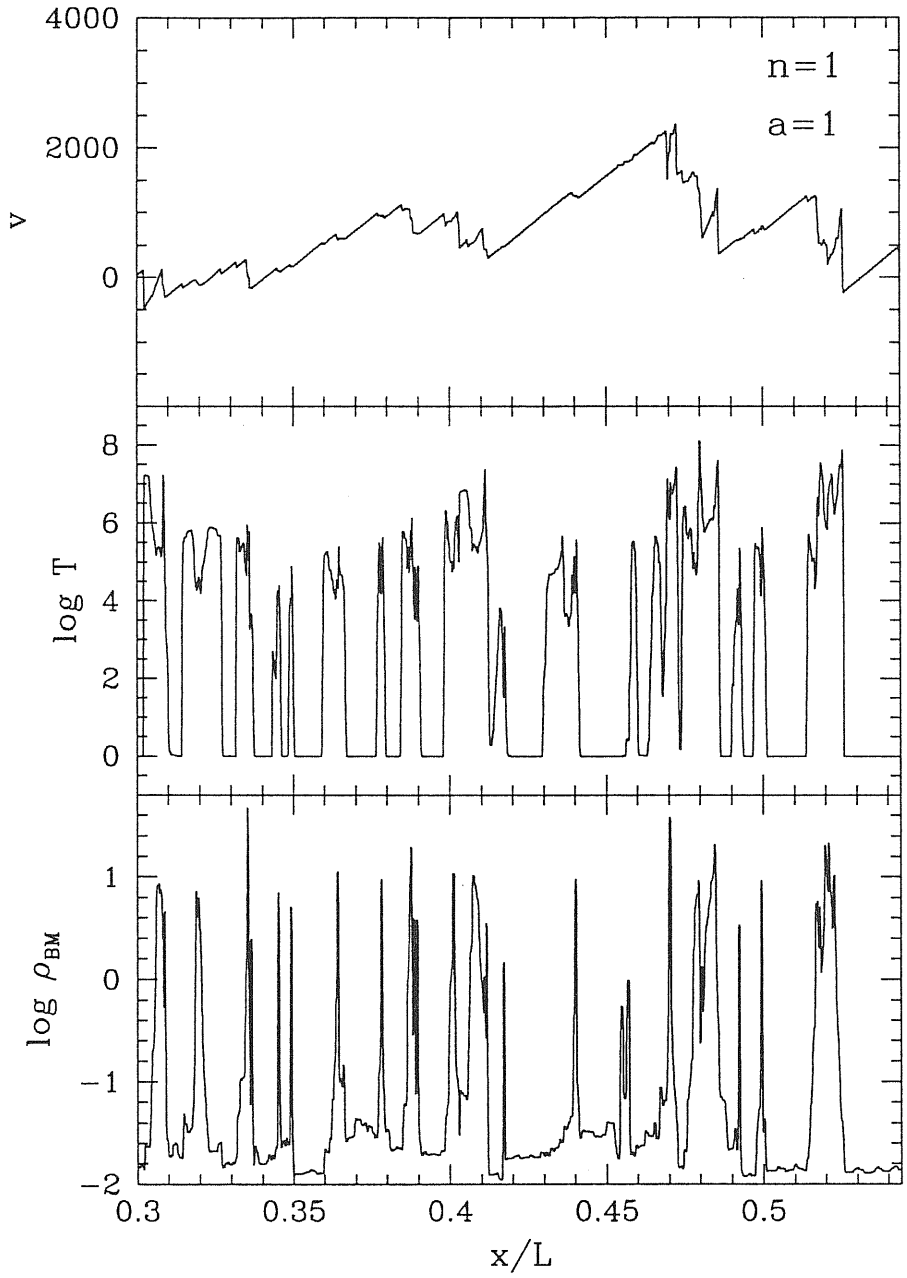

Figure 6.7: As figure 6.6, but at the final time $a = 1$.

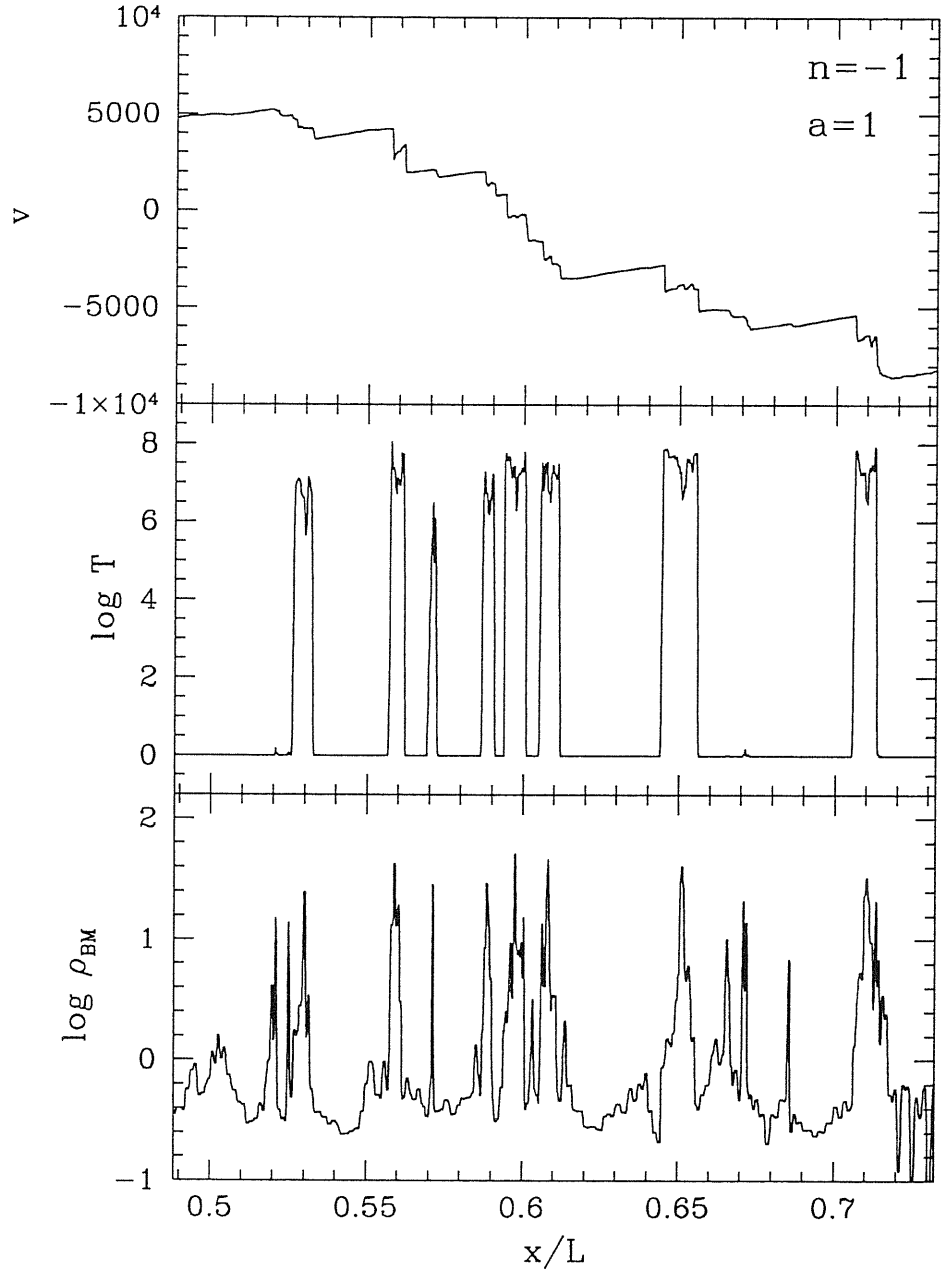

Figure 6.8: As Figure 6.6, but for the model $n = -1$ at the final time $a = 1$.

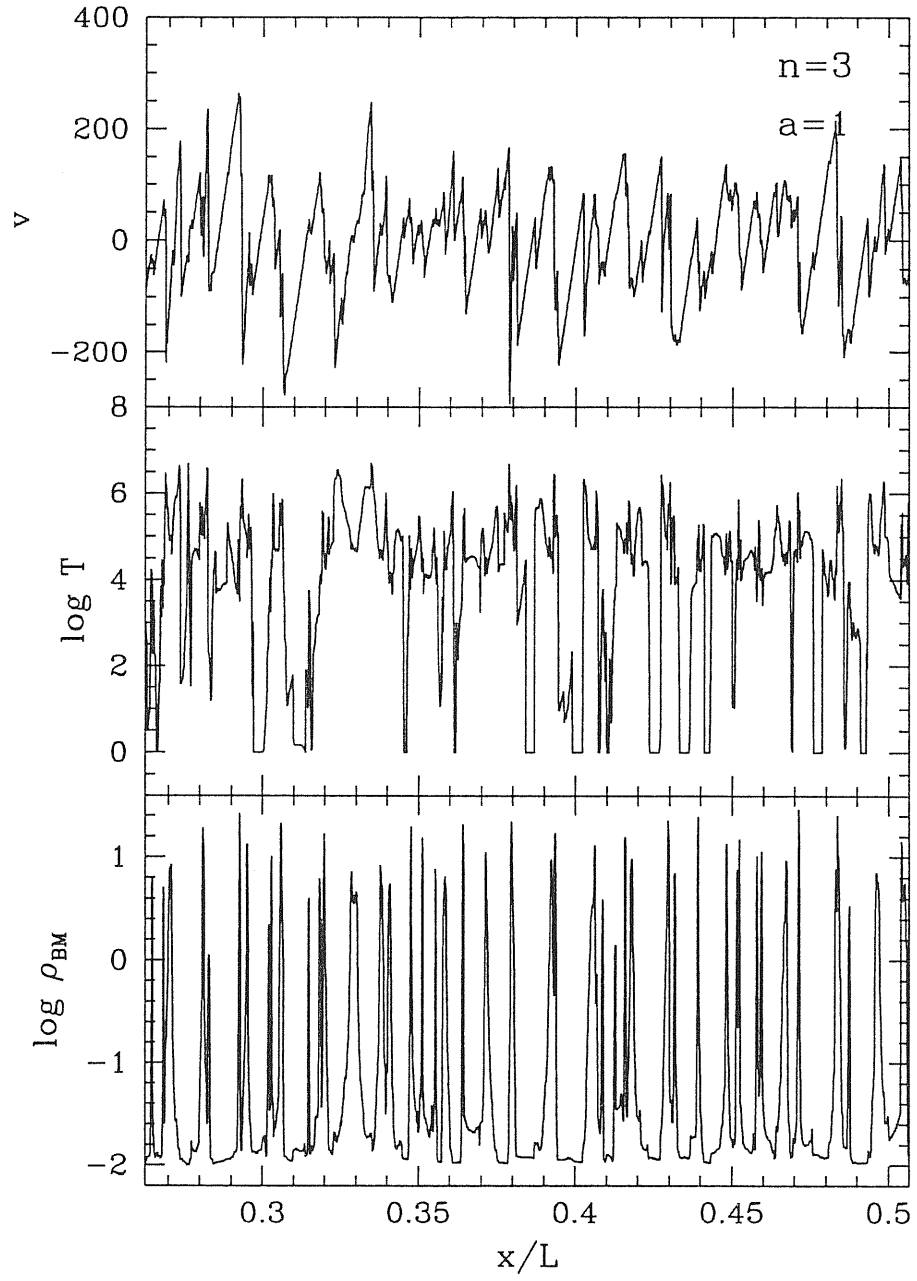

Figure 6.9: As Figure 6.6, but for the model $n = 3$ at the final time $a = 1$.

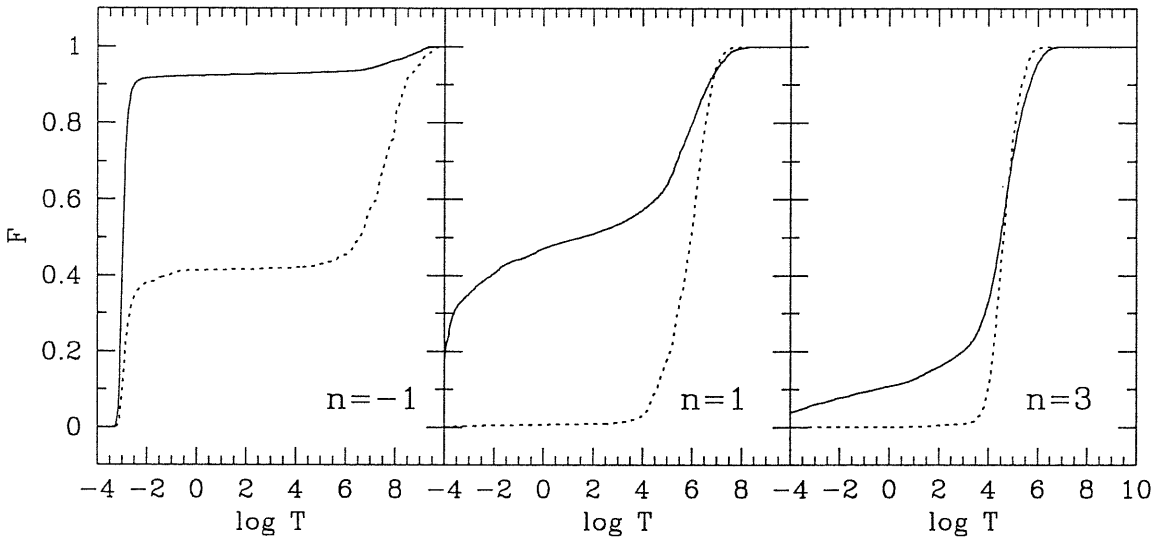

Figure 6.10: The cumulative volume filling factor (solid line) and mass fraction (dotted line) as a function of the temperature T at the final time $a = 1$ for the different models: $n = -1$ (left), $n = 1$ (centre) and $n = 3$ (right).

$\log k \leq 2$.

An interesting way to measure the relative growth of the perturbations is the bias factor b, defined as

$$b(R) = \frac{\sigma_{BM}(R)}{\sigma_{DM}(R)}, \tag{6.3}$$

where $\sigma_i^2(R)$ is the variance of the density fluctuation field in the i–component, smoothed using a Gaussian window of radius R. Figure 6.13 shows the behaviour of b for the three models at $a = 0.5$ (dotted lines) and $a = 1$ (solid lines). The scatter r.m.s. between the different realizations of each model is also plotted only at the final time. The BM appears more clustered than the DM at small scales while at larger scales they have the same clustering properties. The largest bias factor is found in the model $n = -1$ with values higher than 1.4 at scales smaller than $10^{-2}\,L$. It is interesting to compare the time evolution of the bias factor at small ($10^{-4}L$) and intermediate scales ($10^{-2}L$). The formation of shocks halts the collapse of baryonic peaks and this produces a decrease at small scales in the values of b in the $n = 1$ and $n = 3$ models. On the contrary, in the $n = -1$ model, b increases at all scales. This different behaviour is due to the presence of deeper potential wells than in the other models so that pressure forces are not able to stop completely the matter infall. In this case case shocks only reduce the growth of b at small scales.

6.6 Discussion

As a general consideration which applies to all models we can say that baryonic matter is more clumped than dark matter and a single baryonic peak is usually embedded in many DM peaks. This property is well described by the values of the bias factor $b = \sigma_{BM}/\sigma_{DM}$ which are always larger than unity. The formation and expansion of shocks from high density peaks tends to limit or even reduce (for $n = 1, 3$) the time growth of b but it never produces an antibias. We expect that cooling, if included, would enhance the concentrations of baryons with respect to dark matter.

In the BM component the formation of shocks has important consequences on the time evolution of density fluctuations: the pressure can become high enough to stop the grav-

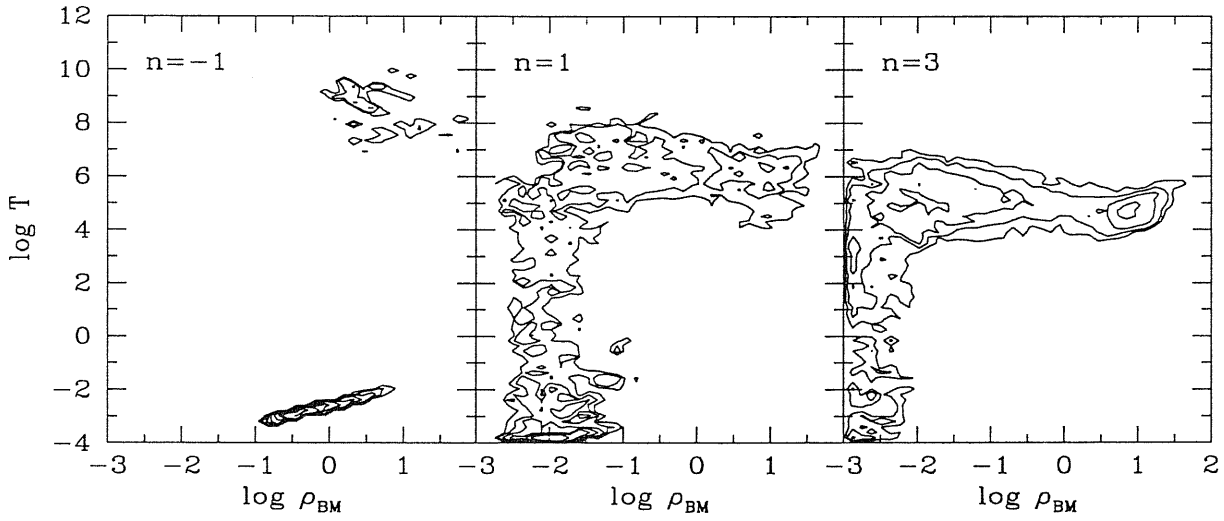

Figure 6.11: Contour plots for the number of cells characterized by a given temperature T and baryonic density ϱ_{BM} at the time $a = 1$ for the different models: $n = -1$ (left), $n = 1$ (centre) and $n = 3$ (right). The contour levels are defined as follows: $10^{I/3}$, where I is a positive integer; the outermost contour corresponds to $I = 3$ and contours inside it have gradually increasing I.

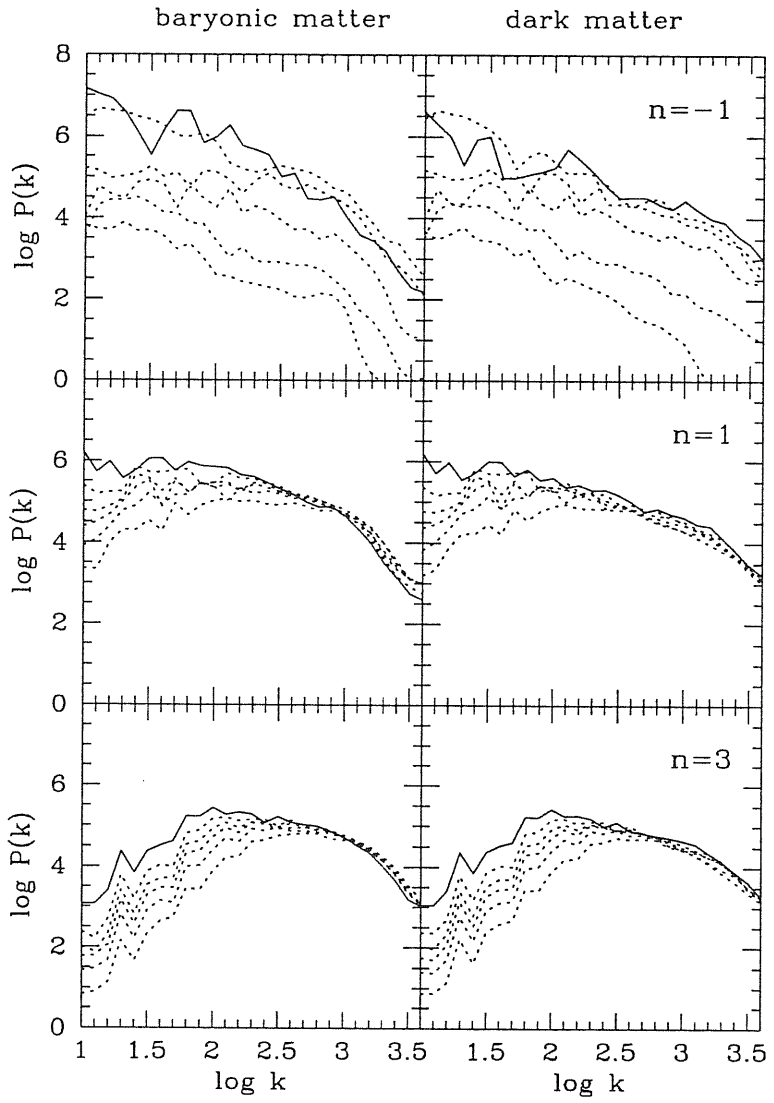

Figure 6.12: The time evolution of the power–spectrum $P(k)$ for baryonic (left column) and dark matter (right column) component for the different models: $n = -1$ (top), $n = 1$ (centre) and $n = 3$ (down). The curves refer to different epochs: $a = 0.09, 0.17, 0.25, 0.33, 0.5$ (dotted lines from down to top) and $a = 1$ (solid line).

itationally driven infall of matter. In some cases this can even produce a diffusion of the central peak. Moreover shock propagation smears out small fluctuations.

The various models characterized by different initial power–spectra show many differences in the evolution and in the final distribution of the relevant physical quantities. When the small wavelengths dominate the spectra, collapse of structures occurs earlier and the distribution of the two components is more similar. Shocks are weaker than in the other models, but they have more time for expanding and at the end a large fraction of the volume is reheated. In this case, however, it is more difficult to reach temperatures as high as those seen in X–ray clusters.

Temperatures higher than 10^8 K are reached for the spectrum with $n = -1$. This is the model where the largest density contrasts are produced and, as a consequence, strong shocks can form. However structures originate later than in the other models and at the final time about 40% of the mass is still collapsing adiabatically. The existence of these cold peaks together with the presence of large underdense regions implies that, in this model, most of the volume is at very low temperature.

The different initial conditions lead also to a different evolution of the power–spectrum. In the $n = -1$ model it grows rapidly on all the scales until the non–linear phase is reached ($a(t) \sim 0.5$). In the other models the growth is much slower, in particular on small scales, where non–linearity is reached since very early evolutionary stages. In all cases we notice that, at the final time, because of the expansion of shocks, the baryonic small–scale power decreases with respect to $a = 0.5$. Moreover a self–similar evolution of the power–spectrum seems to be excluded for both components, with the only exception of the DM in the case $n = 3$ and at large scales ($k < 100$).

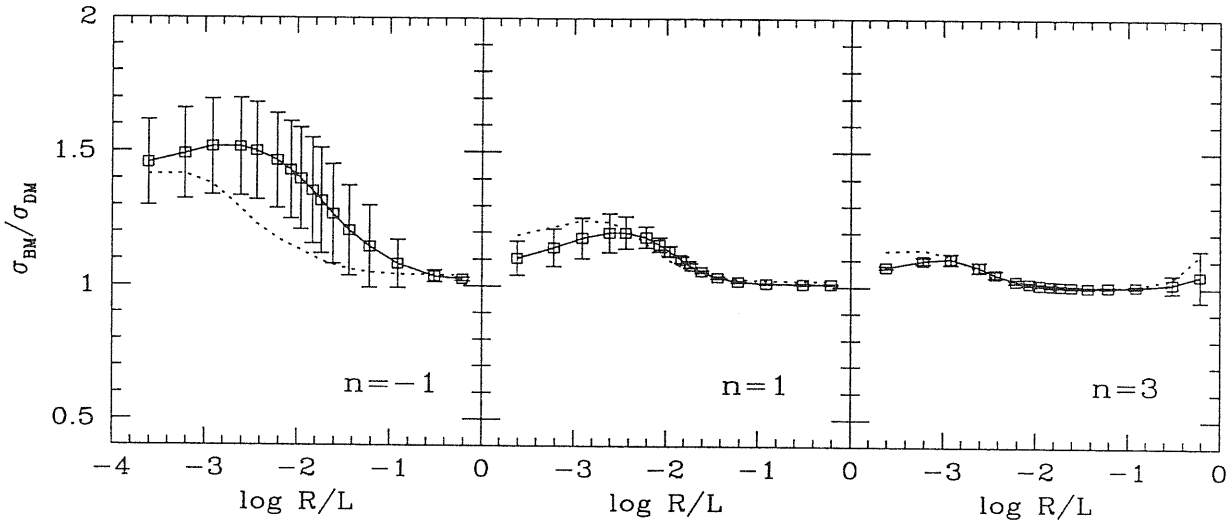

Figure 6.13: The relative bias $b \equiv \sigma_{BM}/\sigma_{DM}$ as a function of the filtering scale R (in units of the whole grid L) at $a = 0.5$ (dotted line) and $a = 1$ (solid line) for the different models: $n = -1$ (left), $n = 1$ (centre) and $n = 3$ (right). Error bars (displayed for clarity only at $a = 1$) represent the r.m.s. scatter between the different simulations.

7 Cluster of Galaxies

Galaxy clusters are the most extended gravitationally bound systems of the Universe. In spite of their size, they are simple objects: their dynamics is governed essentially by the balance between gravitational and pressure forces, controlled by shock heating and adiabatic compression. Other processes, like radiative cooling in cluster cores or population III stars heating, may play a significant role only in some aspects of their history. The evolution and present day properties of clusters are very sensitive to the fundamental cosmological parameters and to the initial power spectrum. Therefore they provide an ideal tool to study the formation of the structures of the universe. Analytic techniques, as the Press-Schechter (1974) formalism, and numerical simulations, based on the Zel'dovich (1970) approximation or on more accurate N-body codes, have been extensively used to put strong constraints on the cosmological scenarios by comparing the model predictions to the observed abundances and clustering properties (see e.g. Borgani *et al.* 1997 and references therein). Further constraints can be obtained by the X–ray observations of galaxy clusters, which have been recently greatly improved, and their comparison with the results of hydrodynamical numerical simulations.

This chapter is intended to give an overview of the fundamental properties of galaxy clusters, introductive to the analysis that will be developed in chapter 8. For an exhaustive review of these subjects we refer to Sarazin (1988).

7.1 Optical Properties of Galaxy Clusters

Optically, galaxy clusters appear as large concentration of galaxies in a small volume of radius of about 1 Mpc. A first classification of clusters is based on their *richness* that is a measure of the number of galaxies associated to the cluster. Abell (1958) has defined the richness as the number of galaxies within two magnitudes of the third brightest galaxy in the cluster which are contained within a cylinder of radius $R_A = 1.5h^{-1}$ Mpc centered on the cluster itself. Clusters are also classified according to their morphological characteristic and goes from regular to irregular systems. The former present a smooth galaxy distribution with a concentrated core and appear to be dynamically more evolved and relaxed than the latter.

The velocity distribution of cluster galaxies is conventionally described by the dispersion σ_r of radial velocities about the mean

$$\sigma_r = \langle (v_r - \langle v_r \rangle)^2 \rangle^{1/2} , \tag{7.1}$$

where v_r is the radial velocity, which is the component of galaxy velocity along the line of sight. The dispersion completely characterize the radial velocity distribution if this is Gaussian

$$f(v_r)dv_r \propto \exp(-(v_r - \langle v_r \rangle)^2/2\sigma^2)dv_r , \tag{7.2}$$

where $f(v_r)dv_r$ is the probability that a galaxy has radial velocity between v_r and $v_r + dv_r$. The Gaussian distribution is obtained for a system of objects in thermodynamical equilibrium and is a consistent fit to the observed distribution function for a number of clusters. However, in many clusters the velocity dispersion generally decreases with the distance from the centre. Furthermore, the velocity dispersion can vary substantially in the different clumps of an irregular cluster. These results suggest that galaxy clusters are at least partially relaxed system but not fully relaxed to thermodynamic equilibrium.

Several models have been proposed to describe the spatial distribution of galaxies in a cluster. Among the simplest there are the isothermal models, for which a Gaussian radial velocity distribution can be assumed. If we also assume that the velocity distribution is

isotropic and independent from position, that the galaxy distribution is stationary and that the galaxy positions are uncorrelated, the galaxy phase space density $f(\mathbf{r}, \mathbf{v})$ becomes:

$$f(\mathbf{r}, \mathbf{v}) = n(r)(2\pi\sigma_r^2)^{-3/2} \exp\left[-\frac{1}{2}\left(\frac{v}{\sigma_r}\right)^2\right] , \tag{7.3}$$

where $n(r)$ is the spatial number density of galaxies at a distance r from the cluster centre. King (1962) has shown that the following function is a reasonable approximation to the inner portions of an isothermal distribution:

$$n(r) \propto [1 + (r/R_c)^2]^{-3/2} , \tag{7.4}$$

where $R_c \sim 0.50h^{-1}$ Mpc is the typical core radius.

7.2 X–ray Properties of Galaxy Clusters

Clusters are strong X–ray emitters. The emission is mainly due to hot and diffuse intra–cluster gas whose mass accounts for several time that of the stars ($M_{gas} \sim 5 - 7M_{star}$). The gas is at a temperature $T_X \sim 10^7$–10^8 K, has a typical central density of $n_X(0) \sim 10^{-3}\text{cm}^{-3}$, and radiates by thermal bremsstrahlung emission.

For very hot gas the X–ray spectrum of galaxy clusters is dominated by the continuum and the only detected strong feature is the emission line due to highly ionized iron. This is actually a blend of lines from Fe^{+24} and Fe^{+25} and weaker lines from nickel ions. These lines are mainly at photon energy between 6.5 and 7 keV and show that the intracluster medium contains at least a significant portion of processed gas. This fact is also confirmed by the detection at lower temperatures of some heavy elements emission lines (O, Si, S, Ar, Ca). The heavy elements have been processed in the cluster galaxies and ejected into the intercluster medium through supernova driven winds or outflows.

In the approximation that the hot emitting gas has primordial composition, $X = 0.76$, $Y = 0.24$, and assuming complete ionization, the emissivity due to thermal bremsstrahlung is (Spitzer 1978; Rybicky & Lightman 1979):

$$\epsilon_\nu = 6.83 \times 10^{-38} Z^2 n_e n_i T^{1/2} \times$$

$$g(\nu, T, Z)\, e^{-h\nu/kT} \text{erg s}^{-1} \text{ cm}^{-3} \text{ Hz}^{-1} , \tag{7.5}$$

where $g(\nu, T, Z)$ is the Gaunt factor which corrects for quantum mechanical and distant collisions effects and is a slowly varying function of frequency and temperature (Karzas & Latter 1981; Kellog 1975), Z is the charge number, n_i and n_e are the ion and the electron density, respectively. If the intracluster gas is all at a single temperature, then equation (7.5) indicates that the X–ray spectrum should be close to an exponential of the frequency. The observed X–ray spectra are generally fitted fairly well by this equation (Sarazin 1988), with gas temperatures between 2×10^7 and 10^8K.

Assuming that the gas, responding to the same gravitational potential as the cluster galaxies, has a temperature such that the typical atomic velocity is close to the velocity of galaxies, we have that

$$\frac{K_B T}{\mu m_p} \sim \sigma_r^2 . \tag{7.6}$$

Thus

$$T \sim 7 \times 10^7 \left(\frac{\sigma_r}{1000\text{km/s}} \right)^2 \text{K} , \tag{7.7}$$

which is in good agreement with the spectral determination.

The bolometric emissivity of the intracluster gas, using a unit Gaunt factor, is equal to

$$\begin{aligned} \epsilon_{bol} &= \int_0^\infty d\nu \epsilon_\nu \\ &= 1.42 \times 10^{-27} Z^2 n_i n_e T^{1/2} \text{erg s}^{-1} \text{ cm}^{-3} . \end{aligned} \tag{7.8}$$

Then the energy radiated within a given energy band E_1 - E_2 can be expressed as

$$\epsilon_{band} = f_{band}(T) \epsilon_{bol}, \tag{7.9}$$

where

$$f_{band} = \int_{E_1/kT}^{E_2/kT} d\eta \bar{g}(\eta) e^{-\eta}. \tag{7.10}$$

The band limited X-ray emission L_x from a given volume is computed integrating the previous expression over the relevant volume V.

$$L_x = 1.25 \times 10^{-27} m_p^{-2} \int_V \varrho_{BM}^2 T^{1/2} f_{band}(T)\, dV \text{ erg s}^{-1} . \tag{7.11}$$

7.3 Cluster Mass

The mass of a cluster of galaxies and its distribution inside it, give many fundamental information about the properties of this system. Several techniques have been developed in order to estimate these quantities. The most straightforward assumes that all the matter is luminous and condensed in the cluster galaxies. Thus the total mass of the cluster is calculated by simply summing the contribution of each element.

A more general technique is based on the assumption that clusters are bound self–gravitating systems. This assumption is reasonable since, if they were not gravitationally bound, they would disperse rather quickly ($\sim 10^9$ years). A first limit on the cluster mass can be obtained by the binding condition:

$$E = T + W < 0 \tag{7.12}$$

where E, T and W are the total, kinetic and gravitational energy of the cluster respectively:

$$T = \frac{1}{2}\sum_i m_i v_i^2 , \tag{7.13}$$

$$W = -\frac{1}{2}\sum_{i\neq j} \frac{G m_i m_j}{r_{ij}} , \tag{7.14}$$

where the sum is over all the particles in a cluster, m_i are the particles mass, v_i their velocity and r_{ij} is the separation between the particles i and j. A more stringent mass limit results assuming a stationary configuration. In this case the Virial theorem gives:

$$W = -2T . \tag{7.15}$$

The total cluster mass is $M_{tot} = \sum m_i$. Defining the mass weighted velocity dispersion

$$\langle v^2 \rangle = \frac{\sum m_i v_i^2}{M_{tot}} , \tag{7.16}$$

and the gravitational radius

$$R_G = 2M_{tot}^2 \left(\sum_{i\neq j} \frac{m_i m_j}{r_{ij}} \right)^{-1} , \tag{7.17}$$

the virial theorem gives

$$M_{tot} = \frac{R_G \langle v^2 \rangle}{G}. \tag{7.18}$$

If now we assume that mass and galaxies have the same spatial distribution we can estimate R_G and $\langle v^2 \rangle$ from the galaxies data. In the further assumption that the positions and the orientation of the velocity vectors of the galaxies are uncorrelated we have that $\langle v^2 \rangle = 3\sigma_r^2$, where σ_r is the mass weighted radial velocity dispersion, and

$$R_G = \pi M_{tot}^2 \left(\sum_{i \neq j} \frac{m_i m_j}{b_{ij}} \right)^{-1}, \tag{7.19}$$

where b_{ij} is the projected separation of two galaxies i and j. Typical determinations of these parameters for rich clusters give $\sigma_r^2 \sim 1000$ Km/s and $R_G \sim 1$ Mpc.

The resulting cluster mass estimate is

$$M_{tot} = 7.0 \times 10^{14} M_\odot \left(\frac{\sigma_r}{1000 \text{ km/s}} \right)^2 \left(\frac{R_G}{\text{Mpc}} \right) \sim 10^{15} M_\odot . \tag{7.20}$$

The mass calculation obtained by the virial theorem give masses much larger than those determined by summing the contributions of the various galaxies. This is clear when these estimates are compared with the corresponding total visual luminosity. Usually this comparison is quantified calculating the *mass to light* ratio of a system in solar units. We typically obtain that $M/L \sim 300 h M_\odot / L_\odot$. The mass to light ratio found for luminous portions of galaxies corresponds to $M/L \sim (1 - 12) h M_\odot / L_\odot$. Therefore, at most the 10% of the mass in clusters can be accounted for by material within the luminous portion of galaxies. Even considering the intracluster gas, this is not sufficient to explain these mass estimates. Then a large part of the cluster mass must be "dark". This is the so called *missing mass* problem and has been one of the first and strongest evidences of the presence in the universe of a dark collisionless component, which could dominate the total energy density.

The virial theorem mass estimates are based on the critical assumption that mass and galaxies have the same distribution and the same kinematical properties. This in general might not be true and the estimates could be seriously affected by this bias. Furthermore

the estimates can be contaminated by several other problems related to the presence of substructure inside the cluster, to the effects of projections, to contamination by background and foreground galaxies and to anisotropies in velocity distribution of galaxies.

A different mass estimate method is based on the observations of the intracluster X–ray emitting gas. In general the elastic collision times for ions and electrons in the intracluster gas are much shorter than the time scale for heating and cooling or for any dynamical process and the gas can be treated as a fluid. Furthermore the time required for a sound wave to cross the cluster, $\sim 6 \times 10^8$ years, is short with respect to the age of the cluster (10^{10}) years. Thus the gas can be considered in hydrostatic equilibrium, that is

$$\nabla p = -\varrho_g \nabla \Phi \,, \tag{7.21}$$

where p and ϱ_g are the pressure and the density of the gas. If we approximate the cluster as being spherically symmetric, equation (7.21) can be written as

$$\frac{1}{\varrho_g}\frac{dP}{dr} = -\frac{d\Phi}{dr} \,. \tag{7.22}$$

From equation (7.22) we obtain

$$M(r) = -\frac{K_B T_g(r)}{G\mu m_p}\left[\frac{d\log \varrho_g(r)}{d\log r} + \frac{d\log T_g(r)}{d\log r}\right] \,, \tag{7.23}$$

where $T_g(r)$ and $\varrho_g(r)$ are the gas radial density profiles. This method of estimating the cluster mass has several advantages with respect to the virial theorem determination (or any other method which uses galaxies as reference objects). First, the gas is a collisional fluid and the particle velocities are isotropically distributed. Cluster galaxies, instead, are collisionless and uncertainties in the velocity anisotropy can significantly affect mass determinations. Second, this method gives the mass as a function of the radius, rather than the total mass alone. Third, the statistical accuracy of this method is not limited by the number of galaxies in the cluster. Finally, there is no contamination problem. On the other hand this method requires the knowledge of the radial profiles of density and temperature, which are very difficult to determine observationally and must be properly modeled.

The simplest distribution of gas temperature is the *isothermal* distribution with constant temperature T_g. The gas can be isothermal if thermal conduction is sufficiently rapid or if the gas is introduced in the cluster with a uniform temperature and this remains unchanged since that time. In this case equation (7.22) can be written as:

$$\frac{d\ln\varrho_g}{dr} = -\frac{\mu m_p}{K_B T_g}\frac{d\Phi}{dr} . \tag{7.24}$$

Assuming a gravitational potential described by the King's isothermal spherical model, the resulting density distribution is (Cavaliere & Fusco Femiano, 1976)

$$\varrho_g(r) = \varrho_g(0)[1+(r/R_c)^2]^{-3\beta/2} \tag{7.25}$$

where R_c is the core radius and

$$\beta = \frac{\sigma_r^2 \mu m_p}{K_B T_g} = 0.76\left(\frac{\sigma_r}{10^3\mathrm{km/s}}\right)^2\left(\frac{T_g}{10^8\mathrm{K}}\right) , \tag{7.26}$$

where $\mu = 0.63$ is fixed assuming solar abundances. The parameter β measures the ratio between the specific kinetic energy of galaxies and the specific thermal energy of particles in the gas.

This model has the advantage of giving an analytic gas distribution and analytic distribution functions of associated quantities which can be directly compared to the observations. For example we can derive the X–ray surface brightness as a function of the projected radius b as

$$S(r) = S_0[1+(b/R_c)^2]^{-3\beta+1/2} . \tag{7.27}$$

The average value of β determined by fits of X–ray surface brightness of a large number of clusters was found to be (Jones & Forman 1982):

$$\langle\beta_{fit}\rangle \sim 0.65. \tag{7.28}$$

Thus the gas density varies on average as

$$\varrho_g(r) \propto [1+(r/R_c)^2]^{-1} \tag{7.29}$$

According to this estimate of β, the gas density fall off less rapidly with radius than galaxy density: thus, the gas distribution is expected to be more extended than that of galaxies which are concentrated in the inner parts of the cluster.

The value of β can be calculated also by equation (7.26), using the X–ray spectral temperatures and the galaxy velocity dispersions of clusters. This kind of estimates give on average

$$\langle \beta_{spec} \rangle \sim 1.2 \sim 2\langle \beta_{fit} \rangle . \tag{7.30}$$

A number of suggestions have been made as the origin of this β *discrepancy.* First the gas may not be isothermal. However it has been shown (Mushotzky 1984) that the same problem occurs also for other thermal distributions. Second, it may be that σ_r does not represent accurately the energy per unit mass of the galaxies. This could be due to anisotropies in the galaxy velocity distribution. Detailed studies (see Kent & Sargent 1983) have shown that a more accurate description of the velocity field reduces the discrepancy, even though it still remains significant. Third, there could be contamination effects of background galaxies, which could affect the cluster galaxy velocity dispersion. This could be affected also by subclustering or non–virialization of the cluster. All of these effects could lead to overestimate the actual velocity dispersion and thus to overestimate β_{spect}. Finally, as pointed out by Navarro Frenk & White (1995), also complex non linear events, like the merging process between different structures, can lead to a high determination of the value of β_{spect}.

If the gas distribution cannot be considered isothermal, but the gas is well–mixed, then the entropy per atom in the gas is constant. In this case the pressure and the density are related by the equation $p \propto \varrho^\gamma$, where $\gamma = 5/3$ for a monoatomic ideal gas. While this value holds for a gas strictly adiabatic, the previous equation is usually used to parametrize the thermal distribution of the intracluster gas, with γ being a proper fitting parameter. These kind of models are called *polytropic.* If $\gamma > 5/3$ the system is convectively unstable. Thus hydrostatic polytropic models must have $1 \leq \gamma \leq 5/3$, the lower limit representing the isothermal distribution. The temperature and the density are then related by

$$\frac{\varrho_g}{\varrho_{g0}} = \left(\frac{T_g}{T_{g0}}\right)^{1/\gamma - 1} , \tag{7.31}$$

where ϱ_{g0} and T_{g0} are the central values of the density and temperature respectively. Observing that

$$\frac{\nabla p}{\varrho_g} = \frac{\gamma}{\gamma - 1}\frac{K_B}{\mu m_p}\nabla T_g \,, \tag{7.32}$$

then the hydrostatic equilibrium condition (7.22) can be rewritten as

$$\frac{\gamma}{\gamma - 1}\frac{K_B}{\mu m_p}\nabla T_g = -\nabla\phi \tag{7.33}$$

so that

$$\frac{T_g}{T_{g0}} = 1 + (\alpha - 1)\left[1 - \frac{\phi(\mathbf{r})}{\phi_0}\right] \,, \tag{7.34}$$

where ϕ_0 is the central value of the gravitational potential. In equation 5.34 T_{g0} and ϕ_0 are related by

$$T_{g0} = \frac{(\gamma - 1)}{\gamma}\frac{\mu m_p \phi_0}{K_B(1 - \alpha)} \,, \tag{7.35}$$

α being an appropriate constant.

The gravitational potential, assuming spherical symmetry, can be again modeled by the King's approximation and the density and the temperature can be obtained as analytic functions of the radius. However in this case the two functions are complex enough that no other derived quantities are analytic, as instead happens for the isothermal model.

More general and complex methods to determine cluster masses based on the X–ray properties of the intracluster gas have been developed by various authors. For an wide review we refer to Sarazin (1988).

The last mass estimate method that we here describe is based on *gravitational lensing*. This method present many advantages over the X–ray mass estimate, first that it does not require any assumption on the mass distribution or on the dynamical state of the cluster. The lensing effect can be divided into two main regimes depending on the lens configuration. The *strong lensing* regime corresponds to a large magnification and strong distortion of the light coming from distant galaxies by foreground clusters. The *weak lensing* regime produces only one image which experiences only a weak distortion of its shape. The intermediate case is known as *arclet* regime. The strong lensing regime constrains the mass enclosed

within the "Einstein radius" r_E defined by equation (7.36), while weak lensing determines the distribution of mass in the outer regions.

The simplest example of gravitational lensing mass estimate is that in which we have strong lensing due to a spherical symmetric lensing cluster, with the system observer–lens–source aligned along the line of sight. In this case the lens mass is given by

$$M = \pi r_E^2 \Sigma_c \,, \tag{7.36}$$

where

$$\Sigma_c = \frac{c^2}{4\pi G} \frac{d_s}{d_l d_{ls}} \,, \tag{7.37}$$

d_s, d_l and d_{ls} being the distance to the source, the distance to the lens and the distance between the lens and the source, respectively.

The main drawback of the lensing method is that it requires an accurate determination of the redshift of distant objects which is generally difficult to obtain. This can introduce large uncertainties in the mass estimate.

The comparison between the determinations of clusters mass obtained with different methods shows a systematic discrepancy between the gravitational lenses and the X–ray estimates (Fahlman *et al.*, 1994; Miralda-Escudé & Babul, 1995), the latter being generally lower than the former. The gravitational lenses estimates are instead in good agreement with the virial calculations.

A common result of all the different methods of calculating the cluster mass is that a major fraction of it is in the form of dark collisionless matter. Numerical simulations like those of Evrard (1990) and Navarro, Frenk & White (1995) have allowed the comparison between the intracluster gas and the dark matter distributions. In both works the cosmological framework is that of a flat, CDM dominated universe with a baryonic fraction $\Omega_{BM} = 0.1$. The results show that the dark matter and the gas density profiles are very similar. However the intracluster gas is more extended than the dark matter and inside the cluster radius the gas fraction is always less than its cosmological average value. This segregation between dark matter and gas is due to the different behaviour of the two components in the merging process. Shocks prevent colliding gas to interpenetrate, with a net

transfer of energy and angular momentum from the dark matter to the gas. Dark matter can then reach a more concentrated stable configuration. As a result, the gas density in the core is found to be only about 0.07 times that of the dark matter, whereas a value of 0.11 would be expected if the two distributions were identical.

David, Jones & Forman (1995) have performed an analysis of the distribution of the various components of galaxy clusters based on the *ROSAT* data. The X–ray emitting gas comes out to be the most extended mass component in clusters, the galaxies are the most centrally concentrated and the dark matter is intermediate between the two. However the estimated gas mass fractions is much higher than that found with numerical simulations: about 15–30% of the total mass. This determination is in agreement with several other studies (White *et al.*, 1993; Briel, Henry & Boehringer, 1992; White & Fabian, 1995; Elbaz, Arnaud & Boehringer 1995; Markevitch *et al.* 1996) which suggest that the baryon fraction could be much higher than the standard value predicted by the cosmological nucleosynthesis model. If we assume that dark matter is distributed similarly to the X–ray gas and take the estimate of the cluster mean baryonic fraction obtained by the collection of data of White & Fabian (1995), we have

$$\frac{\Omega_{BM}}{\Omega_0} = 0.14^{+0.08}_{-0.04}(h/0.5)^{-3/2}\,, \tag{7.38}$$

which, for a $\Omega_0 = 1$, $h = 0.5$ model, is incompatible with the nucleosynthesis estimates. This is known as the *baryon catastrophe.*

There are various ways out of this problem. The most obvious are either that Ω_0 is less than one (as in a open model or in flat Λ model), or that $h < 0.4$, but such value of the Hubble constant is lower than that commonly accepted. Another possibility is that the X–ray gas is more concentrated than the dark matter, but the mechanisms that could drive this process is not obvious. White *et al.* (1993) have shown that gravitational and dissipative effects cannot account for such baryon overdensity. On the other hand, cooling flows, which could lead to high baryon condensations, act only in the most inner parts of the clusters. A different solution is that the gas density has been overestimated. This could be reasonable if the gas were highly clumped as the X–ray luminosity per unit mass

would then increase. However no model has been proposed yet to explain such a clumpy configuration of the gas. A further possibility is that the total mass of the cluster has been underestimated. This solution seems to be strengthened from the recent estimates of the cluster masses via gravitational lensing (Miralda Escudé & Babul, 1995; Wu & Fang, 1996) which are systematically higher than the corresponding estimates obtained by the X–ray analysis.

A final solution is that the estimates of the standard nucleosynthesis model are not correct. This possibility will be discussed in the next chapter.

7.4 X–ray Luminosity and Temperature Functions

The properties of galaxy clusters give many information about the nature of the mechanisms responsible for the formation of the large–scale structure of the universe. Particularly significant is the study of the *abundance*, i.e. the comoving number density of clusters as a function of their X–ray luminosity and temperature. Furthermore, it is interesting to analyze the clusters *X–ray luminosity–temperature* function, which describes the relation between these two quantities.

The abundances are extremely sensitive to the fundamental cosmological parameters. In fact, according to the gravitational instability scenario, galaxy clusters form where the density contrast δ is sufficiently large that the related matter separates from the Hubble expansion and collapse. Therefore the abundance of collapsed objects depends on the amplitude of the density perturbations, that is statistically related to the power spectrum $P(k)$. Since the amplitude decreases with increasing scale, the density contrast required to form large objects, such as galaxy clusters, is a rare event on the tail of the statistical distribution. Then small changes in $P(k)$ leads to large differences in the cluster abundances. Furthermore the rate of cluster evolution is governed by the density parameter Ω and the X–ray luminosity depends strongly on the baryon fraction Ω_{BM}.

Schechter (1976) proposed the following analytic approximation for the differential lu-

minosity function

$$n(L)dL = n_0 \left(\frac{L}{L_*}\right)^{-\alpha} e^{-L/L_*} d(L/L_*) , \tag{7.39}$$

where $n(L)$ is the comoving number density of clusters with luminosity between L and $L + dL$. There are various works concerning the estimate of the luminosity function based on various sample of observational data.

We can mention those of Edge *et al.*(1990) and Henry & Arnaud (1991), based essentially on the data of the *Einstein Observatory* and of *EXOSAT*. The same catalogues has been used also by David *et al.* (1993). It is interesting to notice that both of Edge *et al.* and David *et al.* find evidences of a negative evolution of the luminosity function in the considered redshift ranges, which are $0 \leq z \leq 0.181$ for the former, $0 \leq z \leq 0.28$ for the latter. This means that the comoving number of bright X–ray clusters tend to decrease as we go toward larger z.

More recent works are based on the *ROSAT* survey. Burns *et al.* (1996) have presented a luminosity function for an optically selected sample of 49 poor clusters in the range $0.01 \leq z \leq 0.03$ and a sample of 67 rich clusters with $z \leq 0.15$ in the energy band 0.5–2 keV. The X–ray luminosity range covered by their luminosity function is extended by a factor of 10 with respect to previous determination. The data set of De Grandi (1996) is composed of clusters of galaxies in the southern galactic cap region in the band 0.5–2 keV. Its 111 objects have redshifts $0.02 < z < 0.2$. Finally we have the work of Ebeling *et al.* (1997), who discuss the luminosity function of the *ROSAT* Brightest Cluster Sample (BCS), an X-ray sample of clusters in the northern hemisphere. The sample accounts for the 199 X–ray brightest clusters in the northern hemisphere. The clusters are selected only for their X–ray (and not optical) properties. The luminosity function is estimated in five energy bands ranging from 0.1 to 10 keV. The redshift of the clusters are within $z = 0.3$. Notice that Ebeling *et al.* do not find any significant variation of the luminosity function with redshift. This last work proposes the values for the parameters of the luminosity function in several energy bands. These estimates are shown in Table 7.1. In the table $A = n_0 L_*^{\alpha-1}$ is in units of 10^{-7}Mpc $^{-3}(10^{44}$erg s$^{-1})^{\alpha-1}$, L_* is in units of 10^{44}erg s^{-1}, n_0 and

Table 7.1: Best fit values of the Schechter X–ray luminosity function by Ebeling *et al.*(1997)

Energy band	A	L_*	α
0.1-2.4 keV	$5.06^{+0.50}_{-0.46}$	$9.10^{+2.06}_{-1.49}$	$1.85^{+0.09}_{-0.09}$
0.5-2.0 keV	$3.32^{+0.36}_{-0.33}$	$5.70^{+1.29}_{-0.93}$	$1.85^{+0.09}_{-0.09}$
0.3-3.5 keV	$4.95^{+0.48}_{-0.45}$	$10.7^{+2.4}_{-1.8}$	$1.82^{+0.08}_{-0.09}$
2-10 keV	$2.35^{+0.22}_{-0.18}$	$12.6^{+2.2}_{-1.8}$	$1.54^{+0.05}_{-0.06}$
Bolometric	$6.41^{+0.70}_{-0.61}$	$37.2^{+16.4}_{-3.8}$	$1.84^{+0.09}_{-0.04}$

the errors are at 1σ confidence level.

The comoving number of objects in the temperature interval between T and $T + dT$ has been fitted by a power–law of the form

$$n(T)dT = AT^{-\alpha}\mathrm{Mpc}^{-3}\mathrm{keV}^{-1} . \tag{7.40}$$

Observational estimates of the temperature function has been calculated by Edge *et al.* (1990) and Henry & Arnaud (1991). The data are those used to calculate also the luminosity function. Edge *et al.* found $A = 10^{-3.96\pm0.26}$ and $\alpha = 4.93 \pm 0.37$, while Henry & Arnaud estimated $A = 10^{-2.75\pm0.15}$ and $\alpha = 4.7 \pm 0.5$.

The luminosity–temperature (hereafter L–T) relation gives basic information about the link between the physics of the baryon component and the dynamical properties of the dark matter condensations. In fact the X–ray temperature of a cluster of galaxies is a measure of the depth of the potential well as determined by the total mass distribution of the cluster. On the other hand the X–ray luminosity is very sensitive to the density of the hot emitting baryonic gas.

The L–T relation is usually fitted by a power–law $K_B T = 10^b L_{44}^{\eta}$, where L_{44} is the bolometric X–ray luminosity in units of 10^{44}erg s^{-1}. Henry & Arnaud (1991) have obtained for the two parameters the values $b = 0.62 \pm 0.09$ and $\eta = 0.265 \pm 0.035$, while David *et al.*(1993) have found $b = 0.72 \pm 0.02$ and $\eta = 0.297 \pm 0.004$. The most recent analysis is that

of Mushotzky & Sharf (1997) who have collected data of 38 clusters from the ASCA archive in the redshift range $0.14 \leq z \leq 0.55$. The L–T relation obtained from these data has been compared with that calculated using the low–redshift sample of David *et al.* finding no evidence for evolution. Therefore, at least for $z < 0.5$ the observational estimates of the L–T relation give

$$T \propto L^{0.28-0.37} . \tag{7.41}$$

8 CDM Models with High Baryon Content

For a long period the CDM scenario has been the reference model for the interpretation of the observational data on the large scale structure of the universe. Its standard version (SCDM) assumes a flat universe with a density parameter $\Omega_0 = 1$, a Hubble constant $h = 0.5$, a baryon contribution to the density Ω_{BM} fixed by the standard theory of Big Bang nucleosynthesis, and primordial fluctuations with Gaussian distribution and power spectrum $P(k) \propto k^n$, with $n = 1$. However, the normalization implied by the COBE detection of the microwave anisotropies (Smoot *et al.* 1992; see also Bennett *et al.* 1996) changed the situation, giving a spectrum with too much power on scales smaller than 10 h^{-1} Mpc. As a consequence, the SCDM model is not able to reproduce both the clustering properties of galaxies and the distribution and abundances of clusters.

In order to solve the problems, many alternatives have been proposed and discussed: the short–scale power can be reduced by assuming that a component of the dark matter, about the 20% of the total density, is hot (Shafi & Stecker 1984; Bonometto & Valdarnini 1984; Davis, Summers & Schlegel 1992; Taylor & Rowan-Robinson 1992; Jing *et al* 1994), and allowing a modest tilt in the power spectrum (Liddle & Lyth 1993; Schaefer & Shafi 1994; Pogosyan & Starobinsky 1995; Liddle *et al.* 1996b). This gives a satisfactory solution, but loses the simplicity of having only cold dark matter. A different possibility is given by CDM dominated universes but leaving critical density models, going to low matter density. Viable models of this type are possible both in open universes (Ratra & Peebles, 1994; Górski *et al.*

1995; Liddle *et al.* 1996a; Yamamoto & Bunn 1996) and in universes with a non-vanishing cosmological constant fixed such as its contribution to the density is $\Omega_\Lambda = 1 - \Omega_0$ (Peebles 1984; Turner *et al.* 1984; Kofman & Starobinsky 1985; Efstathiou, Sutherlan & Maddox 1990; Suginohara & Suto 1991; Efstathiou, Bond & White 1992; Kofman, Gnedin & Bahcall 1993; Krauss & Turner 1995; Ostriker & Steinhardt 1995; Stompor, Górski & Banday 1995; Liddle *et al.* 1996c)

If one wants to retain the CDM hypothesis, some modifications to the standard model are required. Two have received particular attention. The first is to reduce the value of the Hubble parameter (Bartlett *et al.* 1995). This leads to a power spectrum with less power on the cluster scales, hence to a lower cluster number density. However, in order to get the correct cluster abundance it seems necessary to reduce h to about 0.35 (Liddle *et al.* 1996b), which is lower than the currently accepted estimates of the Hubble parameter. The second is to *tilt* the initial spectrum, that is to choose a spectral index less than unity. This has the problem that if one tilts the spectrum sufficiently to remove the unwanted short–scale power, then the resulting spectrum of the microwave background anisotropies is not compatible with observations (White *et al.* 1995b, White 1996). These, in fact, implies the existence of a peak in the microwave spectrum at sub–degree scales. The required tilt would suppress this spectral feature. The situation improve somewhat if one combines a smaller tilt with a more modest reduction in h, but again this seems not to be enough to obtain the "correct" results.

White *et al.*(1996) have suggested that also an increase of the baryon content Ω_{BM} can produce critical-density CDM models which fit the observational data in a reasonable way. In the past, the mean baryon density has been considered as a fixed quantity for most of cosmological models, in agreement with the predictions of the standard theory of cosmological nucleosinthesis based on local estimates of light elements abundances.

The standard Big Bang nucleosinthesis model predicts the production of four light isotopes, deuterium, ^{3}He, ^{4}He and ^{7}Li. The abundances of these isotopes depends on the mean baryonic density of the universe. In particular, deuterium can provide strong constraint on

the value of Ω_{BM} since its production decreases rapidly with density. Later, stars can only destroy it, modifying its primordial abundance. Because of this depletion in stars the measurement of present day deuterium abundance represents a lower limit on the primeval value. Since Ω_{BM} decreases as deuterium abundance grows, this correspond to an upper limit on the baryonic abundance. The primordial abundance of deuterium can be recovered in high redshift hydrogen clouds where stellar depletion is not a concern (Adams, 1976). The deuterium Lyman–α line from clouds backlit by distant quasar lead to a measurement of the baryon density to an accuracy of about the 15 %. Songalia *et al.*(1994) and Carswell *et al.*(1994), Rugers & Hogan (1996a,b) and Songaila, Wampler & Cowie (1997) have detected high values of deuterium abundance which indicates values of the baryon density of $(1.3 \pm 0.3) \times 10^{-31}$ which leads to a density parameter close to the range admitted from the standard nucleosynthesis model $0.010 \leq \Omega_{BM} h^2 \leq 0.015$. However, Tytler, Fan & Burles (1996) have recently proposed a series of Lyman–α estimates of deuterium abundance which imply a much higher value of the baryon density of $(4.4 \pm 0.6) \times 10^{-31}$g cm^{-3}. This would lead to $\Omega_{BM} h^2 = 0.024 \pm 0.002 \pm 0.002 \pm 0.001$, with the 1σ uncertainties being statistical, systematic and theoretical, respectively. These last results are also consistent with the lower limits obtained by Rauch *et al.*(1996) by comparing the observed flux decrement distribution function from a sample of seven high resolution QSO spectra to simulations of the Lyα forest. Similar conclusions have been reached also by Weinberg *et al.*(1997) by computing the amount of neutral hydrogen present in the high-redshift intergalactic medium necessary to produce the Lyα absorption in the QSO spectra.

Within the conventional picture, the low deuterium abundance estimates can only be made consistent with the standard nucleosinthesis model if the primordial helium abundance has been underestimate. The value $\Omega_{BM} h^2 = 0.025 - 0.035$ correspond to 25 per cent helium, rather than the usual 23–24 per cent. However, this seems to be entirely within the bound of possibilities (e.g. Olive & Steigman 1995; Burles & Tytler 1995) given several possible systematic uncertainties that could affect the standard determination of the primordial abundances as recently stressed by various authors (Wilson & Rood, 1994; Sasselov &

Goldwirth, 1995; Skillman, Terlevich & Garnet, 1995; Scully *et al.*1996). These uncertainties have broadened the range of possible values for $\Omega_{BM}h^2$, particularly towards the upper end. Recent quoted ranges, at 95% of confidence, include $0.010 < \Omega_{BM}h^2 < 0.022$ by Copi, Shramm & Turner (1995a,b), with similar results by Turner *et al.*(1996). Kernan & Sarkar quoted an upper limit $\Omega_{BM}h^2 < 0.032$, while an analysis by Krauss & Kernan (1995) has also suggested high baryon density, although without quoting a specific range. Therefore both observational results and theoretical predictions suggest that the estimate of Ω_{BM} is much more uncertain than previously thought and high value of this parameter can no more be excluded.

The other salient observational issue is related to the mass estimates of cluster of galaxies (see chapter 7). These give values of the baryon fraction hard to reconcile with a critical–density universe, unless Ω_{BM} is higher than the standard value obtained by the nucleosynthesis model.

By using a semi-analytical approach, White *et al.* have carried out a general exploration of CDM models with high Ω_{BM}, allowing also the Hubble parameter h and the spectral index n to vary. The predictions of these scenarios have been compared with the observations of the clustering properties of galaxies, the cluster abundances, the statistics of the peculiar velocities, the formation of high-redshift objects (i.e. damped Lyα systems, Lyman break galaxies, quasars and clusters) and the cosmic microwave background anisotropies. Their final suggestion is that the models with Ω_{BM} in the range [0.1–0.2], a Hubble parameter $h \approx 0.5$ and a small tilt in the primordial spectrum ($n \approx 0.8$), are in good agreement with all these data. A high baryonic fraction in fact helps "naturally" to suppress the short-scale power, as baryon collapse is stopped until decoupling, and, at the same time, amplifies the first peak of the CMB spectrum, compensating for the loss of height introduced by the tilt (needed to avoid too low values of h, excluded by the observational data). At the end of their analysis they conclude that these models can represent at the moment a viable alternative in the framework of critical-density CDM models.

These conclusions have led us to focus on the same CDM high–baryon models of White

et al. studying the results of a series of numerical simulations obtained using our PPM+PM code. In particular we have concentrated on the X–ray properties of clusters of galaxies. The clusters have been identified by selecting the peaks in the X–ray luminosity field and the resulting catalogues have been analyzed by computing the clusters mass function, luminosity function, temperature function and the luminosity–temperature relation. The prediction of the different models are compared to recent observational data and the results are presented in the following sections.

8.1 The Models

We have considered a series of CDM models with an initial spectrum of perturbations given by equations 1.59 and 1.60 fixing $h = 0.5$ and $n = 0.8$ and allowing the baryon content to vary. We consider four different values for Ω_{BM}: the usual value determined by the standard theory of BBN ($\Omega_{BM} = 0.05$); a baryon abundance consistent with the low deuterium measurements and with the more recent BBN calculations ($\Omega_{BM} = 0.1$); a value close to the estimate resulting from the cluster baryon fraction in the case of critical-density universe ($\Omega_{BM} = 0.15$); a more extreme case representing the upper limit of the range of observed cluster baryon fraction ($\Omega_{BM} = 0.2$). In the following we will label these four models as BM05, BM10, BM15 and BM20, respectively. The normalization of the spectrum, usually parameterized by σ_8, the matter rms fluctuation in a top-hat sphere of radius 8 h^{-1} Mpc, is defined by the four-year COBE data (Bunn & White 1997). The cosmological parameters used for the different models are summarized in Table 8.1 while the initial power spectra are presented in Figure 8.1. As expected from the previous discussion, the figure shows that the power at small scales (i.e. for large k) increases when Ω_{BM} decreases. Consequently we can expect a faster evolution in the models with low baryon content, with a higher production of large overdensities.

For each cosmological model we run one simulation with the initial conditions given by the same random sequence. The initial redshift, fixed in such a way that the maximum initial density fluctuation is less than unity, is approximately $z \approx 20$ for all models. The

Table 8.1: The parameters of the cosmological models. Column 2: the density parameter Ω_0; Column 3: the baryon density Ω_{BM}; Column 4: the primordial spectral index n; Column 5: the Hubble parameter h; Column 6: the shape parameter Γ; Column 7: the spectrum normalization σ_8.

Model	Ω_0	Ω_{BM}	n	h	Γ	σ_8
BM05	1.0	0.05	0.8	0.5	0.44	0.77
BM10	1.0	0.10	0.8	0.5	0.41	0.72
BM15	1.0	0.15	0.8	0.5	0.39	0.66
BM20	1.0	0.20	0.8	0.5	0.36	0.61

box-size has been fixed to 64 h^{-1} Mpc and the number of computational cells is 128^3. Consequently the nominal spatial resolution, which our numerical tests have shown to be very close to the effective one, is 0.5 h^{-1} Mpc. In the analysis of the results we have to be careful to properly evaluate the spurious effects that the limited box-size and the finite grid resolution can produce on the results. In fact the grid resolution prevents us from following the behaviour of matter inside a cell element. This can lead to underestimation of quantities like density and temperature, with a direct influence on the evolutionary history of the X-ray clusters. On the other hand, the limited size of the box has the effect of suppressing the large-scale power, reducing the possibility of forming very bright X-ray clusters with luminosity larger than 10^{45} erg s^{-1}. This kind of object is also likely to be partially missed in our simulations because it is rare: observational data (e.g. Henry & Arnaud 1991; Ebeling *et al.* 1997) show that in a box of 64 h^{-1} Mpc one expects to find at most one such object.

8.2 Cluster Identification

The first step of the data analysis consists of the identification of the X-ray clusters. We first calculate the emissivity of each cell due to thermal bremsstrahlung in a fully ionized plasma ($X = 0.76$, $Y = 0.24$) with temperature T using equation (7.11). The band limited

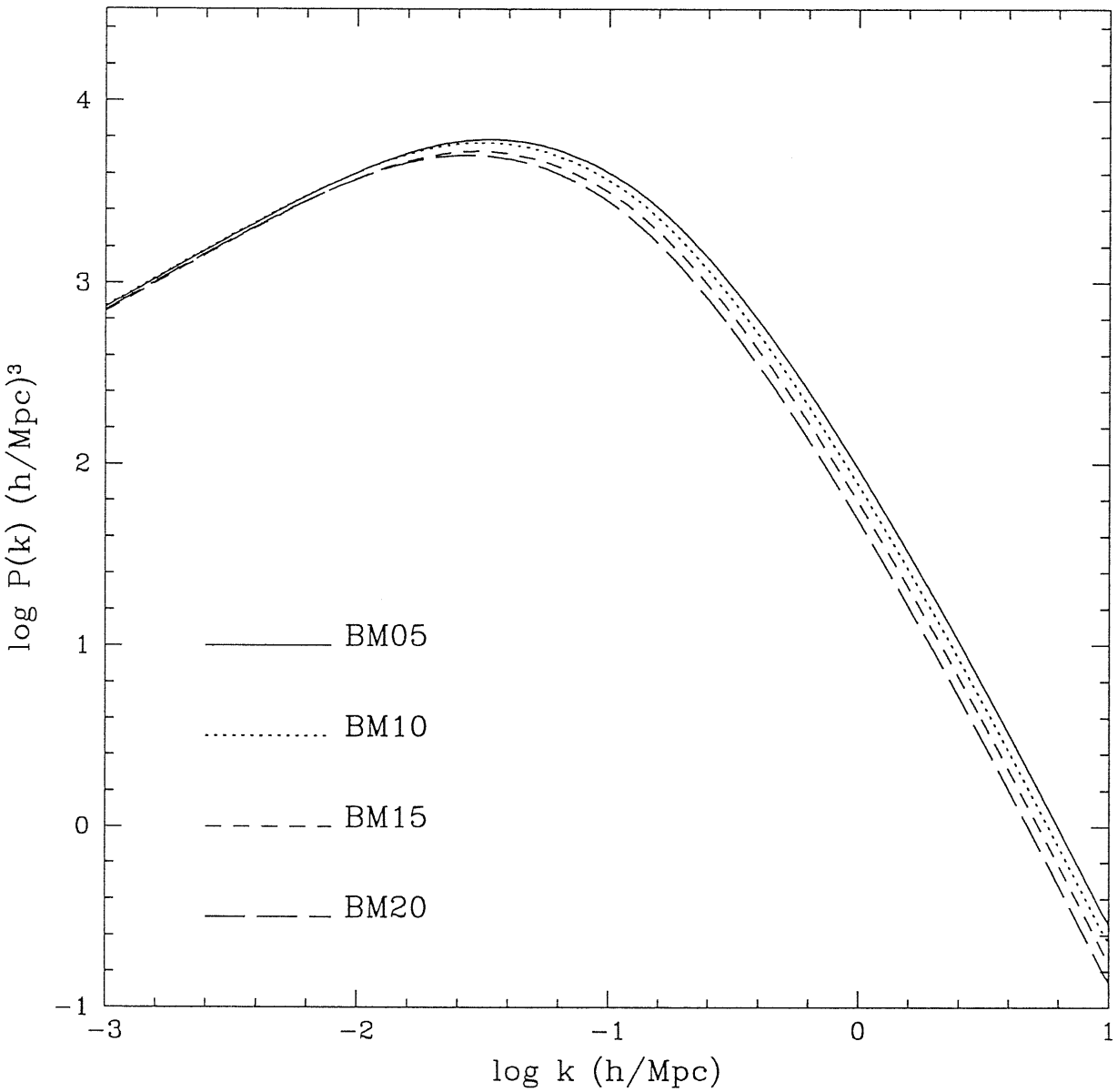

Figure 8.1: The power spectra for the four models considered in this work: BM05 (solid line), BM10 (dotted line), BM15 (short-dashed line) and BM20 (long-dashed line). All the models are normalized to the four-year COBE data. See table 1 for the adopted parameters.

X-ray emission L_x from a given volume is computed integrating the previous expression over the relevant volume. Using the discretization of the simulation, the X-ray luminosity is

$$L_x = 1.25 \times 10^{-27} m_p^{-2} \sum_i \varrho_{BM_i}^2 T_i^{1/2} f_{band}(T_i) \text{ erg s}^{-1} , \quad (8.1)$$

where the sum runs over cells within the volume.

At this point, in order to identify the clusters, we select the cells with

$L_x \geq 10^{40}$ erg s^{-1} which are also local maxima in the X-luminosity field (i.e. their X-luminosity is greater than that of the 26 neighboring cells). These identify the cluster centre. A cluster is defined as the sum of the centre plus the 26 surrounding cells. In this way the total volume of a cluster equals the volume of a sphere of comoving radius 0.93 h^{-1} Mpc, as appropriate for present observed X-ray clusters. In order to avoid double counting of the cells, the distance between cores is checked: if two cores are closer than 2 h^{-1} Mpc the fainter cluster is rejected from the catalogue. Finally, the cluster luminosity and the mass are calculated as the sum of the luminosity and density of each of its cells, respectively, while the temperature is defined as the average over the whole cluster volume.

8.3 Global Properties of the Results

In Figure 8.2–8.5, we show a snapshot of the results in a slice of $64 \times 64 \times 0.5$ h^{-3} Mpc^3 at $z = 0$ for each of the four models. The baryonic matter density field ϱ_{BM}, the dark matter density field ϱ_{DM}, the gas temperature T and the X-ray emission L_x are presented in Figures 8.2, 8.3, 8.4, 8.5, respectively. Since the initial spectrum of fluctuations of all simulations has been generated by using the same random number sequence, the positions of the final structures are quite similar and the densities of each component scale approximatively according to their mean cosmic values. Matter concentrates on filamentary structures and clusters form at the intersection of several filaments.

In the low-Ω_{BM} models, because of the larger power on small scales in the initial spectrum and the lower background pressure, shocks form earlier and are stronger than in the high-Ω_{BM} models. In the latter case, on the other hand, we can observe a stronger X-ray

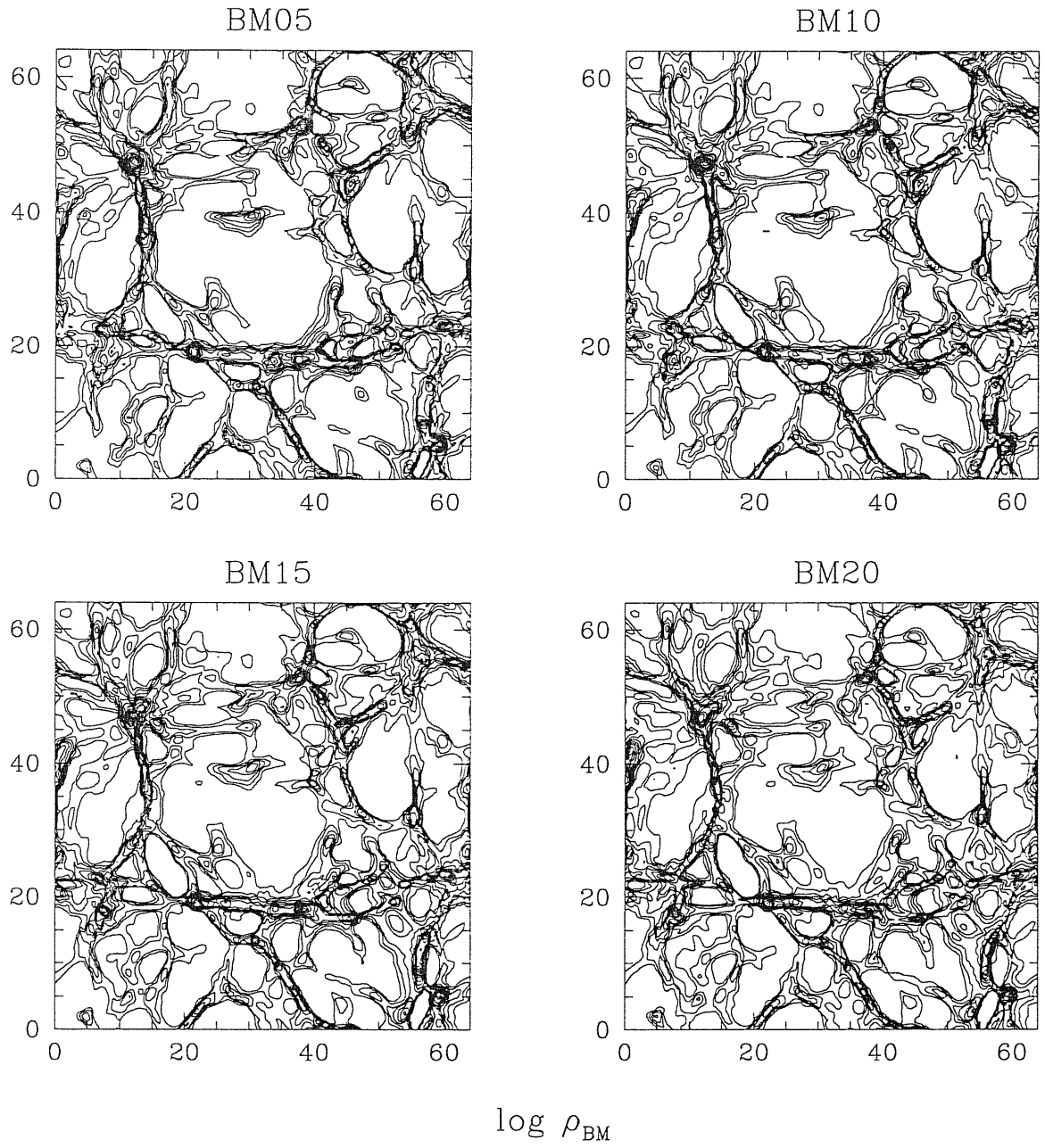

Figure 8.2: The contour plots for the baryonic density ϱ_{BM} in a slice of $64 \times 64 \times 0.5\ h^{-3}$ Mpc^3 at $z = 0$ for the four different models: BM05 (top left), BM10 (top right), BM15 (bottom left), BM20 (bottom right). The baryonic density is normalized to its mean density and the contour levels correspond to $10^{(i-3)/4}$, where $i = 1, 2, ...$

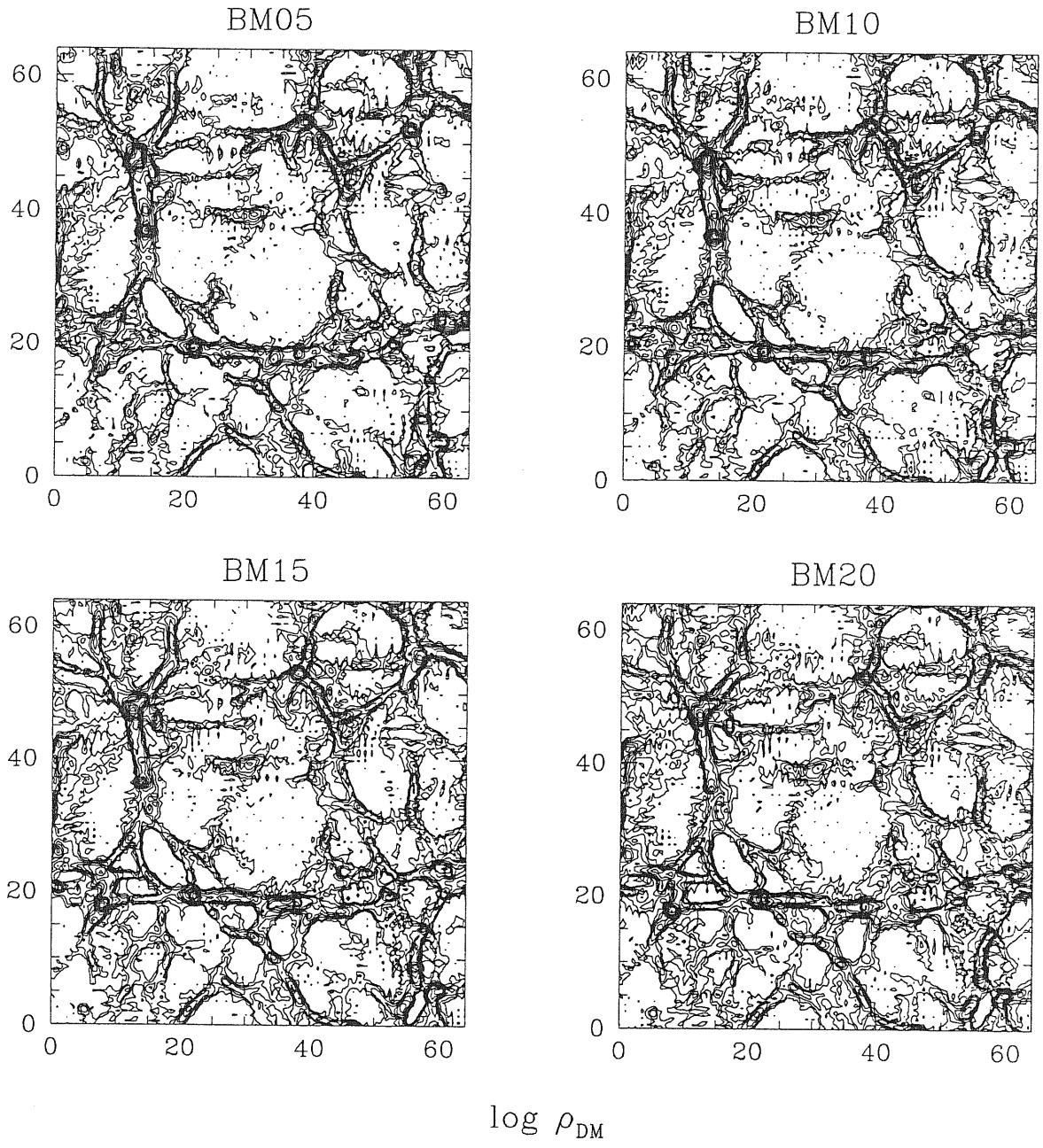

Figure 8.3: The same as Figure 8.2 but for the dark matter density ϱ_{DM} which is normalized to its mean density. The contour levels correspond to $10^{(i-3)/4}$, where $i = 1, 2, ...$

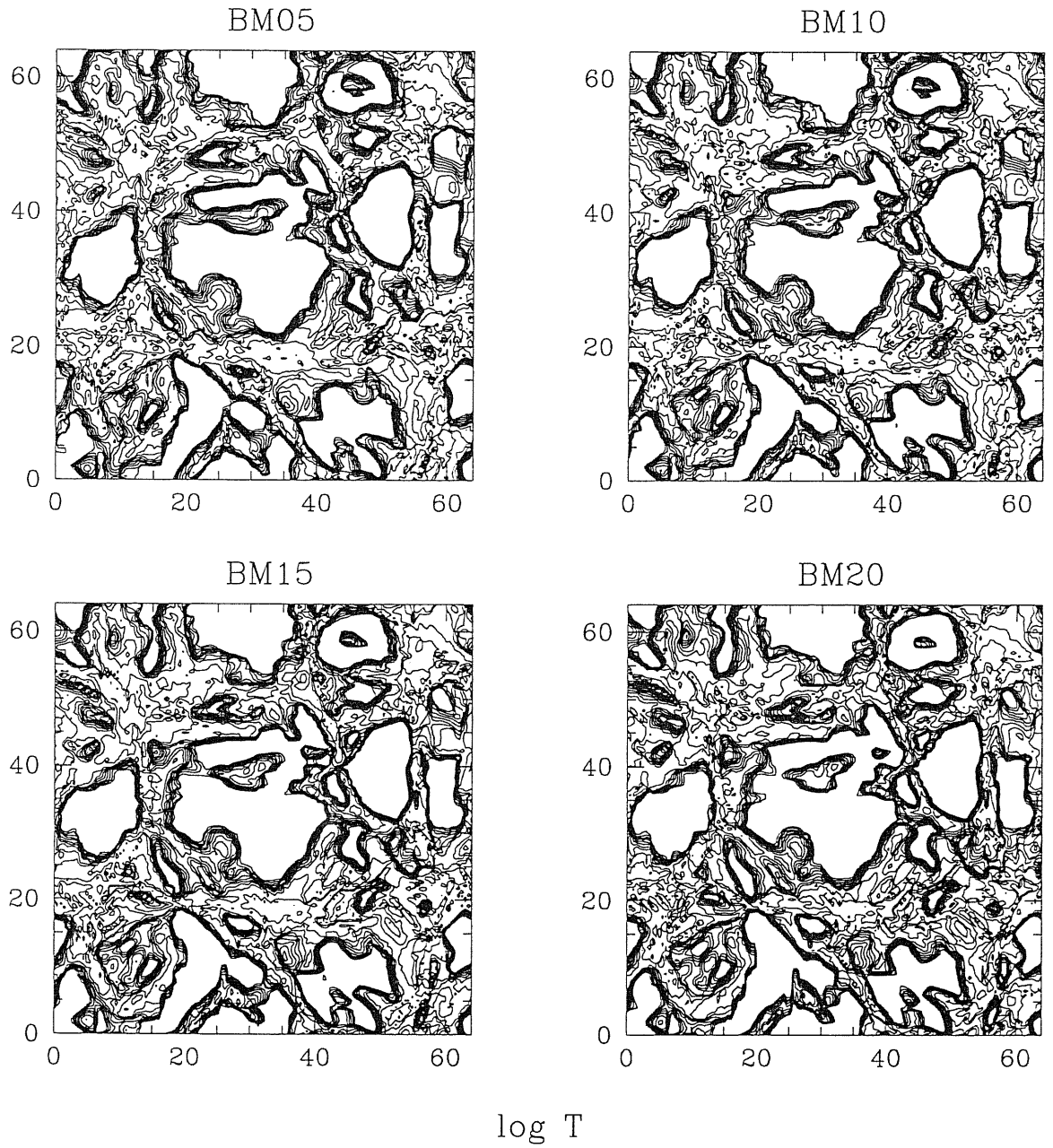

Figure 8.4: The same as Figure 8.2 but for the temperature T which is in units of Kelvin degrees. The contour levels correspond to $10^{2i/3}$, where $i = 1, 2, ...$

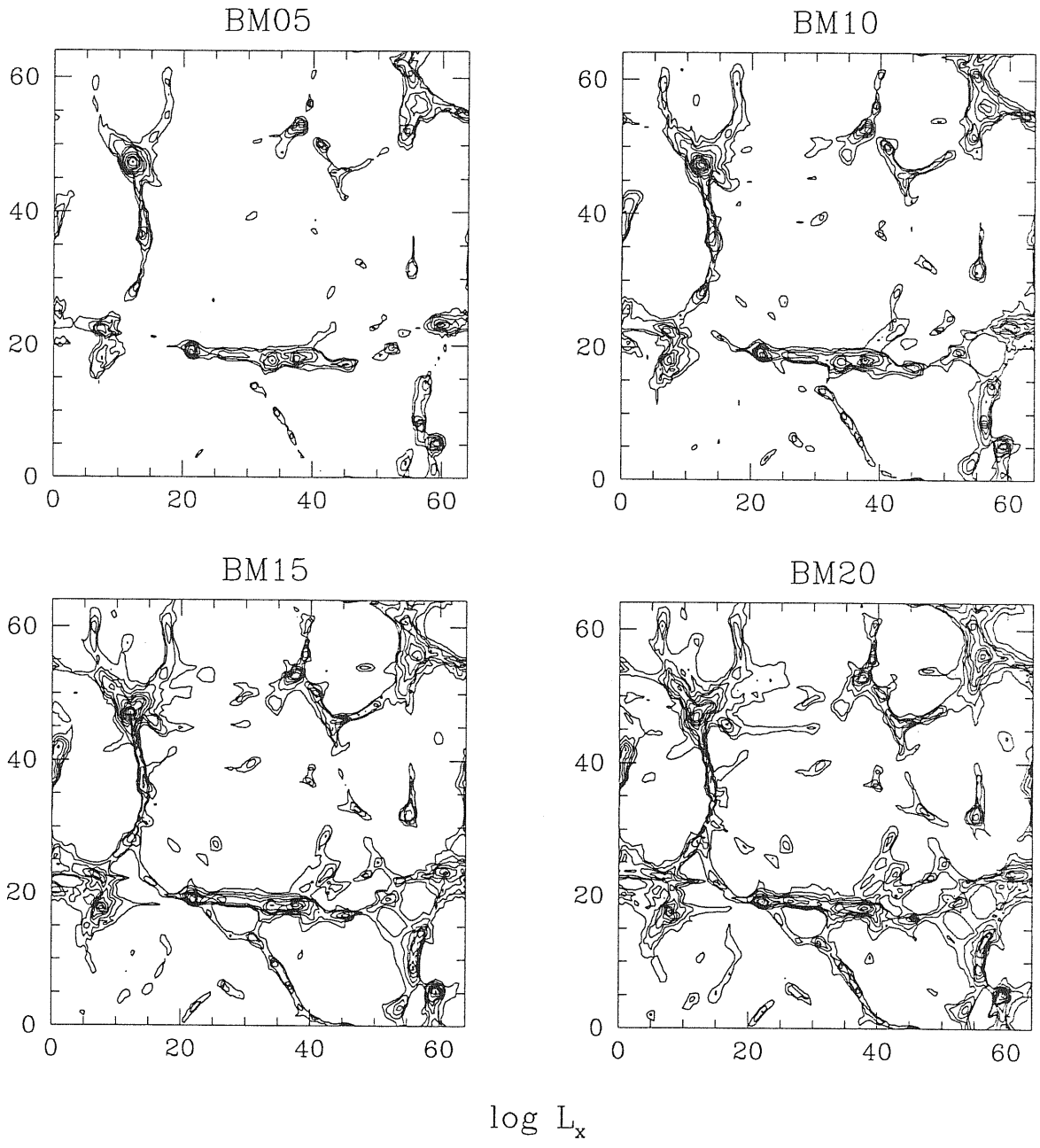

Figure 8.5: The same as Figure 8.2 but for the X-ray luminosity L_x which is in units of 10^{36} erg s^{-1}. The contour levels correspond to $10^{2i/3}$, where $i = 1, 2, ...$

emission due to the higher baryon content of these models.

A close-up at four different redshifts of the most luminous X-ray cluster found in the BM05 simulation is presented in Figure 8.6. The slice is $20 \times 20 \times 0.5\ h^{-3}$ Mpc^3. It is evident the ongoing process of merging and the final virialized state characterized by an extended central isothermal region at high temperature. The cluster tends to a spherical geometry and deviations from sphericity are due to the cluster memory of its merging history (see e.g. Tormen 1997). These satellites, however, being faint X-ray sources, may not be observed in a X-ray map. Similar comments can be repeated for the other models (not shown here).

Dark matter structures appear typically less concentrated than the baryonic counterpart both in clusters and in filaments. In Table 8.2 we present the rms of the DM and BM density fields (σ_{DM} and σ_{BM} respectively) computed on the cell-size scale ($0.5\ h^{-1}$Mpc) and the mean temperature $< T >$ (in Kelvin degrees) at redshifts $z = 1$ and $z = 0$. The density contrasts of the two components are normalized to the corresponding mean cosmological values. A detailed analysis of the time evolution of the rms shows that at very high redshifts, due to absence of pressure forces, DM collapses faster than the baryonic counterpart. However, in all of our models, starting from about $z \sim 3$, baryons tend to concentrate more than the dark component. The absence of dissipative phenomena produces a spreading of DM around the minima of the gravitational potential, while BM, which tends to thermalize, concentrates there. As time goes by, also dark particles fall toward the centre of the potential well and at the final time the rms of the two components is quite similar (see Table 8.2).

Comparing the different models, we observe that both σ_{BM} and σ_{DM} decrease with the increasing of the baryon fraction both at $z = 1$ and $z = 0$. This behaviour is mainly related to the characteristics of the initial spectrum in the different models (see Figure 8.1). Furthermore structures virialize earlier in low-Ω_{BM} models and shocks are stronger and the final temperatures higher than in the high-Ω_{BM} models, because of the lower pressure and higher densities present initially in these models. Between $z = 1$ and $z = 0$ there is a slightly faster evolution of structures in the case of a high baryon content and this is probably favoured by the lower temperatures produced in this case.

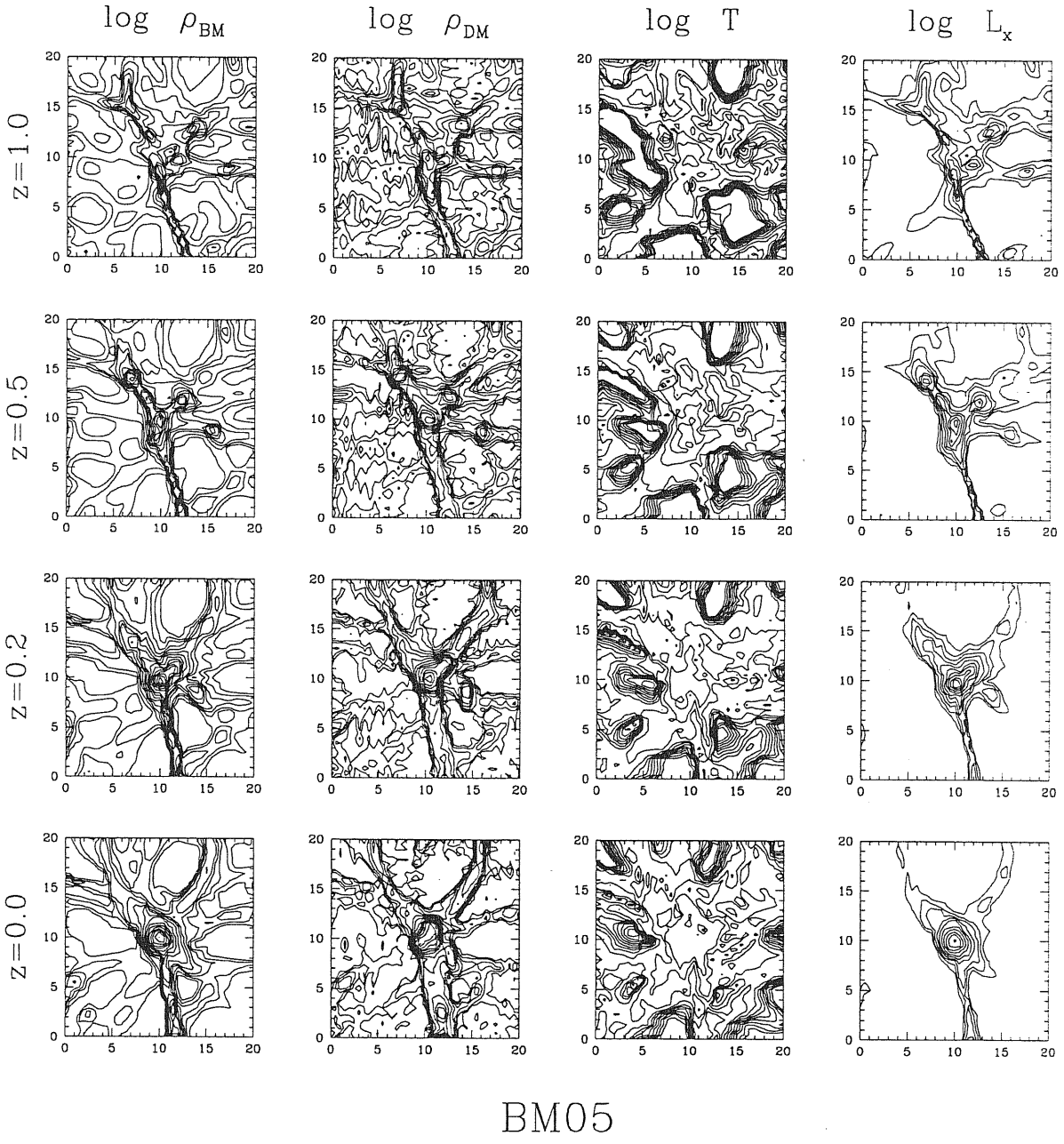

Figure 8.6: The contour plots for the baryonic density ϱ_{BM} (first column), the dark matter density ϱ_{DM} (second column), the temperature T (third column) and the X-ray luminosity L_x (last column) in a slice of $20 \times 20 \times 0.5\ h^{-3}$ Mpc^3 around the most luminous cluster in the BM05 simulation. The different rows show the redshift evolution: $z = 1$, $z = 0.5$, $z = 0.2$ and $z = 0$ from the top to the bottom. The density of each component is normalized to its mean density while the temperature and the luminosity are in units of Kelvin degrees and 10^{36} erg s^{-1}, respectively. The density contour levels correspond to $10^{(i-3)/4}$ while the temperature and the luminosity levels are $10^{2i/3}$, where $i = 1, 2, ...$

Table 8.2: The global properties of the model simulations. The rms of the dark matter, σ_{DM}, the rms of the baryonic matter, σ_{BM}, and the mean temperature $< T >$ (in Kelvin degrees), computed on the cell scale, are shown at redshift $z = 1$ (Columns 2, 3 and 4) and at $z = 0$ (Columns 5, 6 and 7).

Models	σ_{DM}	σ_{BM}	$< T >$ K	σ_{DM}	σ_{BM}	$< T >$ K
	$z = 1$			$z = 0$		
BM05	3.27	3.40	4.86×10^5	7.31	7.34	1.04×10^6
BM10	2.80	3.14	3.86×10^5	6.97	7.00	9.24×10^5
BM15	2.44	2.73	2.97×10^5	6.05	6.27	7.68×10^5
BM20	1.94	2.20	2.20×10^5	5.33	5.45	6.35×10^5

8.4 X-ray Cluster Mass

Clusters in our simulations are identified through their X-ray emission and their characteristic properties, like the total mass, the total luminosity and the mean temperature, are computed by integrating or averaging over a fixed number of cells, as explained in Section 8.2. The values of these quantities could then be affected by the choice of the number of cells used for the calculation. Several tests have shown that our procedure provides good estimates for the temperature and the luminosity of the cluster. In fact the temperature is almost uniform over regions greater than those over which we do our averaging. Moreover the luminosity is proportional to the square of the baryonic density and then its value depends essentially on the cells with highest density which represents the centre of the cluster and which are consequently always included in our integration. The inclusion or missing of some low-density cells does not affect sensibly our estimates for the temperature and the luminosity, but could affect the calculation of the cluster total mass. In summing over a fixed number of cells we tend to overestimate the mass of objects which are not as extended as our reference volume (27 cells) and which are also usually characterized by density lower

that the mean cluster values. The opposite is true for large clusters, although in this case we have verified that, for our choice of the reference volume, the error introduced in the estimation of the mass is less severe and it is at most a factor two. Therefore we have restricted our analysis to clusters with mass greater than $10^{14}M_{\odot}$ (for $h = 0.5$). This lower limit has been fixed in order to avoid the inclusion of too low-mass objects which can be affected by a large error in the mass estimate and whose properties differ considerably from those of a typical galaxy cluster (e.g., their mean density is sensibly lower than that determined from observations). Furthermore their spatial distribution could be affected by the X-luminosity selection criterion used to build our cluster catalogue.

In Figure 8.7 we present, for the four models, the number N_M of clusters with mass greater than $10^{14}M_{\odot}$ found in the whole simulation box at various redshifts. The number of clusters decreases with increasing Ω_{BM} at any redshift. This is a consequence of the amount of power on small scales, which decreases as we increase the baryonic fraction. In the high-Ω_{BM} cases the collapse of massive objects occurs later and, then, if we select clusters by their mass, the models with high baryonic fraction presents less clusters than low-Ω_{BM} models. The behaviour of the mass function depends on the distribution of the total (dark plus baryonic) density and then it is not the preferred quantity for discriminating between our models. Other quantities, like the X-ray luminosity, that depends directly on the BM density, appear to be a more useful quantity for the problem studied here.

Notice that the estimated N_M roughly agrees with the observational data for all the models. This is an expected result, because of the spectra normalizations. In fact it is known that the present abundance of galaxy clusters requires, in the framework of the critical-density models and almost independently of the shape of the primordial spectrum, a normalization $\sigma_8 \approx 0.6$, with a quite large uncertainty (e.g. White, Efstathiou & Frenk 1993; Viana & Liddle 1996; Eke, Cole & Frenk 1996).

8.5 X-ray Cluster Luminosity

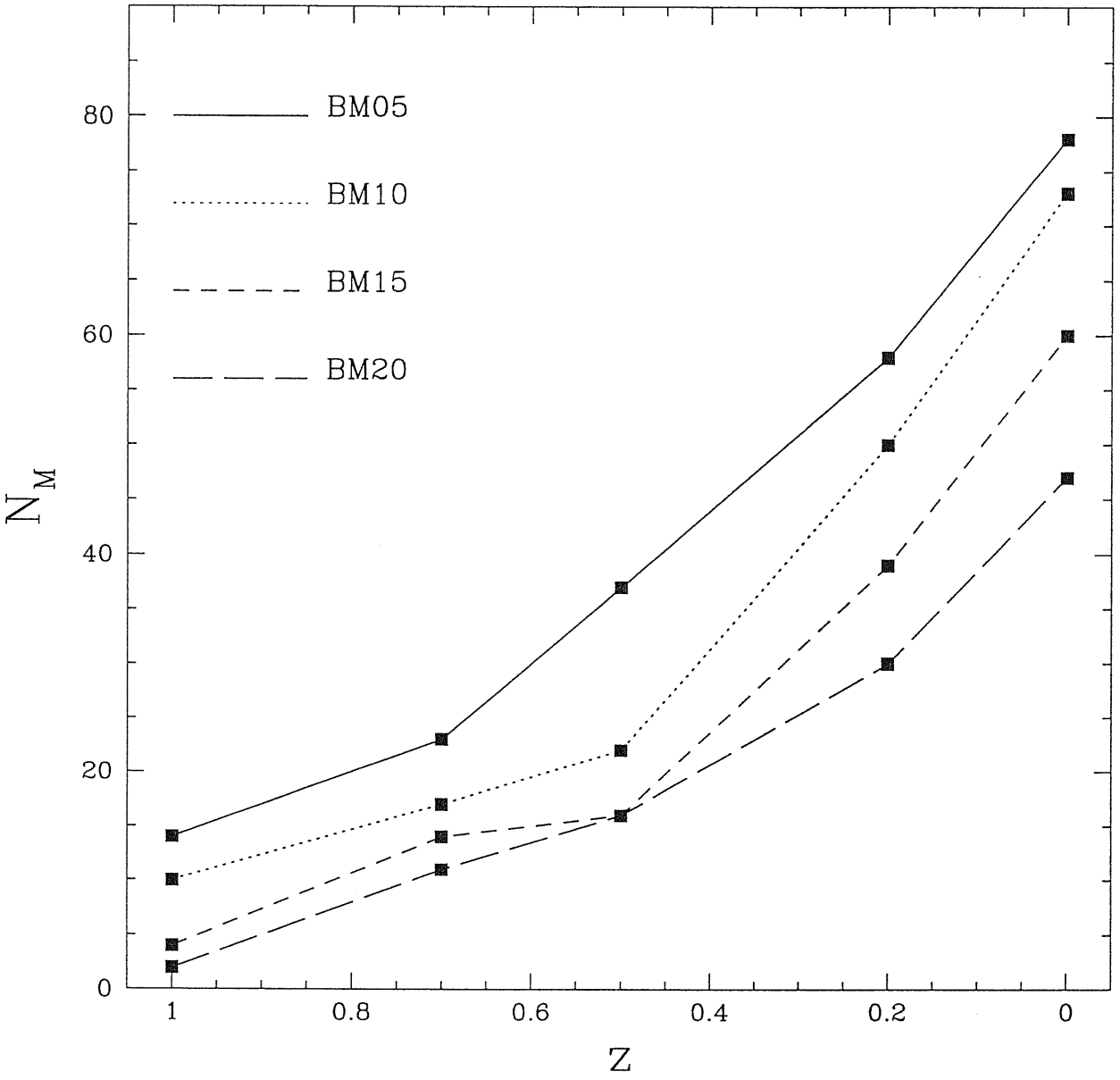

Figure 8.7: The number of clusters N_M with mass $\geq 10^{14} M_\odot$ as a function of the redshift z for the different models: BM05 (solid line), BM10 (dotted line), BM15 (short-dashed line) and BM20 (long-dashed line).

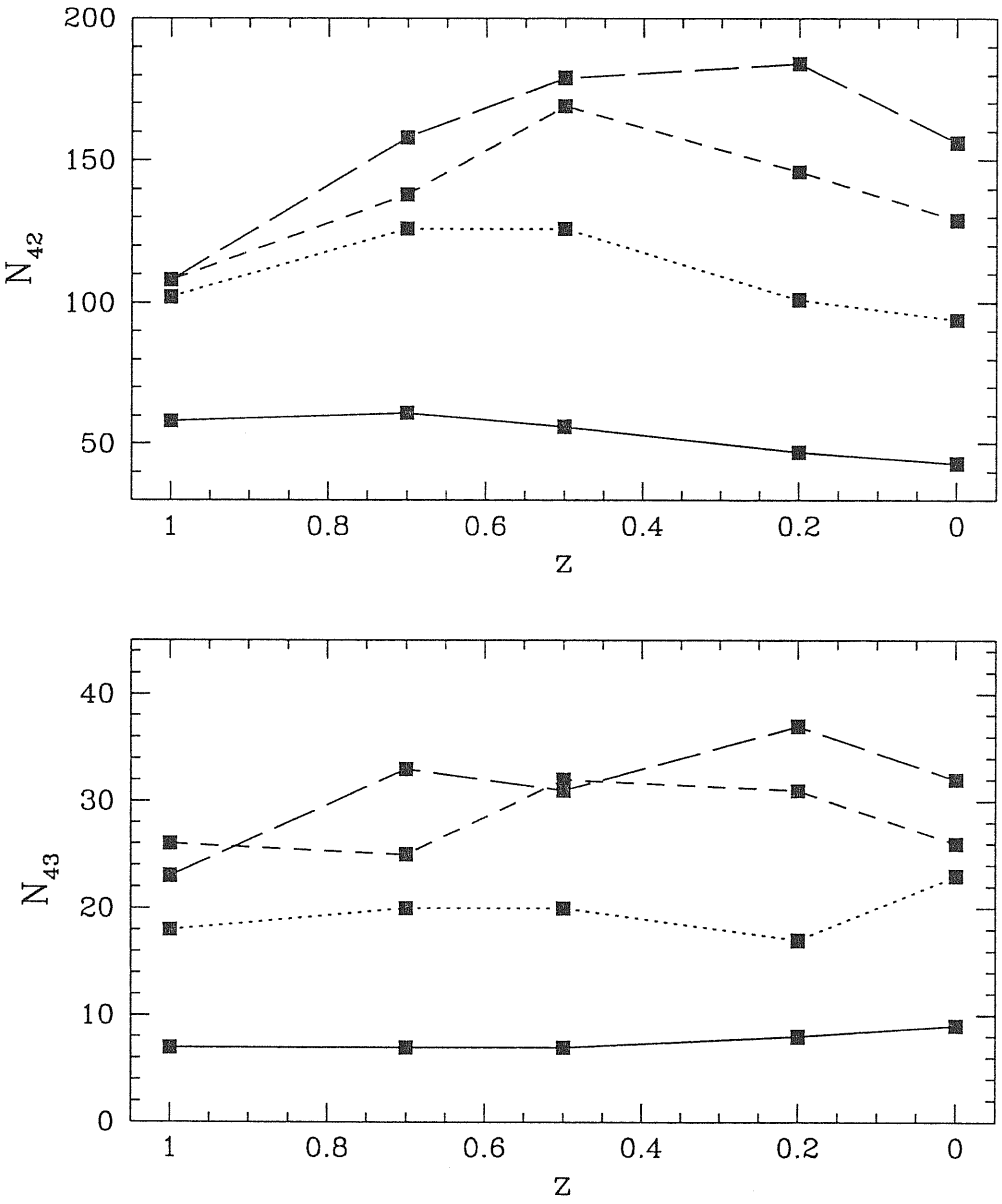

Figure 8.8: The number of clusters with luminosity $L_x \geq 10^{42}$ (N_{42}, upper panel) and $L_x \geq 10^{43}$ erg s^{-1} (N_{43}, bottom panel) as a function of the redshift z for the different models: BM05 (solid line), BM10 (dotted line), BM15 (short-dashed line) and BM20 (long-dashed line).

In Figure 8.8 we present the number of clusters with luminosity greater than $L_x = 10^{42}$ and 10^{43} erg s^{-1} (N_{42} and N_{43}, respectively). This luminosity-based selection criterion leads to results opposite to those obtained by selecting clusters by their masses. In fact at any epoch the number of clusters increases with increasing Ω_{BM}. Furthermore the evolution of N_{42} and N_{43} with redshift is not monotonic: the number of clusters tends to grow until a turn-around redshift after which it starts to decrease. This behaviour is common to all the models and for both of the adopted minimum luminosities. The only exception is N_{43} in the case of BM05, which grows continuously with time, but, because of the small number, this might be not statistically significant. The turn-around is due to the balance between the mechanisms driving the cluster evolution, and it is probably an indication of the epoch when the merging processes of different structures start to dominate over the gravitational collapse of each single object. In fact the merging leads to larger but smoother structures. Since the X-ray emission is proportional to the square of the baryonic density, lower luminosities are expected. The effect of the merging processes is also shown by the simultaneous decrease in the number of fainter clusters (not reported in the figure). The turn-around redshift becomes lower with increasing the baryon fraction ranging from $z = 0.7$ for BM05 to $z = 0.2 - 0.5$ for BM20. This is due to the delayed evolution of the structures in high-Ω_{BM} models.

This behaviour is confirmed by the X-ray emissivity per unit comoving volume due to both the gas in its entirety, j_{gas}, and the clusters, j_{cl} (see Table 8.3). For each model the two quantities evolve in a parallel way, indicating that clusters emit roughly a constant large fraction of the total X-ray radiation. Similar results have been obtained, for the standard CDM model, also by Kang *et al.*(1994a) and Bryan *et al.*(1994a).

The fundamental differences between the cluster abundances in mass (N_M) and in X-ray luminosity (N_{42} and N_{43}) must be kept in mind when the results are compared to the observations. In Figure 8.9 we present the luminosity function for the four models computed at five different redshifts, integrated over the whole range of frequencies. Very bright clusters with luminosity greater than 10^{45} erg s^{-1} are missing in our simulations. The lack of

Table 8.3: The X-ray emissivity (in units of 10^{40} ergs s^{-1} h^3 Mpc^{-3}) for the gas (j_{gas}) and for the clusters (j_{cl}) at various redshifts for the different models.

	BM05		BM10		BM15		BM20	
	j_{gas}	j_{cl}	j_{gas}	j_{cl}	j_{gas}	j_{cl}	j_{gas}	j_{cl}
$z = 1$	0.17	0.12	0.49	0.39	0.66	0.49	0.73	0.55
$z = 0.7$	0.21	0.16	0.54	0.43	0.79	0.62	0.98	0.79
$z = 0.5$	0.20	0.15	0.63	0.46	0.88	0.73	1.53	0.86
$z = 0.2$	0.19	0.14	0.51	0.39	0.87	0.73	1.29	1.12
$z = 0$	0.16	0.13	0.59	0.50	0.96	0.81	1.05	0.85

such clusters can be related to two different effects. Firstly, the size of our computational box limits the amount of large-scale power which we can follow in the simulation, and consequently the maximum temperature that can be produced. Secondly, the grid resolution is likely to underestimate the highest density peaks where brightest clusters are expected to form.

The luminosity functions have been fitted by using a two-parameter function:

$$n(L)dL = n_0 L^{-\alpha} dL \, , \tag{8.2}$$

where $n(L)dL$ is the comoving density of clusters with luminosity between L and $L + dL$, n_0 is in units of 10^{-6} $h^3 \mathrm{Mpc}^{-3}$ and L is in units of 10^{44} erg s^{-1}. The results of the fits are presented in Table 8.4. Notice that for our data a two-parameter fit is more appropriate than the usual Schechter function, as in our results the expected bend at high L is not present, for the reasons given above.

The values of the slope α cannot discriminate between the four models, as the differences are in general within the 1-σ errorbars. The parameter α shows for all the models a slight negative evolution with redshift from $z = 0.5$ to $z = 0$; this behaviour is thought to be the effect of the ongoing processes of gravitational collapse, that produces more concentrated

Table 8.4: The parameters of the fits of the X-ray cluster bolometric luminosity function $n(L) = n_0 L^{-\alpha}$ at various redshifts for the different models.

	BM05		BM10		BM15		BM20	
z	α	n_0	α	n_0	α	n_0	α	n_0
1	1.82±0.09	6.73±0.06	1.72±0.08	18.95±0.23	1.59±0.07	31.66±0.38	1.74±0.06	18.56±0.15
0.7	1.73±0.15	9.72±0.18	1.72±0.09	21.55±0.30	1.71±0.05	26.60±0.24	1.73±0.07	28.44±0.33
0.5	1.74±0.20	8.42±0.20	1.75±0.16	19.46±0.47	1.76±0.09	25.66±0.36	1.69±0.08	33.20±0.46
0.2	1.61±0.07	12.50±0.12	1.68±0.04	20.97±0.12	1.69±0.05	29.12±0.24	1.69±0.11	35.59±0.72
0	1.41±0.11	23.11±0.48	1.67±0.11	18.68±0.31	1.62±0.05	31.69±0.25	1.66±0.03	33.95±0.15

and bright structures, and merging, that leads to the formation of larger and more massive objects at the expense of the smaller ones. For the normalizations n_0, which is the comoving number density of objects with luminosity equal to 10^{44} erg s^{-1}, we can make considerations similar to those previously made for N_{42} and N_{43}.

The hatched region in the figure shows the observational data (with 1-σ errorbars) of Ebeling *et al.*(1997) which refer to the ROSAT Brightest Cluster sample containing 199 objects with redshift $z \leq 0.3$. The observational curves have been fitted by the authors by using a three-parameter function:

$$n(L) = A \exp(-L/L^*) L^{-\alpha} , \tag{8.3}$$

where A is in units of 10^{-7}Mpc$^{-3}(10^{44}$erg s$^{-1})^{\alpha-1}$ and L^* is in units of 10^{44}erg s^{-1}. The values of the fitting parameters are $A = 6.41^{+0.70}_{-0.61}$, $L^* = 37.2^{+16.4}_{-3.8}$ and $\alpha = 1.84^{+0.09}_{-0.04}$.

We can compare these data with the results of the simulations at low redshifts. The models with high baryonic content (BM15 and BM20) have a luminosity function which is significantly too high with respect to the observations. On the contrary the BM05 model and (much more marginally) BM10 are in better agreement with the data.

Similar conclusion can be obtained if we consider the luminosities in the energy band

[0.5–2] keV. The fitting parameters for our simulations are reported in Table 8.5, while the comparison with two different observational datasets is shown in Figure 8.10. The vertically hatched region refers again to the Ebeling *et al.*(1997) sample, whose luminosity function has been fitted by a three-parameter relation with $A = 3.32^{+0.36}_{-0.33}$, $L^* = 5.70^{+1.29}_{-0.93}$ and $\alpha = 1.85^{+0.09}_{-0.09}$. The horizontally hatched region shows instead the results obtained by De Grandi (1996) using a complete flux-limited ROSAT sample selected from the ESOKP redshift survey: in this case the fitting parameters are $A = 4.51$, $L^* = 2.63^{+0.87}_{-0.58}$ and $\alpha = 1.32^{+0.21}_{-0.23}$. These two determinations of the luminosity functions are in good agreement for luminosities larger than $\approx 2 \times 10^{43}$ erg s^{-1}, while for smaller L_x the De Grandi (1996) results are approximately a factor 3 smaller than the Ebeling *et al.*(1997) ones, increasing the discrepancies between the observations and the model predictions of the models with high Ω_{BM}.

In this energy band there is a further luminosity function determined by Burns *et al.*1996), always by using images from the ROSAT all-sky survey. Because of the large errorbars, it completely overlaps both the previous results and for clarity we prefer do not show it in Figure 8.10. However, since in this dataset also nearby poor clusters have been considered, this result allows to extend the previous considerations also to smaller X-ray luminosities (less than 10^{42} erg s^{-1}), not included in the other datasets.

8.6 X–ray Cluster Temperatures

In Figure 8.11 we show the redshift evolution of the distribution of the cluster mean temperature for the four models. The temperatures have been calculated as emission-weighted averages because this is the quantity which is also usually estimated from the observations. The absence of clusters with temperatures above 4 keV is mainly related to the limited size of the box and their rareness. These model predictions can be compared with the observations. In the figure the hatched region refers to the temperature distribution obtained by

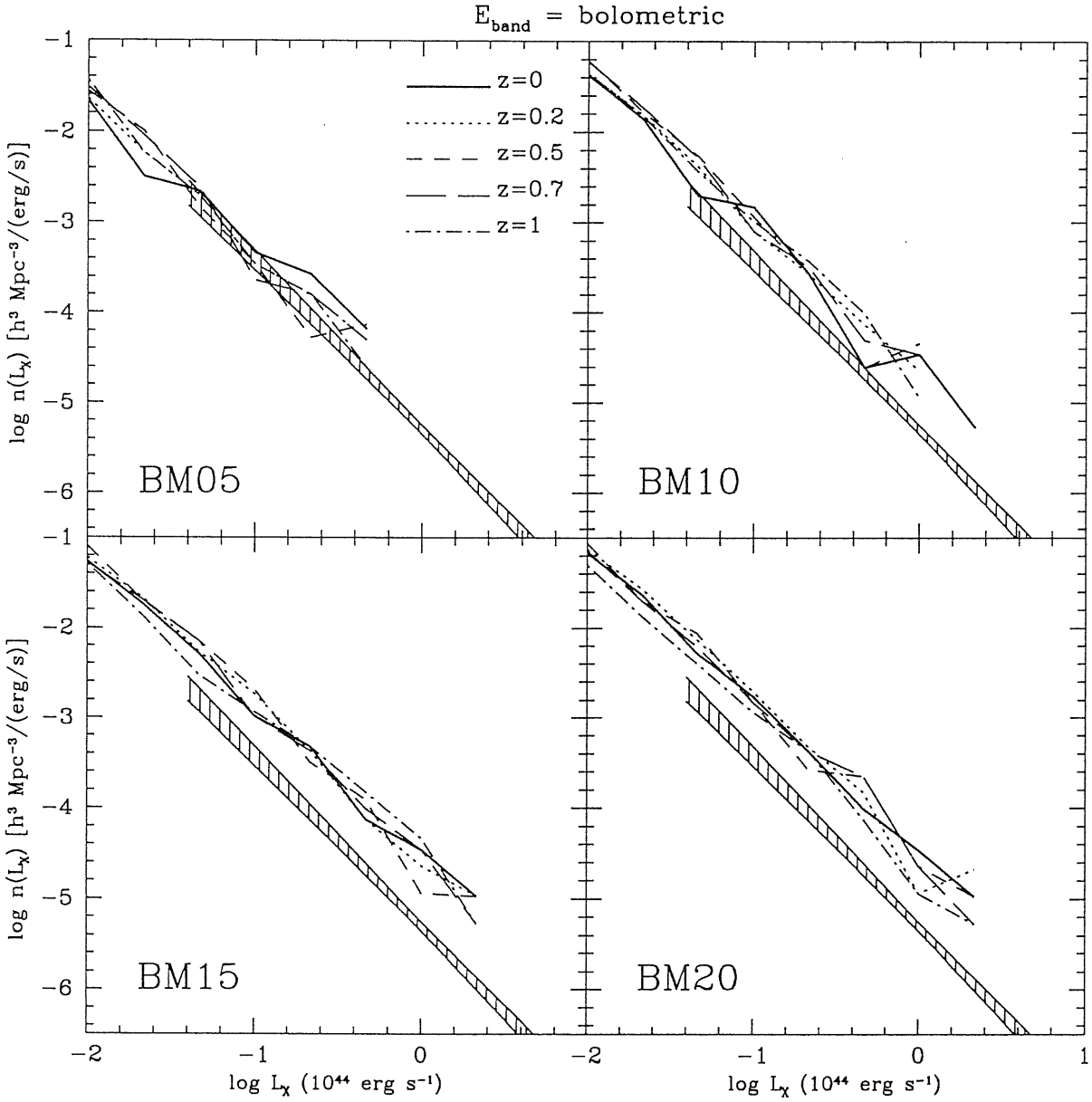

Figure 8.9: The cluster bolometric luminosity function for the different models: BM05 (top left), BM10 (top right), BM15 (bottom left) and BM20 (bottom right). The different curves refer to various redshift: $z = 0$ (solid line), $z = 0.2$ (dotted line), $z = 0.5$ (short-dashed line), $z = 0.7$ (long-dashed line), $z = 1$ (dotted-dashed line). The hatched region shows the observational results (with 1-σ errorbars) obtained by Ebeling *et al.*(1997).

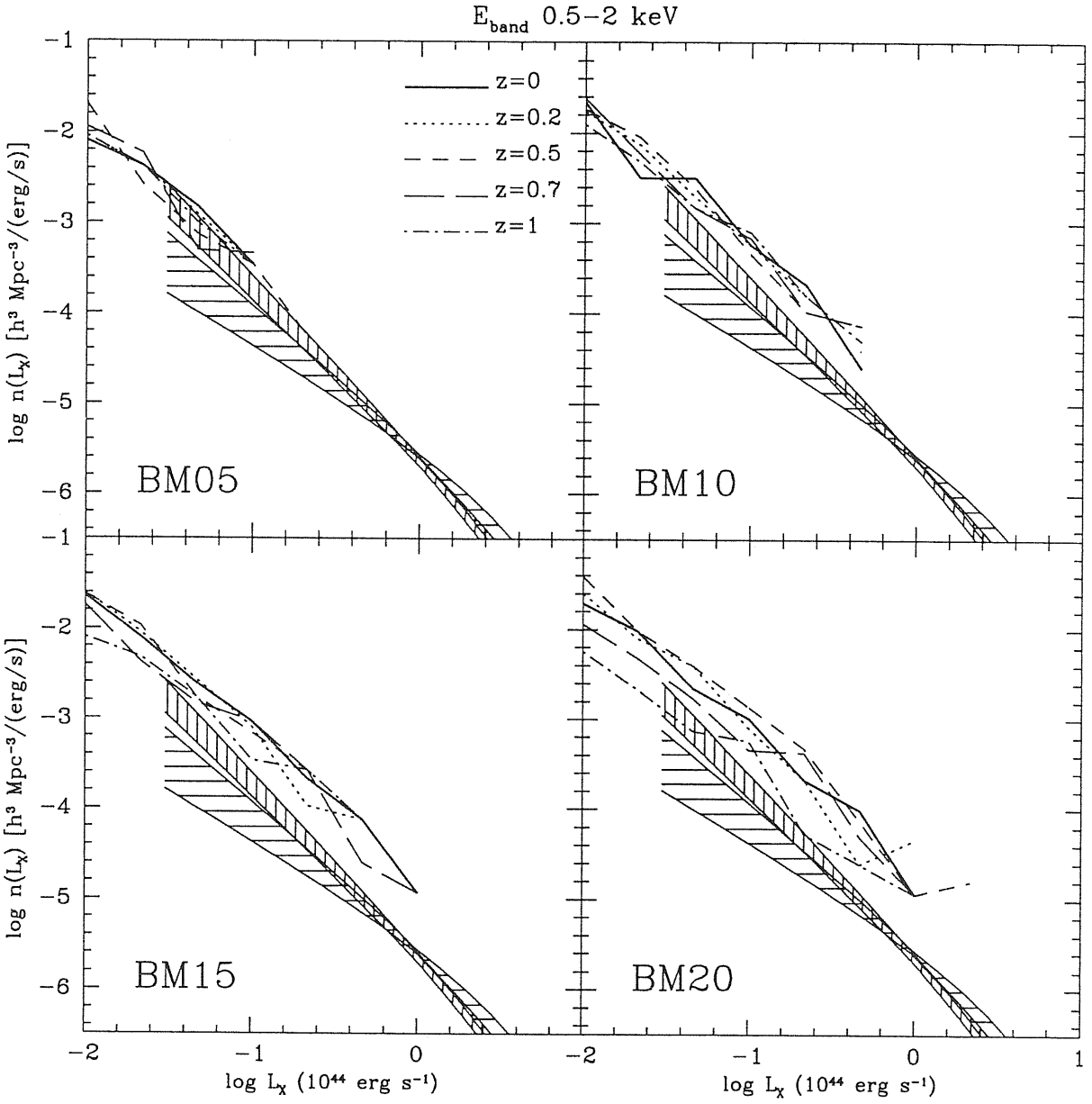

Figure 8.10: The same as Figure 8.9 but in the [0.5–2] keV energy band. The vertically hatched region shows the observational results (with 1-σ errorbars) obtained by Ebeling *et al.*(1997), while the horizontally hatched one refers to the De Grandi (1996) results.

Table 8.5: The parameters of the fits of the X-ray cluster luminosity function $n(L) = n_0 L^{-\alpha}$ computed in the [0.5–2] keV band at various redshifts for the different models.

	BM05		BM10		BM15		BM20	
z	α	n_0	α	n_0	α	n_0	α	n_0
1	1.47±0.11	11.73±0.17	1.43±0.07	19.26±0.24	1.39±0.10	19.19±0.31	1.40±0.11	10.17±0.13
0.7	1.58±0.40	8.40±0.49	1.55±0.11	15.73±0.26	1.58±0.11	12.90±0.20	1.45±0.12	18.25±0.32
0.5	1.81±0.16	5.52±0.04	1.58±0.12	15.09±0.28	1.52±0.07	22.51±0.30	1.57±0.10	28.56±0.48
0.2	1.44±0.11	13.71±0.27	1.55±0.06	15.87±0.17	1.67±0.08	13.63±0.15	1.55±0.11	21.31±0.52
0	1.36±0.17	18.05±0.60	1.63±0.17	11.75±0.28	1.61±0.06	11.75±0.28	1.57±0.09	19.28±0.28

Henry & Arnaud (1991) from a set of local ($z \approx 0$) clusters:

$$n(T) = (1.8^{+0.8}_{-0.5} \times 10^{-3}\ h^3\ \mathrm{Mpc}^{-3}\ \mathrm{keV}^{-1})\ T^{-4.7\pm0.5}, \qquad (8.4)$$

where the uncertainties are 1-σ errorbars and T is expressed in keV.

All the models are in quite good agreement with observations in the overlapping range. Temperature is in fact less sensitive than luminosity to the details of the density distribution and it is related to the maximum wavelength λ of non-linear waves. In fact the post-shock temperature is of the order of $T \propto (H\lambda)^2$, where H is the Hubble constant. Low-Ω_{BM} models have a higher normalization of the primordial spectrum and longer wavelengths can reach the non–linear regime at the final time producing higher values of the temperature. This phenomenon is likely to be strengthened by the different mean background pressure of the various realizations, which is lower in low-Ω_{BM} models. Both effects could explain the higher number of objects with temperature larger than about 1 keV found with decreasing Ω_{BM}.

We have also analysed the redshift evolution of the temperature distributions in our simulations. We found that between $z = 1$ and $z = 0$ such distributions are almost constant for BM05 and BM10 models, with a slow increase in the number of high-temperature objects.

In these models, by $z \sim 1$ the regions heated up by shocks at almost a uniform temperature are larger than the integration volume of our cluster identification method. In general, from that moment, the temperature of these regions increases because of adiabatic compression and merging processes and this explains the rise in the number of high-temperature clusters towards $z = 0$. The models BM15 and BM20, instead, evolve rapidly between $z = 1$ and $z = 0.5$, showing in particular a strong growth in the number density of objects with temperature greater than about 0.5 keV. This corresponds to the later formation and propagation of the shocks in these models. In fact after $z = 0.5$ the situation becomes similar to that of the low-Ω_{BM} models, and the temperature distributions show little further evolution.

8.7 Luminosity-Temperature Relation

In Figure 8.12 we present the distribution of emission-weighted temperature of the clusters as a function of the X-ray bolometric luminosity at three different redshifts: $z = 1$ (crosses), $z = 0.5$ (open circles) and $z = 0$ (filled circles). For all the models there is a similar trend in the luminosity-temperature relation, even though the total number of objects grows with the baryon fraction. We observe that a given temperature corresponds to higher luminosities in high-Ω_{BM} models. This is related to the higher baryonic densities present in these cases.

The luminosity-temperature distributions have been fitted by using a power-law relation of the form $T = 10^b L_x^\eta$, where T is in keV and L_x is in units of 10^{40}erg s^{-1}. The results, reported in Table 8.6, show that for all the models there is a little evolution with time, especially between $z = 0.5$ and $z = 0$, where present-day observational data are available. In particular the parameter η is always inside the 1-σ errorbar range, even if the models with smaller baryonic content tend to have a steeper slope. The normalization b, instead, slightly decreases with increasing redshift and/or Ω_{BM}. This result is in qualitative agreement with the more recent observational analysis, which found no evolution of the temperature-luminosity distribution, at least for $z < 0.5$ (Mushotzky & Scharf 1997).

Our results can be directly compared to the observational data. The hatched region in Figure 8.12 shows the L_x-T relation (always with 1-σ errorbars) obtained by Henry &

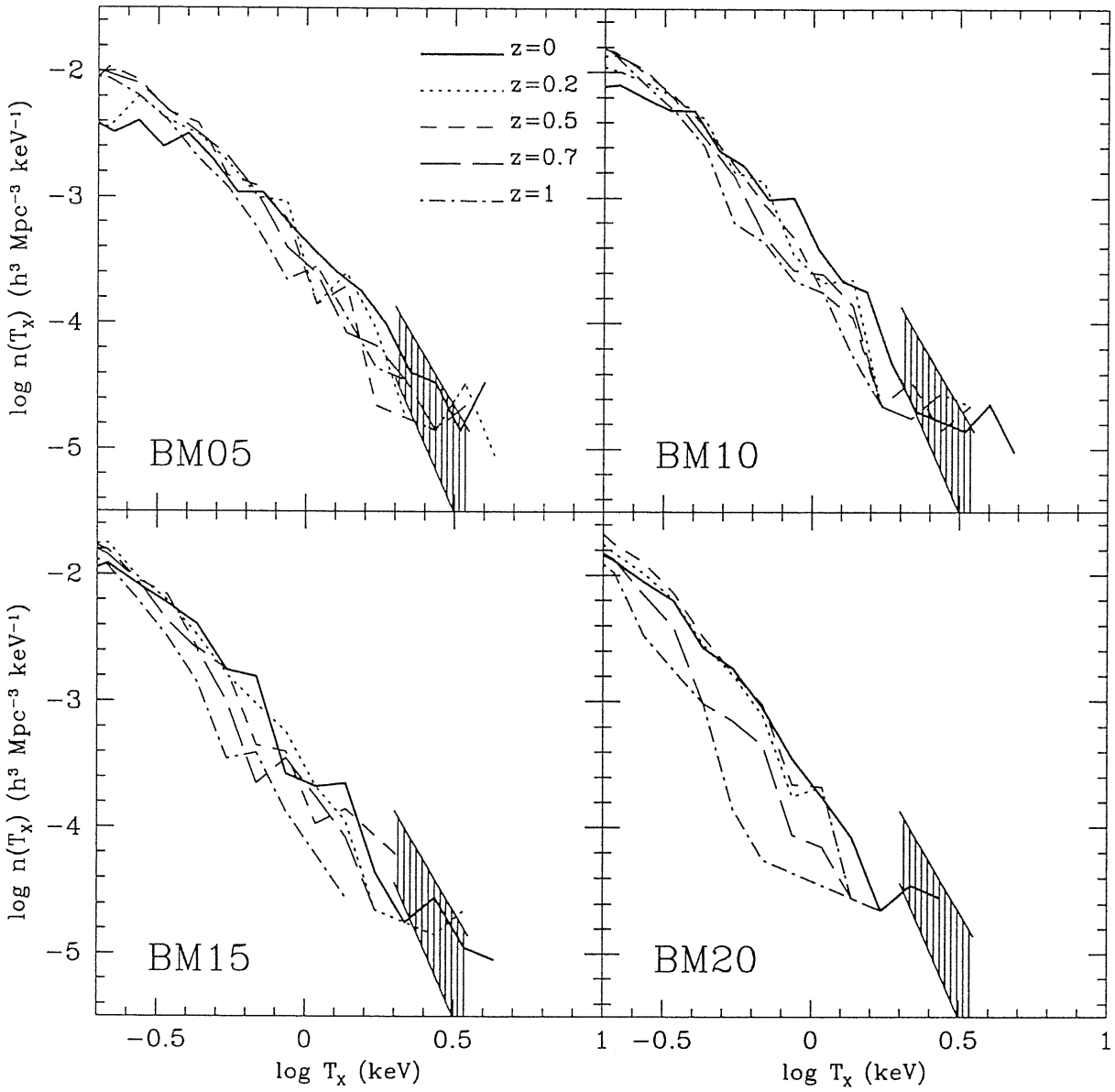

Figure 8.11: The cluster temperature function for the different models: BM05 (top left), BM10 (top right), BM15 (bottom left) and BM20 (bottom right). The different curves refer to various redshift: $z = 0$ (solid line), $z = 0.2$ (dotted line), $z = 0.5$ (short-dashed line), $z = 0.7$ (long-dashed line), $z = 1$ (dotted-dashed line). The hatched region shows the observational results (with 1-σ errorbars) obtained by Henry & Arnaud (1991).

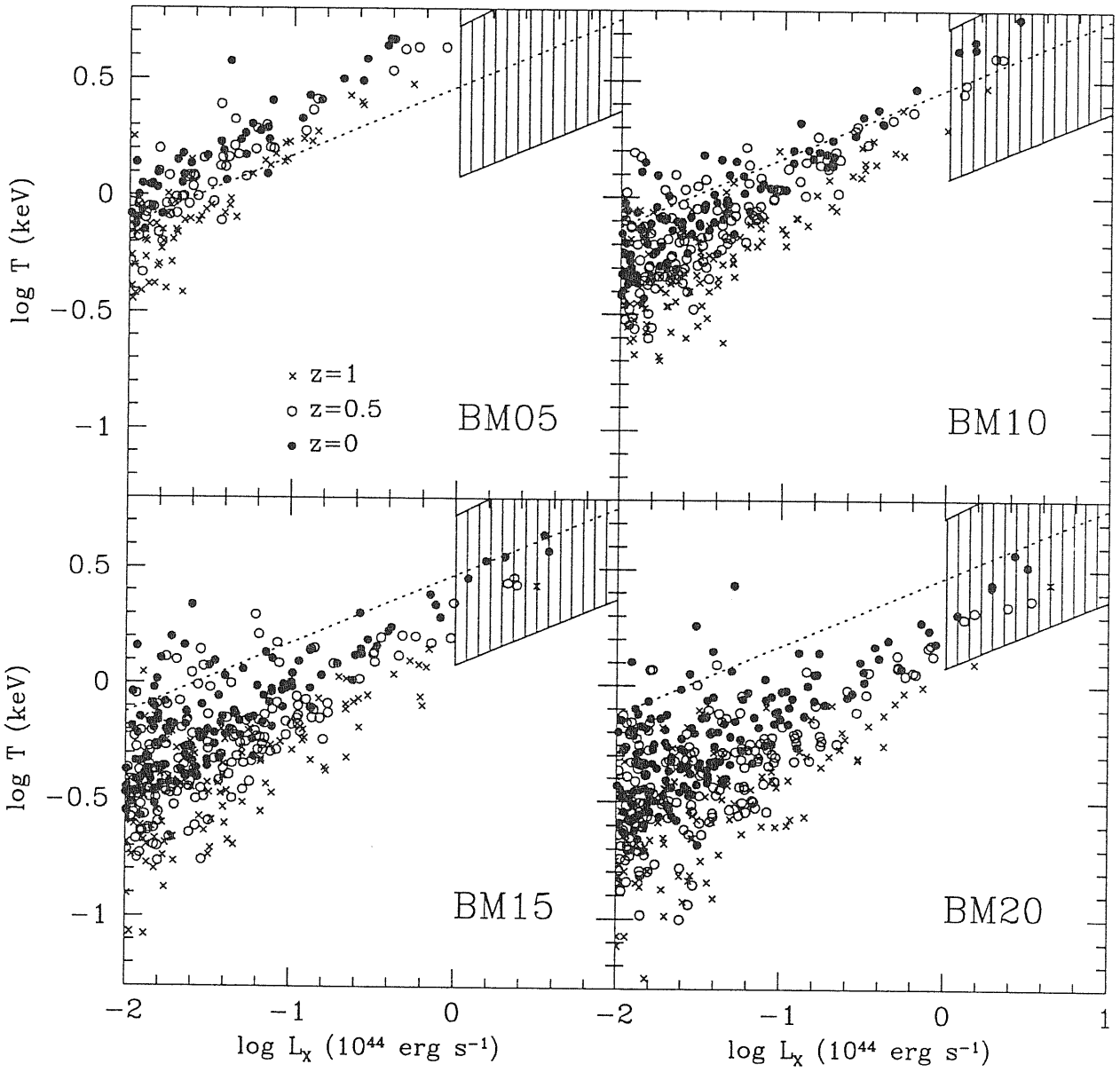

Figure 8.12: Scatter plots of the bolometric X-ray luminosity L_x and the emission-weighted temperature T of the clusters for the different models: BM05 (top left), BM10 (top right), BM15 (bottom left) and BM20 (bottom right). Different redshifts are displayed by different symbols: $z = 1$ (crosses), $z = 0.5$ (open circles) and $z = 0$ (filled circles). The hatched region shows the observational results (with 1-σ errorbars) obtained by Henry & Arnaud (1991); the dotted line refers to the fit obtained from the combined sample of David *et al.*(1993). In this last case the errorbars are not explicitly reported, but they are of the same order of magnitude of the previous ones.

Table 8.6: The parameters of the fits of the Luminosity-Temperature relation $T = 10^b L_x^\eta$, computed at various redshifts for the different models.

	BM05		BM10		BM15		BM20	
	η	b	η	b	η	b	η	b
$z = 1$	0.41±0.04	-1.22±0.09	0.34±0.03	-1.31±0.07	0.30±0.04	-1.38±0.10	0.31±0.04	-1.52±0.11
$z = 0.7$	0.40±0.03	-1.10±0.07	0.33±0.03	-1.20±0.09	0.31±0.04	-1.32±0.09	0.30±0.03	-1.42±0.08
$z = 0.5$	0.42±0.03	-1.06±0.07	0.35±0.03	-1.17±0.09	0.33±0.03	-1.28±0.07	0.30±0.03	-1.35±0.07
$z = 0.2$	0.42±0.02	-0.99±0.06	0.36±0.02	-1.11±0.06	0.33±0.02	-1.17±0.06	0.31±0.03	-1.25±0.08
$z = 0$	0.40±0.02	-0.90±0.06	0.37±0.02	-1.05±0.05	0.35±0.02	-1.14±0.05	0.32±0.02	-1.20±0.06

Arnaud (1991) for clusters with luminosity larger than 10^{44} erg s^{-1}. Even if the statistics are poor, the most luminous clusters for all the models are in good agreement with these data. The dotted line, instead, shows the fit from the combined sample of David *et al.* (1993), which contains clusters with lower luminosities ($L_x > 10^{42}$ erg s^{-1}). In this case the dispersion of the data around the fit (not explicitly reported in the original paper) is of the same order of that shown for the Henry & Arnaud (1991) results. The models with high baryonic fraction, even if they reproduce well the slope of the relation, have a lower normalization: at the same luminosity, the temperature is at least a factor 3 smaller than for the observations. The agreement is better for BM05 and BM10 models which have a steeper (but still consistent) slope.

Notice that it is not possible to present a comparison with the relation obtained by Mushotzky & Scharf (1997) because it refers to clusters with luminosities higher than those reached in our simulations.

8.8 Conclusions

In this chapter we have presented the results of the study of the evolution and the properties of X-ray clusters of galaxies in four different critical-density CDM models, in which the baryon fraction has been varied from $\Omega_{BM} = 0.05$ to $\Omega_{BM} = 0.20$. Models with a baryonic content larger than the predictions of the standard nucleosynthesis have been firstly considered by White *et al.*(1996) who found that they are in good agreement with a large set of observational data when coupled with a small tilt in the primordial spectrum ($n \approx 0.8$). Our results have proved to be useful in order to discriminate between the various models and to decide which of these models, if any, is compatible with observations.

The mass function, the luminosity function, and the luminosity-temperature relation are the quantities that gave the most important hints on the properties of the models. The behaviour of these quantities is determined by the dynamical evolution of the clusters. This is driven from the balance of two phenomena: the gravitational collapse of single objects and the merging of different structures. In the early stages of the evolution, the first effect tends to dominate, and the X-ray emission grows rapidly. The collapse of the baryonic matter is stopped by the formation of the shock. This rises strongly the pressure of the matter that finally is able to counteract the gravitational infall. Then the smaller virialized objects start to merge together, forming larger structures characterized by smoother density fields and hence by lower X-ray emission.

The mass function presents the expected behaviour, with the cluster number density that, at $z = 0$ decreases with increasing baryon fraction. This is mainly due to the different amount of power on small scales in the initial spectra of the density fluctuations. This result is obtained by identifying clusters only by their mass, without considering their luminosity. On the other hand, when clusters are selected by their total X-ray luminosity, the opposite trend is found: high-Ω_{BM} models have the higher number density of X-ray clusters. This is due mainly to the presence of more baryons and so to the growth of higher baryonic density peaks that at last leads to much higher X-luminosity, this quantity depending on the square of the baryonic density itself. The X-ray emission depends also on the cluster temperatures

but these are roughly the same for all the models.

Another difference is shown by the time evolution: while the number of clusters with large mass is a growing function of time for all the models, the abundance of luminous X-ray clusters starts to decrease at some redshift, which is dependent on the cosmological model, being lower for high-Ω_{BM} models.

We compare the predictions of the four different cosmological models to a series of observational results, mainly referring to local ($z \approx 0$) datasets. By analyzing the luminosity function and (more marginally) the luminosity-temperature relation we can conclude that the models with low baryonic content ($\Omega_{BM} \lesssim 0.05$) are in better agreement with the data, while models with 15 or 20 per cent are well outside the 1-σ errorbars. On the contrary the study of the cluster temperature distribution cannot distinguish between the various models. Our result is even more stringent if we observe that our resolution tends to underestimate the luminosities; consequently the differences of the high-Ω_{BM} models with observations would be even higher. Therefore the X-ray properties seem to exclude that the increase of the baryonic content can help to reconcile the cold dark matter scenario in the framework of critical-density models with the observations.

Finally, we found that the luminosity function, the temperature distribution and the luminosity-temperature relation for the simulated clusters present the interesting feature of showing a very little redshift evolution, particularly between $z = 0.5$ and $z = 0$, in good agreement with that which seems to emerge also from very recent observational data.

9 Conclusions and Future Developments

In this thesis we have presented a new numerical code developed for studying the formation and evolution of cosmological structures in both baryonic and collisionless components. Collisional matter is treated as a fluid and the corresponding hydrodynamic equations are solved using the PPM scheme on a fixed Eulerian grid. We have described the changes to the basic method required by the cosmological applications. Particular care has been taken in including expansion and gravity in the Riemann solver and in the final integration step. This has required the calculation of the characteristic form of the hydrodynamic equations in expanding coordinates. A double formulation of the energy equation has allowed a proper treatment of the highly supersonic flows common in cosmological simulations. The behaviour of the dark matter is described using a standard Particle Mesh N–body technique, modified to allow the use of a variable timestep, as desirable for hydrodynamics. The two components are coupled through the gravitational interaction and the gravitational field is calculated from the Poisson equation using an FFT procedure.

We have presented a series of tests selected for their relevance in cosmological applications, paying attention both to the accuracy of the highest resolution results and to the convergence of the method when lower resolutions are used. The one–dimensional tests show that the code can reproduce properly the expected solutions, even when very low resolution is adopted. In particular we present the results of the shock tube test and of single and multiple pancake formation. The CDM test results can be compared with those

presented by Ryu et al. (1994), Kang et al. (1994) and Gnedin (1995) showing a good agreement. We have then verified that the Lax–Wendroff scheme can safely replace the standard Leap–Frog method for the integration of the N–body dynamical equations. All of these tests have demonstrated that our code can be considered a reliable and useful tool for cosmological studies.

The code has been used to simulate the evolution of cosmological structures in various models, both in one and in three dimensions. We have presented the results of a series of one–dimensional simulations which have been used for testing the different clustering properties of baryonic and dark matter in an expanding background. Initial Gaussian random density perturbations with a power–law spectrum $P(k) \propto k^n$ have been assumed. We have analyzed the distribution of density fluctuations and thermodynamical quantities for different spectral indices n and discussed the statistical properties of clustering in the corresponding simulations. At large scales the final distribution of the two components is very similar while at small scales the dark matter presents a lumpiness which is not found in the baryonic matter. The amplitude of density fluctuations in each component depends on the spectral index n but that of the baryonic matter is always larger than the one in the dark component. This result is also confirmed by the behaviour of the bias factor, which is larger than unity in all the models which we have considered. The final temperatures depend on the initial spectral index: the highest values (10^9 K) are obtained for $n = -1$ and are in proximity of high density regions. In the other models, the typical post–shock temperature are smaller (10^5–10^7 K).

We have then studied the properties of X-ray galaxy clusters in four cold dark matter models with different baryon fraction Ω_{BM} ranging from 5 to 20 per cent. We have run simulations on a box with size 64 h^{-1} Mpc and we have identified the clusters by selecting the peaks in the X-ray luminosity field. We have analyzed these catalogues by computing the mass function, the luminosity function, the temperature distribution and the luminosity-temperature relation. By comparing the predictions of the different models to a series of recent observational results, we have found that only the models with low baryonic

content agree with the data, while models with larger baryon fraction are well outside the 1-σ errorbars. In particular, the analysis of the luminosity functions, both bolometric and in the energy band [0.5–2] keV, requires $\Omega_{BM} \lesssim 0.05$. Moreover we have found that, independently of the cosmological scenario, all the considered quantities have a very little redshift evolution, particularly between $z = 0.5$ and $z = 0$.

Further application of our code can lead to interesting results on other problems related to the process of cosmological structures formation. However our present major effort is dedicated to improve the performances of the codes in order to extend the dynamical range that can be included in the simulations as much as possible. Work is in progress in two different directions.

The first is to introduce local refinements of the computational mesh where overdense structures are forming. The PPM scheme is particularly suitable to this *variable-meshed* solution. In fact the basic PPM method is developed for a general one dimensional Lagrangian approach, and can already account for possible variations of the cell size. Then only minor modifications are required to obtain an hydrodynamical variable-meshed code. Particular care must be taken only in the transition between high and low resolution regions, where the change in the cell size can produce numerical errors which appears in the solution in the form of spurious ripples that propagates affecting the result. In Figure 9.1 we show the solution of the one dimensional shock tube test, using a grid with two different resolutions. In the central part of the grid (where the initial discontinuity is placed) the cell size is Δx. Elsewhere the cell size is $4\Delta x$. The solution is comparable to that obtained in section 4.2 (notice that all the waves - the shock, the rarefaction and the contact discontinuity - have already crossed the boundary between zones of different resolution), although a spurious wave forms at the boundary between the two resolutions and then propagates slowly diffusing. This effect can be reduced if we define a boundary zone which connect smoothly the two different resolution (adaptive boundary). In Figure 9.2 we show the case in which the adaptive boundary zone is composed of four cells with width Δx, $2\Delta x$, $3\Delta x$ and $4\Delta x$ respectively.

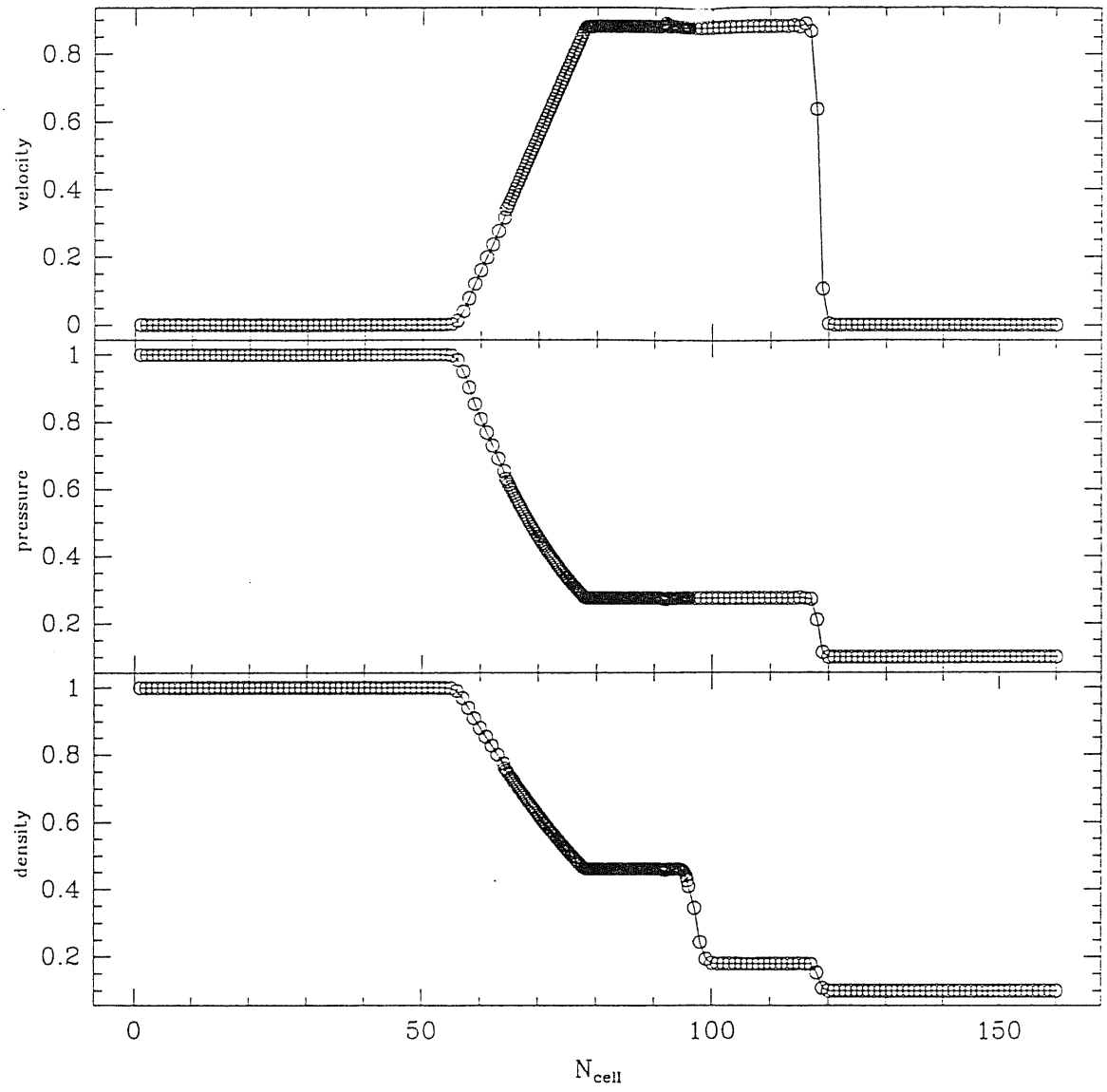

Figure 9.1: Multigrid solution of the shock tube test with no adaptive boundary

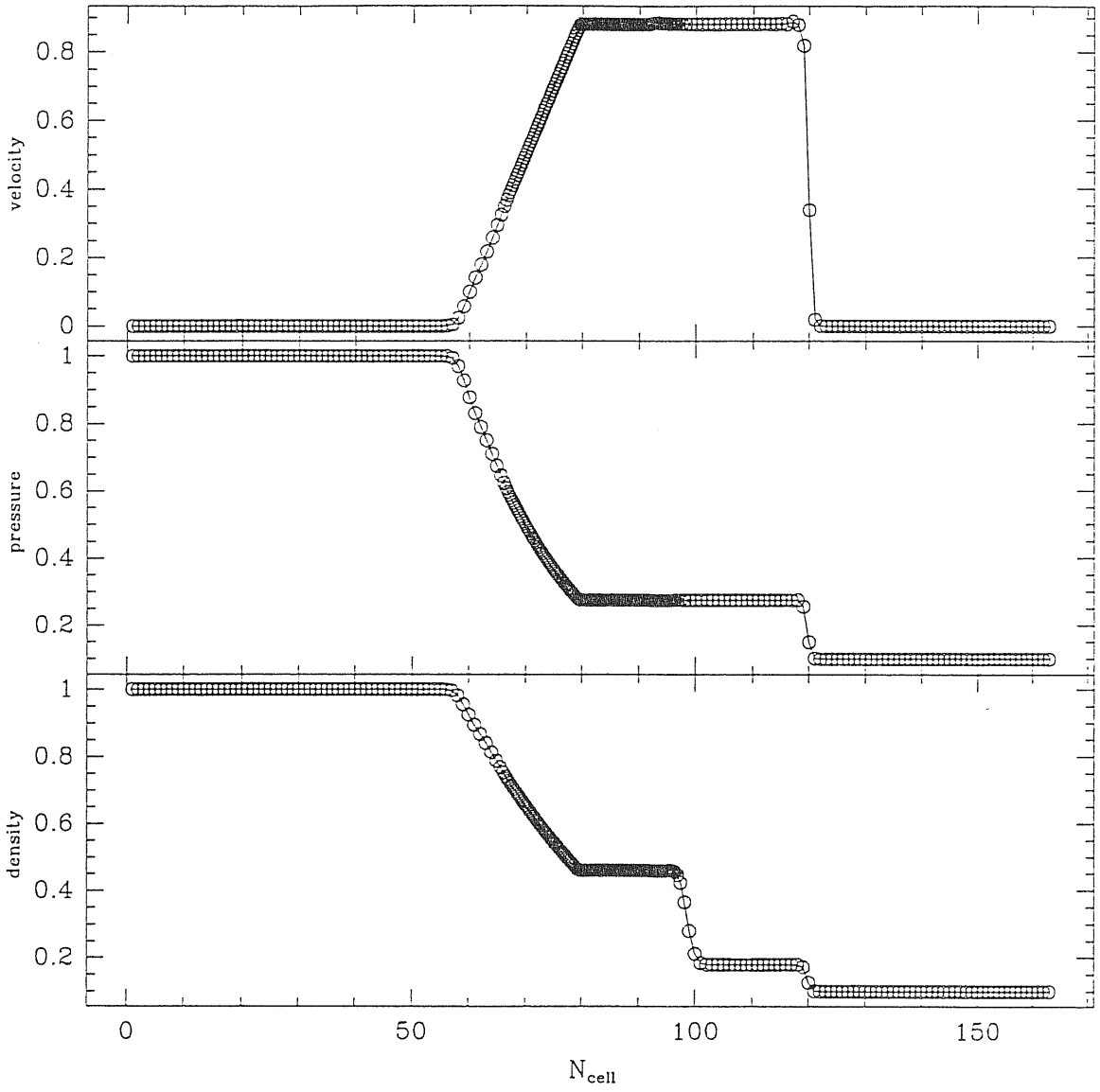

Figure 9.2: Multigrid solution of the shock tube test with adaptive boundary

The variable-meshed extension is not so simple for the gravitational part of the code. In particular FFT can not work on mesh of variable cell size, therefore the use of a multigrid gravitational solver is required. Also the N–body code must be carefully adapted as the change in spatial resolution must be associated also to a change in the mass resolution and so in the weight of the particles between high and low resolution regions.

The second possible direction is take advantage of the properties both of Lagrangian and of Eulerian methods. In particular, we can think of using a Lagrangian method to describe regions in which matter concentrates and which requires high spatial resolution and an Eulerian method to describe lower density regions where high mass resolution is necessary, while high spatial resolution is not so important.

Appendix A

The solution of the Riemann problem, described in detail in section 2.3 (to which we refer for the definition of the quantities used in this appendix), involves an iterative procedure for calculating the values of p^* and v^*. These are the values of the pressure and the velocity of the fluid at the contact discontinuity, which forms in the region between the two waves moving in opposite directions.

A number of Riemann solvers have been developed over the years and different solvers employ different iterative solution techniques with different initial guesses. We have used the method proposed by Van Leer (1979), which ensures good efficiency, a limited computational effort and a good convergency rate.

The Van Leer method is an extension of the Godunov technique (1959, 1961) which relates implicitly p^* to the mass fluxes passing through the left and right waves (A_L and A_R) by the expression

$$p^* = [A_R p_L + A_L p_R + A_L A_R (v_L - v_R)]/(A_L + A_R) , \qquad \text{(A.1)}$$

where

$$A_S = (\gamma \varrho_S p_S)^{1/2} \left[\frac{\gamma+1}{2\gamma} \frac{p^*}{p_S} + \frac{\gamma-1}{2\gamma} \right]^{1/2} \qquad \text{for } p^* \geq p_S \qquad \text{(A.2)}$$

and

$$A_S = \frac{\gamma-1}{2\gamma} (\gamma \varrho_S p_S)^{1/2} \frac{1 - p^*/p_S}{1 - (p^*/p_S)^{(\gamma-1)/2\gamma}} \qquad \text{for } p^* < p_S , \qquad \text{(A.3)}$$

where $S = L$ or R. The two different fluxes are associated to a shock or a rarefaction wave which moves in the S direction.

Van Leer proposed to iterate with respect to the pressure of the states on each side of the contact surface (p^*) and make the flow velocity difference $v_L^* - v_R^*$ equal to zero. Therefore, new values of p^* can be obtained using Newton's method in the form

$$p_{i+1}^* = p_i^* - \frac{v_L^*(p_i^*) - v_R^*(p_i^*)}{v_L^{*'}(p_i^*) - v_R^{*'}(p_i^*)} , \tag{A.4}$$

where the subscript i indicates the i-th iteration and

$$v_L^*(p^*) = v_L - \frac{p^* - p_L}{A_L} \tag{A.5}$$

$$v_R^*(p^*) = v_R + \frac{p^* - p_R}{A_R} . \tag{A.6}$$

The expressions for v_L^* and v_R^* are derived from the wave jump conditions. the quantities $v_L^{*'}$ and $v_R^{*'}$ are the derivatives of v_L^* and v_L^* with respect to p^* and are

$$v_S^{*'} = \pm(A_S^2 + C_S^2)/(2A^3) \qquad \text{for } p^* \geq p_S \tag{A.7}$$

and

$$v_S^{*'} = \pm C_S^{-1}\left[\frac{p^*}{p_S}\right] \qquad \text{for } p^* < p_S , \tag{A.8}$$

where the plus sign holds for $S = R$ and the minus for $S = L$ and $C_S = (\gamma p_S \varrho_S)^{1/2}$.

The initial guess p_0^* to start with the iterative procedure is obtained from the weak waves theory

$$p_0^* = \frac{1}{2}[(p_L + p_R) + k(v_L + v_R)] , \tag{A.9}$$

where

$$k = [\gamma(p_L + p_R)(\varrho_L + \varrho_R)/4]^{1/2} . \tag{A.10}$$

This guess can become inaccurate when strong shocks are involved. We have found that in this case a better guess is given by the condition

$$p_0^* = \max(p_L, p_R) . \tag{A.11}$$

The iterative procedure is stopped when successive values of the pressure differ by some (small) tolerance. At this point the velocity v^* is calculated using the jump conditions, as

$$v^* = (p_L - p_R + A_L v_L + A_R v_R)/(A_L + A_R) \tag{A.12}$$

Bibliography

Abell G.O., 1958, *ApJS*, **3**, 211.

Adams F.T., 1976, *A&A*, **50**, 461.

Anninos P., Norman M.L., Clarke, D.A., 1994, *ApJ*, **436**, 11.

Bardeen J.M., Bond J.R., Kaiser N., Szalay A.S., 1986, *ApJ*, **304**, 15.

Barnes J.E., Hut P., 1986, *Nat*, **324**, 446.

Bartlett J.G., Blanchard A., Silk J., Turner M.S., 1995, *Science*, **267**, 980.

Barnes J., Hut P., 1986, *Nat*, **324**, 446.

Bennett C.L., et al., 1996, *ApJ*, **464**, L1.

Bond J.R. , Szalay A.S., 1983, *ApJ*, 274, 443.

Bonometto S.A., Valdarnini R., 1984, *Phys. Lett.*, **A103**, 369.

Borgani S., Moscardini L., Plionis M., Górski K.M., Holtzman J., Klypin A., Primack J.R., Smith C.C., Stompor R., 1997, *New A*, **1**, 321.

Boris J.P., Book D.L., 1973, *J. Comput. Phys.*, **11**, 38.

Brainerd T., Scherrer R.J., Villumsen J.V., 1992, *ApJ*, **418**, 570.

Brandt A., 1982, *Lectures at the Colorado State University.*

Briel U.G., Henry J.P., Boehringer H., 1992, *A&A*, **259**, L31.

Bryan G.L., Cen R., Norman M.L., Ostriker J.P., Stone J.M., 1994a, *ApJ*, **428**, 405.

Bryan G.L., Norman M.L., Stone J.M., Cen R.Y., Ostriker J.P., 1995, *Comput. Phys. Comm.*, **89**, 149.

Bunn E.F., White M., 1997, *ApJ*, **480**, 6.

Burgers J.M., 1974. *The Nonlinear Diffusion Equation.* Reidel, Dordrecht.

Burles S., Tytler D., 1996. preprint, astro–ph/9603070.

Burns J.O., Ledlow M.J., Loken C., Klypin A., Voges W., Bryan G.L., Norman M.L., White R.A., 1996, *ApJ*, **467**, L49.

Carretti E., Messina A., Ansaloni R., Calori L., 1995a. *Scalable Parallel Computing on Cray Systems*, Berlin 6–8 November 1995.

Carretti E., Messina A., Ansaloni R., Calori L., 1995b. *Congresso Nazionale di Cosmologia*, Frascati 23–25 November 1995.

Carretti E., Messina A., 1997, in preparation.

Carswell R.F., Rauch M., Weymann R.J., Cooke A.J., Webb J.K., 1994, *MNRAS*, **268**, L1.

Cavaliere A., Fusco-Femiano R., 1976, *A&A*, **49**, 137.

Cen R., 1992, *ApJS*, **78**, 341.

Chiang W., Ryu D., Vishniac E.T., 1989, *ApJ*, **339**, 603.

Colella P., 1982, *SIAM J. Sci. Stat. Comput.*, **3**, 76.

Colella P., Woodward P., 1984, *J. Comput. Phys.*, **54**, 174.

Coles P., Melott A.L., Shandarin S.F., 1993, *MNRAS*, **260**, 765.

Coles P., Lucchin F., 1995. *Cosmology: the Origin and Evolution of Cosmic Structure.* Wiley & Sons Ltd., Chichester.

Copi C.J., Shramm D.N., Turner M.S., 1995a, *Science*, **267**, 192.

Copi C.J., Shramm D.N., Turner M.S., 1995b, *Phys. Rev. Lett.*, **75**, 3981.

Courant R, Friedrichs K.O., 1948. *Supersonic Flows and Shock Waves.* Springler-Verlag.

David L.P., Slyz A., Jones C., Forman W., Vrtilek S.D., Arnaud K.A., 1993, *ApJ*, **412**, 479.

David L.P., Jones C., Forman W., 1995, *ApJ*, **445**, 578.

Davis M., Efstathiou G., Frenk C.S., White S.D.M., 1985, *ApJ*, **292**, 371

Davis M., Summers F., Schlegel D., 1992, *Nat*, **359**, 393.

De Grandi S., 1996, *Proc. of Röntgenstrahlung from the Universe*, ed. Zimmermann H.U., Trümper J., Yorke H. (Munich: MPE), 577.

Ebeling H., Edge A.C., Fabian A.C., Allen S.W., Crawford C.S., Böhringer H., 1997, *ApJ*, **479**, L101.

Edge A.C., Stewart G.C., Fabian A.C., Arnaud K.A., 1990, *MNRAS*, **245**, 559.

Efstathiou G., Sutherland W.J., Maddox S.J., 1990, *Nat*, **348**, 705.

Efstathiou G., Bond J.R., White S.D.M., 1992, *MNRAS*, **258**, 1.

Eke V.R., Cole S., Frenk C.S., 1996, *MNRAS*, **282**, 263.

Elbaz D., Arnaud M., Böhringer H., 1995, *A&A*, **393**, 337.

Evrard A.E., 1988, *MNRAS*, **235**, 911.

Evrard A.E., 1990, *ApJ*, **363**, 349.

Fahlman G., Kaiser N., Squires G., Woods D., 1994, *ApJ*, **437**, 56.

Gingold R.A., Monaghan J.J., 1977, *MNRAS*, **181**, 375.

Gnedin N.Y., 1995, *ApJS*, **97**, 231.

Gnedin N.Y., Bertschinger E., 1996, *ApJ*, **470**, 115.

Godunov S.K., 1959, *Mat. Sb.*, **47**, 271.

Godunov S.K., Zabrodin A.V., Prokopov G.P., 1961, *U.S.S.R. Computational Math. and Math. Phys.*, **1**, 1187.

Gourbatov, S.N., Saichev, A.I., Shandarin, S.F., 1985, *Soviet Phys. Dokl.*, **30**, 921.

Górski K.M., Ratra B., Sugiyama N., Banday A.J., 1995, *ApJ*, 444, L65.

Greengard L., Rokhlin V., 1987, *J. Comput. Phys.*, **73**, 125.

Harten A., 1983, *J. Comp, Phys.*, **49**, 357.

Henry J.P., Arnaud K.A., 1991, *ApJ*, **372**, 410.

Hernquist L., Katz N.S., 1989, *ApJS*, **64**, 715.

Hockney R.W., Eastwood J.W., 1981, *Computer Simulations Using Particles.* McGraw-Hill, New York, NY.

Huang K., 1963, *Statistical Mechanics.* Wiley $ Sons. U.S.A.

Jones C., Forman W, 1982, *ApJ*, **276**, 38.

Jing Y.P., Mo H.J., Boerner G., Fang L.Z., 1994, *A&A*, **284**, 703.

Kang H., Cen R., Ostriker J.P., Ryu D., 1994a, *ApJ*, **428**, 1.

Kang H., Ostriker J.P., Cen R., Ryu D., Hernquist L., Evrard A.E., Bryan G.L., Norman M.L., 1994b, *ApJ*, **430**, 83.

Karsas W., Latter R., 1981, *ApJS*, **6**, 167.

Kates R., Muller V., Gottloeber S., Mucket J.P., Retzlaff J., 1995, *MNRAS*, **277**, 1254.

Kellog E.M., 1975, *ApJ*, **197**, 689.

Kent S.M., Sargent W.L., 1983, *Astron. J.*, **88**, 697.

Kernan P.J., Sarkar S., 1996 Case Western Preprint, astro-ph/9603045.

King I.R., 1962, *Astron J.*, **83**, 1549.

Kofman, L., Shandarin, S.F., 1988, *Nat*, **334**, 132.

Kofman L., Starobinsky A.A., 1985, *Sov Astron. Lett.*, **11**, 271.

Kofman L., Gnedin N.Y., Bahcall N.A., 1993, *ApJ*, **413**, 1.

Krauss L.M., Kernan P., 1995, *Phys. Lett. B*, **347**, 347.

Krauss L.M., Turner M.S., 1995, *Gen. Rel. Grav.*, **27**, 1137.

Landau L.D., Lifshits E.M., 1959, *Fluid Dynamics.* Pergamon Press Ltd., London.

Liddle A.R., Lyth D.H., 1993, *Phys. Rep.*, **231**, 1.

Liddle A.R., Lyth D.H., Roberts D., Viana P.T.P., 1996a, *MNRAS*, **278**, 644.

Liddle A.R., Lyth D.H., Schaefer R.K., Shafi Q., Viana P.T.P., 1996b, *MNRAS*, **281**, 531.

Liddle A.R., Lyth D.H., Viana P.T.P., White M., 1996c, *MNRAS*, **282**, 281.

Lucy L.B., 1977, *Astron J.*, **82**, 1013.

Markevitch R., Mushotzky R., Inoue H., Yamashita K., Furuzawa A., Tawara Y., 1996, *ApJ*, **456**, 437.

Matarrese S., Lucchin F., Moscardini L., Saez D., 1992, *MNRAS*, **259**, 437.

Miralda-Escudeé J., Babul A., 1995, *ApJ*, **449**, 18.

Moscardini L., 1990, *Simulazioni Cosmologiche a N-corpi con Condizioni Iniziali non Gaussiane.* PhD Thesis. University of Bologna.

Mushotzky R.F., 1984, *Phys. Scripta*, **T7**, 157.

Mushotzky R.F., Scharf C.A., 1997, *ApJ*, **482**, L13.

Navarro J.F., Frenk C.S., White S.D.M., 1995, *MNRAS*, **275**, 720.

Oran E.S., Boris J.P., 1987. *Numerical Simulation of Reactive Flow*, Elsevier, New York.

Olive K.A., Steigman G., 1995, *ApJS*, **97**, 49.

Ostriker J.P., Steinhardt P.J., 1995, *Nat*, **377**, 600.

Padmanabhan T., 1993, *Structure Formation in the Universe* Cambridge University Press, Cambridge, G.B.

Peebles P.J.E., 1980, *The Large–Scale Structure of the Universe.* Princeton University Press, Princeton.

Peebles P.J.E., 1984, *ApJ*, **284**, 439.

Peebles P.J.E., 1993, *Principles of Physical Cosmology.* Princeton University Press, Princeton.

Pogosyan D.Yu., Starobinsky A.A., 1995, *ApJ*, **447**, 465.

Press W.H., Schechter P., 1974, *ApJ*, **187**, 452.

Primak J.R., 1997, preprint, astro-ph/9707285.

Quilis V., Ibáñez J.M., Saez D., 1994, *A&A*, **286**, 1.

Quilis V., Ibáñez J.M., Saez D., 1996, *ApJ*, **469**, 11 astro–ph/9604037.

Ratra B., Peebles P.J.E., 1994, *ApJ*, **432**, L5.

Rauch M., Sargent W.L.W., Womble D.S., Barlow T.A., 1996, *ApJ*, **467**, L5

Roache P.J., 1982. *Computational Fluid Dynamics*, Hermosa Publishers, Albuquerque.

Roe P.L., 1981, *J. Comput. Phys.*, **43**, 357.

Rugers M., Hogan C.J., 1996a, *ApJ*, **459**, L1.

Rugers M., Hogan C.J., 1996b, *Astron.J*, **111**, 2135.

Rybicki G.B., Lightman A.P., 1979, *Radiative Processes in Astrophysics.* Wiley & Sons, New York, U.S.A.

Ryu D., Ostriker J.P., Kang H., Cen R., 1993, *ApJ*, **414**, 1.

Sanders R.H., Prendergast K.H., 1974, *ApJ*, **188**, 489.

Sarazin C.L., 1988, *X-ray Emission from Clusters of Galaxies*, Cambridge University Press, Cambridge.

Sasselov D., Goldwirth D.S., 1995, *ApJ*, **444**, L5.

Schechter P.L., 1976, *ApJ*, **203**, 297.

Scully S.T., Casse M., Olive K.A., Shramm D.N., Truran J., Vangioni-Flam E., 1996, *ApJ*, **462**, 960.

Shaefer R.K., Shafi Q., 1994, *Phys. Rev. D*, **49**, 4990.

Shafi Q., Stecker F.W., 1984, *Phys. Rev. Lett.*, **53**, 1292.

Shandarin S.F., Zeldovich Ya.B., 1989, *Rev. Mod. Phys.*, **61**, 185.

Shapiro P.R., Struck-Marcell C., 1985, *ApJ*, **57**, 205.

Skilmann E.D., Terlevich R., Garnett D.R., 1996, *ApJ.*

Smoot G.F., et al., 1992, *ApJ*, **396**, L1.

Sod G.A., 1977, *J. Fluid. Mech.*, **83**, 785.

Songaila A., Wampler E.J., Cowie L.L., 1997, *Nat*, **385**, 137.

Songaila A., Cowie L.L., Hogan C.J., Rugers M., 1994, *Nat*, **368**, 599.

Sornborger A., Fryxell B., Olson K., MacNeice P., 1996, preprint astro–ph/9608019.

Spitzer L., 1978. *Physical Processes in the Interstellar Medium.* Wiley & Sons, New York.

Steinmetz M., Muller E., 1993, *A&A*, **268**, 391.

Stompor R., Górski K.M., Banday A.J., 1995, *MNRAS*, **277**, 1225.

Strang G., 1968, SIAM *J. Num. Anal.*, **5**, 506.

Suginohara T., Suto Y., 1991, *PASJ*, **43**, L17.

Sugiyama N., 1995, *ApJS*, **100**, 281.

Taylor A.N., Rowan-Robinson M., 1992, *Nat*, **359**, 396.

Tormen G., 1997, *MNRAS*, in press, astro-ph/9611078.

Turner M.S., Steigman G., Krauss L.M., 1984, *Phys. Rev. Lett.*, **52**, 2090.

Turner M.S., Truran J.W., Sharamm D.N., Copi C.J., 1996, *ApJ*, **323**, 423.

Tytler D., Fan X.-M., Burles S., 1996, *Nat*, **381**, 207.

Van Leer B., 1979, *J. Comput. Phys.*, **32**, 101.

Viana P.T.P., Liddle A.R., 1996, *MNRAS*, **281**, 323.

Weinberg D.H., Miralda-Escudé J., Hernquist L., Katz N., 1997, preprint, astro-ph/9701012.

White D.A., Fabian A.C., 1995, *MNRAS*, **273**, 72.

White D.A., Scott D., Silk J., Davis M., 1995b, *MNRAS*, **276**, L69.

White M., 1996, *Phys. Rev.*, **D53**, 3011.

White M., Viana P.T.P., Liddle A.R., Scott D., 1996, *MNRAS*, **283**, 107.

White S.D.M., Navarro J.F., Evrard A.E., Frenk C.S., 1993, *Nat*, **366**, 429.

White S.D.M., Efstathiou G., Frenk C.S., 1993, *MNRAS*, **262**, 1023.

Wilson T.L., Rood R.T., 1994, *ARA&A*, **32**, 191.

Woodward P., Colella P., 1984, *J. Comput. Phys.*, **54**, 115.

Yamamoto K., Bunn E.F., 1996, *ApJ*, **464**, 8.

Zalesak, S., 1979, *J. Comput. Phys.*, **31**, 335.

Zel'dovich Ya. B., 1970a, *A&A*, **6**, 164.

Zel'dovich Ya. B., 1970b, *A&A*, **5**, 84.

Acknowledgments

At the end of my Ph.D program, I would like to thank my supervisor Prof. John Miller for the interest always shown for me and my work and for the interesting and useful discussions that have helped me to improve the results of my efforts. I am also very grateful to Prof. Dennis Sciama, head of the Astrophysics sector at SISSA, for having always supported me for any need I had during this period.

I am particularly grateful to Dr. Ornella Pantano and Dr. Lauro Moscardini for the continuous help and support dedicated to myself from the beginning of my Laurea thesis to the end of the Ph.D. program, but, first of all, for having behaved always as real friends with me. I want also to thank Prof. Francesco Lucchin for the interest always shown for my work and Prof. Sabino Matarrese for a number of useful suggestions.

Finally I want to thank all the people which have helped me in some part of my work, like Dr. Antonio Lanza, Prof. J.P. Ostriker, Dr. Renyue Cen and Dr. Ettore Carretti.